QC
1
.U56
vol.64A
no.1

Volume 64A

Number 1

Jan.–Feb. 1960

THE UNIVERSITY OF MICHIGAN
MAR 1 1960
LIBRARY

Journal of Research

of the

NATIONAL BUREAU OF STANDARDS

A. PHYSICS AND CHEMISTRY

Journal of Research

of the

National Bureau of Standards

A. Physics and Chemistry

JAN.–FEB. • 1960

VOLUME • 64A

NUMBER • 1

Editor: U. Fano

Associate Editors: L. M. Kushner
J. M. Richardson

Publication dates:
Feb. 1, Apr. 1, June 1, Aug. 1, Oct. 1, Dec. 1, 1960.

JOURNAL OF RESEARCH

The National Bureau of Standards Journal of Research reports research and development in the fields of activity shown at right. Also included from time to time are survey articles and compilations of information on topics closely related to the Bureau's scientific and technical program.

The Journal is published in four separate sections as follows:

A. Physics and Chemistry

Contains papers of interest primarily to scientists working in these fields. Issued six times a year. Annual subscription: domestic, $4.00; foreign, $4.75.

B. Mathematics and Mathematical Physics

Presents studies and compilations designed mainly for the mathematician and the theoretical physicist. Issued quarterly. Annual subscription: domestic, $2.25; foreign, $2.75.

C. Engineering and Instrumentation

Reports research and development results of interest chiefly to the engineer and the applied scientist. Issued quarterly. Annual subscription: domestic, $2.25; foreign, $2.75.

D. Radio Propagation

Reports work in radio propagation, upper atmospheric physics, and communications. Issued six times a year. Annual subscription: domestic, $4.00; foreign, $4.75.

Functions and Activities

The functions of the National Bureau of Standards are set forth in the Act of Congress, March 3, 1901, as amended. These include the development and maintenance of the national standards of measurement and the provision of means and methods for making measurements consistent with these standards; the determination of physical constants and properties of materials; the development of methods and instruments for testing materials, devices, and structures; advisory services to government agencies on scientific and technical problems; invention and development of devices to serve special needs of the Government; and the development of standard practices, codes, and specifications. The work includes basic and applied research, development, engineering, instrumentation, testing, evaluation, calibration services, and various consultation and information services. The Bureau also serves as the Federal technical research center in a number of specialized fields. The scope of activities of the National Bureau of Standards is suggested in the following listing of the divisions and sections engaged in technical work.

Washington, D.C.

Electricity and Electronics. Resistance and Reactance. Electron Devices. Electrical Instruments. Magnetic Measurements. Dielectrics. Engineering Electronics. Electronic Instrumentation. Electrochemistry.

Optics and Metrology. Photometry and Colorimetry. Optical Instruments. Photographic Technology. Length. Engineering Metrology.

Heat. Temperature Physics. Thermodynamics. Cryogenic Physics. Rheology. Molecular Kinetics. Free Radicals Research.

Atomic and Radiation Physics. Spectroscopy. Radiometry. Mass Spectrometry. Solid State Physics. Electron Physics. Atomic Physics. Neutron Physics. Radiation Theory. Radioactivity. X-ray. High Energy Radiation. Nucleonic Instrumentation. Radiological Equipment.

Chemistry. Organic Coatings. Surface Chemistry. Organic Chemistry. Analytical Chemistry. Inorganic Chemistry. Electrodeposition. Molecular Structure and Properties of Gases. Physical Chemistry. Thermochemistry. Spectrochemistry. Pure Substances.

Mechanics. Sound. Mechanical Instruments. Fluid Mechanics. Engineering Mechanics. Mass and Scale. Capacity, Density, and Fluid Meters. Combustion Controls.

Organic and Fibrous Materials. Rubber. Textiles. Paper. Leather. Testing and Specifications. Polymer Structure. Plastics. Dental Research.

Metallurgy. Thermal Metallurgy. Chemical Metallurgy. Mechanical Metallurgy. Corrosion. Metal Physics.

Mineral Products. Engineering Ceramics. Glass. Refractories. Enameled Metals. Constitution and Microstructure.

Building Technology. Structural Engineering. Fire Protection. Air Conditioning, Heating, and Refrigeration. Floor, Roof, and Wall Coverings. Codes and Safety Standards. Heat Transfer. Concreting Materials.

Applied Mathematics. Numerical Analysis. Computation. Statistical Engineering. Mathematical Physics.

Data Processing Systems. SEAC Engineering Group. Components and Techniques. Digital Circuitry. Digital Systems. Analog Systems. Applications Engineering.

• Office of Basic Instrumentation. • Office of Weights and Measures.

Boulder, Colorado

Cryogenic Engineering. Cryogenic Equipment. Cryogenic Processes. Properties of Materials. Gas Liquefaction.

Radio Propagation Physics. Upper Atmosphere Research. Ionosphere Research. Regular Prediction Services. Sun-Earth Relationships. VHF Research. Radio Warning Services. Airglow and Aurora. Radio Astronomy and Arctic Propagation.

Radio Propagation Engineering. Data Reduction Instrumentation. Radio Noise. Tropospheric Measurements. Tropospheric Analysis. Propagation-Terrain Effects. Radio-Meteorology. Lower Atmosphere Physics.

Radio Standards. High-Frequency Electrical Standards. Radio Broadcast Service. Radio and Microwave Materials. Electronic Calibration Center. Microwave Circuit Standards.

Radio Communication and Systems. Low Frequency and Very Low Frequency Research. High Frequency and Very High Frequency Research. Modulation Systems. Antenna Research. Navigation Systems. Systems Analysis. Field Operations.

U.S. DEPARTMENT OF COMMERCE
Frederick H. Mueller, Secretary

NATIONAL BUREAU OF STANDARDS
A. V. Astin, Director

Order all publications from the Superintendent of Documents
U.S. Government Printing Office, Washington 25, D.C.

Use of funds for printing this publication approved by the Director of the Bureau of the Budget (June 24, 1958).

DEPOSITED BY THE UNITED STATES OF AMERICA

JOURNAL OF RESEARCH of the National Bureau of Standards—A. Physics and Chemistry
Vol. 64A, No. 1, January–February 1960

The "1958 He^4 Scale of Temperatures" [1]

Part 1. Introduction

F. G. Brickwedde [2]

Part 2. Tables for the 1958 Temperature Scale

H. van Dijk,[3] M. Durieux,[3] J. R. Clement,[4] and J. K. Logan [4]

(Revision: May 1, 1959)

The generally used practical scale of temperatures between 1° and 5.2° K is the He^4 vapor pressure scale based on an accepted vapor pressure equation or table. In Sèvres (near Paris), October 1958, the International Committee on Weights and Measures recommended for international use the "1958 He^4 Scale" based on a vapor pressure table arrived at through international cooperation and agreement. This table resulted from a consideration of all reliable He^4 vapor pressure data obtained using gas thermometers, and paramagnetic susceptibility and carbon resistor thermometers. The theoretical vapor pressure equation from statistical thermodynamics was used with thermodynamic data on liquid He^4 and the vapor equation of state to insure satisfactory agreement of the vapor pressure table with reliable thermodynamic data.

Part 1. Introduction

The International Committee on Weights and Measures at a meeting in Sèvres (near Paris), France, September 29 to October 3, 1958, approved the "1958 He^4 Vapor Pressure Scale of Temperatures" as an international standard for thermometry from 1° to 5.2° K. This was the culmination of several years of intensive research and cooperation on the helium vapor pressure scale at the Kamerlingh Onnes Laboratory in Leiden, Holland, and the U.S. Naval Research Laboratory in Washington.

The vapor pressure of liquid He^4 has for a long time been used as a standard for thermometry between 1° and 5.2° K. The first measurements of thermodynamic temperatures in the liquid He^4 range were made with constant volume gas thermometers filled with He^4. Simultaneous measurements of the vapor pressure of liquid helium in temperature equilibrium with the gas thermometer established a vapor pressure-temperature relation which then was used as the basis for determining thermodynamic temperatures from vapor pressure measurements. With these vapor pressure-gas thermometer measurements there were measurements of He^4 vapor pressures made simultaneously with measurements of the He^4 isotherms from which temperatures were obtained by extrapolating the isotherms to zero density ($N/V \to 0$) in accordance with the virial equation of state:

$$pV/N = RT\,[1 + B\,(N/V) + C\,(N/V)^2 + \ldots] \quad (1)$$

After the latent and specific heats of liquid He^4 had been measured, the experimental vapor pressure-temperature relation was improved through the use of the theoretical vapor pressure (P) equation:

$$\ln P = i_0 - \frac{L_0}{RT} + \frac{5}{2}\ln T - \frac{1}{RT}\int_0^T S_l\,dT + \frac{1}{RT}\int_0^P V_l\,dP + \epsilon \quad (2)$$

where

$$i_0 \equiv \ln\,(2\pi m)^{3/2}k^{5/2}/h^3 \quad (3)$$

and

$$\epsilon \equiv \ln\,(PV/NRT) - 2B\,(N/V) - (\tfrac{3}{2})\,C\,(N/V)^2. \quad (4)$$

L_0 is the heat of vaporization of liquid He^4 at 0° K, S_l and V_l are the molar entropy and volume of liquid He^4, m is the mass of a He^4 atom, B and C are the virial coefficients in eq (1), and the other symbols have their usual meaning. Both theoretically calculated and directly measured vapor pressures were considered in arriving at the 1958 He^4 Temperature Scale.

Equation (2) presupposes that the thermodynamic properties entering the equation have been measured on the thermodynamic scale, otherwise the use of this equation for the calculation of P is not valid. In practice, however, these properties are measured on an empirical scale that only approximates the thermodynamic scale. In general this empirical scale has been a He^4 vapor pressure scale based on gas thermometer measurements.

[1] This paper will be available as NBS Monograph 10 from the Superintendent of Documents, U.S. Government Printing Office, Washington 25, D.C.
[2] Consultant to NBS. Permanent address: College of Chemistry and Physics, Pennsylvania State University, University Park, Pa.
[3] Kamerlingh Onnes Laboratory, Leiden, Netherlands.
[4] U.S. Naval Research Laboratory, Washington, D.C.

As T is lowered, the fourth, fifth, and sixth terms in eq (2) become smaller and less important relative to the first three terms. At 1.5° K, the inclusion or exclusion of the sum of the fourth, fifth, and sixth terms in eq (2) affects the temperature calculated from a given value of P by only 0.0005 deg. It may be said then, that below 1.5° K, the vapor pressure of He^4 is in effect really determined, within the present accuracy of the vapor pressure measurement, by a single empirical constant, the heat of vaporization of liquid He^4 at 0° K. At present, L_o for He^4 is normally calculated from vapor pressure data obtained with a gas thermometer. The magnitude of the last three terms in eq (2) increases rather rapidly with rising T, and above the λ-point (2.172° K) the accuracy of the evaluation of these terms is a very important consideration.

In Amsterdam in 1948, on the occasion of a General Assembly of the International Union of Physics, a small group of low temperature physicists, meeting informally, agreed to use and recommend for temperature measurements between 1° and 5.2° K, a table of vapor pressures ot He^4, then in use in Leiden, which came to be known as the "1948 Scale" [1].[5] This scale has sometimes been referred to as the "1949" Scale. From 1° to 1.6° K, the "1948 Scale" was based on vapor pressures calculated by Bleaney and Simon [2] using eq (2). From 1.6° to 5.2° K, the scale was based on measured vapor pressures and temperatures determined with gas thermometers. From 1.6° to 4.2° K, it was based primarily on the vapor pressure measurements of Schmidt and Keesom [3].

Even in 1948, when the "1948 Scale" was agreed to, there was evidence in the measurements and calculations of Kistemaker [4] that the "1948 Scale" deviated significantly from the thermodynamic scale. However, it was thought at the time that, on general principles, indicated changes in an existing scale should be made only after these changes had been confirmed. With improvements in the precision and accuracy of physical measurements at low temperatures, irregularities appeared in the temperature variation of physical properties between 1° and 5° K that were in the main reproducible in different substances and properties and were, therefore, attributable to errors in the "1948 Scale" [5]. Stimulated by these results which corroborated Kistemaker's work, the investigations of the He^4 vapor pressure scale were undertaken that culminated in the "1958 He^4 Scale."

Paramagnetic susceptibility and carbon resistor thermometers were later employed in investigations of the He^4 vapor pressure-temperature relation [6]. These thermometers were used for the interpolation of temperatures between calibration points (temperatures) using an assumed relation connecting temperature and paramagnetic susceptibility or carbon resistance for the calculation of the temperatures. For suitably chosen paramagnetic salts, the Curie-Weiss Law was assumed to hold:

$$\chi=\frac{C}{T+\Delta} \tag{5}$$

where χ is the magnetic susceptibility and C and Δ are empirical constants. Measurements at two temperatures would suffice to determine these two empirical constants if the measurement were really of χ or a quantity directly proportional to χ. However, a calibration of the paramagnetic thermometer at a third calibration temperature is necessary because the arbitrariness in the size and arrangement of the paramagnetic salt samples and the induction coils that surround the salt sample for the susceptibility measurement make the measurement a linear function of χ. Interpolation equations for carbon resistor thermometers are not as simple as eq (5) and do not have a theoretical basis. Hence, vapor pressure data obtained with carbon resistor thermometers are of more limited usefulness for the determination of the He^4 vapor pressure-temperature relation. Clement used carbon thermometer data to examine the derivative $d\ (\ln P)/\ d\ (1/T)$, [7].

Important use has been made of He^4 vapor pressure measurements made with magnetic susceptibility and carbon resistor thermometers in arriving at the "1958 He^4 Scale." These vapor pressure measurements were considered along with those made with gas thermometers and vapor pressures calculated using eq (2). Temperature measurements with magnetic and carbon resistor thermometers are much simpler to make than measurements with gas thermometers, and hence vapor pressure data obtained with magnetic and carbon resistor thermometers are more numerous. Also, the measurements made with these secondary thermometers are more precise (to be distinguished from accurate) which makes them especially useful for interpolation between the gas thermometer data.

There are, accordingly, three practical methods for determining the He^4 vapor pressure-temperature relation: (1) By use of the direct vapor pressure measurements made with gas thermometers, (2) through the use of eq (2) with some vapor pressure-gas thermometer data, and (3) through the use of vapor pressure measurements with secondary thermometers which have been calibrated using some gas thermometer data. If all the pertinent experimental data were accurate and all temperatures were on the thermodynamic scale, these three methods would yield results in good agreement with each other, and any one might be relied upon for the construction of the He^4 vapor pressure-temperature table defining the scale. Because of experimental errors, however, the vapor pressures obtained by the different methods differ when carried to the limit of the sensitivity of the measurements. For He^4 between 1° and 4.5° K, different choices of the methods and different selections of the experimental data used, weighting factors and corrections to the published data yield scales all within about 4 millidegrees of each other. The

[5] Figures in brackets indicate the literature references on page 4.

primary evidence for this is that 4 millidegrees is the maximum difference between the L55 Scale [8] obtained by method (2) and the 55E Scale [9] obtained by method (3). This then is a measure of the range (total spread) of uncertainty at present in the He^4 vapor pressure scale of temperatures between 1° and 4.5° K.

All published He^4 vapor pressure measurements, and thermodynamic data needed for eq (2) were independently studied and correlated by H. Van Dijk and M. Durieux at the Kamerlingh Onnes Laboratory in Leiden [8] and by J. R. Clement and J. K. Logan at the U.S. Naval Research Laboratory in Washington [9]. As far as possible, the experimental data of the original investigators were recalculated on the basis of later knowledge of the temperature scale, fundamental constants, and the properties of He^4. In some cases, limitations were imposed on these recalculations by the incomplete reporting of the experimental data by the original investigator.

After working independently, van Dijk and Clement cooperated to compromise their differences. They met first in Leiden, August 1955 and later in Washington, summer of 1957. From January 22 to March 14, 1958, Logan worked at Leiden, and later represented Clement at a conference in Leiden, June 1958, at which agreement was reached on the "1958 He^4 Scale." This cooperation was an important factor in the improvement of the scale.

Where the differences between the values obtained by handling the experimental data differently are largest (4 millidegrees), the "1958 Scale" falls between the extremes. At other places it is close to the mean of these values and at no place does it deviate by more than 2 millidegrees from the mean. The estimated uncertainty of the "1958 He^4 Scale" is accordingly ± 2 millidegrees between 1° and 4.5° K. At higher temperatures, the estimated uncertainty is larger.

Now that the International Committee on Weights and Measures has recommended the "1958 He^4 Scale" as an international standard it is presumed that henceforth the International Committee on Weights and Measures will take the initiative in improving the scale when changes are needed. Before the International Committee on Weights and Measures assumed responsibility for the He^4 vapor pressure scale, the Commission on Very Low Temperature Physics in the International Union of Pure and Applied Physics concerned itself with the scale. This began with the informal meeting in Amsterdam in 1948 that resulted in the "1948 Scale." At the Low Temperature Conferences sponsored by the Commission on Very Low Temperature Physics of the International Union of Physics at Paris in 1955, and at Madison, Wisconsin, in 1957, sessions were held at which the He^4 vapor pressure scale of temperatures was discussed.

The National Bureau of Standards sponsored meetings, for discussion of the helium vapor pressure scale of temperatures, held at the NBS during the spring meetings of the American Physical Society in Washington, 1955 and 1957. Also, the NBS encouraged cooperation in reaching national and international agreement on the scale. It initiated or promoted the meetings for discussion of the differences between the L55 and 55E Scales proposed respectively by Van Dijk and Durieux, and by Clement. These were the meetings held August 26 and 27, 1955 in Leiden (before the Low Temperature Conference in Paris) [10], July 30, 31, and August 1, 1957 in Washington (before the Low Temperature Conference in Madison) [11], and June 13, 14, and 16, 1958 in Leiden (before the meeting of the Advisory Committee on Thermometry of the International Committee on Weights and Measures in Sèvres) [12]. Also, the National Bureau of Standards promoted the arrangement which sent Dr. Logan of the U.S. Naval Research Laboratory to work in the Kamerlingh Onnes Laboratory from January 22, to March 14, 1958.

The Scale agreed upon at Leiden, June 13 to 16, 1958 was presented to the Advisory Committee on Thermometry of the International Committee on Weights and Measures at its meeting in Sèvres, June 20 and 21, 1958. The recommendation of the Advisory Committee to the International Committee was as follows [12]:

"Le Comité Consultatif de Thermométrie,
"ayant reconnu la nécessité d'établir dans le domaine des très basses températures une échelle de température unique,
"ayant constaté l'accord général des spécialistes dans ce domaine de la physique,
"recommande pour l'usage général l' "Echelle ^{4}He 1958," basée sur la tension de vapeur de l'hélium, comme définie par la table annexée.
"Les valeur des températures dans cette échelle sont désignées par le symbole T_{58}."

The table of He^4 vapor pressures that was sent to the International Committee with this recommendation was the table distributed at the Kamerlingh Onnes Conference on Low Temperature Physics at Leiden, June 23 to 28, 1958. It was published in the Proceedings of the Kamerlingh Onnes Conference [13].

On the recommendation of its Advisory Committee on Thermometry, the International Committee on Weights and Measures approved the "1958 He^4 Scale of Temperatures" at its meeting at Sèvres, September 29 to October 3, 1958.

The table adopted by the International Committee on Weights and Measures was a table of vapor pressures at hundredth degree intervals. This table was expanded by Clement and Logan making table I of this paper with millidegree entries. Table I was inverted to give tables II and III which express T as a function of vapor pressures. Auxiliary tables were added including a table of the differences between the 1958 Scale and other earlier used scales. Linear interpolation is valid for all tables except at the lower temperature end of table IV.

The assistance at Leiden of H. ter Harmsel and C. van Rijn, students of Dr. H. van Dijk at the Kamerlingh Onnes Laboratory, with the computations for the defining and auxiliary tables is gratefully acknowledged.

Various members of the Cryogenics Branch of the Naval Research Laboratory at Washington assisted with numerous calculations which contributed toward the development of the present scale. This assistance, especially that of Dr. R. T. Swim, is gratefully acknowledged.

References

[1] H. van Dijk and D. Shoenberg, Nature **164,** 151 (1949); Procès-Verbaux du Comité Consultatif de Thermométrie auprès du Comité International des Poids et Mesures, session de 1952, p. T 151 (Gauthier-Villars, Paris, France).

[2] B. Bleaney and F. Simon, Trans. Faraday Soc. **35,** 1205 (1939).

[3] G. Schmidt and W. H. Keesom, Leiden Comm. 250b and c, Physica **4,** 963 and 971 (1937).

[4] J. Kistemaker and W. H. Keesom, Leiden Comm. 269b and c, Physica **12,** 227 and 272 (1946); J. Kistemaker, Leiden Comm. Suppl. 95a, Physica **12,** 281 (1946).

[5] See: H. van Dijk, Proc. Intern. Conf. Physics Very Low Temp., Mass. Inst. Technol., p. 118 (1949); R. D. Worley, M. W. Zemansky, and H. A. Boorse, Phys. Rev. **93,** 45 (1954); R. A. Erickson and L. D. Roberts, Phys. Rev. **93,** 957 (1954); J. R. Clement, Phys. Rev. **93,** 1420 (1954); R. Berman and C. A. Swenson, Phys. Rev. **95,** 311 (1954); W. E. Keller, Phys. Rev. **97,** 1 (1955), **98,** 1571 (1955), and **100,** 1790 (1955); H. van Dijk, Temperature, its measurement and control **2,** p. 199 (Reinhold Publishing Corp., New York, N. Y., 1955) and Leiden Comm. Suppl. 112c; W. S. Corak, M. P. Garfunkel, C. B. Satterthwaite, and A. Wexler, Phys. Rev. **98,** 1699 (1955); J. R. Clement, J. K. Logan, and J. Gaffney, Phys. Rev. **100,** 743 (1955); E. Ambler and R. P. Hudson, J. Research NBS **56,** 99 (1956) RP2654, and **57,** 23 (1956) RP2689.

[6] H. van Dijk, Proc. Intern. Conf. Physics Very Low Temp., Mass. Inst. Technol., p. 118 (1949); R. A. Erickson and L. D. Roberts, Phys. Rev. **93,** 957 (1954); H. van Dijk, Temperature, its measurement and control **2,** p. 199 (Reinhold Publishing Corp., New York, N.Y., 1955) and Leiden Comm. Suppl. 112c; E. Ambler and R. P. Hudson, J. Research NBS **56,** 99 (1956) RP2654 and **57,** 23 (1956) RP2689; H. van Dijk and M. Durieux, Progress in low temperature physics, vol. II, chap. XIV (North-Holland Publishing Co., Amsterdam, Netherlands, 1957).

[7] J. R. Clement, Low temperature physics and chemistry, Proc. Fifth Intern. Conf., p. 187 (Univ. Wis. Press, Madison, Wis., 1958).

[8] H. van Dijk and M. Durieux, Proc. Conf. Physics Low Temp., Paris, 1955, p. 595 (Annexe 1955–3, Suppl. au bulletin de l'Institut Intern. du Froid, Paris); Progress in low temperature physics, vol. II, chap. XIV (North-Holland Publishing Co., Amsterdam, Netherlands, 1957); and Leiden Comm. Suppl. 113c, Physica **24,** 1 (1958).

[9] J. R. Clement, J. K. Logan, and J. Gaffney, Proc. Conf. Physics Low Temp., Paris, 1955, p. 601 (Annexe 1955–3, Suppl. au bulletin de l'Institut Intern. du Froid, Paris); Phys. Rev. **100,** 743 (1955); U.S. Naval Research Rept. 4542 (Wash., May 1955); Liquid helium vapor pressure-temperature scale, rept. compiled by J. R. Clement, distributed at the Baton Rouge, La. Conf. Low Temp. Physics and Chem. (Dec. 1955); J. R. Clement, Low temperature physics and chemistry, Proc. Fifth Intern. Conf., p. 187 (Univ. Wis. Press, Madison, Wis., 1958).

[10] F. G. Brickwedde, Report on the conference agreement on the helium vapor pressure scale of temperatures, Proc. Conf. Physics Low Temp., Paris, 1955, p. 608 (Annexe 1955–3, Suppl. au bulletin de L'Institut Intern. du Froid, Paris).

[11] See F. G. Brickwedde, Physics Today **11,** 23 (1958).

[12] F. G. Brickwedde, Physica **24,** Suppl. p. S 128 (1958).

[13] H. van Dijk, M. Durieux, J. R. Clement, and J. K. Logan, Physica **24,** Suppl., S 129 (1958); H. van Dijk and M. Durieux, Leiden Comm. Suppl. 115a, Physica **24,** 920 (1958); Procès-Verbaux des Séances du Comité International des Poids et Mesures—2e Serie, tome 26–A, Annexe T22 in the Procès-Verbaux des Séances, 5e Session (1958) du Comité Consultatif de Thermométrie.

Part 2. Tables for the 1958 Temperature Scale

H. van Dijk, M. Durieux, J. R. Clement, and J. K. Logan

1. Introduction

The tables which follow are these:

TABLE I. *Vapor pressure of* He^4 *(1958 Scale) in microns (*10^{-3} *mm) mercury at 0° C and standard gravity (980.665 cm/sec*^{2}). This table is an expanded version, with pressure values at millidegree intervals, of the table which defines the vapor pressure on the 1958 scale at 10-millidegree intervals.

TABLE II. *1958* He^4 *vapor pressure-temperature scale,* T *in °K as a function of* P *in millimeters mercury at 0° C and standard gravity.* This table is an inversion of table I for appropriate ranges of pressures and pressure intervals. Since this table contains differences between successive entries, it furnishes a convenient means for converting a measured vapor pressure to a temperature within 0.1 millidegree.

TABLE III. *1958* He^4 *vapor pressure-temperature scale,* T *in °K as a function of* P *in centimeters mercury at 0° C and standard gravity.* This table is an extension of table II for pressures greater than 80 cm mercury. It is numbered independently because the pressure unit is centimeters mercury rather than millimeters mercury.

TABLE IV. *Temperature derivative in millimeters* Hg/°K *for the 1958* He^4 *Scale.* This table gives values of the first derivative, dP/dT, to four significant digits. These values are smoother and more precise than values obtained directly from table I by simple difference calculation, and they represent true derivatives of the scale defined by table I.

TABLE V. *Auxiliary table for making hydrostatic head correction.* This table gives, as a function of pressure, values of the ratio between the density of liquid He I and the density of mercury at 0° C.

TABLE VI. *Deviations of earlier scales from the 1958 scale.* The definitions of earlier scales used for obtaining the values in this table are explicitly given in explanatory notes which accompany it.

TABLE VII. *Auxiliary table for making corrections for the density of mercury at temperatures other than*

$0°$ C. This table gives values of the ratio between the density of mercury at temperatures between 10° and 39° C and the density at 0° C. Following this table is an equation useful for making another correction which in precise work must be applied to the observed height of a mercury column. This equation gives an empirical relation between the acceleration due to gravity and the local latitude and altitude. If the local value of this acceleration is unknown, the equation will yield a value sufficiently accurate for the purpose of manometry.

2. Constants Used in the Computation of the Scale

Certain constants are necessary for computing a vapor pressure-temperature scale. The values of these constants adopted for the computation of the 1958 scale are tabulated below. The significance of the L_0 value may be found in Part 1, Introduction by F. G. Brickwedde. These constants are: $i_0 = 12.2440$ cgs units; $L_0 = 59.62$ j/mole; $R = 8.31662$ j/mole·deg; density of mercury at 0° C = 13.5951 g/cm^3; standard gravity = 980.665 cm/sec^2; pressure at the λ-point = 37.80 mm mercury at 0° C and standard gravity.

3. Fixed Points on the Scale

The boiling point is at 4.2150° K for $P = 760.00$ mm mercury at 0° C and standard gravity (or 1013250 dynes/cm^2). The λ-point is at 2.1720° K for P as noted above. The critical point, if the critical pressure is taken to be 1718 mm mercury (Kamerlingh Onnes, Leiden Comm. 124b) at 0° C and standard gravity, is at 5.1994° K.

4. Comments on Determining Temperature by Measuring Vapor Pressure

Two techniques are commonly used for determining a temperature by measuring the vapor pressure of liquid He^4. In one, the pressure at some point above a bath of liquid helium is measured. In this case, standard practice has been to add to the measured pressure, when above the λ-point pressure, an amount equal to the pressure exerted by the column of helium between the point where the pressure is measured and the point in the bath occupied by the object whose temperature is desired. Below the λ-point, no correction of the observed pressure is ordinarily made, although the pressure drop in the gas due to pumping may become significant at low pressures. In the other technique, the pressure over a small amount of helium condensed in a "vapor pressure bulb" is measured. Since this "bulb" is normally placed close to the point in the bath occupied by the object whose temperature is desired, correction of the observed pressure is usually considered unnecessary above, as well as below, the λ-point. Numerous arrangements have been used for the pressure-transmitting line from the "bulb" to the manometer, but no standard practice seems to prevail. In any such apparatus, thermomolecular pressure differences between the cold "bulb" and the warm manometer arise at sufficiently low pressures.

It is generally known that various adaptations of these two techniques yield slightly different pressures and therefore slightly different temperatures, especially above the λ-point. Although these temperatures usually differ by no more than 0.01° K, special attention to technique seems required when precision exceeding 0.01° K is desired. Two conditions necessary to any satisfactory technique for determining the temperature of an object by measuring the vapor pressure of a liquid seem obvious. First, there must be thermal equilibrium between the object and the liquid. Second, the pressure at which the liquid is in equilibrium with its saturated vapor must somehow be determined. In the case of He^4 there is one criterion which, if satisfied, probably assures that these conditions are met. Differences between the thermal properties of He^4 above and below the λ-point are so large that, if the calibration of a secondary thermometer yields a continuous curve through the λ-point, the technique by which the calibration was obtained is probably satisfactory.

TABLE I. *Vapor pressure of* He^4 *(1958 scale) in microns (10^{-3} mm) mercury at 0° C and standard gravity (980.665 cm/sec^2)*

T°K	0.000	0.001	0.002	0.003	0.004	0.005	0.006	0.007	0.008	0.009
0.50	0.016342	0.016901	0.017476	0.018069	0.018680	0.019309	0.019956	0.020623	0.021310	0.022017
.51	.022745	.023494	.024265	.025058	.025875	.026714	.027578	.028467	.029381	.030321
.52	.031287	.032280	.033301	.034351	.035431	.036541	.037681	.038852	.040055	.041291
.53	.042561	.043865	.045205	.046581	.047993	.049443	.050932	.052461	.054030	.055640
.54	.057292	.058987	.060727	.062512	.064343	.066221	.068147	.070123	.072149	.074226
.55	.076356	.078540	.080779	.083074	.085426	.087836	.090306	.092837	.095431	.098088
.56	.10081	.10360	.10646	.10938	.11237	.11544	.11858	.12179	.12508	.12845
.57	.13190	.13543	.13904	.14274	.14652	.15039	.15435	.15840	.16254	.16678
.58	.17112	.17555	.18008	.18471	.18945	.19430	.19926	.20433	.20951	.21480
.59	.22021	.22574	.23139	.23716	.24306	.24908	.25524	.26153	.26795	.27451

TABLE I. *Vapor pressure of* He^4 *(1958 scale) in microns (10^{-3} mm) mercury at 0° C and standard gravity (980.665 cm/sec²)*—Con.

T°K	0.000	0.001	0.002	0.003	0.004	0.005	0.006	0.007	0.008	0.009
0.60	0.28121	0.28805	0.29504	0.30218	0.30947	0.31691	0.32450	0.33225	0.34017	0.34825
.61	.35649	.36490	.37349	.38225	.39120	.40032	.40963	.41912	.42881	.43869
.62	.44877	.45905	.46953	.48023	.49113	.50225	.51358	.52514	.53692	.54894
.63	.56118	.57366	.58638	.59935	.61256	.62603	.63975	.65374	.66799	.68250
.64	.69729	.71236	.72771	.74334	.75926	.77548	.79200	.80882	.82595	.84340
.65	.86116	.87925	.89766	.91641	.93550	.95493	.97471	.99484	1.0153	1.0362
.66	1.0574	1.0790	1.1010	1.1233	1.1461	1.1692	1.1928	1.2167	1.2411	1.2659
.67	1.2911	1.3168	1.3429	1.3694	1.3964	1.4238	1.4518	1.4802	1.5090	1.5384
.68	1.5682	1.5985	1.6293	1.6607	1.6925	1.7249	1.7578	1.7913	1.8253	1.8598
.69	1.8949	1.9306	1.9669	2.0037	2.0412	2.0792	2.1179	2 1571	2.1970	2.2375
.70	2.2787	2.3205	2.3629	2.4061	2.4499	2.4944	2.5395	2.5853	2 6319	2.6792
.71	2.7272	2.7760	2.8255	2.8757	2.9267	2 9785	3.0311	3.0845	3.1386	3.1936
.72	3.2494	3.3060	3.3635	3.4218	3.4810	3.5411	3.6021	3.6639	3.7266	3.7903
.73	3.8549	3.9204	3.9869	4.0544	4.1228	4.1922	4.2626	4.3340	4.4064	4.4798
.74	4.5543	4.6298	4.7064	4.7841	4.8629	4.9428	5.0238	5.1059	5.1891	5.2735
.75	5.3591	5.4459	5.5338	5.6230	5.7134	5.8050	5.8978	5.9919	6.0873	6.1840
.76	6.2820	6.3813	6.4819	6.5839	6.6872	6.7919	6.8980	7.0055	7.1144	7.2247
.77	7.3365	7.4498	7.5645	7.6807	7.7985	7.9178	8.0386	8.1610	8.2849	8.4104
.78	8.5376	8.6664	8.7968	8.9289	9.0627	9.1981	9.3352	9.4741	9.6147	9.7571
.79	9.9013	10.047	10.195	10.345	10.496	10.650	10.805	10.962	11.121	11.282
.80	11.445	11.610	11.777	11.946	12.117	12.290	12.465	12.642	12.822	13.003
.81	13.187	13.373	13.561	13.751	13.944	14.138	14.335	14.535	14.737	14.941
.82	15.147	15.356	15.567	15.781	15.997	16.216	16 437	16.661	16 887	17.116
.83	17.348	17.582	17.819	18.058	18.300	18.545	18.793	19.043	19.296	19.552
.84	19.811	20.073	20.337	20.605	20.875	21.149	21.425	21.704	21.987	22.272
.85	22.561	22.853	23.148	23.446	23.747	24.052	24.360	24.671	24 985	25.303
.86	25.624	25.948	26.276	26.608	26.943	27.281	27.623	27.969	28.318	28.671
.87	29.027	29.387	29.751	30.119	30.490	30.865	31.245	31.628	32.014	32.405
.88	32.800	33.199	33.602	34 009	34 420	34.835	35 254	35.678	36.106	36.538
.89	36.974	37.415	37.860	38.309	38.763	39.221	39.684	40.151	40.623	41.100
.90	41.581	42.067	42.557	43.053	43.553	44 058	44.568	45.082	45.602	46.126
.91	46.656	47.191	47.730	48.275	48 825	49.380	49.940	50.505	51.076	51.652
.92	52 234	52.821	53.414	54.012	54.615	55.224	55 839	56.459	57.085	57.717
.93	58.355	58 999	59.648	60.303	60.964	61.632	62 305	62.984	63.670	64.361
.94	65.059	65.763	66.473	67.190	67.913	68 642	69.378	70.120	70.869	71.624
.95	72 386	73 155	73.930	74.713	75.502	76 298	77.101	77.910	78 727	79.551
.96	80.382	81.220	82 066	82.918	83.778	84 645	85.520	86.402	87.291	88.188
.97	89.093	90.005	90.925	91.853	92.789	93 732	94.683	95.642	96.609	97.584
.98	98.567	99.558	100.557	101.565	102.581	103 605	104.638	105.679	106 728	107.786
.99	108.853	109.928	111.012	112.104	113.205	114 315	115.434	116.562	117.699	118.845
1.00	120.000	121.165	122 339	123.523	124.716	125.918	127.129	128.350	129.580	130.820
1.01	132.070	133.330	134 600	135.880	137.169	138 468	139.778	141.097	142.427	143.766
1.02	145.116	146.477	147.848	149.230	150.622	152.025	153 438	154.862	156.297	157.742
1.03	159.198	160.666	162.145	163.634	165.135	166.647	168.170	169.704	171.250	172.806
1.04	174.375	175.956	177.548	179.152	180.768	182.395	184.035	185.686	187.349	189.024
1.05	190.711	192.412	194.124	195.849	197.587	199.336	201.098	202.874	204.661	206.461
1.06	208.274	210.101	211.941	213.794	215.660	217.538	219.431	221.335	223.255	225.187
1.07	227.132	229.092	231.065	233.052	235.053	237.068	239.096	241.138	243.195	245.265
1.08	247.350	249.450	251.565	253.694	255.838	257.995	260.168	262.355	264.557	266.774
1.09	269.006	271.254	273.516	275.794	278.087	280.396	282.719	285.058	287.413	289.783
1.10	292.169	294.572	296.991	299.426	301.877	304 344	306.828	309.327	311.843	314.375
1.11	316.923	319.489	322.072	324.671	327.287	329.920	332.570	335.237	337.921	340.622
1.12	343.341	346 079	348 834	351.606	354.397	357.205	360.030	362.874	365 735	368.614
1.13	371.512	374.429	377.364	280.318	383.290	286.280	389.290	392.317	395.364	398.430
1.14	401.514	404.619	407.744	410.887	414.050	417.232	420.434	423.655	426 896	430.156
1.15	433.437	436.739	440.060	443.402	446.764	450.146	453 549	456.972	460.416	463.880
1.16	467.365	470.873	474.402	477.951	481.522	485.114	488.728	492.363	496 019	499.697
1.17	503.396	507.118	510.863	514.630	518 418	522.229	526.062	529.917	533.794	537.694
1.18	541.617	545.564	549.535	553.528	557 544	561.583	565.645	569.731	573 840	577.972
1.19	582.129	586.310	590.515	594.744	598.998	603.275	607.576	611.901	616.251	620.626
1.20	625.025	629.450	633.901	638.377	642.877	647.403	651.954	656 530	661.131	665.758
1.21	670.411	675.091	679.797	684.529	689.287	694.071	698.881	703.717	708.580	713.470
1.22	718.386	723.331	728.303	733.301	738 327	743.380	748 461	753 569	758 704	763.866
1.23	769.057	774.277	779.525	784.801	790.105	795.437	800.798	806.187	811.605	817.052
1.24	822.527	828.033	833.569	839.135	844.730	850.353	856.006	861.689	867.402	873.144
1.25	878.916	884.720	890.555	896.420	902.315	908.241	914.197	920.184	926.202	932.250
1.26	938.330	944.442	950.585	956.759	962.965	969.203	975.473	981.774	988.107	994.472
1.27	1000.87	1007.30	1013.77	1020.27	1026.80	1033.36	1039.95	1046.58	1053.24	1059.94
1.28	1066.67	1073.44	1080.24	1087.07	1093.93	1100.83	1107.77	1114 74	1121.74	1128.78
1.29	1135.85	1142.96	1150.10	1157.28	1164.49	1171.74	1179.02	1186.34	1193.69	1201.08

TABLE I. *Vapor pressure of* He^4 *(1958 scale) in micron (10^{-3} mm) mercury at 0° C and standard gravity (980.665 cm/sec²)*—Con.

T°K	0.000	0.001	0.002	0.003	0.004	0.005	0.006	0.007	0.008	0.009
1.30	1208.51	1215.98	1223.48	1231.02	1238.59	1246.20	1253.85	1261.54	1269.26	1277.02
1.31	1284.81	1292.64	1300.51	1308.42	1316 37	1324 35	1332.37	1340.43	1348.53	1356.66
1.32	1364.83	1373.04	1381.30	1389.59	1397.92	1406 29	1414.70	1423.15	1431.64	1440.16
1.33	1448.73	1457.34	1465.98	1474.67	1483.40	1492.17	1500.97	1509.82	1518.71	1527.64
1.34	1536.61	1545.62	1554.68	1563.78	1572.91	1582.09	1591.31	1600.57	1609.88	1619.23
1.35	1628.62	1638.06	1647.54	1657.06	1666.62	1676 23	1685.88	1695.57	1705.31	1715.09
1.36	1724.91	1734.78	1744.69	1754.65	1764.65	1774.69	1784.78	1794.91	1805.09	1815.31
1.37	1825.58	1835.90	1846.26	1856.66	1867.11	1877.61	1888.16	1898.75	1909.38	1920.06
1.38	1930.79	1941.57	1952.39	1963.26	1974.18	1985.14	1996.15	2007.21	2018.32	2029.47
1.39	2040.67	2051.92	2063.22	2074.57	2085.96	2097.40	2108.89	2120.43	2132.02	2143.66
1.40	2155.35	2167.09	2178.88	2190.72	2202.61	2214.54	2226.53	2238.57	2250.66	2262.80
1.41	2274.99	2287.23	2299.52	2311.87	2324.27	2336.72	2349.22	2361.77	2374.37	2387.02
1.42	2399.73	2412.49	2425.30	2438.17	2451.09	2464.06	2477.09	2490.17	2503.30	2516.48
1.43	2529.72	2543.01	2556.36	2569.76	2583.21	2596.72	2610.29	2623.91	2637.58	2651.31
1.44	2665.09	2678.93	2692.82	2706.77	2720.78	2734.84	2748.96	2763.13	2777.36	2791.65
1.45	2805.99	2820.39	2834.85	2849.37	2863.95	2878.58	2893.27	2908.02	2922.82	2937.68
1.46	2952.60	2967.58	2982.62	2997.72	3012.88	3028.09	3043.36	3058.69	3074.08	3089.53
1.47	3105.04	3120.61	3136.24	3151.94	3167.69	3183.50	3199.37	3215.30	3231.30	3247.36
1.48	3263.48	3279.66	3295.90	3312 20	3328.57	3345.00	3361.49	3378.04	3394.65	3411.33
1.49	3428.07	3444.87	3461.74	3478.67	3495.66	3512.72	3529.84	3547.03	3564.28	3581.59
1.50	3598.97	3616.41	3633.92	3651.49	3669.13	3686.83	3704.60	3722.43	3740.33	3758.29
1.51	3776.32	3794.42	3812.59	3830.82	3849.12	3867.49	3885.92	3904.42	3922.99	3941.62
1.52	3960.32	3979.09	3997.93	4016.83	4035.80	4054.84	4073.95	4093.12	4112.37	4131.69
1.53	4151.07	4170.52	4190.05	4209.65	4229.32	4249.06	4268.87	4288.74	4308.68	4328.70
1.54	4348.79	4368.95	4389.17	4409.47	4429.84	4450.28	4470.80	4491.39	4512.05	4532.78
1.55	4553.58	4574.46	4595.41	4616.44	4637.54	4658.71	4679.96	4701.28	4722.67	4744.14
1.56	4765.68	4787.29	4808.98	4830.74	4852.58	4874.49	4896.48	4918.54	4940.68	4962.89
1.57	4985.18	5007.54	5029.98	5052.50	5075.09	5097.76	5120.51	5143.33	5166.23	5189.21
1.58	5212.26	5235.39	5258.60	5281.89	5305.26	5328.71	5352.23	5375.83	5399.51	5423.27
1.59	5447.11	5471.03	5495.02	5519.10	5543.26	5567.49	5591.81	5616.21	5640.68	5665.24
1.60	5689.88	5714.60	5739.40	5764.28	5789.25	5814.30	5839.42	5864.63	5889.92	5915.30
1.61	5940.76	5966.30	5991.92	6017.62	6043.41	6069.28	6095.24	6121.28	6147.40	6173.61
1.62	6199.90	6226.27	6252.72	6279.26	6305.88	6332.59	6359.39	6386.27	6413.23	6440.28
1.63	6467.42	6494.64	6521.95	6549.35	6576.84	6604.41	6632.07	6659.81	6687.64	6715.56
1.64	6743.57	6771.66	6799.84	6828.11	6856.47	6884.91	6913.44	6942.07	6970.78	6999.58
1.65	7028.47	7057.45	7086.52	7115.67	7144.92	7174.26	7203.69	7233.21	7262.82	7292.52
1.66	7322.31	7352.19	7382.15	7412.21	7442.36	7472.60	7502.94	7533.37	7563.89	7594.50
1.67	7625.21	7656.01	7686.90	7717.88	7748.96	7780.13	7811.40	7842.76	7874.21	7905.76
1.68	7937.40	7969.13	8000.96	8032.88	8064.90	8097.01	8129.22	8161.53	8193.93	8226.43
1.69	8259.02	8291.70	8324.48	8357.36	8390.33	8423.40	8456.57	8489.84	8523.20	8556.66
1.70	8590.22	8623.87	8657.62	8691.47	8725.42	8759.47	8793.62	8827.86	8862.20	8896.64
1.71	8931.18	8965.82	9000.56	9035.40	9070.33	9105.36	9140.50	9175.74	9211.08	9246.52
1.72	9282.06	9317.70	9353.44	9389.28	9425.22	9461.26	9497.41	9533.66	9570.01	9606.46
1.73	9643.02	9679.68	9716.45	9753.32	9790.29	9827.36	9864.54	9901.82	9939.21	9976.70
1.74	10014.3	10052.0	10089.8	10127.7	10165.7	10203.8	10242.0	10280.3	10318.7	10357.3
1.75	10395.9	10434.6	10473.4	10512.4	10551.5	10590.7	10630.0	10669.4	10708.9	10748.5
1.76	10788.2	10828.0	10867.9	10907.9	10948.0	10988.3	11028.7	11069.2	11109.7	11150.4
1.77	11191.2	11232.1	11273.1	11314.2	11355.4	11396.7	11438.1	11479.7	11521.4	11563.2
1.78	11605.1	11647.1	11689.2	11731.4	11773.7	11816.1	11858.7	11901.4	11944.2	11987.1
1.79	12030.1	12073.2	12116.4	12159.7	12203.1	12246.6	12290.3	12334.1	12378.0	12422.0
1.80	12466.1	12510.3	12554.7	12599.2	12643.8	12688.5	12733.3	12778.2	12823.2	12868.4
1.81	12913.7	12959.1	13004.6	13050.2	13095.9	13141.8	13187.8	13233.9	13280.1	13326.4
1.82	13372.8	13419.3	13466.0	13512.8	13559.7	13606.7	13653.8	13701.1	13748.5	13796.0
1.83	13843.6	13891.3	13939.1	13987.1	14035.2	14083.4	14131.7	14180.1	14228.6	14277.3
1.84	14326.1	14375.0	14424.0	14473.2	14522.5	14571.9	14621.4	14671.0	14720.8	14770.7
1.85	14820.7	14870.8	14921.0	14971.4	15021.9	15072.5	15123.2	15174.0	15225.0	15276.1
1.86	15327.3	15378.6	15430.1	15481.7	15533.4	15585.2	15637.2	15689.3	15741.5	15793.8
1.87	15846.3	15898.9	15951.6	16004.4	16057.3	16110.4	16163.6	16216.9	16270.4	16324.0
1.88	16377.7	16431.5	16485.5	16539.6	16593.8	16648.1	16702.6	16757.2	16811.9	16866.7
1.89	16921.7	16976.8	17032.0	17087.3	17142.8	17198.4	17254.1	17309.9	17365.9	17422.0
1.90	17478.2	17534.6	17591.1	17647.7	17704.5	17761.4	17818.4	17875.5	17932.8	17990.2
1.91	18047.7	18105.4	18163.2	18221.1	18279.1	18337.3	18395.6	18454.0	18512.6	18571.3
1.92	18630.1	18689.0	18748.1	18807.3	18866.7	18926.2	18985.8	19045.5	19105.4	19165.4
1.93	19225.5	19285.8	19346.2	19406.7	19467.4	19528.2	19589.1	19650.1	19711.3	19772.6
1.94	19834.1	19895.7	19957.4	20019.2	20081.2	20143.3	20205.6	20268.0	20330.5	20393.1
1.95	20455.9	20518.8	20581.9	20645.1	20708.4	20771.8	20835.4	20899.1	20963.0	21027.0
1.96	21091.1	21155.4	21219.8	21284.3	21348.9	21413.7	21478.6	21543.7	21608.9	21674.2
1.97	21739.7	21805.3	21871.1	21937.0	22003.0	22069.2	22135.5	22201.9	22268.5	22335.2
1.98	22402.0	22469.0	22536.1	22603.3	22670.7	22738.2	22805.9	22873.7	22941.6	23009.7
1.99	23077.9	23146.2	23214.7	23283.3	23352.1	23421.0	23490.0	23559.1	23628.4	23697.8

TABLE I. *Vapor pressure of* He^4 *(1958 scale) in microns (10^{-3} mm) mercury at 0° C and standard gravity (980.665 cm/sec²)*—Con.

T°K	0.000	0.001	0.002	0.003	0.004	0.005	0.006	0.007	0.008	0.009
2.00	23767.4	23837.1	23907.0	23977.0	24047.2	24117.5	24187.9	24258.4	24329.1	24399.9
2.01	24470.9	24542.0	24613.2	24684.6	24756.1	24827.8	24899.6	24971.5	25043.6	25115.8
2.02	25188.1	25260.6	25333.2	25406.0	25478.9	25551.9	25625.1	25698.4	25771.9	25845.5
2.03	25919.2	25993.1	26067.1	26141.3	26215.6	26290.0	26364.6	26439.3	26514.1	26589.1
2.04	26664.2	26739.5	26814.9	26890.5	26966.2	27042.0	27118.0	27194.1	27270.4	27346.8
2.05	27423.3	27500.0	27576.8	27653.8	27730.9	27808.1	27885.4	27962.9	28040.6	28118.4
2.06	28196.3	28274.4	28352.6	28430.9	28509.4	28588.0	28666.8	28745.7	28824.7	28903.9
2.07	28983.2	29062.7	29142.3	29222.1	29302.0	29382.0	29462.2	29542.5	29622.9	29703.5
2.08	29784.2	29865.1	29946.1	30027.2	30108.5	30189.9	30271.5	30353.2	30435.0	30517.0
2.09	30599.1	30681.4	30763.8	30846.4	30929.1	31011.9	31094.9	31178.0	31261.2	31344.6
2.10	31428.1	31511.8	31595.6	31679.6	31763.7	31847.9	31932.3	32016.8	32101.4	32186.2
2.11	32271.1	32356.2	32441.4	32526.8	32612.3	32697.9	32783.6	32869.5	32955.5	33041.7
2.12	33128.0	33214.5	33301.1	33387.8	33474.6	33561.6	33648.7	33736.0	33823.4	33910.9
2.13	33998.6	34086.4	34174.4	34262.5	34350.7	34439.0	34527.5	34616.1	34704.9	34793.8
2.14	34882.8	34971.9	35061.2	35150.6	35240.2	35329.9	35419.7	35509.7	35599.8	35690.0
2.15	35780.3	35870.7	35961.3	36052.0	36142.9	36233.9	36325.0	36416.3	36507.7	36599.2
2.16	36690.9	36782.7	36874.6	36966.6	37058.8	37151.1	37243.5	37336.0	37428.6	37521.4
2.17	37614.3	37707.4	37800.6	37893.9	37987.3	38080.8	38174.4	38268.1	38362.0	38456.0
2.18	38550.2	38644.5	38739.0	38833.6	38928.4	39023.3	39118.4	39213.6	39309.0	39404.6
2.19	39500.3	39596.2	39692.2	39788.3	39884.6	39981.0	40077.6	40174.4	40271.3	40368.4
2.20	40465.6	40563.0	40660.5	40758.2	40856.0	40954.0	41052.2	41150.6	41249.1	41347.8
2.21	41446.6	41545.6	41644.7	41744.0	41843.4	41943.0	42042.8	42142.7	42242.8	42343.1
2.22	42443.5	42544.1	42644.8	42745.7	42846.8	42948.0	43049.4	43150.9	43252.6	43354.5
2.23	43456.5	43558.7	43661.0	43763.5	43866.2	43969.0	44072.0	44175.2	44278.5	44382.0
2.24	44485.7	44589.5	44693.5	44797.6	44901.9	45006.4	45111.0	45215.8	45320.8	45426.0
2.25	45531.3	45636.8	45742.4	45848.2	45954.1	46060.2	46166.5	46273.0	46379.7	46486.5
2.26	46593.5	46700.6	46807.9	46915.4	47023.0	47130.8	47238.8	47347.0	47455.3	47563.8
2.27	47672.5	47781.3	47890.3	47999.5	48108.9	48218.4	48328.1	48438.0	48548.0	48658.2
2.28	48768.6	48879.2	48989.9	49100.8	49211.8	49323.0	49434.4	49546.0	49657.8	49769.7
2.29	49881.8	49994.1	50106.5	50219.1	50331.9	50444.9	50558.0	50671.3	50784.8	50898.5
2.30	51012.3	51126.3	51240.5	51354.8	51469.3	51584.0	51698.9	51814.0	51929.2	52044.6
2.31	52160.2	52276.0	52391.9	52508.0	52624.3	52740.8	52857.4	52974.2	53091.2	53208.4
2.32	53325.8	53443.3	53561.0	53678.9	53797.0	53915.3	54033.7	54152.3	54271.1	54390.1
2.33	54509.2	54628.5	54748.0	54867.7	54987.6	55107.6	55227.8	55348.2	55468.8	55589.6
2.34	55710.5	55831.6	55952.9	56074.4	56196.1	56318.0	56440.0	56562.2	56684.6	56807.2
2.35	56930.0	57053.0	57176.1	57299.4	57422.9	57546.6	57670.5	57794.6	57918.8	58043.2
2.36	58167.8	58292.6	58417.5	58542.6	58668.0	58793.5	58919.2	59045.0	59171.1	59297.4
2.37	59423.8	59550.5	59677.3	59804.3	59931.5	60058.9	60186.5	60314.3	60442.3	60570.5
2.38	60698.8	60827.3	60955.9	61084.7	61213.8	61343.1	61472.5	61602.1	61731.9	61861.9
2.39	61992.0	62122.4	62253.0	62383.7	62514.6	62645.8	62777.1	62908.6	63040.3	63172.2
2.40	63304.3	63436.5	63569.0	63701.6	63834.4	63967.4	64100.5	64233.9	64367.5	64501.2
2.41	64635.2	64769.4	64903.7	65038.2	65173.0	65307.9	65443.0	65578.3	65713.8	65849.5
2.42	65985.4	66121.5	66257.7	66394.2	66530.8	66667.7	66804.7	66941.9	67079.4	67217.0
2.43	67354.8	67492.8	67631.0	67769.4	67907.9	68046.7	68185.7	68324.8	68464.2	68603.7
2.44	68743.5	68883.5	69023.6	69164.0	69304.5	69445.3	69586.2	69727.4	69868.7	70010.3
2.45	70152.0	70294.0	70436.1	70578.4	70721.0	70863.7	71006.6	71149.7	71293.0	71436.5
2.46	71580.2	71724.1	71868.2	72012.5	72157.0	72301.6	72446.5	72591.6	72736.9	72882.4
2.47	73028.1	73174.0	73320.1	73466.4	73612.8	73759.5	73906.4	74053.5	74200.8	74348.3
2.48	74496.0	74643.9	74792.0	74940.3	75088.8	75237.6	75386.5	75535.6	75685.0	75834.5
2.49	75984.2	76134.2	76284.3	76434.7	76585.3	76736.1	76887.1	77038.3	77189.7	77341.3
2.50	77493.1	77645.1	77797.3	77949.7	78102.3	78255.1	78408.1	78561.3	78714.7	78868.4
2.51	79022.2	79176.3	79330.5	79485.0	79639.7	79794.6	79949.7	80105.0	80260.5	80416.3
2.52	80572.2	80728.3	80884.7	81041.2	81198.0	81354.9	81512.1	81669.5	81827.1	81984.9
2.53	82142.9	82301.1	82459.6	82618.2	82777.1	82936.1	83095.4	83254.9	83414.6	83574.5
2.54	83734.6	83894.9	84055.4	84216.2	84377.1	84538.3	84699.6	84861.2	85023.0	85185.0
2.55	85347.2	85509.6	85672.3	85835.2	85998.2	86161.5	86325.0	86488.7	86652.7	86816.8
2.56	86981.2	87145.8	87310.6	87475.6	87640.8	87806.3	87971.9	88137.8	88303.9	88470.2
2.57	88636.7	88803.4	88970.4	89137.6	89304.9	89472.5	89640.3	89808.4	89976.7	90145.1
2.58	90313.8	90482.7	90651.8	90821.2	90990.8	91160.5	91330.5	91500.7	91671.1	91841.8
2.59	92012.6	92183.7	92355.0	92526.6	92698.3	92870.3	93042.5	93214.9	93387.5	93560.3
2.60	93733.4	93906.7	94080.2	94253.9	94427.8	94602.0	94776.3	94950.9	95125.7	95300.8
2.61	95476.0	95651.5	95827.2	96003.1	96179.3	96355.6	96532.2	96709.0	96886.1	97063.3
2.62	97240.8	97418.5	97596.5	97774.7	97953.1	98131.7	98310.6	98489.6	98668.9	98848.5
2.63	99028.2	99208.2	99388.4	99568.8	99749.4	99930.3	100111	100293	100474	100656
2.64	100838	101020	101202	101385	101568	101751	101934	102117	102301	102485
2.65	102669	102854	103038	103223	103409	103594	103780	103966	104152	104338
2.66	104525	104712	104899	105086	105273	105461	105649	105837	106026	106214
2.67	106403	106592	106781	106971	107161	107351	107541	107731	107922	108113
2.68	108304	108495	108687	108879	109071	109263	109456	109648	109841	110035
2.69	110228	110422	110616	110810	111004	111199	111393	111588	111784	111979

TABLE I. *Vapor pressure of* He^4 *(1958 scale) in microns (10^{-3} mm) mercury at 0° C and standard gravity (980.665 cm/sec²)*—Con.

T°K	0.000	0.001	0.002	0.003	0.004	0.005	0.006	0.007	0.008	0.009
2.70	112175	112371	112567	112764	112960	113157	113354	113552	113749	113947
2.71	114145	114343	114542	114741	114940	115139	115339	115538	115738	115939
2.72	116139	116340	116541	116742	116943	117145	117346	117548	117751	117953
2.73	118156	118359	118562	118766	118970	119174	119378	119583	119788	119993
2.74	120198	120403	120609	120815	121021	121228	121434	121641	121848	122055
2.75	122263	122471	122679	122887	123096	123305	123514	123723	123933	124143
2.76	124353	124563	124773	124984	125195	125406	125617	125829	126041	126253
2.77	126465	126678	126891	127104	127317	127531	127745	127959	128173	128388
2.78	128603	128818	129033	129249	129465	129681	129897	130114	130331	130548
2.79	130765	130983	131200	131419	131637	131855	132074	132293	132513	132732
2.80	132952	133172	133392	133613	133834	134055	134276	134498	134720	134942
2.81	135164	135387	135609	135832	136056	136279	136503	136727	136952	137176
2.82	137401	137626	137851	138077	138303	138529	138755	138982	139209	139436
2.83	139663	139890	140118	140346	140574	140803	141032	141261	141490	141719
2.84	141949	142179	142409	142640	142870	143101	143333	143564	143796	144028
2.85	144260	144493	144725	144958	145192	145425	145659	145893	146128	146362
2.86	146597	146832	147068	147304	147540	147776	148012	148249	148486	148723
2.87	148961	149199	149437	149675	149913	150152	150391	150630	150869	151109
2.88	151349	151589	151830	152070	152312	152553	152794	153036	153278	153520
2.89	153763	154006	154249	154493	154736	154980	155224	155469	155714	155959
2.90	156204	156450	156695	156941	157188	157434	157681	157928	158176	158423
2.91	158671	158919	159168	159416	159665	159914	160164	160413	160663	160914
2.92	161164	161415	161666	161917	162169	162421	162673	162925	163178	163431
2.93	163684	163937	164191	164445	164699	164954	165208	165463	165719	165974
2.94	166230	166486	166742	166999	167256	167513	167770	168028	168285	168544
2.95	168802	169061	169320	169579	169839	170099	170359	170619	170880	171141
2.96	171402	171663	171925	172187	172449	172712	172974	173237	173501	173764
2.97	174028	174292	174557	174821	175086	175352	175617	175883	176149	176415
2.98	176682	176949	177216	177484	177752	178020	178288	178557	178825	179095
2.99	179364	179634	179904	180174	180444	180715	180986	181257	181529	181801
3.00	182073	182345	182618	182891	183164	183438	183712	183986	184260	184535
3.01	184810	185085	185361	185636	185912	186189	186465	186742	187019	187296
3.02	187574	187852	188130	188409	188687	188967	189246	189525	189805	190086
3.03	190366	190647	190928	191209	191491	191773	192055	192338	192621	192904
3.04	193187	193471	193755	194039	194324	194608	194894	195179	195465	195751
3.05	196037	196323	196610	196897	197184	197472	197760	198048	198336	198625
3.06	198914	199203	199492	199783	200073	200363	200654	200945	201237	201528
3.07	201820	202112	202405	202697	202991	203284	203578	203871	204166	204460
3.08	204755	205050	205346	205641	205937	206233	206530	206827	207124	207421
3.09	207719	208017	208315	208614	208912	209221	209511	209810	210110	210411
3.10	210711	211012	211313	211614	211916	212218	212520	212823	213125	213429
3.11	213732	214036	214340	214644	214949	215254	215559	215865	216171	216477
3.12	216783	217090	217397	217704	218012	218320	218628	218937	219246	219555
3.13	219864	220174	220484	220794	221105	221416	221727	222039	222350	222663
3.14	222975	223288	223601	223914	224227	224541	224855	225170	225485	225800
3.15	226115	226431	226747	227063	227379	227696	228013	228331	228649	228967
3.16	229285	229604	229922	230242	230561	230881	231201	231521	231842	232163
3.17	232484	232806	233128	233450	233772	234095	234418	234742	235066	235390
3.18	235714	236039	236364	236689	237014	237340	237666	237993	238320	238647
3.19	238974	239302	239630	239958	240287	240616	240946	241275	241605	241935
3.20	242266	242597	242928	243259	243591	243923	244255	244588	244920	245254
3.21	245587	245920	246255	246589	246924	247259	247595	247930	248266	248602
3.22	248939	249276	249613	249951	250289	250627	250965	251304	251643	251982
3.23	252322	252662	253002	253343	253684	254025	254367	254709	255051	255393
3.24	255736	256079	256423	256767	257111	257455	257800	258145	258490	258836
3.25	259182	259528	259875	260222	260569	260916	261264	261612	261960	262309
3.26	262658	263007	263357	263707	264057	264408	264759	265110	265462	265814
3.27	266166	266519	266871	267225	267578	267932	268286	268641	268995	269351
3.28	269706	270062	270418	270774	271131	271488	271845	272203	272561	272919
3.29	273278	273637	273996	274355	274715	275075	275435	275796	276157	276518
3.30	276880	277242	277605	277967	278331	278694	279058	279422	279786	280151
3.31	280516	280881	281247	281613	281979	282346	282712	283080	283447	283815
3.32	284183	284552	284920	285290	285659	286029	286399	286770	287140	287512
3.33	287883	288255	288627	288999	289372	289745	290118	290492	290866	291240
3.34	291615	291990	292365	292741	293117	293493	293870	294247	294624	295002
3.35	295380	295758	296137	296516	296895	297275	297655	298035	298416	298797
3.36	299178	299560	299941	300324	300706	301089	301472	301856	302239	302624
3.37	303008	303393	303778	304163	304549	304935	305322	305709	306096	306483
3.38	306871	307259	307648	308037	308426	308815	309205	309595	309986	310377
3.39	310768	311159	311551	311943	312335	312728	313121	313515	313908	314302

TABLE I. *Vapor pressure of* He^4 *(1958 scale) in microns* (10^{-3} *mm*) *mercury at 0° C and standard gravity* (*980.665 cm/sec²*)—Con.

T°K	0.000	0.001	0.002	0.003	0.004	0.005	0.006	0.007	0.008	0.009
3.40	314697	315092	315487	315882	316278	316674	317070	317467	317864	318261
3.41	318659	319057	319455	319854	320253	320652	321052	321452	321852	322253
3.42	322654	323055	323457	323859	324262	324665	325068	325471	325875	326279
3.43	326684	327089	327493	327899	328305	328711	329118	329525	329932	330339
3.44	330747	331155	331564	331973	332382	332792	333202	333612	334023	334434
3.45	334845	335257	335668	336081	336493	336906	337319	337733	338147	338561
3.46	338976	339391	339806	340222	340638	341054	341471	341888	342305	342723
3.47	343141	343559	343978	344397	344817	345237	345657	346077	346498	346919
3.48	347341	347763	348185	348608	349030	349454	349877	350301	350725	351150
3.49	351575	352000	352426	352852	353278	353705	354132	354560	354987	355416
3.50	355844	356273	356702	357131	357561	357991	358422	358852	359284	359715
3.51	360147	360579	361012	361445	361878	362312	362746	363180	363615	364050
3.52	364485	364921	365357	365794	366231	366668	367106	367544	367982	368421
3.53	368860	369299	369739	370179	370619	371060	371501	371943	372384	372826
3.54	373269	373712	374155	374599	375043	375487	375932	376377	376822	377268
3.55	377714	378160	378607	379054	379502	379950	380398	380846	381295	381744
3.56	382194	382644	383094	383545	383996	384447	384899	385351	385804	386257
3.57	386710	387164	387617	388072	388526	388982	389437	389893	390349	390805
3.58	391262	391719	392177	392634	393092	393551	394010	394469	394929	395389
3.59	395849	396310	396770	397232	397693	398155	398618	399081	399544	400007
3.60	400471	400935	401400	401865	402330	402796	403262	403728	404195	404662
3.61	405130	405598	406066	406535	407004	407473	407943	408413	408883	409354
3.62	409825	410296	410768	411240	411713	412186	412659	413133	413607	414081
3.63	414556	415031	415507	415983	416459	416935	417412	417890	418367	418846
3.64	419324	419803	420282	420761	421241	421721	422202	422683	423164	423646
3.65	424128	424610	425093	425576	426060	426543	427028	427512	427997	428482
3.66	428968	429454	429941	430427	430915	431402	431890	432379	432867	433356
3.67	433846	434336	434826	435316	435807	436298	436790	437282	437774	438267
3.68	438760	439254	439748	440242	440737	441232	441727	442223	442719	443216
3.69	443713	444210	444708	445206	445704	446203	446702	447201	447701	448201
3.70	448702	449203	449704	450206	450708	451211	451714	452217	452721	453225
3.71	453729	454234	454739	455244	455750	456257	456763	457270	457778	458286
3.72	458794	459303	459812	460321	460831	461341	461851	462362	462873	463385
3.73	463897	464409	464922	465435	465949	466463	466977	467492	468007	468522
3.74	469038	469554	470071	470588	471105	471623	472141	472660	473179	473698
3.75	474218	474738	475258	475779	476300	476822	477344	477866	478389	478912
3.76	479435	479959	480483	481008	481533	482058	482584	483110	483637	484164
3.77	484691	485219	485747	486275	486804	487333	487863	488393	488923	489454
3.78	489985	490516	491048	491580	492113	492646	493180	493713	494247	494782
3.79	495317	495852	496388	496924	497461	497998	498535	499073	499611	500149
3.80	500688	501227	501767	502307	502847	503388	503929	504471	505013	505555
3.81	506098	506641	507185	507729	508273	508818	509363	509908	510454	511000
3.82	511547	512094	512642	513190	513738	514287	514836	515385	515935	516485
3.83	517036	517587	518139	518690	519243	519795	520348	520901	521455	522009
3.84	522564	523119	523674	524230	524786	525343	525900	526457	527015	527573
3.85	528132	528691	529250	529810	530370	530930	531491	532053	532614	533176
3.86	533739	534302	534865	535429	535993	536558	537123	537688	538254	538820
3.87	539387	539954	540521	541089	541657	542226	542795	543364	543934	544504
3.88	545075	545646	546218	546790	547362	547935	548508	549082	549656	550230
3.89	550805	551380	551956	552531	553108	553684	554262	554839	555417	555995
3.90	556574	557153	557732	558312	558893	559473	560054	560636	561218	561800
3.91	562383	562966	563550	564133	564718	565303	565889	566474	567060	567647
3.92	568234	568821	569409	569997	570586	571175	571764	572354	572944	573535
3.93	574126	574717	575309	575902	576494	577087	577681	578275	578869	579464
3.94	580059	580655	581251	581847	582444	583041	583639	584237	584836	585435
3.95	586034	586634	587234	587835	588436	589037	589639	590241	590844	591447
3.96	592051	592655	593259	593864	594470	595075	595681	596288	596895	597502
3.97	598110	598718	599327	599936	600545	601155	601765	602376	602987	603598
3.98	604210	604822	605435	606048	606662	607276	607890	608505	609120	609736
3.99	610352	610969	611586	612203	612821	613439	614058	614677	615297	615917
4.00	616537	617158	617779	618401	619023	619645	620268	620891	621515	622139
4.01	622764	623389	624014	624640	625266	625893	626520	627148	627776	628404
4.02	629033	629662	630292	630922	631553	632184	632815	633447	634079	634712
4.03	635345	635979	636613	637247	637882	638517	639153	639789	640426	641063
4.04	641700	642338	642976	643615	644254	644894	645534	646174	646815	647457
4.05	648099	648741	649384	650027	650671	651315	651959	652604	653249	653895
4.06	654541	655188	655836	656482	657130	657778	658427	659076	659726	660376
4.07	661026	661677	662328	662980	663632	664284	664938	665591	666245	666899
4.08	667554	668209	668865	669521	670177	670834	671491	672149	672807	673466
4.09	674125	674784	675444	676105	676766	677427	678089	678751	679413	680076

TABLE I. *Vapor pressure of* He^4 *(1958 scale) in microns (10^{-3} mm) mercury at 0° C and standard gravity (980.665 cm/sec²)*—Con.

T°K	0.000	0.001	0.002	0.003	0.004	0.005	0.006	0.007	0.008	0.009
4.10	680740	681404	682068	682733	683398	684064	684730	685397	686064	686731
4.11	687399	688067	688736	689405	690075	690745	691416	692087	692759	693431
4.12	694103	694776	695449	696123	696797	697471	698146	698822	699498	700174
4.13	700851	701528	702206	702884	703562	704241	704921	705601	706281	706962
4.14	707643	708325	709007	709689	710372	711055	711739	712423	713108	713793
4.15	714479	715165	715852	716538	717226	717914	718602	719291	719980	720670
4.16	721360	722050	722741	723433	724124	724817	725509	726203	726896	727590
4.17	728285	728980	729675	730371	731067	731764	732461	733159	733857	734556
4.18	735255	735954	736654	747354	738055	738756	739458	740160	740863	741566
4.19	742269	742973	743677	744382	745087	745793	746499	747205	747912	748620
4.20	749328	750036	750745	751454	752164	752874	753584	754295	755007	755719
4.21	756431	757144	757857	758571	759285	759999	760714	761430	762146	762862
4.22	763579	764296	765014	765732	766451	767170	767889	768609	769330	770051
4.23	770772	771494	772216	772938	773662	774385	775109	775834	776559	777284
4.24	778010	778736	779463	780190	780918	781646	782375	783104	783833	784563
4.25	785294	786025	786756	787488	788220	788953	789686	790419	791153	791888
4.26	792623	793358	794094	794831	795568	796305	797043	707781	798520	799259
4.27	799999	800739	801480	802221	802962	803705	804447	805190	805934	806678
4.28	807422	808167	808912	809658	810405	811152	811899	812647	813395	814144
4.29	814893	815643	816393	817143	817894	818646	819398	820151	820904	821657
4.30	822411	823166	823921	824676	825432	826188	826945	827703	828461	829219
4.31	829978	830737	831497	832257	833018	833779	834541	835303	836065	836828
4.32	837592	838356	839121	839886	840651	841417	842184	842951	843718	844486
4.33	845255	846024	846793	847563	848334	849104	849876	850648	851420	852193
4.34	852966	853740	854514	855289	856064	856839	857616	858392	859169	859947
4.35	860725	861504	862283	863062	863842	864623	865404	866185	866967	867750
4.36	868533	869317	870101	870885	871670	872455	873241	874028	874815	875602
4.37	876390	877178	877967	878757	879546	880337	881128	881919	882711	883503
4.38	884296	885089	885883	886678	887472	888268	889064	889860	890657	891454
4.39	892252	893050	893849	894649	895448	896249	897050	897851	898653	899455
4.40	900258	901061	901865	902669	903474	904279	905085	905891	906698	907505
4.41	908313	909121	909930	910739	911549	912359	913170	913981	914793	915605
4.42	916418	917231	918045	918859	919674	920489	921305	922121	922938	923755
4.43	924573	925391	926210	927029	927849	928669	929490	930311	931133	931955
4.44	932778	933601	934425	935249	936074	936899	937725	938551	939378	940205
4.45	941033	941861	942690	943519	944349	945179	946010	946841	947673	948505
4.46	949338	950171	951005	951839	952674	953509	954345	955181	956018	956855
4.47	957693	958531	959370	960209	961049	961890	962730	963572	964414	965256
4.48	966099	966942	967786	968631	969476	970321	971167	972013	972860	973708
4.49	974556	975405	976254	977104	977954	978804	979656	980508	981360	982213
4.50	983066	983920	984774	985629	986485	987340	988197	989054	989911	990769
4.51	991628	992487	993346	994206	995066	995927	996788	997650	998513	999376
4.52	1000239	1001103	1001968	1002833	1003699	1004565	1005432	1006300	1007168	1008036
4.53	1008905	1009774	1010644	1011514	1012385	1013256	1014128	1015001	1015874	1016747
4.54	1017621	1018496	1019371	1020246	1021122	1021999	1022876	1023754	1024632	1025511
4.55	1026390	1027270	1028150	1029031	1029913	1030795	1031677	1032561	1033444	1034328
4.56	1035213	1036098	1036984	1037870	1038756	1039643	1040531	1041419	1042308	1043197
4.57	1044087	1044977	1045868	1046759	1047651	1048544	1049437	1050330	1051224	1052119
4.58	1053014	1053910	1054806	1055703	1056600	1057498	1058396	1059295	1060194	1061094
4.59	1061995	1062896	1063797	1064700	1065602	1066505	1067409	1068313	1069218	1070123
4.60	1071029	1071935	1072842	1073749	1074656	1075565	1076474	1077383	1078293	1079203
4.61	1080114	1081026	1081938	1082850	1083763	1084677	1085591	1086506	1087422	1088338
4.62	1089254	1090171	1091089	1092007	1092925	1093845	1094764	1095685	1096606	1097527
4.63	1098449	1099372	1100295	1101218	1102142	1103067	1103992	1104918	1105845	1106772
4.64	1107699	1108627	1109555	1110484	1111414	1112344	1113274	1114205	1115137	1116069
4.65	1117002	1117935	1118869	1119803	1120738	1121674	1122610	1123546	1124483	1125421
4.66	1126359	1127298	1128237	1129177	1130118	1131059	1132000	1132942	1133885	1134828
4.67	1135772	1136716	1137661	1138606	1139552	1140499	1141446	1142393	1143341	1144290
4.68	1145239	1146189	1147139	1148090	1149041	1149993	1150945	1151899	1152852	1153806
4.69	1154761	1155716	1156672	1157629	1158585	1159543	1160501	1161460	1162419	1163379
4.70	1164339	1165300	1166261	1167223	1168186	1169149	1170112	1171076	1172041	1173006
4.71	1173972	1174938	1175905	1176873	1177841	1178810	1179779	1180749	1181719	1182690
4.72	1183662	1184634	1185606	1186580	1187553	1188527	1189502	1190478	1191453	1192430
4.73	1193407	1194385	1195363	1196342	1197321	1198301	1199281	1200262	1201244	1202226
4.74	1203209	1204192	1205176	1206160	1207145	1208130	1209116	1210103	1211090	1212078
4.75	1213066	1214055	1215044	1216035	1217025	1218016	1219008	1220001	1220993	1221987
4.76	1222981	1223976	1224971	1225967	1226964	1227961	1228959	1229957	1230956	1231955
4.77	1232955	1233955	1234956	1235957	1236959	1237962	1238965	1239969	1240973	1241978
4.78	1242983	1243989	1244996	1246003	1247011	1248019	1249028	1250037	1251047	1252058
4.79	1253069	1254081	1255093	1256106	1257119	1258133	1259148	1260163	1261179	1262195

TABLE I. *Vapor pressure of* He^4 *(1958 scale) in microns (10^{-3} mm) mercury at 0° C and standard gravity (980.665 cm/sec²)*—Con.

T°K	0.000	0.001	0.002	0.003	0.004	0.005	0.006	0.007	0.008	0.009
4.80	1263212	1264230	1265248	1266266	1267286	1268306	1269326	1270347	1271369	1272391
4.81	1273414	1274437	1275461	1276486	1277511	1278536	1279562	1280589	1281616	1282644
4.82	1283673	1284702	1285732	1286762	1287793	1288825	1289857	1290889	1291923	1292957
4.83	1293991	1295026	1296062	1297098	1298134	1299172	1300210	1301248	1302287	1303327
4.84	1304367	1305408	1306449	1307491	1308534	1309577	1310621	1311665	1312710	1313756
4.85	1314802	1315849	1316896	1317944	1318993	1320042	1321092	1322142	1323193	1324245
4.86	1325297	1326350	1327403	1328457	1329511	1330566	1331622	1332678	1333735	1334792
4.87	1335850	1336908	1337968	1339027	1340088	1341148	1342210	1343272	1344335	1345398
4.88	1346462	1347527	1348592	1349658	1350724	1351791	1352859	1353927	1354996	1356066
4.89	1357136	1358207	1359278	1360350	1361422	1362495	1363569	1364643	1365718	1366794
4.90	1367870	1368947	1370024	1371101	1372180	1373258	1374338	1375418	1376499	1377580
4.91	1378662	1379745	1380828	1381912	1382996	1384081	1385167	1386253	1387340	1388428
4.92	1389516	1390605	1391694	1392783	1393874	1394965	1396056	1397149	1398241	1399335
4.93	1400429	1401524	1402619	1403715	1404812	1405909	1407007	1408105	1409204	1410304
4.94	1411404	1412505	1413606	1414708	1415810	1416913	1418017	1419121	1420226	1421332
4.95	1422438	1423545	1424652	1425760	1426869	1427978	1429088	1430198	1431309	1432421
4.96	1433533	1434646	1435760	1436874	1437988	1439104	1440220	1441336	1442454	1443572
4.97	1444690	1445809	1446929	1448050	1449171	1450293	1451415	1452538	1453662	1454786
4.98	1455911	1457036	1458162	1459288	1460415	1461543	1462671	1463800	1464930	1466060
4.99	1467191	1468323	1469455	1470588	1471721	1472855	1473990	1475125	1476261	1477398
5.00	1478535	1479673	1480811	1481950	1483089	1484230	1485370	1486512	1487654	1488797
5.01	1489940	1491084	1492229	1493374	1494520	1495667	1496814	1497962	1499110	1500259
5.02	1501409	1502559	1503710	1504862	1506014	1507167	1508320	1509474	1510629	1511784
5.03	1512940	1514097	1515254	1516412	1517570	1518730	1519889	1521050	1522211	1523373
5.04	1524535	1525698	1526861	1528025	1529190	1530356	1531522	1532688	1533856	1535023
5.05	1536192	1537361	1538531	1539701	1540872	1542044	1543216	1544389	1545563	1546737
5.06	1547912	1549088	1550264	1551441	1552619	1553797	1554976	1556155	1557336	1558516
5.07	1559698	1560880	1562062	1563246	1564429	1565614	1566799	1567985	1569171	1570358
5.08	1571546	1572734	1573923	1575113	1576303	1577494	1578685	1579878	1581070	1582264
5.09	1583458	1584653	1585849	1587045	1588242	1589439	1590638	1591836	1593036	1594236
5.10	1595437	1596638	1597841	1599043	1600247	1601451	1602656	1603861	1605067	1606274
5.11	1607481	1608689	1609897	1611107	1612316	1613527	1614738	1615950	1617162	1618375
5.12	1619589	1620803	1622018	1623234	1624450	1625667	1626884	1628102	1629321	1630541
5.13	1631761	1632982	1634204	1635426	1636649	1637872	1639096	1640321	1641547	1642773
5.14	1644000	1645228	1646456	1647685	1648914	1650144	1651375	1652606	1653839	1655071
5.15	1656305	1657539	1658773	1660008	1661244	1662481	1663718	1664956	1666194	1667433
5.16	1668673	1669913	1671155	1672396	1673639	1674882	1676126	1677370	1678616	1679862
5.17	1681108	1682355	1683603	1684852	1686102	1687352	1688602	1689854	1691106	1692359
5.18	1693612	1694866	1696120	1697375	1698631	1699888	1701145	1702403	1703661	1704920
5.19	1706180	1707441	1708702	1709964	1711228	1712490	1713754	1715019	1716284	1717550
5.20	1718817	1720084	1721352	1722621	1723891	1725161	1726431	1727703	1728975	1730248
5.21	1731521	1732795	1734069	1735345	1736620	1737897	1739174	1740452	1741731	1743010
5.22	1744290									

TABLE II. *1958* He^4 *vapor pressure-temperature scale, T in °K as a function of P in millimeters mercury at 0° C and standard gravity, 980.665 cm/sec²*

P	0		1		2		3		4		5		6		7		8		9	
0.01	0.7907	65	7972	61	8033	57	8090	53	8143	50	8193	47	8240	45	8285	43	8328	40	8368	39
.02	.8407	38	8445	35	8480	35	8515	33	8548	32	8580	32	8612	30	8642	29	8671	28	8699	28
.03	.8727	27	8754	26	8780	25	8805	25	8830	24	8854	24	8878	23	8901	22	8923	22	8945	22
.04	.8967	21	8988	21	9009	20	9029	20	9049	19	9068	20	9088	18	9106	19	9125	18	9143	18
.05	.9161	18	9179	17	9196	17	9213	17	9230	16	9246	17	9263	16	9279	15	9294	16	9310	15
.06	.9325	15	9340	15	9355	15	9370	15	9385	14	9399	14	9413	14	9427	14	9441	14	9455	13
.07	.9468	14	9482	13	9495	13	9508	13	9521	13	9534	12	9546	13	9559	12	9571	12	9583	12
.08	.9595	12	9607	12	9619	12	9631	12	9643	11	9654	11	9665	12	9677	11	9688	11	9699	11
.09	.9710	11	9721	11	9732	10	9742	11	9753	10	9763	11	9774	10	9784	10	9794	10	9804	10
.10	.9814	10	9824	10	9834	10	9844	10	9854	9	9863	10	9873	10	9883	9	9892	9	9901	10
.11	.9911	9	9920	9	9929	9	9938	9	9947	9	9956	9	9965	9	9974	9	9983	8	9991	9
.12	1.0000	9	0009	8	0017	9	0026	8	0034	8	0042	9	0051	8	0059	8	0067	8	0075	8
.13	1.0083	8	0091	8	0099	8	0107	8	0115	8	0123	8	0131	8	0139	7	0146	8	0154	8
.14	1.0162	7	0169	8	0177	7	0184	8	0192	7	0199	7	0206	8	0214	7	0221	7	0228	8
.15	1.0236	7	0243	7	0250	7	0257	7	0264	7	0271	7	0278	7	0285	7	0292	7	0299	6
.16	1.0305	7	0312	7	0319	7	0326	6	0332	7	0339	7	0346	6	0352	7	0359	6	0365	7
.17	1.0372	6	0378	7	0385	6	0391	7	0398	6	0404	6	0410	7	0417	6	0423	6	0429	6
.18	1.0435	6	0441	7	0448	6	0454	6	0460	6	0466	6	0472	6	0478	6	0484	6	0490	6
.19	1.0496	6	0502	6	0508	5	0513	6	0519	6	0525	6	0531	6	0537	5	0542	6	0548	6

TABLE II. *1958 He^4 vapor pressure-temperature scale, T in °K as a function of P in millimeters mercury at 0° C and standard gravity, 980.665 cm/sec²*—Continued

P	0		1		2		3		4		5		6		7		8		9	
0.2	1.0554	55	0609	54	0663	52	0715	49	0764	49	0813	46	0859	45	0904	44	0948	43	0991	41
.3	1.1032	41	1073	39	1112	38	1150	38	1188	36	1224	36	1260	35	1295	34	1329	33	1362	33
.4	1.1395	32	1427	32	1459	31	1490	30	1520	30	1550	29	1579	29	1608	28	1636	27	1663	28
.5	1.1691	27	1718	26	1744	26	1770	26	1796	25	1821	25	1846	25	1871	24	1895	24	1919	23
.6	1.1942	24	1966	23	1989	22	2011	23	2034	22	2056	22	2078	21	2099	21	2120	21	2141	21
.7	1.2162	21	2183	20	2203	20	2223	20	2243	20	2263	20	2283	19	2302	19	2321	19	2340	19
.8	1.2359	18	2377	18	2395	19	2414	18	2432	17	2449	18	2467	18	2485	17	2502	17	2519	17
.9	1.2536	17	2553	17	2570	16	2586	17	2603	16	2619	16	2635	16	2651	16	2667	16	2683	16
1.0	1.2699	15	2714	16	2730	15	2745	15	2760	15	2775	15	2790	15	2805	15	2820	14	2834	15
1.1	1.2849	14	2863	15	2878	14	2892	14	2906	14	2920	14	2934	14	2948	13	2961	14	2975	14
1.2	1.2989	13	3002	13	3015	14	3029	13	3042	13	3055	13	3068	13	3081	13	3094	13	3107	12
1.3	1.3119	13	3132	13	3145	12	3157	12	3169	13	3182	12	3194	12	3206	12	3218	12	3230	12
1.4	1.3242	12	3254	12	3266	12	3278	12	3290	11	3301	12	3313	12	3325	11	3336	12	3348	11
1.5	1.3359	11	3370	11	3381	12	3393	11	3404	11	3415	11	3426	11	3437	11	3448	11	3459	10
1.6	1.3469	11	3480	11	3491	10	3501	11	3512	11	3523	10	3533	11	3544	10	3554	10	3564	11
1.7	1.3575	10	3585	10	3595	10	3605	10	3615	10	3625	10	3635	10	3645	10	3655	10	3665	10
1.8	1.3675	10	3685	10	3695	9	3704	10	3714	10	3724	9	3733	10	3743	9	3752	10	3762	9
1.9	1.3771	9	3780	10	3790	9	3799	10	3809	9	3818	9	3827	9	3836	9	3845	9	3854	9
2	1.3863	89	3952	86	4038	82	4120	80	4200	77	4277	75	4352	73	4425	71	4496	69	4565	67
3	1.4632	65	4697	63	4760	63	4823	60	4883	60	4943	58	5001	56	5057	56	5113	55	5168	53
4	1.5221	53	5274	51	5325	51	5376	49	5425	49	5474	48	5522	47	5569	47	5616	46	5662	45
5	1.5707	44	5751	44	5795	43	5838	42	5880	42	5922	41	5963	41	6004	40	6044	40	6084	39
6	1.6123	39	6162	38	6200	38	6238	37	6275	37	6312	36	6348	36	6384	36	6420	35	6455	35
7	1.6490	35	6525	34	6559	34	6593	33	6626	33	6659	33	6692	32	6724	32	6756	32	6788	32
8	1.6820	31	6851	31	6882	31	6913	30	6943	30	6973	30	7003	30	7033	29	7062	29	7091	29
9	1.7120	28	7148	29	7177	28	7205	28	7233	28	7261	27	7288	28	7316	27	7343	27	7370	26
10	1.7396	27	7423	26	7449	26	7475	26	7501	26	7527	25	7552	26	7578	25	7603	25	7628	25
11	1.7653	25	7678	24	7702	25	7727	24	7751	24	7775	24	7799	24	7823	23	7846	24	7870	23
12	1.7893	23	7916	23	7939	23	7962	23	7985	23	8008	22	8030	23	8053	22	8075	22	8097	22
13	1.8119	22	8141	22	8163	21	8184	22	8206	21	8227	22	8249	21	8270	21	8291	21	8312	21
14	1.8333	20	8353	21	8374	21	8395	20	8415	20	8435	21	8456	20	8476	20	8496	20	8516	20
15	1.8536	19	8555	20	8575	20	8595	19	8614	20	8634	19	8653	19	8672	19	8691	19	8710	19
16	1.8729	19	8748	19	8767	18	8785	19	8804	19	8823	18	8841	19	8860	18	8878	18	8896	18
17	1.8914	18	8932	18	8950	18	8968	18	8986	18	9004	18	9022	17	9039	18	9057	17	9074	18
18	1.9092	17	9109	17	9126	18	9144	17	9161	17	9178	17	9195	17	9212	17	9229	17	9246	16
19	1.9262	17	9279	17	9296	16	9312	17	9329	16	9345	17	9362	16	9378	16	9394	17	9411	16
20	1.9427	16	9443	16	9459	16	9475	16	9491	16	9507	16	9523	16	9539	15	9554	16	9570	16
21	1.9586	16	9602	15	9617	15	9632	16	9648	15	9663	16	9679	15	9694	15	9709	15	9724	16
22	1.9740	15	9755	15	9770	15	9785	15	9800	15	9815	15	9830	14	9844	15	9859	15	9874	15
23	1.9889	14	9903	15	9918	14	9932	15	9947	14	9961	15	9976	14	9990	15	0005	14	0019	14
24	2.0033	15	0048	14	0062	14	0076	14	0090	14	0104	14	0118	14	0132	14	0146	14	0160	14
25	2.0174	14	0188	14	0202	13	0215	14	0229	14	0243	14	0257	13	0270	14	0284	13	0297	14
26	2.0311	13	0324	14	0338	13	0351	14	0365	13	0378	13	0391	14	0405	13	0418	13	0431	13
27	2.0444	14	0458	13	0471	13	0484	13	0497	13	0510	13	0523	13	0536	13	0549	13	0562	13
28	2.0575	13	0588	12	0600	13	0613	13	0626	13	0639	13	0652	12	0664	13	0677	13	0690	12
29	2.0702	13	0715	12	0727	13	0740	12	0752	13	0765	12	0777	13	0790	12	0802	12	0814	13
30	2.0827	12	0839	12	0851	12	0863	13	0876	12	0888	12	0900	12	0912	12	0924	12	0936	13
31	2.0949	12	0961	12	0973	12	0985	12	0997	12	1009	12	1021	11	1032	12	1044	12	1056	12
32	2.1068	12	1080	12	1092	11	1103	12	1115	12	1127	12	1139	11	1150	12	1162	12	1174	11
33	2.1185	12	1197	11	1208	12	1220	11	1231	12	1243	11	1254	12	1266	11	1277	12	1289	11
34	2.1300	12	1312	11	1323	11	1334	12	1346	11	1357	11	1368	11	1379	12	1391	11	1402	11
35	2.1413	11	1424	12	1436	11	1447	11	1458	11	1469	11	1480	11	1491	11	1502	11	1513	11
36	2.1524	11	1535	11	1546	11	1557	11	1568	11	1579	11	1590	11	1601	11	1612	11	1623	11
37	2.1634	10	1644	11	1655	11	1666	11	1677	11	1688	10	1698	11	1709	11	1720	11	1731	10
38	2.1741	11	1752	11	1763	10	1773	11	1784	11	1795	10	1805	11	1816	10	1826	11	1837	11
39	2.1848	10	1858	11	1869	11	1880	10	1890	10	1900	10	1910	11	1921	10	1931	11	1942	10
40	2.1952	10	1962	11	1973	10	1983	10	1993	11	2004	10	2014	10	2024	10	2034	10	2044	11
41	2.2055	10	2065	10	2075	10	2085	10	2095	10	2105	10	2115	11	2126	10	2136	10	2146	10
42	2.2156	10	2166	10	2176	10	2186	10	2196	10	2206	10	2216	9	2225	10	2235	10	2245	10
43	2.2255	10	2265	10	2275	10	2285	9	2294	10	2304	10	2314	10	2324	10	2334	9	2343	10
44	2.2353	10	2363	9	2372	10	2382	10	2392	9	2401	10	2411	10	2421	9	2430	10	2440	10
45	2.2450	9	2459	9	2468	10	2478	10	2488	10	2498	9	2507	9	2516	9	2525	10	2535	9
46	2.2544	10	2554	9	2563	10	2573	9	2582	9	2591	10	2601	9	2610	9	2619	10	2629	9
47	2.2638	9	2647	9	2656	10	2666	9	2675	9	2684	9	2693	10	2703	9	2712	9	2721	9
48	2.2730	9	2739	9	2748	9	2757	10	2767	9	2776	9	2785	9	2794	9	2803	9	2812	9
49	2.2821	9	2830	9	2839	9	2848	9	2857	9	2866	9	2875	9	2884	9	2893	9	2902	9
50	2.2911	88	2999	87	3086	86	3172	85	3257	84	3341	83	3424	82	3506	81	3587	79	3666	79
60	2.3745	78	3823	78	3901	76	3977	75	4052	75	4127	74	4201	73	4274	73	4347	71	4418	71
70	2.4489	71	4560	69	4629	69	4698	68	4766	68	4834	67	4901	66	4967	66	5033	66	5099	64
80	2.5163	64	5227	64	5291	63	5354	63	5417	62	5479	61	5540	61	5601	61	5662	60	5722	59
90	2.5781	60	5841	58	5899	59	5958	57	6015	58	6073	57	6130	56	6186	57	6243	55	6298	56

TABLE II. *1958* He^4 *vapor pressure-temperature scale, T in °K as a function of P in millimeters mercury at 0° C and standard gravity, 980.665 cm/sec²*—Continued

P	0		1		2		3		4		5		6		7		8		9	
100	2.6354	55	6409	55	6464	54	6518	54	6572	53	6625	54	6679	53	6732	52	6784	52	6836	52
110	2.6888	52	6940	51	6991	51	7042	51	7093	50	7143	50	7193	50	7243	49	7292	49	7341	49
120	2.7390	49	7439	48	7487	48	7535	48	7583	48	7631	47	7678	47	7725	47	7772	46	7818	47
130	2.7865	46	7911	46	7957	45	8002	46	8048	45	8093	45	8138	44	8182	45	8227	44	8271	44
140	2.8315	44	8459	43	8402	44	8446	43	8489	43	8532	43	8575	42	8617	42	8659	43	8702	42
150	2.8744	41	8785	42	8827	42	8869	41	8910	41	8951	41	8992	40	9032	41	9073	40	9113	40
160	2.9153	40	9193	40	9233	40	9273	39	9312	40	9352	39	9391	39	9430	39	9469	39	9508	38
170	2.9546	39	9585	38	9623	38	9661	38	9699	38	9737	37	9774	38	9812	38	9850	36	9886	38
180	2.9924	37	9961	36	9997	37	0034	37	0071	36	0107	36	0143	36	0179	36	0215	36	0251	36
190	3.0287	36	0323	35	0358	35	0393	36	0429	35	0464	35	0499	35	0534	34	0568	35	0603	34
200	3.0637	35	0672	34	0706	34	0740	34	0774	34	0808	34	0842	34	0876	33	0909	34	0943	33
210	3.0976	34	1010	33	1043	33	1076	33	1109	33	1142	32	1174	33	1207	33	1240	32	1272	32
220	3.1304	33	1337	32	1369	32	1401	32	1433	32	1465	31	1496	32	1528	32	1560	31	1591	31
230	3.1622	32	1654	31	1685	31	1716	31	1747	31	1778	31	1809	31	1840	30	1870	31	1901	30
240	3.1931	31	1962	30	1992	30	2022	30	2052	30	2082	30	2112	30	2142	30	2172	30	2202	29
250	3.2231	30	2261	30	2291	29	2320	29	2349	30	2379	29	2408	29	2437	29	2466	29	2495	29
260	3.2524	28	2552	29	2581	29	2610	28	2638	29	2667	28	2695	29	2724	28	2752	28	2780	28
270	3.2808	28	2836	28	2864	28	2892	28	2920	28	2948	28	2976	27	3003	28	3031	27	3058	28
280	3.3086	27	3113	28	3141	27	3168	27	3195	27	3222	27	3249	27	3276	27	3303	27	3330	27
290	3.3357	27	3384	26	3410	27	3437	26	3463	27	3490	26	3516	27	3543	26	3569	26	3595	27
300	3.3622	26	3648	26	3674	26	3700	26	3726	26	3752	26	3778	25	3803	26	3829	26	3855	25
310	3.3880	26	3906	25	3931	26	3957	25	3982	26	4008	25	4033	25	4058	25	4083	26	4109	25
320	3.4134	25	4159	25	4184	25	4209	24	4233	25	4258	25	4283	25	4308	24	4332	25	4357	25
330	3.4382	24	4406	25	4431	24	4455	24	4479	25	4504	24	4528	24	4552	24	4576	25	4601	24
340	3.4625	24	4649	24	4673	24	4697	24	4721	23	4744	24	4768	24	4792	24	4816	23	4839	24
350	3.4863	23	4886	24	4910	23	4933	24	4957	23	4980	24	5004	23	5027	23	5050	23	5073	24
360	3.5097	23	5120	23	5143	23	5166	23	5189	23	5212	23	5235	23	5258	22	5280	23	5303	23
370	3.5326	23	5349	22	5371	23	5394	23	5417	22	5439	23	5462	22	5484	22	5506	23	5529	22
380	3.5551	22	5573	23	5596	22	5618	22	5640	22	5662	22	5684	22	5706	22	5728	22	5750	22
390	3.5772	22	5794	22	5816	22	5838	22	5860	21	5881	22	5903	22	5925	22	5947	21	5968	22
400	3.5990	21	6011	22	6033	21	6054	22	6076	21	6097	22	6119	21	6140	21	6161	21	6182	22
410	3.6204	21	6225	21	6246	21	6267	21	6288	21	6309	21	6330	21	6351	21	6372	21	6393	21
420	3.6414	21	6435	21	6456	21	6477	20	6497	21	6518	21	6539	20	6559	21	6580	21	6601	20
430	3.6621	21	6642	20	6662	21	6683	20	6703	21	6724	20	6744	20	6764	21	6785	20	6805	20
440	3.6825	20	6845	21	6866	20	6886	20	6906	20	6926	20	6946	20	6966	20	6986	20	7006	20
450	3.7026	20	7046	20	7066	20	7086	19	7105	20	7125	20	7145	20	7165	19	7184	20	7204	20
460	3.7224	19	7243	20	7263	19	7282	20	7302	20	7322	19	7341	19	7360	20	7380	19	7399	20
470	3.7419	19	7438	19	7457	20	7477	19	7496	19	7515	19	7534	19	7553	20	7573	19	7592	19
480	3.7611	19	7630	19	7649	19	7668	19	7687	19	7706	19	7725	19	7744	19	7763	18	7781	19
490	3.7800	19	7819	19	7838	19	7857	18	7875	19	7894	19	7913	18	7931	19	7950	19	7969	18
500	3.7987	19	8006	18	8024	19	8043	18	8061	19	8080	18	8098	19	8117	18	8135	18	8153	19
510	3.8172	18	8190	18	8208	19	8227	18	8245	18	8263	18	8281	18	8299	18	8317	19	8336	18
520	3.8354	18	8372	18	8390	18	8408	18	8426	18	8444	18	8462	18	8480	18	8498	18	8516	17
530	3.8533	18	8551	18	8569	18	8587	18	8605	17	8622	18	8640	18	8658	18	8676	17	8693	18
540	3.8711	17	8728	18	8746	18	8764	17	8781	18	8799	17	8816	18	8834	17	8851	18	8869	17
550	3.8886	17	8903	18	8921	17	8938	17	8955	18	8973	17	8990	17	9007	18	9025	17	9042	17
560	3.9059	17	9076	17	9093	18	9111	17	9128	17	9145	17	9162	17	9179	17	9196	17	9213	17
570	3.9230	17	9247	17	9264	17	9281	17	9298	17	9315	17	9332	17	9349	16	9365	17	9382	17
580	3.9399	17	9416	17	9433	16	9449	17	9466	17	9483	16	9499	17	9516	17	9533	16	9549	17
590	3.9566	17	9583	16	9599	17	9616	16	9632	17	9649	16	9665	17	9682	16	9698	17	9715	16
600	3.9731	16	9747	17	9764	16	9780	17	9797	16	9813-	16	9829	17	9846	16	9862	16	9878	16
610	3.9894	17	9911	16	9927	16	9943	16	9959	16	9975	16	9991	16	0007	17	0024	16	0040	16
620	4.0056	16	0072	16	0088	16	0104	16	0120	16	0136	16	0152	16	0168	16	0184	15	0199	16
630	4.0215	16	0231	16	0247	16	0263	16	0279	16	0295	15	0310	16	0326	16	0342	16	0358	15
640	4.0373	16	0389	16	0405	15	0420	16	0436	16	0452	15	0467	16	0483	15	0498	16	0514	16
650	4.0530	15	0545	16	0561	15	0576	16	0592	15	0607	16	0623	15	0638	15	0653	16	0669	15
660	4.0684	16	0700	15	0715	15	0730	16	0746	15	0761	15	0776	16	0792	15	0807	15	0822	15
670	4.0837	16	0853	15	0868	15	0883	15	0898	15	0913	15	0928	16	0944	15	0959	15	0974	15
680	4.0989	15	1004	15	1019	15	1034	15	1049	15	1064	15	1079	15	1094	15	1109	15	1124	15
690	4.1139	15	1154	15	1169	15	1184	14	1198	15	1213	15	1228	15	1243	15	1258	15	1273	14
700	4.1287	15	1302	15	1317	15	1332	14	1346	15	1361	15	1376	15	1391	14	1405	15	1420	15
710	4.1435	14	1449	15	1464	14	1478	15	1493	15	1508	14	1522	15	1537	14	1551	15	1566	14
720	4.1580	15	1595	14	1609	15	1624	14	1638	15	1653	14	1667	14	1681	15	1696	14	1710	15
730	4.1725	14	1739	14	1753	15	1768	14	1782	14	1796	15	1811	14	1825	14	1839	14	1853	15
740	4.1868	14	1882	14	1896	14	1910	15	1925	14	1939	14	1953	14	1967	14	1981	14	1995	14
750	4.2009	15	2024	14	2038	14	2052	14	2066	14	2080	14	2094	14	2108	14	2122	14	2136	14
760	4.2150	14	2164	14	2178	14	2192	14	2206	14	2220	14	2234	14	2248	14	2262	13	2275	14
770	4.2289	14	2303	14	2317	14	2331	14	2345	14	2358	14	2372	14	2386	14	2400	14	2414	13
780	4.2427	14	2441	14	2455	14	2469	13	2482	13	2496	14	2510	13	2523	14	2537	14	2551	13
790	4.2564	14	2578	14	2592	13	2605	14	2619	13	2632	14	2646	13	2659	14	2673	13	2686	14

TABLE III. *1958* He^4 *vapor pressure-temperature scale,* T *in ° K as a function of* P *in centimeters mercury at 0° C and standard gravity, 980.665 cm/sec²*

P	0		1		2		3		4		5		6		7		8		9	
80	4.2700	135	2835	133	2968	132	3100	131	3231	131	3362	129	3491	128	3619	127	3746	126	3872	125
90	4.3997	124	4121	123	4244	122	4366	122	4488	120	4608	120	4728	118	4846	118	4964	117	5081	116
100	4.5197	116	5313	114	5427	114	5541	113	5654	112	5766	112	5878	111	5989	110	6099	109	6208	109
110	4.6317	108	6425	107	6532	107	6639	106	6745	105	6850	105	6955	104	7059	103	7162	103	7265	102
120	4.7367	102	7469	101	7570	100	7670	100	7770	100	7870	98	7968	99	8067	97	8164	97	8261	97
130	4.8358	96	8454	96	8550	95	8645	94	8739	94	8833	94	8927	93	9020	92	9112	92	9204	92
140	4.9296	91	9387	91	9478	90	9568	90	9658	89	9747	89	9836	89	9925	88	0013	88	0101	87
150	5.0188	87	0275	86	0361	86	0447	86	0533	85	0618	85	0703	84	0787	84	0871	84	0955	83
160	5.1038	83	1121	82	1203	83	1286	81	1367	82	1449	81	1530	81	1611	80	1691	80	1771	80
170	5.1851	79	1930	79	2009	79	2088	78	2166	78										

TABLE IV. *Temperature derivative,* dP/dT, *in millimeters* Hg/° *K for the 1958* He^4 *vapor pressure-temperature scale,* P *in millimeters mercury at 0° C and standard gravity, 980.665 cm/sec²*

T	0.00	0.01	0.02	0.03	0.04	0.05	0.06	0.07	0.08	0.09
0.5	0.0005503	0.0007383	0.0009799	0.001287	0.001674	0.002157	0.002755	0.003489	0.004384	0.005468
.6	.006772	.008329	.01018	.01236	.01493	.01792	.02141	.02544	.03008	.03540
.7	.04148	.04838	.05622	.06506	.07501	.08617	.09863	.1125	.1280	.1451
.8	.1640	.1848	.2077	.2328	.2602	.2902	.3228	.3583	.3968	.4385
.9	.4835	.5320	.5843	.6406	.7008	.7654	.8346	.9084	.9871	1.071
1.0	1.160	1.255	1.355	1.462	1.575	1.694	1.820	1.953	2.093	2.240
1.1	2.395	2.557	2.728	2.907	3.095	3.291	3.496	3.711	3.935	4.169
1.2	4.412	4.666	4.930	5.205	5.491	5.788	6.096	6.416	6.747	7.090
1.3	7.445	7.813	8.194	8.587	8.993	9.413	9.846	10.29	10.75	11.23
1.4	11.72	12.22	12.73	13.26	13.81	14.37	14.95	15.54	16.15	16.77
1.5	17.41	18.06	18.73	19.42	20.12	20.84	21.58	22.33	23.10	23.88
1.6	24.68	25.50	26.33	27.18	28.05	28.94	29.84	30.76	31.69	32.64
1.7	33.61	34.59	35.59	36.61	37.64	38.69	39.76	40.84	41.94	43.05
1.8	44.18	45.33	46.49	47.67	48.86	50.06	51.28	52.52	53.77	55.03
1.9	56.30	57.59	58.89	60.20	61.52	62.85	64.19	65.54	66.91	68.28
2.0	69.65	71.03	72.42	73.81	75.20	76.60	77.99	79.39	80.79	82.20
2.1	83.60	85.00	86.38	87.74	89.09	90.41	91.71	92.96	94.28	95.77
2.2	97.31	98.88	100.5	102.1	103.7	105.4	107.1	108.8	110.5	112.2
2.3	113.9	115.7	117.5	119.2	121.0	122.9	124.7	126.5	128.4	130.3
2.4	132.1	134.1	136.0	137.9	139.9	141.8	143.8	145.8	147.8	149.8
2.5	151.9	153.9	156.0	158.1	160.2	162.3	164.5	166.6	168.8	171.0
2.6	173.2	175.4	177.6	179.8	182.0	184.3	186.6	188.8	191.2	193.5
2.7	195.9	198.2	200.6	202.9	205.3	207.7	210.1	212.5	215.0	217.4
2.8	219.9	222.4	224.9	227.4	230.0	232.4	235.0	237.6	240.1	242.7
2.9	245.4	248.0	250.6	253.3	256.0	258.6	261.3	264.1	266.8	269.5
3.0	272.3	275.1	277.9	280.7	283.5	286.3	289.2	292.0	294.9	297.8
3.1	300.7	303.7	306.6	309.5	312.5	315.5	318.5	321.5	324.5	327.6
3.2	330.6	333.7	336.8	339.9	343.0	346.1	349.3	352.4	355.6	358.7
3.3	361.9	365.1	368.4	371.6	374.8	378.1	381.4	384.7	388.0	391.3
3.4	394.6	398.0	401.3	404.7	408.1	411.5	414.9	418.3	421.7	425.2
3.5	428.7	432.1	435.6	439.1	442.7	446.2	449.7	453.3	456.9	460.5
3.6	464.1	467.7	471.3	474.9	478.6	482.3	486.0	489.7	493.4	497.2
3.7	500.9	504.6	508.4	512.2	516.0	519.8	523.6	527.5	531.3	535.2
3.8	539.1	543.0	546.9	550.8	554.8	558.8	562.8	566.8	570.8	574.9
3.9	578.9	583.0	587.1	591.2	595.4	599.5	603.7	607.9	612.1	616.3
4.0	620.6	624.8	629.1	633.3	637.6	642.0	646.3	650.6	655.0	659.4
4.1	663.7	668.1	672.6	677.0	681.4	685.9	690.3	694.8	699.2	703.7
4.2	708.1	712.6	717.1	721.6	726.1	730.7	735.3	740.0	744.7	749.4
4.3	754.1	758.9	763.7	768.6	773.4	778.3	783.2	788.1	793.0	797.9
4.4	802.9	807.9	812.9	817.9	822.9	828.0	833.1	838.1	843.2	848.4
4.5	853.5	858.7	863.9	869.1	874.3	879.5	884.8	890.1	895.3	900.7
4.6	906.0	911.4	916.7	922.1	927.6	933.0	938.5	943.9	949.4	955.0
4.7	960.5	966.1	971.7	977.3	982.9	988.6	994.4	1000	1006	1011
4.8	1017	1023	1029	1035	1041	1046	1052	1058	1064	1070
4.9	1076	1082	1088	1094	1100	1107	1113	1119	1125	1131
5.0	1137	1144	1150	1156	1163	1169	1175	1182	1188	1195
5.1	1201	1207	1214	1221	1227	1234	1240	1247	1254	1260
5.2	1267	1274	1280							

TABLE V. *Auxiliary table for use in making hydrostatic head correction*

Table gives values of the ratio between the density of liquid He I at its saturated vapor pressure and the density of mercury at 0° C. (P in centimeters mercury at 0° C and standard gravity, 980.665 cm/sec^2.) The density of mercury has been taken as 13.5951 g/cm^3. If densities of liquid He I constitute critical data in an analysis, examination of the original literature is recommended.

P	0		1		2		3		4		5		6		7		8		9	
0	0.01								0754	37	0717	35	0682	33	0649	30	0619	29	0590	29
10	.010561	27	0534	26	0508	26	0482	25	0457	24	0433	24	0409	23	0386	23	0363	23	0340	23
20	.010317	22	0295	22	0273	22	0251	21	0230	21	0209	21	0188	21	0167	21	0146	20	0126	21
30	.010105	20	0085	20	0065	20	0045	20	0025	20	0005	20	9985	20	9965	19	9946	20	9926	19
40	.009907	20	9887	20	9867	19	9848	20	9828	19	9809	20	9789	19	9770	20	9750	19	9731	20
50	.009711	19	9692	19	9673	20	9653	19	9634	20	9614	20	9594	20	9574	19	9555	19	9536	20
60	.009516	20	9496	19	9477	19	9458	20	9438	19	9419	20	9399	19	9380	20	9360	20	9340	19
70	.009321	20	9301	19	9282	19	9263	20	9243	19	9224	19	9205	19	9186	19	9167	20	9147	19
80	.009128	19	9109	19	9090	20	9070	19	9051	20	9031	19	9012	20	8992	20	8972	20	8952	20
90	.008932	19	8913	20	8893	20	8873	20	8853	20	8833	21	8812	20	8792	21	8771	20	8751	21
100	.008730	21	8709	22	8687	21	8666	22	8644	21	8623	21	8602	22	8580	22	8558	22	8536	23
110	.008513	23	8490	22	8468	23	8445	23	8422	24	8398	23	8375	24	8351	24	8327	25	8302	24
120	.008278	24	8254	24	8230	25	8205	26	8179	26	8153	26	8127	27	8100	26	8074	27	8047	28
130	.008019	28	7991	28	7963	28	7935	29	7906	29	7877	29	7848	30	7818	31	7787	32	7755	32
140	.007723	33	7690	32	7658	33	7625	34	7591	36	7555	36	7519	37	7482	38	7444	39	7405	41
150	.007364	42	7322	43	7279	44	7235	46	7189	48	7141	49	7092	51	7041	53	6988	56	6932	59
160	.006873	61	6812	64	6748	68	6680	73	6607	79	6528	87	6441	103	6338	130	6208	154	6054	190
170	.005864	229	5635	287	5348															

TABLE VI. *Deviations of earlier scales from the 1958 scale,*[a] $T_n - T_{58}$ *in millidegrees*

T_n / n	L55	55E	48	BS	37	32	29	24	T_n / n	L55	55E	48	BS	37	32	29	24
K									K								
0.7	−1.1	+1.0	+0.4	+0.3	.....	−18.4	−2.7	−2.1	3.0	−.6	−1.1	+5.6	.....	+4.2	−3.5	−3.5	+66.8
.8	−1.2	+1.1	+.5	+.3	.....	−20.4	−10.3	−2.3									
.9	−1.3	+1.2	+.6	+.4	−31.9	−22.1	−17.3	−2.4	3.1	−.2	−1.1	+6.0	.....	+5.3	−4.5	−4.5	+57.2
									3.2	+.2	−0.9	+8.0	.....	+6.7	−5.2	−5.2	+47.7
1.0	−1.5	+1.3	+.3	+.4	−26.8	−23.5	−23.5	−2.6	3.3	+.7	−.7	+8.6	.....	+7.9	−5.7	−5.7	+38.4
1.1	−1.6	+1.4	−.2	+.4	−21.5	−24.7	−28.5	−2.7	3.4	+1.3	−.5	+8.7	.....	+8.7	−5.9	−5.9	+29.4
1.2	−1.7	+1.5	+.4	+.5	−15.2	−25.4	−32.1	−2.8	3.5	+1.9	−.3	+8.8	.....	+8.9	−5.8	−5.8	+21.0
1.3	−1.8	+1.5	+.3	+.6	−8.1	−25.7	−34.1	−3.0	3.6	+2.5	−.1	+8.7	.....	+9.0	−5.5	−5.5	+13.2
1.4	−1.9	+1.6	+1.0	+.8	−2.3	−25.5	−34.5	−3.2	3.7	+2.9	0	+8.6	.....	+8.6	−4.8	−4.8	+6.2
1.5	−2.0	+1.6	+1.3	+1.2	+1.1	−24.7	−33.2	−3.5	3.8	+3.2	0	+7.7	.....	+7.5	−3.9	−3.9	−0.1
1.6	−2.1	+1.5	+2.9	+1.8	+2.6	−23.2	−30.3	+0.2	3.9	+3.2	−.1	+6.6	.....	+6.3	−2.6	−2.6	−5.4
1.7	−2.1	+1.4	+3.8	+2.6	+3.2	−21.0	−25.9	+33.0	4.0	+3.0	−.2	+5.0	.....	+4.7	−0.9	−0.9	−9.6
1.8	−2.2	+1.1	+3.9	+3.4	+3.5	−18.6	−20.2	+58.6									
1.9	−2.2	+0.8	+5.1	+4.1	+4.2	−14.2	−13.3	+78.5	4.1	+2.4	−.3	+2.6	.....	+2.8	+1.2	+1.2	−12.7
									4.2	+1.2	−.6	+0.5	.....	+1.1	+3.7	+3.7	−14.6
2.0	−2.2	+.6	+6.0	+4.6	+5.6	−9.7	−5.6	+93.6	4.3	0	−1.0	−.4	.....	−0.5	+6.6	+6.6	−15.3
2.1	−2.2	+.6	+8.4	+5.1	+7.1	−4.5	+2.5	+104.5	4.4	−.9	−1.4	+.9	.....	.....	+10.0	+10.0	−14.6
2.2	−2.2	+.8	+9.4	.....	+9.3	+8.2	+8.2	+111.2	4.5	−1.5	−1.9	+3.8	.....	.....	+14.0	+14.0	−12.4
2.3	−2.1	+.5	+8.5	.....	+8.2	+7.0	+7.0	+113.3	4.6	−1.7	−2.3	+7.7	.....	.....	+18.5	+18.5	−8.8
2.4	−2.0	0	+7.0	.....	+6.9	+5.4	+5.4	+111.2	4.7	−1.5	−2.8	+11.9	.....	.....	+23.6	+23.6	−3.7
2.5	−1.9	−.4	+5.6	.....	+5.5	+3.8	+3.8	+106.8	4.8	−0.9	−3.2	+15.8	.....	.....	+29.3	+29.3	+3.0
2.6	−1.8	−.7	+5.0	.....	+4.4	+2.1	+2.1	+100.7	4.9	+.2	−3.7	+18.6	.....	.....	+35.7	+35.7	+11.1
2.7	−1.5	−.9	+4.5	.....	+3.6	+0.6	+0.6	+93.4	5.0	+1.7	−4.1	+19.0	.....	.....	+42.6	+42.6	+20.8
2.8	−1.3	−1.1	+3.6	.....	+3.4	−.9	−.9	+85.2									
2.9	−0.9	−1.1	+4.7	.....	+3.6	−2.2	−2.2	+76.3	5.1	+3.7	−4.5	+15.8	.....	.....	.....	.....	+32.1
									5.2	+6.3	−5.0	+6.5	.....	.....	.....	.....	+45.0

[a] Explanatory notes concerning table of deviations of earlier scales from the 1958 scale:

T_{24}: Defined by equation on p. 33 of Leiden Comm. No. 147b (Kamerlingh Onnes and Weber) and by last equation on p. 23 of Leiden Comm. Suppl. No. 49 (Verschaffelt). These equations yield equal pressures at about 1.59° K. Therefcre, values up through 1.5° K were derived from Verschaffelt's equation and those above from that of Kamerlingh Onnes and Weber.

T_{28}: Defined by eq (6) on p. 36 of Leiden Comm. No. 202c (Keesom, Weber, and Schmidt). These equations give equal pressures at 2.1765° K. The authors state in the last paragraph of the communication, p. 37, that the first of the equations fits reasonably well the data of Comm. No. 147b up to 5° K. Therefore, deviations up to 5.0° K have been included in the table.

T_{32}: Defined by the first of eq (6) on p. 36 of Leiden Comm. No. 202c (Keesom, Weber, and Schmidt) and by the equation on p. 8 of Leiden Comm. No. 219a (Keesom). T_{32} and T_{29} are thus identical above the lambda point. These two equations are discontinuous by about 0.008° at 2.190° K and this fact was noted by Keesom (Leiden Comm. Suppl. 71d).

T_{37}: Defined by T_{32} together with curves in figure 1 of Leiden Comm. No. 250c (Schmidt and Keesom). Differences between T_{37} and T_{32} were determined directly from figure 1 with sufficient precision to determine differences between T_{58} and T_{37} to 0.1 millidegree.

T_{BS}: Defined by eq (9) and curve of figure 4, p. 1212 of Trans Faraday Soc. **35** (Bleaney and Simon, 1939). Part, or all, of this scale is sometimes referred to as T_{39}. In order to obtain differences between this scale and T_{58}, pressures were calculated from the equation and curve with sufficient precision to yield differences to 0.1 millidegree.

(*Continued on page 17*)

T_{58}: Defined by tables I and II on pages T153 to T159 and by second equation on p. T152 of Procès-Verbaux des séances du Comité International des Poids et Mesures **23B**, T151 (1952). Values given in the table were obtained in the following ways. First, values of the difference between this scale and the 1958 scale were calculated at every 0.01° interval between 0.95° and 4.25° K from data of table II on pp. T158 and T159. The tabulated values from 1.0° through 4.2° K were then obtained by averaging the calculated differences between $T-0.05°$ and $T+0.05°$, with weights of ½ assigned to the values at $T-0.05°$ and $T+0.05°$ and unit weights to all values at intermediate temperatures. For example, the tabulated value at 2.0° K is actually 1/20 of the sum of the differences at 1.95° and 2.05° plus 1/10 of the sum of the differences at 1.96°, 1.97°, 1.98°, 1.99°, 2.00°, 2.01°, 2.02°, 2.03°, and 2.04° K. The tabulated values at 0.7°, 0.8°, and 0.9° K were obtained by calculating the pressure corresponding to each 0.01° interval between 0.65° and 0.95° K from the data on p. T153 of table I and averaging the results in the manner just described. At 4.3° K and above, the tabulated values were obtained directly from the equation given on p. T152. Tables and equation have been published also by C. F. Squire, *Low temperature physics*, pp. 229 to 233 and p. 26 (McGraw-Hill Book Co., Inc., New York, N.Y., 1953).

T_{1948}: Defined by the unnumbered equations on p. 188, *Low temperature physics and chemistry* (Clement), Proc. Fifth Intern. Conf. (Univ. of Wisconsin Press, Madison, Wis., 1958). Values of vapor pressure in millimeters mercury at 20° C were calculated by the computer at the U.S. Naval Research Laboratory (the NAREC) and values in millimeters mercury at 0° C were calculated by the computer at Los Alamos Scientific Laboratory (the MANIAC). The MANIAC calculation was used for obtaining the values in the table.

T_{1955}: Defined by table VII on p. 461, *Progress in low temperature physics* (Van Dijk and Durieux), (North-Holland Publishing Co., Amsterdam, Netherlands, 1957). Values below 0.9° K were obtained from the tables mentioned in section 23 of the reference. Table VII mentioned above is the same as table V published in Physica **24,** 1 (1958) and in Leiden Comm. Suppl. 113c.

TABLE VII. *Auxiliary table for use in making corrections for density of mercury at temperatures other than 0°C*[a]

Table gives values of the ratio between the density of mercury at the indicated temperature (° C) and that at 0° C.

t° C	0	1	2	3	4	5	6	7	8	9
10	0.99818	800	782	764	746	728	710	692	674	655
20	.99637	619	601	583	565	547	529	511	493	475
30	.99457	439	421	403	385	367	349	331	313	295

[a] Smithsonian Physical Tables, Ninth Revised Ed., edited by W. E. Forsythe, p. 153 (The Smithsonian Inst., Washington, D.C., 1954).

Equation for Computing Local Acceleration Due to Gravity [1, 2]

Most frequently the vapor pressure is measured as a distance between two mercury levels. After corrections for capillarity and for the temperature of the mercury and the scale have been applied, the height, h, has to be reduced to standard gravity. The reduced height, h_0, can be computed from $h_0=hg/980.665$. If the local value of g is unknown, it may be computed with sufficient accuracy for correcting the height of a mercury column from

$$g=980.632-2.586\cos 2\phi+0.003\cos 4\phi \\ -0.0003086\,H$$

where ϕ is the local latitude and H the local altitude in meters. The unit of g is cm/sec^2.

[1] Procès-Verbaux des séances du Comité International des Poids et Mesures **22,** pp. 96 to 98, 114 to 118, 129 to 134 (1950).

[2] G. D. Garland, pp. 221, 222, Karl Jung, p. 564, Handbuch der Physik edited by J. Bartels **47,** (Springer-Verlag, Berlin, 1956).

WASHINGTON, D.C. (Paper 64A1–25)

JOURNAL OF RESEARCH of the National Bureau of Standards—A. Physics and Chemistry
Vol. 64, No. 1, January–February 1960

Energy Levels and Spectrum of Neutral Helium (^{4}He I)

William C. Martin

(August 24, 1959)

A table of energy levels based on the most accurate observations now available is given for the neutral ^{4}He atom. The wavelengths contained in a revised list of ^{4}He I lines from 320 A to 21132 A are also based on the best measurements, over half of them having been calculated from the wavenumber separations of appropriate levels. Several previously disturbing features of the ^{4}He term scheme are obviated by the revised level values. In a discussion of the experimental results for this spectrum some comparisons with theory are made.

1. Introduction

It seems important that an up-to-date helium line list and a table of revised energy levels be made generally available. The use of helium in many kinds of spectroscopic sources, in studies of electrical discharge mechanisms and of plasma conditions, and the importance of helium in astrophysics combine to make He I one of the spectra most frequently observed. The most recent essentially complete compilation of helium wavelengths, contained in *A Multiplet Table of Astrophysical Interest* and *An Ultraviolet Multiplet Table* [1],[1] appeared in 1945 and 1950. Although these lists have advantages over earlier compilations [2, 3] in having line classifications in modern notation and containing more recent wavelength values, improved measurements of many He I lines have been made since they were published. The most notable of these are probably Herzberg's [4] recent observations, which have decreased the uncertainty in the connection between the ground state and the higher levels about one hundredfold. His measurements, combined with others made since the publication of volume 1 of *Atomic Energy Levels* [5], have led to the present complete revision of the He I level values. These new level values allow the calculation of helium wavelengths which, for over half the known lines, are believed to be more accurate than the available observed wavelengths.

In pointing out the need for the present revision of the He I level values, it may be well to emphasize the special place of two-electron atoms in atomic theory. Since these are the simplest atoms for which exact calculations in either nonrelativistic or Dirac's relativistic wave mechanics cannot at present be made, they furnish excellent testing grounds for the various approximation methods of quantum mechanics and theories of the interaction between electrons. Indeed, until the recent beautiful measurements by Herzberg [4] the theoretically predicted ground-state energy of helium was more accurate than the experimental determination. The fact that Herzberg was able to verify field theory (Lamb) effects in two two-electron atoms (^{4}He and ^{3}He) illustrates the importance of maintaining as accurate data on the helium-type atoms as contemporary experimental techniques allow.

Naturally, the present discussion of experimental results will stress the more recent observations. The references are mainly to work done since the appearance of volume VII of the *Handbuch der Spectroscopie* [3]. Since the article on helium in that superb work contains a practically complete list of references through 1927, it and this paper together furnish a guide to the principal experimental energy level determinations for ^{4}He I to date.

No attempt has been made in this paper to deal with the interesting and important ^{3}He I spectrum. Because of the large percentage mass difference of ^{3}He and ^{4}He and because ^{3}He has a nonzero nuclear magnetic moment giving rise to hyperfine structure, the ^{3}He I spectrum differs in detail a good deal from ^{4}He I. A reasonably comprehensive article on the experimental results for ^{3}He I would be about as long as this one. Perhaps one of the investigators of that spectrum will supply such an article.

2. Spectrum

Except for a few normally very weak "forbidden" lines, table 1 contains wavelengths for all He I lines which have been observed in the laboratory. It has already been mentioned that well over half these wavelengths were calculated from newly-derived energy level values (see the following section). In the first column of the table, opposite each calculated wavelength, appears a symbol denoting the source of what is probably the most accurate measurement of the line. The symbol in the second column gives the actual source of each wavelength in the table. The meanings of the symbols are given in the appendix following the table.

The wavelengths of the vacuum ultraviolet lines were calculated from adopted level values except for the line at 320.392 A. Wu [6] has made a convincing argument for assigning this line to the transition give in the table. Edlén's [7] suggested classification, $1s2s\ ^3\mathrm{S}-2s2p\ ^3\mathrm{P}^\circ$, is open to objection since the upper term is subject to autoionization into the ^{3}P° continuum above the $1s\infty p$ series limit. A

[1] Figures in brackets indicate the literature references on pages 22 and 23.

weaker line observed by Kruger [8] at 357.507 A has been the subject of speculation by Kruger himself and by Wu [6] and Holøien [9]. These last two authors find that none of the suggested transitions satisfactorily accounts for both the position and width of the line. For this reason it is not listed here. (Both Wu and Holøien incorrectly state that Compton and Boyce observed this line.)

The original investigation of the helium spectrum in the vacuum ultraviolet was made by Lyman [11], who discovered the resonance series and the intercombination line 591 A. Suga [12] has obtained the resonance series $1s^2\ {}^1S_0—np\ {}^1P^\circ_1$ to $n=15$, as well as the forbidden transitions $1s^2\ {}^1S_0—ns\ {}^1S_0$ to $n=7$, $1s^2\ {}^1S_0—2p$, $3p\ {}^3P^\circ_1$, and $1s^2\ {}^1S_0—3d\ {}^1D_2$. Bomke [13] had earlier found the lower members of these forbidden series. The most accurate of the older measurements of the He I spectrum in the vacuum ultraviolet were those of Hopfield [14], of Kruger (as given by Paschen [15]), and of Boyce (measurements of the lines 584 A and 537 A given by Boyce and Robinson [16]). Paschen calculated the best absolute value for $1s^2\ {}^1S_0$ as 198307.9 cm^{-1} from Kruger's measurements. From this adopted value for the ground term he then calculated wavelengths for the $1s^2\ {}^1S_0—np\ {}^1P^\circ_1$ series to $n=12$. Using this procedure, which is essentially that followed here, Boyce and Robinson [16] obtained from Boyce's measurements of the lines 584 A and 537 A what were undoubtedly the best values for the higher resonance lines previous to this paper. They are systematically below the wavelengths in table 1 by only 0.004 to 0.005 A.

The earlier wavelength measurements made in the vacuum ultraviolet region are, of course, superseded by the work of Herzberg [4] and by the values in table 1 based on his work. Herzberg conservatively estimated the uncertainty in his measurements of the lines at 584, 591, and 537 A to be 0.0005 A.

The intensities for the vacuum ultraviolet lines in table 1 are based on those given by Hopfield [14], Compton and Boyce [10], and Kruger [8]. The spectrograms published by Suga [12] were used in an attempt to put these values on a consistent scale. It should be remembered that the relative intensities of these lines are very strongly dependent on the excitation conditions. For most sources, the decreases in the intensities of the higher series members relative to the lowest member would be much sharper than is indicated in table 1. The intensities and, indeed, the appearance or nonappearance of the forbidden lines are especially affected by source conditions.

Care has been taken to assure that the wavelengths given for lines in the air region should also be the best values now available. Almost all of the 192 lines given for this region have been observed, but wavelengths calculated from adopted level differences are considered more accurate than observed values for about half of these. Most of the wavelengths which are taken directly from observation also correspond exactly to the level differences involved, since they were used to determine these differences. Besides the 100 calculated air wavelengths, the table includes 27 other new air values; these are mostly either unpublished measurements by Shenstone [17] or weighted averages from the literature. The wavenumbers given for some of the calculated lines and for several lines which are averages from observations do not agree in the last significant figure with the wavenumbers which would be obtained by applying the Edlén conversion formula to the corresponding wavelengths in table 1. In these cases it is the *wavenumber* which is the primary adopted quantity, and the wavelength is taken from the Edlén formula to the number of figures regarded as significant.

Only two "forbidden" lines in the air region are given in table 1. These are measurements by Herzberg [4] of the intercombinations used to determine the relative positions of the singlet and triplet systems. In addition to other intercombination lines, numerous transitions violating the electric-dipole-radiation parity-change rule have been found near the strong allowed lines. The observations of Jacquinot [18] indicate that the forbidden lines are usually less than one-thousandth the strength of the corresponding allowed lines. If the need occurs, their wavelengths can be computed from the corresponding energy level differences.

Normally unobserved forbidden transitions in helium appear quite readily when the radiating gas is in a strong electric field. Investigations of the Stark effect in He I probably culminated in the beautiful work of Foster [19, 20], whose papers the reader may consult for other references.

Most investigations of the Zeeman effect in He I carried out in the last 30 years have been concerned with forbidden lines. The work of J. Brochard and P. Jacquinot [21] is rather comprehensive. A noteworthy achievement is the determination of the g_J-value for $2s\ {}^3S_1$ to an accuracy of 1 ppm by Drake et al. [22] using microwave techniques.

The quantitative intensity measurements of Crosswhite and Dieke [23] show striking changes in the relative intensities of various helium lines when only the gas pressure is changed. As in the vacuum ultraviolet region, the intensities given for lines above 2615 A are not valid for all commonly occurring excitation conditions.

C. J. Humphreys [24] has very kindly furnished unpublished quantitative intensity measurements for the infrared region beyond 10912 A. His source was an electrodeless tube filled to 3.5 mm (Hg), and care was taken to obtain precise intensities. Humphreys states that the intensity of the triplet at 10830 A is 5 to 10 times that of the singlet line at 20581 A which has intensity 20850 on his scale. Since this intensity ratio would not be much different at the pressure (7.5 mm) at which Crosswhite and Dieke [23] obtained an intensity of 105,000 for the 10830 triplet, it seems that these observers have used very nearly the same scale.

It is hoped that the intensities given in table 1 for lines from 2644 to 21132 A are on this reasonably consistent scale with the relative intensities of the stronger lines being useful for most sources operating at a few millimeters (Hg) pressure of helium.

(The intensities of the weaker lines are especially dependent on excitation conditions other than pressure.) In addition to the article of Crosswhite and Dieke, almost every paper referred to here which gives intensities in the region 2644 to 10912 A has been consulted. The intensities in this region are also based in part on observations made at NBS.

3. Energy Levels

A new square array has been made for the ^{4}He I spectrum. The first step in obtaining revised energy level values (based on the value 0.00 for the $1s^2\ ^1S_0$ ground state) was to fix the $2p\ ^3P^\circ_1-2p\ ^1P^\circ_1$ and $2p\ ^1P^\circ_1-3p\ ^1P^\circ_1$ separations. Herzberg [4] observed the vacuum ultraviolet transitions from each of these three odd levels to the ground state with an accuracy of ± 0.0005 A at 500 to 600 A. From the best values for these separations as determined by the relevant observations in the air region, and from Herzberg's wavenumbers for the vacuum ultraviolet lines, the positions of $2p\ ^3P^\circ_1$, $2p\ ^1P^\circ_1$, and $3p\ ^1P^\circ_1$ were fixed as given in table 2. With the ground state thus determined relative to the other energy levels, new values for all levels have been calculated from the best available measurements. The relative positions of the singlet and triplet systems are based primarily on Herzberg's measurements of the intercombination lines $2p\ ^1P^\circ_1-3d\ ^3D_2$ (6679.683 A) and $2p\ ^3P^\circ_1-3d\ ^1D_2$ (5874.463 A). The resulting positions give good agreement with Mlle. Pilon's measurement [25] of the $3d\ ^3D-3d\ ^1D$ separation, and it is unlikely that the intersystem connection is in error by more than 0.02 cm^{-1}. A recent unpublished interferometric measment of $2s\ ^1S_0-2p\ ^1P^\circ_1$ (4857.454 cm^{-1}) has been combined with the average of two recent interferometric determinations of $2s\ ^1S^\circ-3p\ ^1P^\circ_1$ to obtain the $2p\ ^1P^\circ_1-3p\ ^1P^\circ_1$ separation. Since these measurements (the sources of which are given in table 1) are much more accurate than any other pair determining this separation, its value is based entirely on them. The positions of the higher terms relative to the ground state have been taken so that subtraction of the resulting level values for $2p\ ^3P^\circ_1$, $2p\ ^1P^\circ_1$, and $3p\ ^1P^\circ_1$ from the corresponding "observed" values of Herzberg yields, respectively, -0.11, $+0.04$, and $+0.11$ cm^{-1}. Herzberg's estimated uncertainty in the wavenumbers of the observed lines is ± 0.15 cm^{-1}.

The measurements used here to determine the resolved fine structure intervals deserve some discussion, since all of these have been improved in the last few years. The $2p\ ^3P^\circ_1-2p\ ^3P^\circ_0$ splitting is taken from the paper of Brochard et al. [26], while the much smaller $2p\ ^3P^\circ_2-2p\ ^3P^\circ_1$ interval is a conversion to wavenumbers of the microwave frequency measurements by Wieder and Lamb [27]. (This last measurement gave the 2–1 splitting to a higher accuracy than is shown in the present table—for those who may need this accuracy the result of Wieder and Lamb is $2p\ ^3P^\circ_2-2p\ ^3P^\circ_1=2291.72\pm 0.36$ Mc/sec.) In 1929 Houston [28] gave the $3p\ ^3P^\circ$ intervals as $2-1=0.02$ cm^{-1} and $1-0=0.27$ cm^{-1}. He had not resolved the smaller separation, but guessed at it from the analogy with the $2p\ ^3P^\circ$ term and his measurement of the $3p\ ^3P^\circ_{2,1}-{}^3P^\circ_0$ splitting. At the time the first volume of AEL [5] appeared, it was thought that Houston's measurements had been superseded by those of Gibbs and Kruger [29]. These latter observers found the $3p\ ^3P^\circ_2-3p\ ^3P^\circ_1$ and $3p\ ^3P^\circ_1-3p\ ^3P^\circ_0$ intervals to be 0.165 and 0.192 cm^{-1}, respectively. These results proved in disagreement with theoretical expectations [30], which confirmed Houston's assumption that the ratio of $np\ ^3P^\circ_2-np\ ^3P^\circ_1$ to $np\ ^3P^\circ_1-np\ ^3P^\circ_0$ should be roughly independent of n. However, only in 1951 did Fred et al. [31] point out that the intervals of Gibbs and Kruger were spurious. The error was apparently caused by self-reversal in the strong unresolved line at 3888 A, which arises from the $2s\ ^3S_1-3p\ ^3P^\circ_{2,1}$ transitions. Bradley and Kuhn [32] and Brochard et al. [33] also obtained results in essential agreement with the early work of Houston. Brochard et al. [33] first resolved the $3p\ ^3P^\circ_2-3p\ ^3P^\circ_1$ splitting, and in 1957 they improved their accuracy [26]. The results of their optical measurements are in excellent agreement with the $3p\ ^3P^\circ$ intervals given in table 2, which are taken from the very accurate microwave observations by Wieder and Lamb [27]. The $2p$ and $3p$ triplet levels are given to four decimal places in table 2 in order to exhibit the accurately known term intervals. The inter-term separations are, of course, not known to this accuracy.

Note added in proof: The results of very recent high-accuracy measurements of the $2p\ ^3P^\circ$ intervals in He I are given in reference [38].

Theoretical calculations of $np\ ^3P^\circ$ fine structures in He I have been made by Breit [34] and Araki [30]. A more approximate, but simpler, treatment given in the article of Bethe and Salpeter [35] predicts that the splitting is independent of n except for an overall multiplying factor of n^{-3}. This result holds for any series of terms in a helium-like atom. How well this approximation is obeyed in the $2p$ and $3p$ triplets of ^{4}He I may be seen from table 3. The fine structure measurements by Brochard et al. [26] yield the results shown in table 4 for the $3d\ ^3D$ and $4d\ ^3D$ terms. The quite small $^3D_3-{}^3D_2$ intervals (0.0030 ± 0.0008 cm^{-1} for $3d$, and 0.0018 ± 0.001 for $4d$) are not accurately enough measured to check on the constancy of the interval ratio given in the table, and the values given can only be taken as indicative. Brochard et al. [26] compare their observations of all the known ^{4}He I fine-structure intervals with the results of various theoretical calculations

The new positions given in table 2 for the $4f\ ^1F^\circ$ and $4f\ ^3F^\circ$ terms are based primarily on Mlle. Pilon's measurements [25] of the $4d\ ^1D-4f\ ^1F^\circ$ and $4d\ ^3D-4f\ ^3F^\circ$ separations. To a lesser extent they are also based on the measurements by C. J. Humphreys and H. J. Kostkowski [36] of the infrared transitions from the $4f$ terms to $3d$ terms. The agreement is within the expected error of Humphreys and Kostkowski, and the $5f$ terms positions given here are based entirely on their measurements.

In his investigations of the Stark effect in He I, J. S. Foster [19] observed transitions to the $2p\ ^1P^\circ$ level from terms of every possible L-value belonging

to the configurations $1s\ 5l$, $6l$, and $7l$. Since his measurements were made in rather strong electric fields, they cannot be used directly to obtain unperturbed energy levels. From a comparison of Foster's estimated wavelengths for certain transitions at zero field with those calculated from the $6f$ and $7f$ term values in table 2, it appears that his wavelengths are probably systematically slightly in error. However, approximate term values have been obtained from Foster's work by using his measured separations of the lines in a group $2p\ ^1P^\circ_1 - nl\ ^{3,1}L$ from one of these lines whose zero-field wavenumber was known. These separations could be corrected to zero-field strength by comparing Foster's $nd\ ^1D - np\ ^1P^\circ$ separation with the known zero-field separation of these levels for each n. The term positions were also based on values found from plotting the very regular Rydberg denominators, particularly in the case of the $7l$ terms. In this manner the positions of terms belonging to the $5g$, $6g$, $6h$, $7g$, and $7h$ configurations have been calculated and included in table 2.

New level values based on recent improved series measurements and the accurate connection between the singlet and triplet systems have obviated several features of the He-atom energy level scheme which were previously disturbing. The best previous list of helium energy levels (AEL [5], vol. 1), following Paschen-Götze, had the nf singlet series members falling below the corresponding triplets from $n=5$ on. (Indeed, Humphreys and Kostkowski [36] listed both $4f\ ^1F^\circ$ and $5f\ ^1F^\circ$ slightly below the corresponding $^3F^\circ$ terms on the basis of their improved measurements in the infrared—however, they also assumed the old Paschen-Götze singlet-triplet connection based on series limit determinations.) Similarly, the earlier data indicated that the $nd\ ^1D$ series crossed over and fell below the $nd\ ^3D$ series at $n=9$. It is now clear that this puzzling behavior was not real. Shenstone's much improved measurements [17] of the nd triplet and singlet series from $8d$ on showed that the apparent crossing-over of those series at $9d$ was due to inaccurate observations. His measurements were essentially confirmed and the singlet series extended to $18d$ by Herzberg [4]. The new connection between the singlet and triplet systems, which raises the singlet system about 0.10 cm^{-1} relative to the triplets, has removed the slight crossing-over at $13d$ which remained after Shenstone's work. This accurate connection is also mainly responsible for rendering the nf series quite regular with the singlets probably slightly above the triplets. The observations are, however, not sufficiently accurate above $4f$ to fix the relative positions of the terms. One can say, however, that beyond $5f$ the $^1F^\circ$ terms are probably not separated from the corresponding $^3F^\circ$ terms by more than 0.1 cm^{-1}.

The energies for members of the series $np\ ^1P^\circ$ from $11p$ on are taken from a series formula. Paschen and Götze apparently thought this method would give better values than any measurements available to them; since there have been no new observations, the series has been recalculated to $20p$. Higher members of the $^3P^\circ$ series were obtained by converting wavelengths from Paschen-Götze to vacuum wavenumbers according to Edlén's tables. Several numerical errors occurring in Paschen-Götze have been corrected.

Combining the limits obtained by Herzberg [4] for three separate series with energies for the three appropriate fixed terms from the new array yields the following values for the ionization energy of helium:

From the series $3d\ ^3D - nf\ ^3F^\circ$:

$$3d\ ^3D + \text{limit} = 186101.65\ \text{cm}^{-1} + 12209.20\ \text{cm}^{-1} = 198310.85\ \text{cm}^{-1};$$

from the series $2p\ ^3P^\circ_{2,1} - nd\ ^3D$:

$$2p\ ^3P^\circ_{2,1} + \text{limit} = 169086.89\ \text{cm}^{-1} + 29223.90\ \text{cm}^{-1} = 198310.79\ \text{cm}^{-1};$$

from the series $2p\ ^1P^\circ_1 - nd\ ^1D_2$:

$$2p\ ^1P^\circ_1 + \text{limit} = 171135.00\ \text{cm}^{-1} + 27175.78\ \text{cm}^{-1} = 198310.78\ \text{cm.}^{-1}.$$

The average of these values, 198310.81 cm^{-1}, is in excellent agreement with the experimental ionization energy of ^4He adopted by Herzberg in his paper, 198310.82 ± 0.15 cm^{-1}. The spread in the three values obtained here is reduced from that obtained by Herzberg, no doubt because the available data have already been averaged once in obtaining values for the fixed term of each series.

In conclusion, it might be mentioned that the excellent article by Bethe and Salpeter [35] on the theory of one- and two-electron atoms gives numerous references to theoretical work on helium-like atoms through 1956. The informative paper by Bengt Edlén [37] on experimental results for the He I isoelectronic sequence will also prove helpful to those interested in two-electron atoms.

Charlotte E. Moore has made available the extensive files of spectroscopic literature kept by her in this laboratory. She has also been of much assistance in deciding on matters of notation and format. The author expresses his gratitude for her support in this work.

Prof. A. G. Shenstone of Princeton, Dr. G. Herzberg of the National Research Council in Ottawa, and Dr. C. J. Humphreys of the U.S. Naval Ordnance Laboratory, Corona, Calif., have supplied unpublished data on the helium spectrum. The kindness of each is greatly appreciated.

4. References

[1] C. E. Moore, A Multiplet Table of Astrophysical Interest (rev. ed., Princeton Univ. Observatory Contr. No. 20, 1945); An Ultraviolet Multiplet Table, NBS Circ. 488, sec. 1 (1950).

[2] F. Paschen and R. Götze, Seriengesetze der Linienspektren, p. 26 (Julius Springer, Berlin, 1922).

[3] H. Kayser and H. Konen, Handbuch der Spectroscopie, vol. 7, p. 606 (S. Hirzel, Leipzig, 1934).

[4] G. Herzberg, Proc. Roy. Soc. (London) [A] **248,** 309 (1958).

[5] C. E. Moore, Atomic Energy Levels, NBS Circ. 467, I (1949); II (1952); III (1958).

[6] T.-Y. Wu, Phys. Rev. **66,** 291 (1944).
[7] B. Edlén, Nova Acta Reg. Soc. Sci. Uppsala [IV] **9,** No. 6, 30 (1934).
[8] P. G. Kruger, Phys. Rev. **36,** 855 (1930).
[9] E. Holøien, Proc. Phys. Soc. (London) **71,** 357 (1958).
[10] K. T. Compton and J. C. Boyce, J. Franklin Inst. **205,** 497 (1928).
[11] T. Lyman, Astrophys. J. **60,** 1 (1924).
[12] T. Suga, Sci. Papers Inst. Phys. Chem. Research (Tokyo) **34,** 7 (1937).
[13] H. Bomke, Physik. Z. **36,** 158 (1935).
[14] J. J. Hopfield, Astrophys. J. **72,** 133 (1930).
[15] F. Paschen, Sitz. Berlin Akad. Wiss. **30,** 662 (1929).
[16] J. C. Boyce and H. A. Robinson, J. Opt. Soc. Am. **26,** 133 (1936).
[17] A. G. Shenstone, unpublished measurements; a list of energy levels based on this work appears at the end of [5], vol. III.
[18] P. Jacquinot, Compt. Rend. **208,** 1896 (1939).
[19] J. S. Foster, Phys. Rev. **23,** 667 (1924).
[20] J. S. Foster, Proc. Roy. Soc. (London) **114,** 47 (1927).
[21] J. Brochard and P. Jaquinot, Ann. Phys. **20,** 509 (1945).
[22] Drake, Hughes, Lurio, and White, Phys. Rev. **112,** 1627 (1958).
[23] H. M. Crosswhite and G. H. Dieke, Am. Inst. Phys. Handbook, sec. 7, p. 44 (McGraw-Hill Book Co., New York, N. Y., 1957).
[24] C. J. Humphreys, private communication, June, 1959.
[25] A.-M. Pilon, J. phys. radium **15,** 692 (1954).
[26] J. Brochard, R. Chabbal, H. Chantrel, and P. Jacquinot, J. phys. radium **18,** 596 (1957).
[27] I. Wieder and W. E. Lamb, Jr., Phys. Rev. **107,** 125 (1957).
[28] W. V. Houston, Proc. Nat. Acad. Sci. US **13,** 91 (1927).
[29] R. C. Gibbs and P. G. Kruger, Phys. Rev. **37,** 1559 (1931).
[30] G. Araki, Proc. Phys. Math. Soc. Japan **19,** 128 (1937).
[31] M. Fred, F. S. Tomkins, J. K. Brody, and M. Hamermesh, Phys. Rev. **82,** 406 (1951).
[32] L. C. Bradley III, and H. Kuhn, Proc. Roy. Soc. (London) **209,** 327 (1951).
[33] J. Brochard, R. Chabbal, H. Chantrel, and P. Jacquinot, J. phys. radium **13,** 433 (1952).
[34] G. Breit, Phys. Rev. **36,** 383 (1930).
[35] H. A. Bethe and E. E. Salpeter, Quantum Mechanics of One- and Two-Electron Atoms (Academic Press, Inc., New York, 1957); Encylopedia of Physics, vol. XXXV (Springer-Verlag, Berlin, 1956).
[36] C. J. Humphreys and H. J. Kostkowski, J. Research NBS **49,** 73 (1952) RP2345.
[37] B. Edlén, Arkiv Fysik **4,** 441 (1952).
[38] F. D. Colegrove, P. A. Franken, R. R. Lewis, and R. H. Sands, Phys. Rev. Letters **3,** 420 (1959).

TABLE 1.—*Wavelengths and classifications for the lines of the* ^{4}He I *spectrum*

The meanings of the symbols in the first two columns will be understood from the discussion in the text and the explanations given at the end of this table.

Observer		λ (vac)	Intensity	cm^{-1}	Classification
1	2				
Kg	Kg	320. 392	10	312118.	$1s2p\ ^3P^\circ$ — $2p^2\ ^3P$
Su	CS	505. 5001	2	197823. 91	$1s^2\ ^1S_0$ —$15p\ ^1P_1^\circ$
Su	CS	505. 6840	3	197751. 94	$1s^2\ ^1S_0$ —$14p\ ^1P_1^\circ$
Su	CS	505. 9122	4	197662. 75	$1s^2\ ^1S_0$ —$13p\ ^1P_1^\circ$
Su	CS	506. 2000	5	197550. 36	$1s^2\ ^1S_0$ —$12p\ ^1P_1^\circ$
Hp	CS	506. 5702	7	197405. 99	$1s^2\ ^1S_0$ —$11p\ ^1P_1^\circ$
Hp	C	507. 0576	10	197216. 24	$1s^2\ ^1S_0$ —$10p\ ^1P_1^\circ$
Hp	C	507. 7178	15	196959. 79	$1s^2\ ^1S_0$ — $9p\ ^1P_1^\circ$
Hp	C	508. 6431	20	196601. 51	$1s^2\ ^1S_0$ — $8p\ ^1P_1^\circ$
Hp	C	509. 9979	25	196079. 24	$1s^2\ ^1S_0$ — $7p\ ^1P_1^\circ$
Su	C	510. 2586	----------	195979. 04	$1s^2\ ^1S_0$ — $7s\ ^1S_0$
Hp	C	512. 0982	35	195275. 04	$1s^2\ ^1S_0$ — $6p\ ^1P_1^\circ$
Su	C	512. 5183	----------	195115. 00	$1s^2\ ^1S_0$ — $6s\ ^1S_0$
Hp	C	515. 6165	50	193942. 57	$1s^2\ ^1S_0$ — $5p\ ^1P_1^\circ$
Su	C	516. 3592	----------	193663. 63	$1s^2\ ^1S_0$ — $5s\ ^1S_0$
Hp	C	522. 2128	80	191492. 82	$1s^2\ ^1S_0$ — $4p\ ^1P_1^\circ$
Su	C	523. 7238	----------	190940. 33	$1s^2\ ^1S_0$ — $4s\ ^1S_0$
Hz	C	537. 0296	200	186209. 47	$1s^2\ ^1S_0$ — $3p\ ^1P_1^\circ$
Su	C	537. 3309	----------	186105. 06	$1s^2\ ^1S_0$ — $3d\ ^1D_2$
Su	C	538. 8956	----------	185564. 68	$1s^2\ ^1S_0$ — $3p\ ^3P_1^\circ$
Su	C	540. 9354	----------	184864. 94	$1s^2\ ^1S_0$ — $3s\ ^1S_0$
Hz	C	584. 3340	500	171135. 00	$1s^2\ ^1S_0$ — $2p\ ^1P_1^\circ$
Hz	C	591. 4117	20	169086. 94	$1s^2\ ^1S_0$ — $2p\ ^3P_1^\circ$
Kg	C	601. 4041	----------	166277. 55	$1s^2\ ^1S_0$ — $2s\ ^1S_0$
		λ (air)			
	P–G	2615. 184	----------	38226. 82	$2s\ ^3S_1$ —$22p\ ^3P^\circ$
	P–G	2616. 711	----------	38204. 51	$2s\ ^3S_1$ —$21p\ ^3P^\circ$
	P–G	2618. 478	----------	38178. 73	$2s\ ^3S_1$ —$20p\ ^3P^\circ$
	P–G	2620. 534	----------	38148. 78	$2s\ ^3S_1$ —$19p\ ^3P^\circ$
	P–G	2622. 947	----------	38113. 68	$2s\ ^3S_1$ —$18p\ ^3P^\circ$
	P–G	2625. 806	----------	38072. 19	$2s\ ^3S_1$ —$17p\ ^3P^\circ$
	P–G	2629. 229	----------	38022. 62	$2s\ ^3S_1$ —$16p\ ^3P^\circ$
	P–G	2633. 375	----------	37962. 76	$2s\ ^3S_1$ —$15p\ ^3P^\circ$
	P–G	2638. 462	----------	37889. 58	$2s\ ^3S_1$ —$14p\ ^3P^\circ$
	P–G	2644. 802	2	37798. 76	$2s\ ^3S_1$ —$13p\ ^3P^\circ$

TABLE 1. *Wavelengths and classifications for the lines of the* ^{4}He I *spectrum*—Continued

The meanings of the symbols in the first two columns will be understood from the discussion in the text and the explanations given at the end of this table.

Observer		λ (air)	Intensity	cm^{-1}	Classification
1	2				
	P–G	2652. 848	3	37684. 12	$2s\ ^3S_1 - 12p\ ^3P^\circ$
	P–G	2663. 271	4	37536. 65	$2s\ ^3S_1 - 11p\ ^3P^\circ$
	P–G	2677. 135	5	37342. 27	$2s\ ^3S_1 - 10p\ ^3P^\circ$
	P–G	2696. 119	7	37079. 35	$2s\ ^3S_1 - 9p\ ^3P^\circ$
	P–G	2723. 191	10	36710. 75	$2s\ ^3S_1 - 8p\ ^3P^\circ$
P–G	C	2763. 804	20	36171. 33	$2s\ ^3S_1 - 7p\ ^3P^\circ$
P–G	C	2829. 076	40	35336. 84	$2s\ ^3S_1 - 6p\ ^3P^\circ$
	Me	2945. 106	100	33944. 71	$2s\ ^3S_1 - 5p\ ^3P^\circ$
P–G	CS	3147. 779		31759. 24	$2s\ ^1S_0 - 20p\ ^1P_1^\circ$
P–G	CS	3150. 713		31729. 66	$2s\ ^1S_0 - 19p\ ^1P_1^\circ$
P–G	CS	3154. 156		31695. 03	$2s\ ^1S_0 - 18p\ ^1P_1^\circ$
P–G	CS	3158. 234		31654. 10	$2s\ ^1S_0 - 17p\ ^1P_1^\circ$
P–G	CS	3163. 114		31605. 27	$2s\ ^1S_0 - 16p\ ^1P_1^\circ$
P–G	CS	3169. 021		31546. 36	$2s\ ^1S_0 - 15p\ ^1P_1^\circ$
P–G	CS	3176. 267		31474. 39	$2s\ ^1S_0 - 14p\ ^1P_1^\circ$
P–G?	CS	3185. 293		31385. 20	$2s\ ^1S_0 - 13p\ ^1P_1^\circ$
	Me	3187. 745	200	31361. 07	$2s\ ^3S_1 - 4p\ ^3P^\circ$
P–G	CS	3196. 742	2	31272. 81	$2s\ ^1S_0 - 12p\ ^1P_1^\circ$
P–G	CS	3211. 568	2	31128. 44	$2s\ ^1S_0 - 11p\ ^1P_1^\circ$
	P–G	3231. 266	3	30938. 69	$2s\ ^1S_0 - 10p\ ^1P_1^\circ$
	P–G	3258. 275	5	30682. 24	$2s\ ^1S_0 - 9p\ ^1P_1^\circ$
P–G	C	3296. 773	7	30323. 96	$2s\ ^1S_0 - 8p\ ^1P_1^\circ$
P–G	C	3354. 550	10	29801. 69	$2s\ ^1S_0 - 7p\ ^1P_1^\circ$
P–G	C	3447. 586	15	28997. 49	$2s\ ^1S_0 - 6p\ ^1P_1^\circ$
	P–G	3450. 22		28975. 4	$2p\ ^3P_{2,1}^\circ - 21d\ ^3D$
	P–G	3453. 21		28950. 3	$2p\ ^3P_{2,1}^\circ - 20d\ ^3D$
	Hz	3456. 841		28919. 86	$2p\ ^3P_{2,1}^\circ - 19d\ ^3D$
	Hz	3461. 000		28885. 11	$2p\ ^3P_{2,1}^\circ - 18d\ ^3D$
	Hz*	3465. 925		28844. 07	$2p\ ^3P_{2,1}^\circ - 17d\ ^3D$
	Sh	3467. 539		28830. 64	$2p\ ^3P_{2,1}^\circ - 17s\ ^3S_1$
Hz	C	3471. 818		28795. 11	$2p\ ^3P_{2,1}^\circ - 16d\ ^3D$
Hz	C	3471. 943		28794. 07	$2p\ ^3P_0^\circ - 16d\ ^3D_1$
	Sh	3473. 764		28778. 98	$2p\ ^3P_{2,1}^\circ - 16s\ ^3S_1$
Hz	C	3478. 957	2	28736. 02	$2p\ ^3P_{2,1}^\circ - 15d\ ^3D$
Hz	C	3479. 083		28734. 98	$2p\ ^3P_0^\circ - 15d\ ^3D_1$
	Sh	3481. 355		28716. 23	$2p\ ^3P_{2,1}^\circ - 15s\ ^3S_1$
Hz	C	3487. 723	2	28663. 80	$2p\ ^3P_{2,1}^\circ - 14d\ ^3D$
Hz	C	3487. 850		28662. 76	$2p\ ^3P_0^\circ - 14d\ ^3D_1$
	Sh	3490. 685		28639. 48	$2p\ ^3P_{2,1}^\circ - 14s\ ^3S_1$
Hz	C	3498. 645	3	28574. 32	$2p\ ^3P_{2,1}^\circ - 13d\ ^3D$
Hz	C	3498. 772		28573. 28	$2p\ ^3P_0^\circ - 13d\ ^3D_1$
	Sh	3502. 379	2	28543. 86	$2p\ ^3P_{2,1}^\circ - 13s\ ^3S_1$
Hz	C	3512. 512	4	28461. 52	$2p\ ^3P_{2,1}^\circ - 12d\ ^3D$
Hz	C	3512. 640		28460. 48	$2p\ ^3P_0^\circ - 12d\ ^3D_1$
	Sh	3517. 317	2	28422. 63	$2p\ ^3P_{2,1}^\circ - 12s\ ^3S_1$
Hz	C	3530. 491	5	28316. 58	$2p\ ^3P_{2,1}^\circ - 11d\ ^3D$
Hz	C	3530. 621		28315. 54	$2p\ ^3P_0^\circ - 11d\ ^3D_1$
	Sh	3536. 809	3	28266. 00	$2p\ ^3P_{2,1}^\circ - 11s\ ^3S_1$
	Hz	3554. 415	7	28125. 99	$2p\ ^3P_{2,1}^\circ - 10d\ ^3D$
Hz	C	3554. 547		28124. 95	$2p\ ^3P_0^\circ - 10d\ ^3D_1$
	Sh	3562. 979	4	28058. 39	$2p\ ^3P_{2,1}^\circ - 10s\ ^3S_1$
	Hz	3587. 270	10	27868. 39	$2p\ ^3P_{2,1}^\circ - 9d\ ^3D$
Hz	C	3587. 405	2	27867. 35	$2p\ ^3P_0^\circ - 9d\ ^3D_1$
	Sh	3599. 314	5	27775. 15	$2p\ ^3P_{2,1}^\circ - 9s\ ^3S_1$
P–G	C	3599. 448	2	27774. 11	$2p\ ^3P_0^\circ - 9s\ ^3S_1$
	Me	3613. 643	30	27665. 02	$2s\ ^1S_0 - 5p\ ^1P_1^\circ$
P–G	C	3634. 232	15	27508. 29	$2p\ ^3P_{2,1}^\circ - 8d\ ^3D$

TABLE 1. *Wavelengths and classifications for the lines of the* ^{4}He I *spectrum*—Continued

The meanings of the symbols in the first two columns will be understood from the discussion in the text and the explanations given at the end of this table.

Observer		λ (air)	Intensity	cm^{-1}	Classification
1	2				
P–G	C	3634. 369	2	27507. 25	$2p\ ^3P^o_0$ — $8d\ ^3D_1$
	Sh	3651. 990	7	27374. 53	$2p\ ^3P^o_{2,1}$— $8s\ ^3S_1$
P–G	C	3652. 130	2	27373. 49	$2p\ ^3P^o_0$ — $8s\ ^3S_1$
	Me	3705. 005	30	26982. 84	$2p\ ^3P^o_{2,1}$— $7d\ ^3D$
P–G	C	3705. 148	3	26981. 80	$2p\ ^3P^o_0$ — $7d\ ^3D_1$
	Hz	3725. 130		26837. 07	$2p\ ^1P^o_1$ —$18d\ ^1D_2$
	Hz	3730. 839		26796. 00	$2p\ ^1P^o_1$ —$17d\ ^1D_2$
P–G	C	3732. 865	10	26781. 46	$2p\ ^3P^o_{2,1}$— $7s\ ^3S_1$
P–G	C	3733. 010	3	26780. 42	$2p\ ^3P^o_0$ — $7s\ ^3S_1$
	Hz	3737. 674		26747. 01	$2p\ ^1P^o_1$ —$16d\ ^1D_2$
	Hz, Sh	3745. 943		26687. 96	$2p\ ^1P^o_1$ —$15d\ ^1D_2$
	Sh	3747. 208		26678. 95	$2p\ ^1P^o_1$ —$15s\ ^1S_0$
	Hz, Sh	3756. 107		26615. 75	$2p\ ^1P^o_1$ —$14d\ ^1D_2$
	Sh	3757. 670		26604. 67	$2p\ ^1P^o_1$ —$14s\ ^1S_0$
	Hz, Sh	3768. 784	2	26526. 22	$2p\ ^1P^o_1$ —$13d\ ^1D_2$
	Sh	3770. 751		26512. 38	$2p\ ^1P^o_1$ —$13s\ ^1S_0$
	Hz, Sh	3784. 862	2	26413. 54	$2p\ ^1P^o_1$ —$12d\ ^1D_2$
	Sh	3787. 424		26395. 68	$2p\ ^1P^o_1$ —$12s\ ^1S_0$
	Hz, Sh	3805. 740	3	26268. 64	$2p\ ^1P^o_1$ —$11d\ ^1D_2$
	CS	3809. 105		26245. 44	$2p\ ^1P^o_1$ —$11s\ ^1S_0$
	Mt	3819. 6072	100	26173. 275	$2p\ ^3P^o_{2,1}$— $6d\ ^3D$
P–G	C	3819. 758	10	26172. 239	$2p\ ^3P^o_0$ — $6d\ ^3D_1$
	Hz, Sh	3833. 554	4	26078. 06	$2p\ ^1P^o_1$ —$10d\ ^1D_2$
	Sh	3838. 100	2	26047. 17	$2p\ ^1P^o_1$ —$10s\ ^1S_0$
P–G	C	3867. 475	30	25849. 34	$2p\ ^3P^o_{2,1}$— $6s\ ^3S_1$
P–G	C	3867. 630	5	25848. 30	$2p\ ^3P^o_0$ — $6s\ ^3S_1$
	Hz	3871. 791	5	25820. 52	$2p\ ^1P^o_1$ — $9d\ ^1D_2$
	Sh	3878. 181	3	25777. 98	$2p\ ^1P^o_1$ — $9s\ ^1S_0$
	Me	3888. 648	10000	25708. 594	$2s\ ^3S_1$ — $3p\ ^3P^o_{2,1}$
P–G	C	3926. 534	7	25460. 54	$2p\ ^1P^o_1$ — $8d\ ^1D_2$
	Sh	3935. 912	4	25399. 88	$2p\ ^1P^o_1$ — $8s\ ^1S_0$
	Mt	3964. 7289	200	25215. 271	$2s\ ^1S_0$ — $4p\ ^1P^o_1$
P–G	C	4009. 268	10	24935. 16	$2p\ ^1P^o_1$ — $7d\ ^1D_2$
	P–G	4023. 973	5	24844. 04	$2p\ ^1P^o_1$ — $7s\ ^1S_0$
	Mt	4026. 1912	500	24830. 353	$2p\ ^3P^o_{2,1}$— $5d\ ^3D$
P–G	C	4026. 359	50	24829. 317	$2p\ ^3P^o_0$ — $5d\ ^3D_1$
	Mt	4120. 815	120	24260. 197	$2p\ ^3P^o_{2,1}$— $5s\ ^3S_1$
P–G	C	4120. 992	15	24259. 161	$2p\ ^3P^o_0$ — $5s\ ^3S_1$
	Me	4143. 761	30	24125. 86	$2p\ ^1P^o_1$ — $6d\ ^1D_2$
	Of	4168. 967	5	23980. 00	$2p\ ^1P^o_1$ — $6s\ ^1S_0$
	Mt	4387. 9294	100	22783. 391	$2p\ ^1P^o_1$ — $5d\ ^1D_2$
	Me	4437. 551	30	22528. 627	$2p\ ^1P^o_1$ — $5s\ ^1S_0$
	Mt, Pé	4471. 479	2000	22357. 692	$2p\ ^3P^o_{2,1}$— $4d\ ^3D_{3,2}$
P–G	C	4471. 682	250	22356. 676	$2p\ ^3P^o_0$ — $4d\ ^3D_1$
	Mt	4713. 1455	300	21211. 318	$2p\ ^3P^o_{2,1}$— $4s\ ^3S_1$
P–G	C	4713. 376	40	21210. 282	$2p\ ^3P^o_0$ — $4s\ ^3S_1$
	Mt	4921. 9310	200	20311. 559	$2p\ ^1P^o_1$ — $4d\ ^1D_2$
	Mt, Se-F	5015. 6779	1000	19931. 925	$2s\ ^1S_0$ — $3p\ ^1P^o_1$
	Me	5047. 738	100	19805. 331	$2p\ ^1P^o_1$ — $4s\ ^1S_0$
	Hz	5874. 463		17018. 116	$2p\ ^3P^o_1$ — $3d\ ^1D_2$
	Pé, Me	5875. 621	15000	17014. 760	$2p\ ^3P^o_{2,1}$— $3d\ ^3D_{3,2}$
P–G	C	5875. 966	2000	17013. 763	$2p\ ^3P^o_0$ — $3d\ ^3D_1$
	Pé, Me	6678. 151	2000	14970. 071	$2p\ ^1P^o_1$ — $3d\ ^1D_2$
	Hz	6679. 683		14966. 637	$2p\ ^1P^o_1$ — $3d\ ^3D_2$
	Me	7065. 190	5000	14150. 000	$2p\ ^3P^o_{2,1}$— $3s\ ^3S_1$
Of	C	7065. 707	600	14148. 964	$2p\ ^3P^o_0$ — $3s\ ^3S_1$
	Me, Of	7281. 349	1000	13729. 936	$2p\ ^1P^o_1$ — $3s\ ^1S_0$
P-Rt	C	7816. 15	10	12790. 51	$3s\ ^3S_1$ — $7p\ ^3P^o$
Mg-D	C	8361. 69	20	11956. 02	$3s\ ^3S_1$ — $6p\ ^3P^o$

TABLE 1. *Wavelengths and classifications for the lines of the* ^{4}He I *spectrum*—Continued

The meanings of the symbols in the first two columns will be understood from the discussion in the text and the explanations given at the end of this table.

Observer 1	Observer 2	λ (air)	Intensity	cm^{-1}	Classification
Hz†	C	8444. 48		11838. 81	$3p\ ^3P^\circ_{2,1}$—$11d\ ^3D$
	Hz†	8518. 04		11736. 57	$3s\ ^1S_0$ — $8p\ ^1P^\circ_1$
	Hz	8528. 991		11721. 495	$3d\ ^3D$ —$15f\ ^3F^\circ$
	Hz†	8582. 65		11648. 21	$3p\ ^3P^\circ$ —$10d\ ^3D$; $3d\ ^3D$ —$14f\ ^3F^\circ$
	Hz	8648. 257		11559. 85	$3d\ ^3D$ —$13f\ ^3F^\circ$
	Hz	8733. 431		11447. 11	$3d\ ^3D$ —$12f\ ^3F^\circ$
Hz†	C	8776. 74	5	11390. 62	$3p\ ^3P^\circ_{2,1}$— $9d\ ^3D$
	Hz	8845. 373	2	11302. 24	$3d\ ^3D$ —$11f\ ^3F^\circ$
P-Rt	C	8914. 74	5	11214. 30	$3s\ ^1S_0$ — $7p\ ^1P^\circ_1$
	Hz	8996. 978	5	11111. 79	$3d\ ^3D$ —$10f\ ^3F^\circ$
Mg-D	C	9063. 27	15	11030. 52	$3p\ ^3P^\circ_{2,1}$— $8d\ ^3D$
Mg-D	C	9085. 45	2	11003. 59	$3p\ ^1P^\circ_1$ —$10d\ ^1D_2$
Mg-D	C	9174. 52	5	10896. 76	$3p\ ^3P^\circ_{2,1}$— $8s\ ^3S_1$
	Hz	9210. 337	20	10854. 39	$3d\ ^3D$ — $9f\ ^3F^\circ$
	Mg-D	9213. 1	2	10851. 1	$3d\ ^1D_2$ — $9f\ ^1F^\circ_3$
Mg-D	C	9303. 19	3	10746. 05	$3p\ ^1P^\circ_1$ — $9d\ ^1D_2$
P-Rt	C	9463. 61	100	10563. 89	$3s\ ^3S_1$ — $5p\ ^3P^\circ$
P-Rt	C	9516. 60	40	10505. 07	$3p\ ^3P^\circ_{2,1}$— $7d\ ^3D$
P-Rt	C	9516. 87	5	10504. 78	$3p\ ^3P^\circ_0$ — $7d\ ^3D_1$
	Mg-D	9526. 17	30	10494. 52	$3d\ ^3D$ — $8f\ ^3F^\circ$
	Mg-D	9529. 27	10	10491. 10	$3d\ ^1D_2$ — $8f\ ^1F^\circ_3$
Mg-D	C	9552. 89	3	10465. 17	$3d\ ^3D$ — $8p\ ^3P^\circ$
P-Rt	C	9603. 42	10	10410. 10	$3s\ ^1S_0$ — $6p\ ^1P^\circ_1$
Mg-D	C	9625. 64	5	10386. 07	$3p\ ^1P^\circ_1$ — $8d\ ^1D_2$
Mg-D	C	9682. 19	2	10325. 41	$3p\ ^1P^\circ_1$ — $8s\ ^1S_0$
P-Rt	C	9702. 60	30	10303. 69	$3p\ ^3P^\circ_{2,1}$— $7s\ ^3S_1$
	Mg-D	10027. 73	60	9969. 61	$3d\ ^3D$ — $7f\ ^3F^\circ$
	Mg-D	10031. 16	20	9966. 20	$3d\ ^3D_1$ — $7f\ ^1F^\circ_3$
Mg-D	C	10072. 04	5	9925. 75	$3d\ ^3D$ — $7p\ ^3P^\circ$
Mg-D	C	10138. 50	10	9860. 69	$3p\ ^1P^\circ_1$ — $7d\ ^1D_2$
Mg-D	C	10233. 06	3	9769. 57	$3p\ ^1P^\circ_1$ — $7s\ ^1S_0$
Mg-D	C	10311. 23	100	9695. 504	$3p\ ^3P^\circ_{2,1}$— $6d\ ^3D$
	C	10311. 54	15	9695. 220	$3p\ ^3P^\circ_0$ — $6d\ ^3D_1$
Mg	C	10667. 65	30	9371. 57	$3p\ ^3P^\circ_{2,1}$— $6s\ ^3S_1$
	C	10667. 98		9371. 28	$3p\ ^3P^\circ_0$ — $6s\ ^3S_1$
Mg	C	10829. 088	10000	9231. 859	$2s\ ^3S_1$ — $2p\ ^3P^\circ_0$
Mg	C	10830. 248	30000	9230. 871	$2s\ ^3S_1$ — $2p\ ^3P^\circ_1$
Mg	C	10830. 337	50000	9230. 795	$2s\ ^3S_1$ — $2p\ ^3P^\circ_2$
Mg	C	10902. 16		9169. 98	$3d\ ^1D_2$ — $6p\ ^1P^\circ_1$
	Mg	10912. 92	120*	9160. 94	$3d\ ^3D$ — $6f\ ^3F^\circ$
	Mg	10916. 98	34	9157. 53	$3d\ ^1D_2$ — $6f\ ^1F^\circ_3$
Mg	C	10996. 56		9091. 26	$3d\ ^3D$ — $6p\ ^3P^\circ$
Mg	C	11013. 07	16	9077. 63	$3s\ ^1S_0$ — $5p\ ^1P^\circ_1$
Mg	C	11045. 00	17	9051. 39	$3p\ ^1P^\circ_1$ — $6d\ ^1D_2$
Mg	C	11225. 90		8905. 53	$3p\ ^1P^\circ_1$ — $6s\ ^1S_0$
Mg	C	11969. 07	440	8352. 584	$3p\ ^3P^\circ_{2,1}$— $5d\ ^3D$
	C	11969. 48		8352. 298	$3p\ ^3P^\circ_0$ — $5d\ ^3D_1$
Mg	C	12527. 51	190	7980. 25	$3s\ ^3S_1$ — $4p\ ^3P^\circ$
	C	12755. 66		7837. 51	$3d\ ^1D_2$ — $5p\ ^1P^\circ_1$
	Hu-Ko	12784. 79	810	7819. 66	$3d\ ^3D$ — $5f\ ^3F^\circ$
	Hu-Ko	12790. 27	250	7816. 31	$3d\ ^1D_2$ — $5f\ ^1F^\circ_3$
Hu-Pl	C	12845. 95	61	7782. 426	$3p\ ^3P^\circ_{2,1}$— $5s\ ^3S_1$
	C	12846. 42		7782. 142	$3p\ ^3P^\circ_0$ — $5s\ ^3S_1$
Hu-Pl	C	12968. 44	100	7708. 920	$3p\ ^1P^\circ_1$ — $5d\ ^1D_2$
	C	12984. 93		7699. 13	$3d\ ^3D$ — $5p\ ^3P^\circ$
Hu-Pl	C	15083. 66	120	6627. 881	$3s\ ^1S_0$ — $4p\ ^1P^\circ_1$
Hu-Ko	C	17002. 38	4600	5879. 925	$3p\ ^3P^\circ_{2,1}$— $4d\ ^3D$
	C	17003. 15		5879. 657	$3p\ ^3P^\circ_0$ — $4d\ ^3D_1$

TABLE 1. *Wavelengths and classifications for the lines of the* ^{4}He I *spectrum*—Continued

The meanings of the symbols in the first two columns will be understood from the discussion in the text and the explanations given at the end of this table.

Observer		λ (air)	Intensity	cm^{-1}	Classification
1	2				
Hu-Pl	C	18555. 55	13	5387. 752	$3d\ ^1D_2$ — $4p\ ^1P^\circ_1$
Hu-Ko	C	18685. 96	7250	5350. 15	$3d\ ^3D$ — $4f\ ^3F^\circ$
Hu-Ko	C	18696. 94	3175	5347. 01	$3d\ ^1D_2$ — $4f\ ^1F^\circ_3$
Hu-Pl	C	19089. 37	1100	5237. 088	$3p\ ^1P^\circ_1$ — $4d\ ^1D_2$
Hu-Pl	C	19543. 13	130	5115. 49	$3d\ ^3D$ — $4p\ ^3P^\circ$
	Hu	20581. 30	20850	4857. 454	$2s\ ^1S_0$ — $2p\ ^1P^\circ_1$
Hu-Pl	C	21120. 04	600	4733. 547	$3p\ ^3P^\circ_{2,1}$ — $4s\ ^3S_1$
Hu-Pl	C	21121. 31		4733. 263	$3p\ ^3P^\circ_0$ — $4s\ ^3S_1$
Hu-Pl	C	21132. 04	95	4730. 860	$3p\ ^1P^\circ_1$ — $4s\ ^1S_0$

*From 10912 A on, the intensities are measurements by C. J. Humphreys [24].

Explanation of Symbols

C—Wavelength calculated from vacuum wavenumber difference of relevant energy levels from table 2.

CS—Same as C, the upper energy level being obtained from a series formula.

B–Rs—J. C. Boyce and H. A. Robinson, J. Opt. Soc. Am. **26,** 133 (1936).

Hp—J. J. Hopfield, Astrophys. J. **72,** 133 (1930).

Hu—C. J. Humphreys, unpublished wavelength, privately communicated to author, August 1959.

Hu–Ko—C. J. Humphreys and H. J. Kostkowski, J. Research NBS **49,** 73 (1952).

Hu–Pl—C. J. Humphreys and E. Paul, Jr., NAVORD Report 4589, 25 (1956); J. Opt. Soc. Am. **46,** 999 (1956).

Hz—G. Herzberg, Proc. Roy. Soc. (London) [A] **248,** 309 (1958).

Hz*—The air wavelength given for this line by Herzberg (above) is incorrect; the wavelength in his paper is actually the vacuum wavelength.

Hz†—Unpublished observations by Herzberg, privately communicated to the author. Of these lines, only 8776 A has been previously recorded (P-Rt); Herzberg's observed value of 8776.725±0.02 A is in good agreement with the calculated wavelength. The value 8518.040±0.02 A from Herzberg figured in determining the position of $8p\ ^1P^\circ_1$, and his measurement of 8444 A is the same as the calculated value.

Kg—P. G. Kruger, Phys. Rev. **36,** 855 (1930).

Mt—W. C. Martin, J. Opt. Soc. Am. (to be published). The vacuum wavelengths given in table 2 of this reference have been converted to air values according to the formula of Edlén. These wavelengths were further decreased by 0.0002 A for inclusion here because such a correction to the values assumed by Martin for the mercury-198 standards at 5462 A and 4359 A appeared probable at the time the new array was worked out. It now appears the correction should at most have been −0.0001 A; except for 5015 A, either correction is insignificant compared to the probable errors.

Me—P. W. Merrill, Bul. BS **14,** 159 (1917); Astrophys. J. **46,** 357 (1917). Merrill's wavelengths have all been increased by 0.002 A because of a systematic difference found to exist throughout the visible range between his measurements and those of Martin (above).

Mg—W. F. Meggers, J. Research NBS **14,** 487 (1935).

Mg–D—W. F. Meggers and G. H. Dieke, BS J. Research **9,** 121 (1952).

Of—H. C. Offerhaus, Physica **3,** 309 (1923).

P–G—F. Paschen and R. Götze, Seriengesetze der Linienspectren, p. 26 (Julius Springer, Berlin, 1922).

P–Rt—F. Paschen and R. Ritschl, Ann. Physik **18,** 867 (1933). In table 8a of this paper the designations "$3\ ^3P_2$" and "$3\ ^3P_1$" should be replaced by "$3\ ^3P_{2,1}$" and "$3\ ^3P_0$", respectively (see text).

Pé—A. Pérard, Rev. Optique **7,** 1 (1928).

Se–F—G. W. Series and J. C. Field, Proceedings of the Symposium on Interferometry, Teddington, England, June 1959 (to be published)

Sh—A. G. Shenstone, unpublished measurements

Su—T. Suga, Sci. Papers Inst. Phys. Chem. Research (Tokyo) **34,** 7 (1937).

(Where two or more symbols separated by commas are given in the second column, a weighted average has been taken.)

TABLE 2. *Energy levels of* ^{4}He I

Term designation	J	Level
$1s^2\ ^1S$	0	0. 00±0. 15
$2s\ ^3S$	1	159856. 069
$2s\ ^1S$	0	166277. 546
$2p\ ^3P^\circ$	2	*169086. 8636*
	1	*169086. 9400*
	0	*169087. 9280*
$2p\ ^1P^\circ$	1	*171135. 000*
$3s\ ^3S$	1	183236. 892
$3s\ ^1S$	0	184864. 936
$3p\ ^3P^\circ$	2	*185564. 6540*
	1	*185564. 6760*
	0	*185564. 9466*
$3d\ ^3D$	3	186101. 643
	2	186101. 646
	1	186101. 691
$3d\ ^1D$	2	186105. 065
$3p\ ^1P^\circ$	1	*186209. 471*
$4s\ ^3S$	1	190298. 210
$4s\ ^1S$	0	190940. 331
$4p\ ^3P^\circ$	2, 1, 0	*191217. 14*
$4d\ ^3D$	3	191444. 583
	2	191444. 585
	1	191444. 604

TABLE 2. *Energy levels of* ^{4}He I—Continued

Term designation	J	Level	Term designation	J	Level	Term designation	J	Level
$4d\ ^1D$	2	191446.559	$8f\ ^3F°$	4, 3, 2	*196596.17*	$14s\ ^3S$	1	197726.37
$4f\ ^3F°$	4, 3, 2	*191451.80*	$8f\ ^1F°$	3	*196596.16*	$14s\ ^1S$	0	197739.67
$4f\ ^1F°$	3	*191452.08*	$8p\ ^1P°$	1	*196601.51*	$14p\ ^3P°$	2, 1, 0	*197745.65*
$4p\ ^1P°$	1	*191492.817*	$9s\ ^3S$	1	196862.04	$14d\ ^3D$	3, 2, 1	197750.69
$5s\ ^3S$	1	193347.089	$9s\ ^1S$	0	196912.98	$14d\ ^1D$	2	197750.75
$5s\ ^1S$	0	193663.627	$9p\ ^3P°$	2, 1, 0	*196935.42*	$14f\ ^3F°$	4, 3, 2	----------
$5p\ ^3P°$	2, 1, 0	*193800.78*	$9d\ ^3D$	3, 2, 1	196955.28	$14p\ ^1P°$	1	*197751.94*
$5d\ ^3D$	3, 2, 1	193917.245	$9d\ ^1D$	2	196955.52	$15s\ ^3S$	1	197803.12
$5d\ ^1D$	2	193918.391	$9f\ ^3F°$	4, 3, 2	*196956.04*	$15s\ ^1S$	0	197813.95
$5f\ ^3F°$	4, 3, 2	*193921.31*	$9f\ ^1F°$	3	*196956.2*	$15p\ ^3P°$	2, 1, 0	[c]*197818.83*
$5f\ ^1F°$	3	*193921.37*	$9p\ ^1P°$	1	*196959.79*	$15d\ ^3D$	3, 2, 1	197822.91
$5g\ ^{3,1}G$	5, 4, 4, 3	193922.5	$10s\ ^3S$	1	197145.28	$15d\ ^1D$	2	197822.96
$5p\ ^1P°$	1	*193942.57*	$10s\ ^1S$	0	197182.17	$15f\ ^3F°$	4, 3, 2	*197823.15*
$6s\ ^3S$	1	194936.23	$10p\ ^3P°$	2, 1, 0	*197198.34*	$15p\ ^1P°$	1	*197823.91*
$6s\ ^1S$	0	195115.00	$10d\ ^3D$	3, 2, 1	197212.88	$16s\ ^3S$	1	197865.87
$6p\ ^3P°$	2, 1, 0	*195192.91*	$10d\ ^1D$	2	197213.06	$16p\ ^3P°$	2, 1, 0	*197878.69*
$6d\ ^3D$	3, 2, 1	195260.167	$10f\ ^3F°$	4, 3, 2	*197213.44*	$16d\ ^3D$	3, 2, 1	197882.00
$6d\ ^1D$	2	195260.86	$10p\ ^1P°$	1	*197216.24*	$16d\ ^1D$	2	197882.01
$6f\ ^3F°$	4, 3, 2	*195262.59*	$11s\ ^3S$	1	197352.89	$16p\ ^1P°$	1	*197882.82*
$6f\ ^1F°$	3	*195262.59*	$11s\ ^1S$	0	[b]197380.44	$17s\ ^3S$	1	197917.53
$6g\ ^{3,1}G$	5, 4, 4, 3	195263.2	$11p\ ^3P°$	2, 1, 0	*197392.72*	$17p\ ^3P°$	2, 1, 0	*197928.26*
$6h\ ^{3,1}H°$	6, 5, 5, 4	*195263.8*	$11d\ ^3D$	3, 2, 1	197403.47	$17d\ ^3D$	3, 2, 1	197930.96
$6p\ ^1P°$	1	*195275.04*	$11d\ ^1D$	2	197403.64	$17d\ ^1D$	2	197931.00
$7s\ ^3S$	1	195868.35	$11f\ ^3F°$	4, 3, 2	*197403.89*	$17p\ ^1P°$	1	*197931.65*
$7s\ ^1S$	0	195979.04	$11p\ ^1P°$	1	[c]*197405.99*	$18p\ ^3P°$	2, 1, 0	*197969.75*
$7p\ ^3P°$	2, 1, 0	*196027.40*	$12s\ ^3S$	1	197509.52	$18d\ ^3D$	3, 2, 1	197972.00
$7d\ ^3D$	3, 2, 1	196069.73	$12s\ ^1S$	0	197530.68	$18d\ ^1D$	2	197972.07
$7d\ ^1D$	2	196070.16	$12p\ ^3P°$	2, 1, 0	*197540.19*	$18p\ ^1P°$	1	*197972.58*
$7f\ ^3F°$	4, 3, 2	*196071.26*	$12d\ ^3D$	3, 2, 1	197548.41	$19p\ ^3P°$	2, 1, 0	*198004.85*
$7f\ ^1F°$	3	*196071.26*	$12d\ ^1D$	2	197548.54	$19d\ ^3D$	3, 2, 1	198006.75
$7g\ ^{3,1}G$	5, 4, 4, 3	196071.7	$12f\ ^3F°$	4, 3, 2	*197548.76*	$19p\ ^1P°$	1	*198007.21*
$7h\ ^{3,1}H°$	6, 5, 5, 4	*196072.0*	$12p\ ^1P°$	1	*197550.36*	$20p\ ^3P°$	2, 1, 0	*198034.80*
$7i\ ^{3,1}I$[a]	7, 6, 6, 5	----------	$13s\ ^3S$	1	197630.75	$20d\ ^3D$	3, 2, 1	[f]198036.4
$7p\ ^1P°$	1	*196079.24*	$13p\ ^3P°$	2, 1, 0	*197654.83*	$20p\ ^1P°$	1	*198036.79*
$8s\ ^3S$	1	196461.42	$13s\ ^1S$	0	[d]197647.38	$21p\ ^3P°$	2, 1, 0	*198060.58*
$8s\ ^1S$	0	196534.88	$13d\ ^3D$	3, 2, 1	197661.21	$21d\ ^3D$	3, 2, 1	198062.3
$8p\ ^3P°$	2, 1, 0	*196566.82*	$13d\ ^1D$	2	197661.22	$22p\ ^3P°$	2, 1, 0	*198082.89*
$8d\ ^3D$	3, 2, 1	196595.18	$13f\ ^3F°$	4, 3, 2	*197661.50*	He II($^2S_{0\frac{1}{2}}$)	**Limit**	**198310.81**
$8d\ ^1D$	2	196595.54	$13p\ ^1P°$	1	*197662.75*	$2p^2\ ^3P$	2, 1, 0	481205.

[a] Although it is not possible to give the unperturbed position of these terms, Foster [19] found transitions from them to $2p\ ^1P°$ in the spectrum emitted by helium atoms in a strong electric field.

[b] Level value found by plotting the Rydberg denominators of the $ns\ ^1S$ series.

[c] The $np\ ^1P°$ levels were obtained from a series formula from $11p$ on.

[d] An incorrect value was given for this term by Paschen-Götze. The wavelength listed there for the transition $2p\ ^1P_1°-13s\ ^1S_0$ is in error.

[e] The value given for this term in Paschen-Götze is incorrect.

[f] The energy for this term was calculated from a series formula. The values of Paschen-Götze for $18d$, $19d$, ^1D are in disagreement with those of Herzberg by about 0.5 cm^{-1}.

TABLE 3. *Fine-structure regularities observed for the 2p and 3p triplets in* He I.

np	$\frac{^3P_2^\circ-{}^3P_0^\circ}{^3P_2^\circ-{}^3P_1^\circ}$	$n^3(^3P_2^\circ-{}^3P_0^\circ)$
$2p$	13.9	8.523 cm^{-1}
$3p$	13.3	7.90

TABLE 4. *Observed fine-structure ratios and n^{-3} dependence for the 3d and 4d triplets of* He I.

nd	$\frac{^3D_3-{}^3D_1}{^3D_3-{}^3D_2}$	$n^3(^3D_3-{}^3D_1)$
$3d$	16	1.30 cm^{-1}
$4d$	11	1.31

WASHINGTON, D.C. (Paper 64A1–26)

JOURNAL OF RESEARCH of the National Bureau of Standards—A. Physics and Chemistry
Vol. 64, No. 1, January–February 1960

Vibration-Rotation Structure in Absorption Bands for the Calibration of Spectrometers From 2 to 16 Microns[1]

Earle K. Plyler, Alfred Danti,[2] L. R. Blaine, and E. D. Tidwell

(September 23, 1959)

Suitable bands of common gases have been tabulated and remeasured wherever necessary from 2 to 16 microns to obtain an accuracy of about 0.03 cm^{-1} throughout the region and to provide good calibrating points at frequent intervals. Some 600 rotation-vibration lines are illustrated in 20 spectrograms and wavenumbers are listed in companion tables with considerable intercomparison with worthy data obtained in other laboratories. The absorpotion bands were remeasured or calibrated by using either a precisely graduated grating circle or standard atomic lines with the fringe system formed by a Fabry-Perot interferometer. Characteristic features of the individual bands are discussed briefly and references to other publications are given. The substances used for calibration include H_2O, CO_2, CO, HCl, HBr, NH_3, C_2H_2, CH_4, N_2O, and polystyrene film.

1. Introduction

In recent years, infrared spectroscopists have expressed concern regarding satisfactory methods and wavelengths for calibrating good prism and small grating spectrometers [1, 2, 3, 4].[3] In the past, a number of publications [5, 6, 7, 8, 9, 10, 11] from several laboratories did tend to ease the immediate requirements; but with the influx of finer instruments the need for more thorough, suitable, and precise coverage has arisen. Professor Mizushima and fellow workers have clearly indicated in their detailed measurements [12] that the small grating instruments are certainly capable of producing rather precise data. The present work addressed itself to the need for bringing together and remeasuring suitable bands of common gases in order to certify absolute accuracy to within several hundredths of a cm^{-1} throughout the region and to provide calibration points at frequent intervals.

2. Utility of the Molecular Band Method

Although in several cases (extremely precise measurements on CO [13, 14, 15] and HCN [16]) the use of molecular bands for calibration purposes is probably as good as the use of atomic lines, this method should not take preference over the use of atomic lines when precise measurement is being considered. However, when measurements good to several hundredths of a cm^{-1} are sufficient or in cases where other limiting factors enter, viz, broad bands, then this method may offer a number of advantages. In the case of prism instruments, the use of appropriate atomic lines for calibration is rather limited to the visible and near infrared regions and the need for single order coverage throughout is apparent. Present day commercial instruments are more easily calibrated in absorption than in emission and the molecular band method obviates the need for a full battery of atomic line equipment as well as personnel capable of using it. In addition, only available or easily obtainable substances have been used in this work so that laboratories should experience little difficulty in using this method. Most of the gases are available in typical chemistry laboratories and it will be mentioned that work in this laboratory has indicated that, in general, natural gas from commercial lines and acetylene drawn from the welder's tank are suitable for calibration purposes. Should impurity peaks arise in these bands, use can still be made of the lines which are clearly those tabulated and illustrated in the following sections.

Some 600 lines, which provide rather thorough coverage, are tabulated and illustrated in 20 spectrograms. For certain bands, the number can be appropriately increased by having reference to recommended publications given in the discussion section. Attempts were made to keep the number of different gases used at a minimum and they include: H_2O, CO_2, CO, HCl, HBr, NH_3, C_2H_2, CH_4, and N_2O. Also a polystyrene film has been included.

3. Instruments and Methods Used in Calibrating the Standard Lines

Two instruments in the Radiometry Section of the NBS were used in measuring the bands and in the 2- to 4-μ region most bands were measured on both instruments at different resolution and the results compared.

[1] This research was supported by the Air Force Cambridge Research Center and by a NASF grant to MIT.
[2] Guest worker from MIT.
[3] Figures in brackets indicate the literature references at the end of this paper.

3.1. 5 to 16 Micron Region

a. Instrument

The previously described [17] grating spectrometer with an off-axis collimating mirror of 1-m focal length was used in conjunction with an extremely precise grating circle reported to be accurate to at least 3 sec of arc for any angle [18]. For the longer wave work (5 to 16 μ) the lead telluride detector was replaced with a thermocouple detector. When this instrument was used in the 2- to 4-μ region, the thermocouple detector was purposefully used so that resolution could be lowered and made comparable to that of small grating instruments. A KBr foreprism arrangement with fixed foreprism slits and a manually adjustable prism was used for order separation throughout this work. Under these stated conditions the instrument was capable of resolving lines separated by 0.3 cm^{-1} in the 7- to 16-μ region and up to about 1 cm^{-1} in the 2.5- to 6.5-μ region.

b. Method of Calibration

With a microscope attachment, angles were read off the inscribed circle, centered with respect to the spindle of the cone which rotates the grating, and fiducial marks recorded on the chart. During measuring runs, readings were taken every 5 min of arc and a slow drive speed ($\sim$23 min per deg) was used. It was found that proper positioning of the foreprism energy upon the entrance slit of the spectrometer proper was necessary in the sense that for extreme settings, where the maximum of energy being admitted to the spectrometer would come about 5 grating degrees away from the point of interest, the frequencies of measured lines would be in error by several hundredths of a cm^{-1}. By making frequent settings of the foreprism (about every 2 deg of grating angle) so that the energy would be maximized and hence placed symmetrically on the entrance slit, these effects could be ignored. Such considerations were, of course, of greater importance in regions where wide spectrometer slits were required or at long wavelengths where the dispersion of KBr is greatest. (This matter was considered in some detail, since it is felt that it is a frequently overlooked source of error occurring with the use of foreprisms.) In the course of any complete run (standards plus spectrum to be measured) no changes were made in instrumental conditions (viz, retardation resulting from changes in amplifier response settings may shift the line center) unless absolutely necessary.

At the start of the work, it was decided that the precisely measured CO fundamental lines (see ref. [13]) (table 4) be used as standards wherever possible. The procedure devised was that of using the simplified grating relation, $n\lambda = K \sin \Theta$, where an "effective" grating constant, K_{air}, incorporating spectrometer characteristics, could be calculated by measuring about 15 CO lines and the physical central image. This was done with the grating being turned first in one direction then in the reverse direction. If slightly different, the K's obtained separately for each direction would be averaged. Once a good value of K had been determined for a grating, the central image was always calculated from the 10 (or so) standard lines recorded either before or immediately following a measuring run. Using this procedure, the frequency of standard CO lines could always be recalculated from chart measurements to within about ± 0.01 cm^{-1} of the accepted value. With good spectrometer and grating alinement, it was felt that CO standards could be used to calibrate NH_3, CH_4, and H_2O lines even though the grating angle for the standards differed appreciably from that of the lines in question. In calibrating the lines, both standards and runs to be measured would be recorded with the grating being turned in the same direction. As is often the case, it was found that slightly different values would be obtained for the two directions. Final values represented the average of an equal number of measurements in each direction. It is believed that the tabulated values are accurate to ± 0.02 cm^{-1} in this region.

c. Chart Reduction

Wherever possible single lines were picked out for measuring, but in some instances certain complex lines were measured since they are particularly suited for direct prism observation. It is advisable to record spectra on ruled chart paper where the ruled lines are reproducible perpendicular to the chart edge. The determined center point of the line to be measured can then be easily projected to a suitable measuring base line on the chart by using a pair of dividers and the nearest ruled line. The center of the line should be determined with a pair of stiff dividers at about the 2/3 absorption point and not at the peak or apparent maximum of absorption. If the spectrum is particularly noisy the center should be determined at a number of places from the 2/3 to 3/4 point of the maximum of absorption and the average taken. Fractional distances between "pip" marks should be measured to within 0.005 in. using a steel rule and visual enlarger if necessary. For the majority of measuring runs, 5 min of grating are corresponded to 2 in. on the chart.

d. Instrument and Calibration

The instrument, which uses the double-pass system and is capable of resolving about 0.03 cm^{-1} has been described [19] and only a few details need be added. Standard atomic lines and the fringe system described in a previous paper (see ref. [17]) were used to calibrate the molecular bands. By scanning the spectrum slowly and averaging several runs, a set of relative values for the lines of a band can be determined to a few thousandths of a cm^{-1} and the absolute to ± 0.01 cm^{-1}. With scanning at a medium rate, absolute values are probably in error by ± 0.03 cm^{-1}. The accuracy of measurement of this instrument is increased by the lines being very narrow (0.03 cm^{-1}). Measurements made under lower resolution (about 1 cm^{-1}) with the other instrument in this region agreed with these to about ± 0.05 cm^{-1}. This indicates that low resolution

spectrometers can measure with an error of about 1/10 of the resolution.

e. Refractive Index

In this laboratory measurements on both instruments are carried out with the grating in air so that reported frequencies were corrected to vacuum by using refractive index tables, and temperature and pressure corrections given by Penndorf [20].

4. Comments on Measuring Technique and Use of the Standard Lines

For the present-day molecular spectroscopist who wishes to carry out precise measurements, useful points on measurement technique, whether on standard or unknown lines, have already been mentioned in previous sections on method of calibration, instrument performance, chart reduction and also in reference [17]. Concerning a spectrum to be measured, in cases where the instrument is being used at or near its resolution limit (ripple spectrum) or in the case of complex lines or shoulders, then the best possible "center" point must be picked and this may necessarily have to be near the absorption peak since lines may not be well enough developed to permit measurement at the 2/3 to 3/4 absorption point.

It is advisable to record both spectra and standards for each direction of grating turn if the driving mechanism is equally accurate in both directions. Provisions or modifications should be made on commercial or laboratory instruments so that the grating can be used in both directions with near equal accuracy and the results averaged. Undoubtedly, in most laboratories the standards will be used in conjunction with reproducible pip marks. Data will be extracted from simple pip or drum number versus frequency (cm^{-1}) relations by fitting a straight line to two end points and an extended deviation curve plotted. In view of extremely precise data for certain bands (CO, HCN) the utility of using these standard lines in higher orders for the same grating angle should not be overlooked. In terms of precision measurement, it would appear that the R branch (1,000 to 1,200 cm^{-1}) of the $\mu/_2$ NH_3 band might also be classified in this category. This higher order procedure, of course, requires refractive index considerations for conversion to vacuum and each spectral region must be handled independently.

In making use of the standard lines under lower or higher resolution, workers should exercise necessary care. For example, in the CO bands where (apart from some isotopic overlap) the lines are single and suitably spaced throughout, even ripple peaks observed with a prism instrument would serve as satisfactory calibration points. Whereas, in many other bands proper usage under lower resolution may require judicious use of sufficiently low pressures and slow scanning speeds to assure the proper development of lines and eliminate "pulling" by strong neighboring absorption.

5. Discussion of Spectograms

In general, the runs made on white chart paper for illustration purposes were made at somewhat faster speeds and with much more chart concentration than was the case for the measuring runs. On some of the illustrations, sloping or bowing backgrounds are due either to foreprism effects or the joining of separate sections.

5.1. CO_2, ν_2 Fundamental

Some 20 lines in this band were remeasured and comparison is made with the work of Rossman,[1] Rao, and Nielsen [21–A, 21–B] and also with the values reported by Mizushima et al. (see ref. [12]). Although our measurements were somewhat handicapped by the overly strong absorption (7-m path) and also by poorer grating resolution in this region, the agreement is quite good. It appears that the values reported by Rossman, Rao, and Nielsen (also additional unpublished work communicated by Dr. Rao) are accurate and that lines they report both at higher and lower frequency as well as those given in table 1 may be used for calibration purposes provided the atmospheric absorption is augmented by CO_2 used in a vapor cell. The spectrum is illustrated in figure 1.

TABLE 1. *Absorption lines of ν_2 fundamental of CO_2 from 635 to 700 cm^{-1}*

J	$R(J)$			$P(J)$		
	Rossman, Rao, and Nielsen [a] ν cm^{-1} (vac.) observed	This work ν cm^{-1} (vac.) observed	Mizushima et al. [b] ν cm^{-1} (vac.) observed	Rossman, Rao, and Nielsen [a] ν cm^{-1} (vac.) observed	This work ν cm^{-1} (vac.) observed	Mizushima et al. [b] ν cm^{-1} (vac.) observed
2	669.75	----------	----------	665.83	----------	----------
4	71.34	----------	.28	64.28	----------	----------
6	72.88	.88	.87	62.71	----------	----------
8	74.45	.46	.43	61.18	.15	.15
10	76.02	.06	.02	59.64	.55	.60
12	77.60	----------	.59	58.08	.06	.09
14	79.20	----------	.16	56.55	.51	.53
16	80.78	----------	.76	55.02	4.98	.00
18	82.36	.39	.35	53.48	.48	.47
20	83.95	.98	.95	51.95	.91	.94
22	85.55	.56	.55	50.41	.39	.41
24	87.16	.17	.14	48.90	----------	.89
26	88.77	.79	.78	47.39	----------	.38
28	90.38	.36	.36	45.90	.89	.87
30	91.99	.97	.99	44.37	----------	.39
32	93.59	----------	.60	42.86	----------	.88
34	95.19	----------	.20	41.35	.40	.38
36	96.82	----------	.82	39.83	----------	.90
38	98.44	----------	.42	38.34	----------	.35
40	700.07	----------	.04	36.87	----------	.89
42	01.69	----------	.68	35.38	----------	.40
Q Branch	[c] (10°0–>01¹0)	720.46	----------			

[a] Rossman, Rao, and Nielsen [21].
[b] Mizushima et al. [12].
[c] The measuring point of this band was taken at the 2/3 absorption point.

5.2. Acetylene, ν_5 Fundamental

This band was included in order to provide useful calibration points between the end of the strong 15-μ CO_2 band and the ammonia band. On the low-

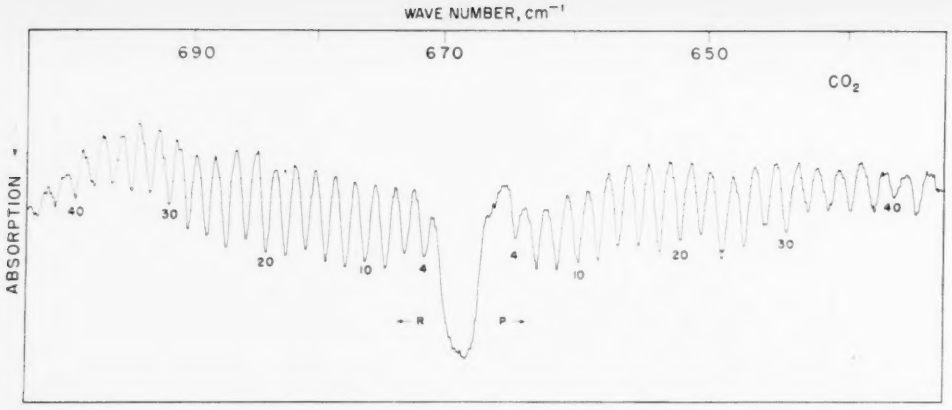

FIGURE 1. *The ν_2 fundamental of CO_2 recorded in the first order of an 1,800 lines/in. grating under atmospheric conditions and 7-m path.*

Spectral slit width about 0.5 cm^{-1}.

frequency end, our values are in excellent agreement with the recently published values of Rao, Ryan, and Nielsen [22] and table 2 includes additional values as reported by these authors. At higher frequency, results are also compared with the work of Christensen, Eaton, Green, and Thompson [23]. The agreement is quite good except between lines 29 to 39, where several lines appear to be pulled out of position by an overlapping band. These lines are set out by parentheses. Results of recent measurements by Jones and Nadeau of the National Research Council, Ottawa, Canada are also included. The spectrogram is illustrated in figure 2.

5.3. NH_3, ν_2 Fundamental

Table 3 gives values obtained in four different laboratories for this band. Since these four works are of about equal quality, the average value reported in the last column represents a simple numerical average (within arbitrary ± 0.04-cm^{-1} exclusion conditions). The average values are probably better than individual determinations, and it is estimated that they are good to within ± 0.01-cm^{-1} absolute on the average. The region from 1,000 to 1,200 cm^{-1} is particularly good. We have cause for suspicioning some of our low-frequency lines (numbers 1, 3, and 6) due to the fact that the grating was being used at exceedingly high angle. As more experimental and theoretical data become available for ammonia, a good set of calculated values may ultimately replace the average value column. The spectrum is shown in figure 3.

5.4. Methane, ν_4 Fundamental

This band serves the purpose of providing connection between the ammonia and water bands and is included mainly because workers with small instruments may have difficulty in observing weak water lines in this region. We are unable to compare these

TABLE 2. *Absorption lines of ν_5 fundamental of acetylene from 680 to 790 cm^{-1}*

Line serial number	This work ν cm^{-1} (vac.) observed	Rao, Ryan, and Nielsen [a] ν cm^{-1} (vac.) observed	C., E., G., and T [b] ν cm^{-1} (vac.) observed	Jones and Nadeau [c] ν cm^{-1} (vac.) observed
1	.....	686.77	.....	686.66
2	.....	89.11	.....	89.15
3	.....	91.47	.....	91.39
4	.....	93.80	.....	93.79
5	.....	96.19	.....	96.15
6	698.53	98.52	698.50	98.57
7	.....	700.89	700.88	700.88
8	703.28	03.24	03.19	03.23
9	[d] (05.66)	05.60	05.56	05.53
10	07.96	07.96	07.94	07.94
11	10.30	10.30	10.37	10.29
12	12.68	.....	12.67	12.60
13	15.08	.....	15.03	15.12
14	16.36	.....	.....	.....
15	17.35	.....	17.35	17.35
16	19.90 (peak)	.....	19.90	19.84
17	(22.15)	.....	22.06	21.96
18	24.39	.....	24.35	.....
19	36.17	.....	36.18	36.14
20	38.56	.....	38.56	38.54
21	40.89	.....	40.88	40.85
22	43.29	.....	43.31	43.20
23	45.64	.....	45.64	45.65
24	47.97	.....	48.02	47.95
25	50.36	.....	50.37	50.29
26	52.66	.....	52.74	52.70
27	(55.12)	.....	55.14	55.10
28	57.42	.....	57.45	57.43
29	(59.85)	.....	59.86	59.68
30	62.11	.....	62.18	62.10
31	(64.46)	.....	64.52	64.50
32	66.74	.....	66.87	66.68
33	69.08	.....	69.21	69.13
34	71.39	.....	71.53	71.46
35	73.71	.....	73.84	73.80
36	(76.02)	.....	76.17	76.12
37	78.42	.....	78.52	78.42
38	(80.70)	.....	80.82	80.73
39	83.07	.....	83.09	83.00
40	85.43	.....	85.45	85.37
41	87.75	.....	87.74	.....
42	90.10	.....	90.12	.....

[a] Rao, Ryan, and Nielsen [22].
[b] Christensen, Eaton, Green, and Thompson [23].
[c] Jones and Nadeau, National Research Council, Ottawa, Canada, unpublished work.
[d] Parentheses around values in second column indicate poorer lines.

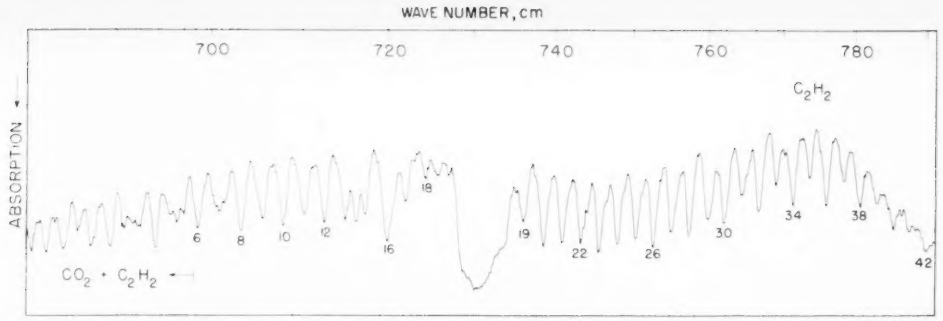

FIGURE 2. *The ν_5 fundamental of acetylene recorded in the first order of an 1,800 lines/in. grating with 8-cm pressure and 5-cm path.*

Spectral slit width about 0.7 cm^{-1}. The low frequency end of the P branch overlaps with atmospheric absorption of CO_2 and the strong Q branch (hot band) of CO_2 at 720.46 cm^{-1} also contributes to absorption at this point.

TABLE 3. *Absorption lines of ν_2 fundamental of NH_3 from 760 to 1,210 cm^{-1}*

Line serial number	This work ν cm^{-1} (vac.) observed	Garing and Nielsen [a] ν cm^{-1} (vac.) observed	Price and coworkers [b] ν cm^{-1} (vac.) observed	Mizushima et al.[c] ν cm^{-1} (vac.) observed	Average value [d] ν cm^{-1} (vac.)
1	760.72	.69	.69		.70
2	70.96	.91	.90	.96	.93
3	78.33	.29	.27	.33	.30
4	91.76	.72	.76	.75	.75
5	96.17	.14	.16	.15	.16
6	809.76	.72	.71	.74	.73
7	14.27	.25	.22	.24	.24
8	30.68	.65	.70	.67	.68
9	34.86	.82	.84	.83	.84
10	51.36	.32	.36	.32	.34
11	52.77	.71	.76	.73	.74
12	67.83 (blend)	(.53, .74, .93)	(.53, .73, .95)	.82	.82
13	71.77	.73	.74	.79	.76
14	72.59	.56	.58	.58	.58
15	87.99	.99	8.02	.96	.99
16	92.06 (blend)	(1.88, .14)	(1.88, .14)	.10	.08
17	908.21	.17	.15	.24	.18
18	18.65	.62	.61		.63
19	35.85 (poor)	.90	.90		.88
20	48.25	.22	.25	.27	.25
21	51.83	.77	.80		.80
22	61.01 (poor)	.06	(0.89, .12)		
23	71.91	.89	.92	.90	.90
24	91.71	.68	.71		.70
25	92.60 (blend)	(.45, .70)	(.46, .71)	.64	.62
26	1,007.55	.54	.56	.48	.55
27	11.20	.20	.22	.24	.22
28	27.04	.04	.04	6.92	.04
29	32.14	.13	.13	.12	.13
30	46.41	.40	.42	.27	.41
31	53.14	.13	.14	.14	.14
32	65.58	.57	.55	.46	.57
33	70.60	.59	.59	.53	.59
34	74.17	.14	.17	.13	.15
35	84.61	.60	.62	.56	.61
36	89.38	.42	.39	.31	.40
37	95.15	.15	.16	.15	.15
38	1,103.44	.46	.42	.44	.44
39	10.67	.69	.69	.67	.68
40	16.02	.03	.03	5.97	.03
41	22.15	.14	.13	.10	.14
42	31.85	.86	.89		.87
43	36.78	.76	.75		.76
44	40.62	.65	.65	.58	.64
45	47.53	.52	.54		.53
46	52.86	.86	.87		.86
47	58.93	.98	.95	.90	.95
48	77.09	.08	.10		.09
49	95.02	.00	4.99		5.00
50	1,212.66	.68	.69		.68

[a] Garing, Nielsen, and Rao [24].
[b] Price and coworkers [33].
[c] Mizushima et al. [12].
[d] Numerical average of the 4 determinations. If a number differed by 0.04 cm^{-1} or more from the average of the other 3, it was excluded from the average.

numbers with others, as there are no other precision measurements available but our results (see table 4) would appear to be good to about ± 0.02-cm^{-1} absolute. The spectrum is shown in figure 4.

5.5. H_2O, ν_2 Fundamental

Some 50 good lines of varying intensity were picked out for measurement. (See table 5.) Wherever possible, the lines are compared with recent precision determinations of Rao, Ryan, and Nielsen (see ref. [22]). These authors indicate that their values are, on the average, about 0.07-cm^{-1} lower than those reported by Dalby and Nielsen [25] for the region 1,450 to 1,650 cm^{-1}. Our results, when compared with Dalby and Nielsen's values, would indicate that this is the case throughout the band. Wherever possible, mild flushing or pumping down of the spectrometer housing is to be recommended for cleaner development of the lines but our results indicate that good calibration measurements can be made even on saturated lines provided the line is not a complex one. This band is illustrated in figure 5.

TABLE 4. *Substructure of ν_4 band of CH_4 from 1,200 to 1,370 cm^{-1}*

Serial number	This work ν cm^{-1} (vac.) observed
1	1,216.26
2	30.12
3	33.47
4	41.01
5	47.81
6	56.60
7	65.52
8	75.20
9	81.59
10	92.61
11	97.63
12	1,311.42
13	22.09
14	27.20
15	32.41
16	41.79
17	46.70
18	53.06
19	66.04

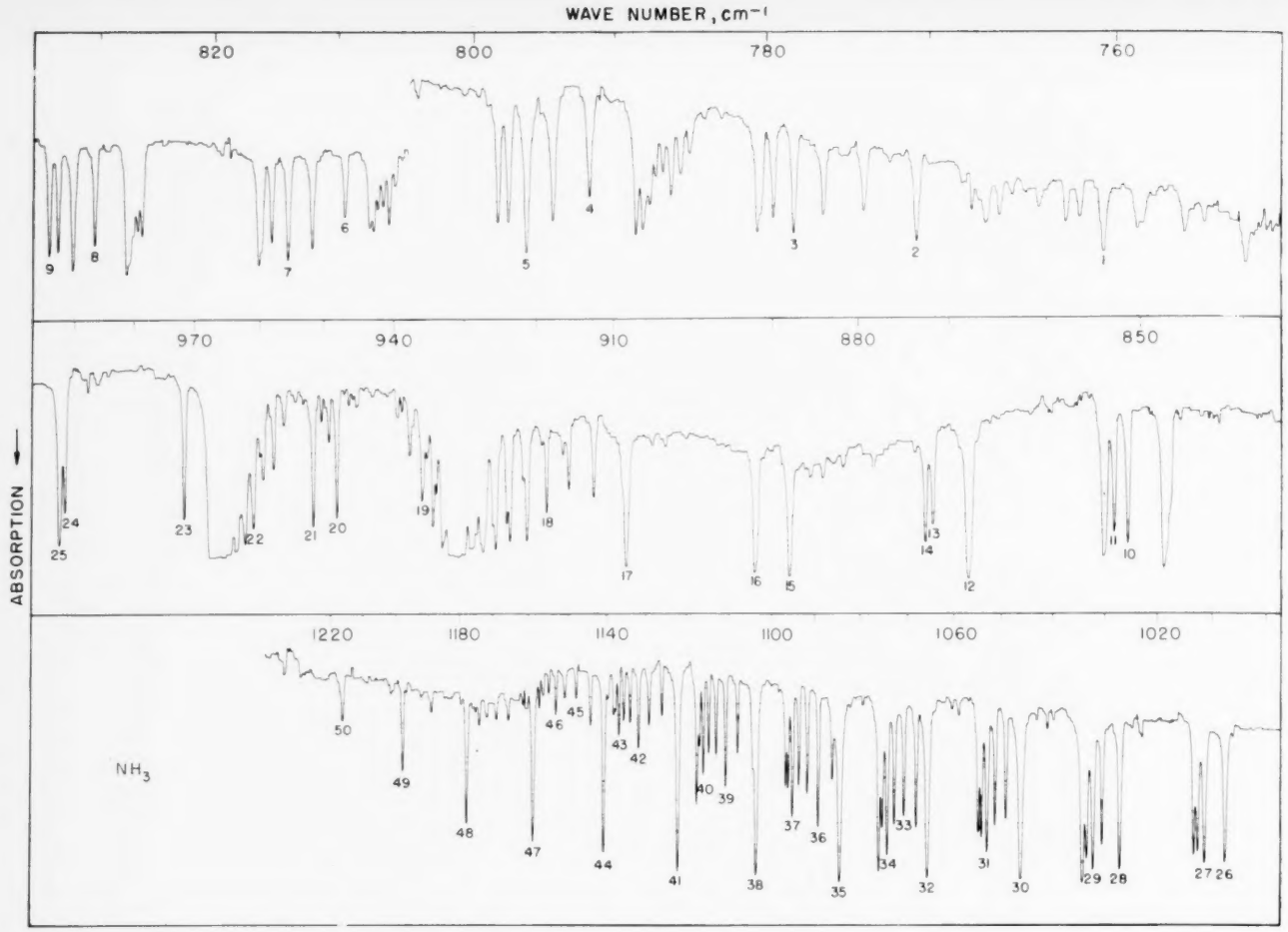

FIGURE 3. *The ν_2 fundamental of NH_3 recorded in the first order of a 3,600 lines/in. grating with 7-cm pressure near the band center and 12-cm for the wings, both with 5-cm path.*

Spectral slit width about 0.3 cm⁻¹.

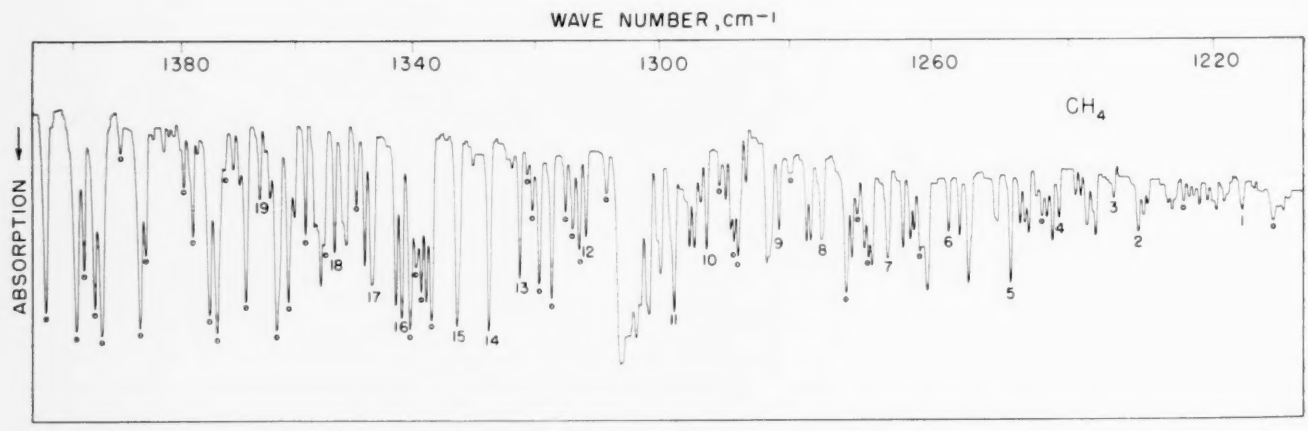

FIGURE 4. *The ν_4 fundamental of CH_4 recorded in the first order of a 3,600 lines/in. grating with 12-cm pressure and 5-cm path.*

Spectral slit width about 0.5 cm⁻¹. The open circles refer to atmospheric water peaks.

TABLE 5. *Absorption lines of ν_2 fundamental of H_2O from 1,300 to 2,000 cm^{-1}*

Line serial number	This work ν cm^{-1} (vac.) observed	Rao, Ryan, and Nielsen [a] ν cm^{-1} (vac.) observed	Line serial number	This work ν cm^{-1} (vac.) observed	Rao, Ryan, and Nielsen [a] ν cm^{-1} (vac.) observed
1	1,312.55	.....	26	16.77	16.72
2	18.92	.....	27	27.88	.....
3	36.68	.....	28	37.53	.....
4	54.83	.....	29	40.31	.....
5	61.08	.....	30	62.82	.....
6	68.62	.....	31	71.49	.....
7	75.07	.....	32	90.15	.....
8	94.46	.....	33	1,704.49	.....
9	1,404.99	.....	34	10.23	.....
10	17.42	.....	35	23.49	.....
11	29.94	.....	36	56.81	.....
12	47.93	.....	37	68.17	.....
13	52.04	.....	38	75.64	.....
14	64.92	64.91	39	84.95	.....
15	81.25	.....	40	[b] (90.94)	.....
16	87.29	.....	41	99.60	.....
17	98.80	.....	42	1,810.63	.....
18	1,512.30	.....	43	25.24	.....
19	28.57	.....	44	47.80	.....
20	[b](45.09)	.....	45	69.35	.....
21	64.93	64.91	46	89.59	.....
22	94.52	94.51	47	95.19	.....
23	96.29	96.27	48	1,918.05	.....
24	1,601.25	01.23	49	42.60	.....
25	09.46	.....	50	88.43	.....
			51	[b] (2,016 79)	.....

[a] Rao, Ryan, and Nielsen [22].
[b] These lines are less accurate.

5.6. CO Fundamental

The CO fundamental band at 4.67 μ was measured accurately by Plyler, Blaine, and Connor (see ref. [13]) in 1955. With the measurement of the CO harmonic (2.33 μ), it was possible to calculate the position of the fundamental band. This has been done by Rank and his colleagues (see ref. [14]) and a very good agreement with the observed values was obtained. There was a slight difference in values for the high J's in the R branch. Recently the R branch has been remeasured and a better correspondence with the calculated values is obtained. The accuracy of the calculated values approaches a few thousandths of a cm^{-1}. The spectrum is shown in figure 6 and the values are listed in table 6.

5.7. $C^{13}O_2$, ν_3 Fundamental

The $C^{13}O_2$ band is excellent for calibration from 2,240 to 2,280 cm^{-1} and connects with the ν_3 band of $C^{12}O_2$. This spectrum was measured in 1955 by Plyler, Blaine, and Tidwell [26]. In this work, the lines of this band have been remeasured and the values check closely with the first determination. Unfortunately, the J values were incorrectly listed in table 1 of the above publication and each J of the P branch should be reduced by 2; that is, P 44 should

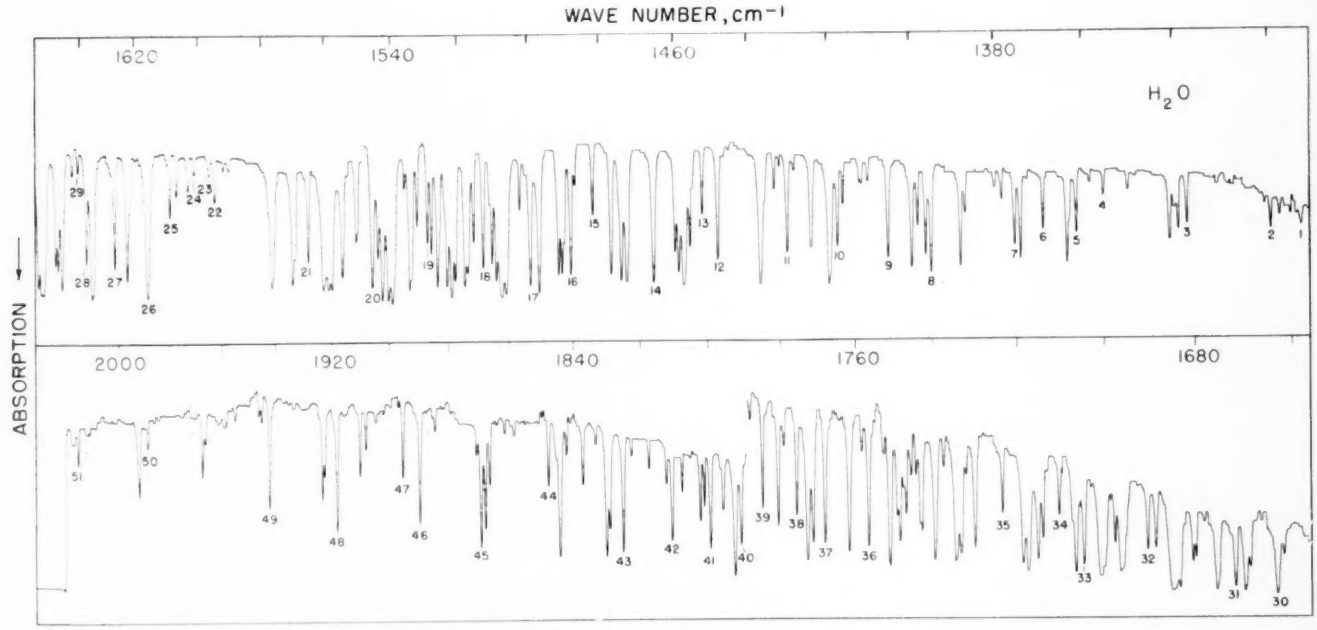

FIGURE 5. *The ν_2 fundamental of H_2O recorded with a 3,600 lines/in. grating under atmospheric conditions ($T=21°$ C, humidity 21%) and 7-m path.*

The upper spectrogram was recorded in the first order and the lower in the second order. Spectral slit width about 0.6 to 0.7 cm^{-1} for both spectrograms.

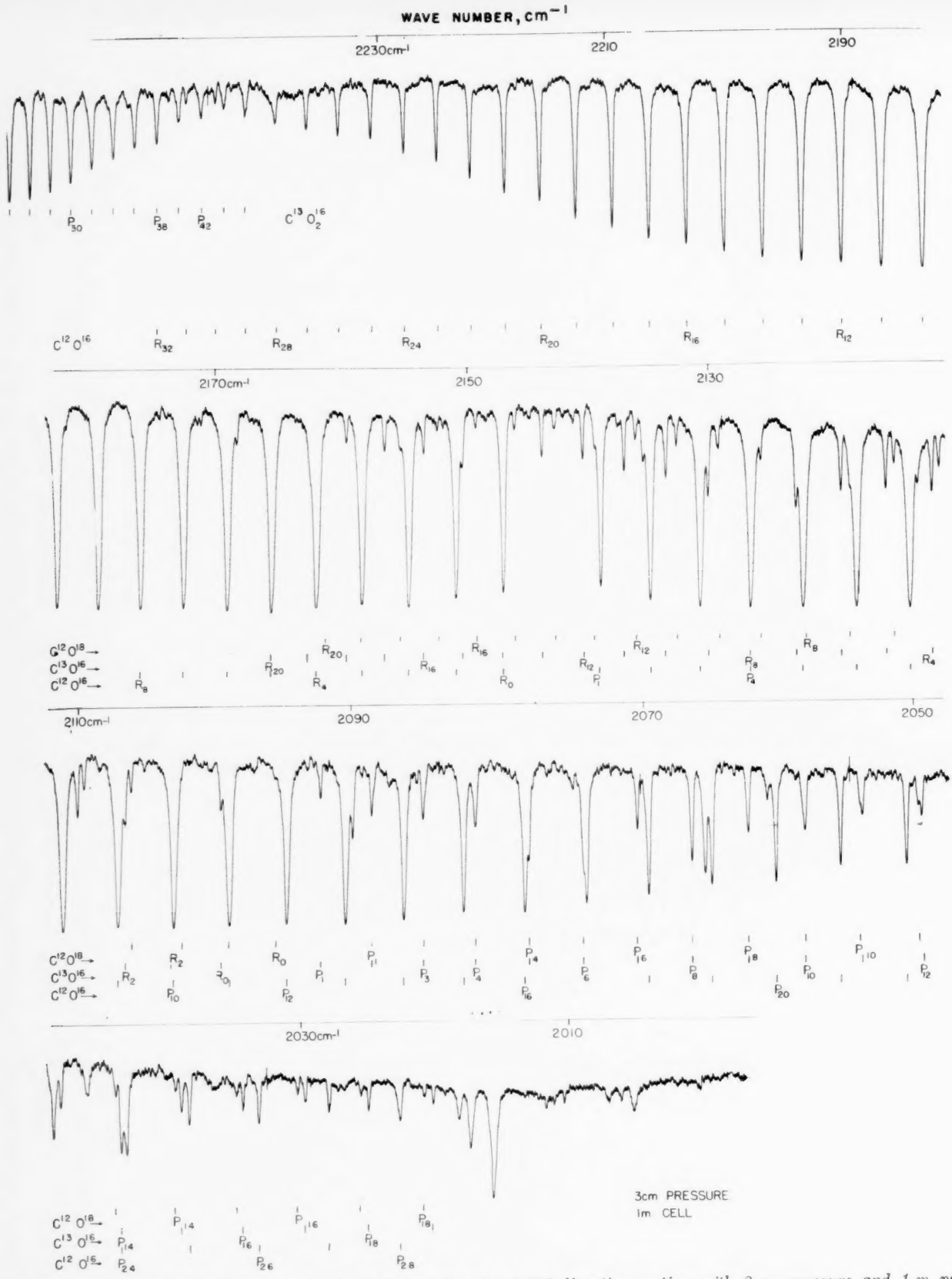

FIGURE 6. *Absorption band of CO recorded in the first order of a 7,500 lines/in. grating with 3-cm pressure and 1-m path.* Spectral slit width about 0.3 cm^{-1}.

TABLE 6. *Absorption lines of* CO *from 2,020 to 2,240 cm⁻¹*

Line No.	Plyler, Blaine, and Connor [a] ν cm⁻¹ (vac.) observed	Rank et al. [b] ν cm⁻¹ (vac.) calculated	Line No.	Plyler, Blaine, and Connor [a] ν cm⁻¹ (vac.) observed		Rank et al. [b] ν cm⁻¹ (vac.) calculated
P 28	2,022.899	.915	*R* 0			
27	27.635	.650	1			
26	32.349	.354	2	2,154.596		.598
25	37.030	.026	3	58.309		.302
24	41.663	.668	4			
23	46.271	.278	5	65.602		.604
22			6			
21	55.391	.402	7	72.759		.761
20	59.911	.916	8	76.287		.286
19			9	79.761		.774
18	68.851	.849	10	83.226		.226
17			11	86.636		.641
16	77.650	.652	12	90.010		.020
15	82.009	.005	13	93.357		.361
14	86.322	.324	14	96.661		.665
13	90.603	.611	15	99.929		.933
12	94.870	.855	16	2,203.147		.163
11	99.096	.085	17	06.345		.355
10	2,103.265	.272	18	09.498		.510
9	07.413	.426	19	12.600		.626
8	11.555	.546	20	15.685		.705
7			21	18.733		.746
6	19.677	.684	22	21.732	[c] 21.750	.749
5	23.700	.702	23	24.694	24.712	.713
4			24		27.638	
3	31.639	.635	25		30.526	
2	35.554	.549	26		33.362	
1	39.432	.429	27		36.186	
			28		38.958	

[a] Plyler, Blaine, and Connor [13].
[b] Rank et al. [14].
[c] New measurements agreeing more closely with calculated values.

TABLE 7–A. *Absorption lines of* ν_3 *fundamental of* $C^{13}O_2^{16}$ *from 2,240 to 2,300 cm⁻¹*

Line number	This work ν cm⁻¹ (vac.) observed	Previous work Plyler, Blaine, and Tidwell [a] ν cm⁻¹ (vac.) observed	Mizushima et al. [b] cm⁻¹ (vac.) observed	Line number	This work ν cm⁻¹ (vac.) observed	Previous work this laboratory [c] ν cm⁻¹ (vac.) observed	Mizushima et al. [b] ν cm⁻¹ (vac.) observed
P 40	2,247.68	2,247.66		*R* 0	2,284.24		
38	49.68	.68		2	85.79	.76	.83
36	51.70	.67		4	87.31	.33	.34
34	53.66			6	88.81	.80	.83
32	55.59			8	90.23	.20	.29
				10	91.62	.62	.73
30	57.52	.52	2,257.48	12	93.10	.12	
28	59.41	.42	.40	14	94.45	.46	
26	61.29	.30	.35	16	95.89		.91
24	63.13	.14	.30	18	97.18	.20	.26
22	64.95	.96	5.04	20	98.50		.57
				22	99.76	.74	
20	66.75	.76	.85	24	2,301.05	.06	
18	68.54	.55	.65				
16	70.29	.31	.37				
14	72.03						
12	73.73	.74	.73				
10	75.42						
8	77.09	.08	.03				
6	78.71	.71	.64				
4	80.33	.31	.18				
2	81.94						

[a] Plyler, Blaine, and Tidwell [26].
[b] Mizushima et al. [12].
[c] E. K. Plyler and L. R. Blaine, unpublished work.

be *P* 42, etc. The work with a small grating spectrometer of Mizushima and his colleagues (see ref. [12]) has also been included and there is very good agreement between the two lists of frequencies. The spectrum of this band is shown in figure 7–A and the values are listed in table 7–A.

5.8. $C^{12}O_2$, ν_3 Band

The only precision work for this band is the work which was done at the NBS. The frequencies were first published in 1955 (see ref. [26]) and since then two other determinations have been made. With the long paths employed in this laboratory, it is not possible to measure the central part of the band. Figure 7–B shows how use can be made of the entire band by purging the instrument housing and containing the CO_2 in a cell. (Dr. Norman Jones of the National Research Council of Canada has furnished the spectogram as observed with a purged small grating instrument.) Table 7–B gives observed values for the band wings and calculated values for the central part. In view of the fact that molecular constants calculated from the observed lines agree well with those of Courtoy [27] obtained from many bands and agreement with observed lines is good, it is felt that workers can use either the observed or calculated values of table 7–B equally well provided the intensity and resolution of the band is close to that of figure 7–B. Both

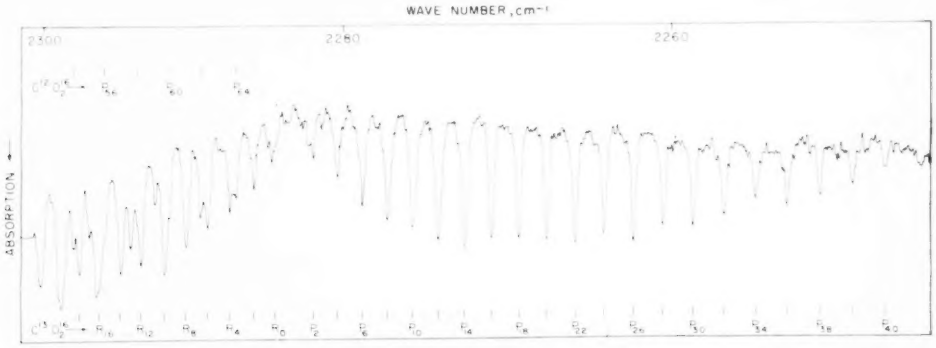

FIGURE 7–A. *The ν_3 fundamental of $C^{13}O_2^{16}$ recorded in the first order of a 7,500 lines/in. grating under atmospheric conditions and 6-m path.*

Spectral slit width about 0.3 cm⁻¹.

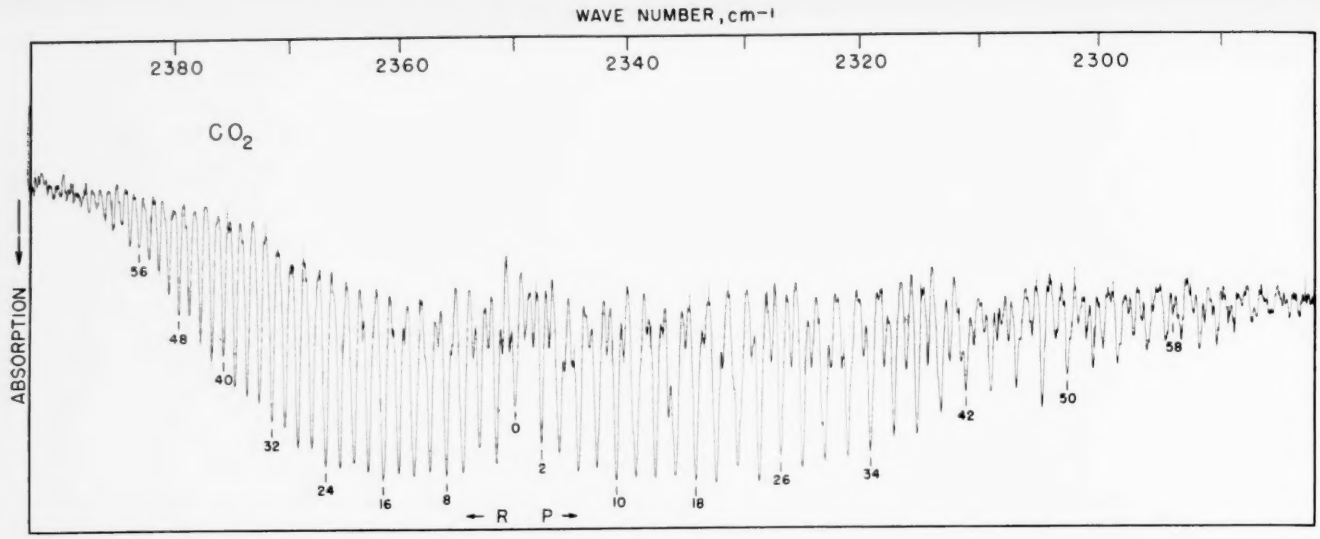

FIGURE 7–B. *The ν_3 fundamental of $C^{12}O_2^{16}$ recorded in the third order of a 70 lines/mm grating with a small grating instrument.*
The spectrometer housing was purged of atmospheric CO_2 with dry nitrogen and the spectrum recorded with 30-mm CO_2 in a 10-cm cell. Spectral slit width about 0.25 cm^{-1}.

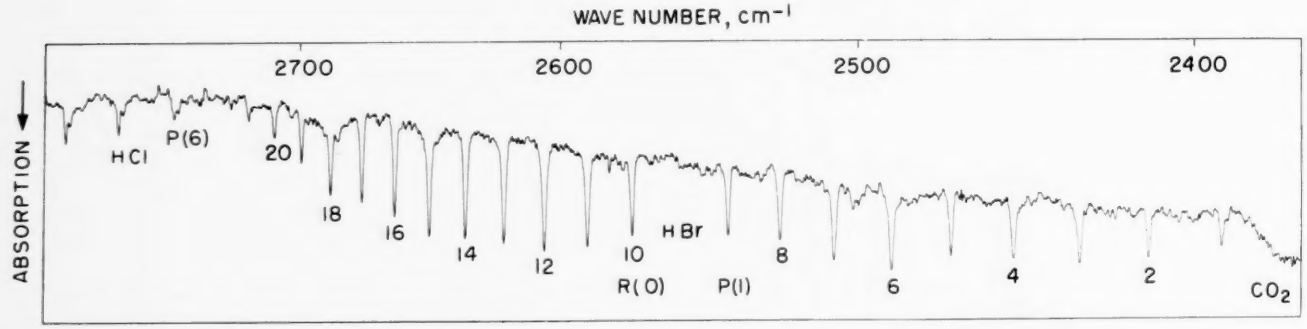

FIGURE 8–A. *Absorption band of* HBr *recorded in the second order of a 5,000 lines/in. grating with 40-cm pressure and 5-cm path.*
Spectral slit width about 0.8 cm^{-1}. The CO_2 band just appears at the low frequency end and the HCl band at the high frequency side. HCl was present in the HBr as an impurity.

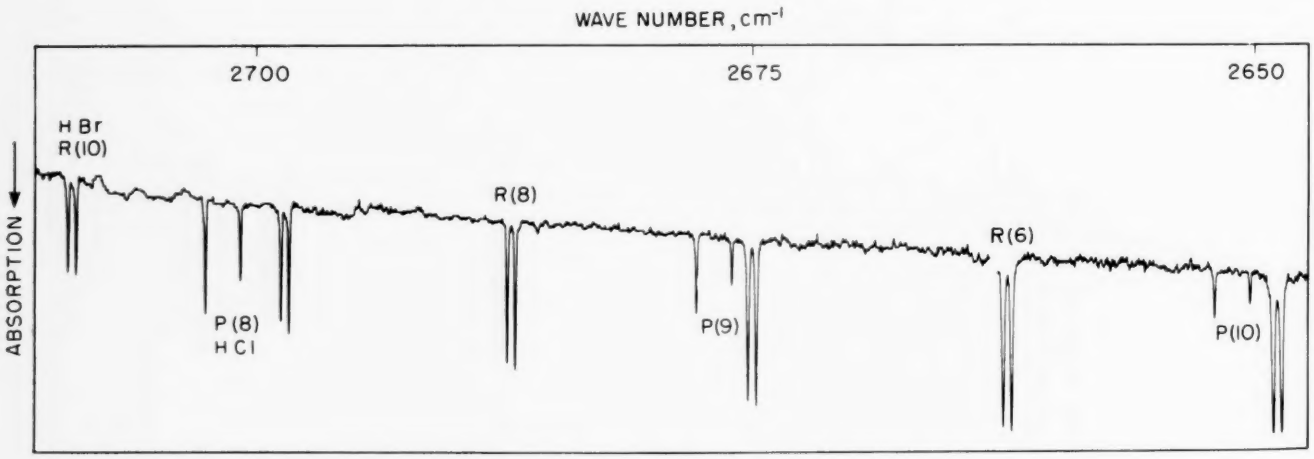

FIGURE 8–B. *A section of the* $HBr^{79, 81}$ *bands with* $HCl^{35, 37}$ *overlapping.*
Recorded with a 10,000 lines/in. grating singly passed with 2.5-mm pressure of each acid in a 6-m cell. Spectral slit width about 0.06 cm^{-1}.

TABLE 7-B. *Absorption lines of ν_3 fundamental of $C^{12}O_2^{16}$ from 2,280 cm^{-1} to 2,390 cm^{-1}*

Line number	This work ν cm^{-1} (vac.) observed	Previous work this laboratory [a] ν cm^{-1} (vac.) observed	Line number	This work ν cm^{-1} (vac.) observed	Previous work this laboratory [a] ν cm^{-1} (vac.) observed
P 68	2,282.21		*R* 48		2,379.80
66			50		80.74
64	86.93		52		81.65
62	89.23		54		82.51
60			56	2,383.39	83.38
58	93.81	2,293.81	58	84.22	84.21
56	96.03	96.03	60	85.01	85.01
54	98.30		62	85.80	85.79
52	2,300.50		64	86.55	86.55
50		2,302.70	66		87.26
48		04.84	68		87.97
46		06.96	70		88.64
			72		89.32
			74		89.91
R 30		2,370.36	76		90.49
32		71.48			
34		72.65	78		91.10
36		73.71	80		91.61
38		74.79	82		92.16
			84		
40		75.83	86		93.09
42		76.87			
44		77.88	88		93.55
46		78.86	90		93.96
Calculated values for lines near band center					
P 44		2,309.05	*R* 0		2,349.97
42		11.13	2		51.50
40		13.19	4		53.01
38		15.22	6		54.49
36		17.23	8		55.95
34		19.21	10		57.38
32		21.17	12		58.78
30		23.11	14		60.16
28		25.02	16		61.52
26		26.91	18		62.86
24		28.77	20		64.16
22		39.60	22		65.44
20		32.41	24		66.70
18		34.20	26		67.93
16		35.97	28		69.13
14		37.71			
12		39.43			
10		41.12			
8		42.78			
6		44.42			
4		46.04			
2		47.63			

[a] E. K. Plyler and L. R. Blaine, unpublished work.

observed and calculated values should be good to about ± 0.02-cm^{-1} absolute. Since the band consists of a collection of no less than four overlapped bands, results are subject to being extremely resolution sensitive and workers should not use lines exhibiting pronounced overlap. (The *R* branch is comparatively free of such difficulties.)

5.9. HBr Fundamental

As shown in figures 8–A and 8–B, this band was measured under considerably different resolution. With the conditions describing figure 8–A, there was no evidence to the effect that the components arising from HBr^{79} and HBr^{81} were being resolved out. This was done intentionally to see whether, when measured as a single peak, the frequency agreed with the average determined for each component under resolution approaching 0.05 cm^{-1}. The low resolution single-peak frequency agreed with the high resolution average value to within 0.05 cm^{-1} on the average (See table 8). This relatively good agreement does indicate that the high resolution results are correct in the absolute sense and that apart from greater inability to determine the center of the single

TABLE 8. *Absorption lines of* HBr^{79} *and* HBr^{81} *together with single unresolved peaks at lower resolution (2,390–2,750 cm^{-1})*

Serial number	This work high resolution isotopic components ν cm^{-1} (vac.) observed	High resolution average	This work low resolution single peak ν cm^{-1} (vac.) observed
1	Br^{81} 2,392.61	2,392.78	
	Br^{79} 92.94		
2	Br^{81} 2,412.73	2,412.89	2,412.93
	Br^{79} 13.06		
3	Br^{81} 32.43	32.60	32.65
	Br^{79} 32.77		
4	Br^{81} 51.73	51.91	51.94
	Br^{79} 52.08		
5	Br^{81} 70.61	70.79	70.82
	Br^{79} 70.97		
6	Br^{81} 89.08	89.26	89.30
	Br^{79} 89.43		
7	Br^{81} 2,507.11	2,507.30	2,507.24
	Br^{79} 07.48		
8	Br^{81} 24.71	24.90	24.83
	Br^{79} 25.08		
9	Br^{81} 41.87	42.06	41.99
	Br^{79} 42.25		
10	Br^{81} 74.80	74.99	74.98
	Br^{79} 75.19		
11	Br^{81} 90.56	90.76	90.67
	Br^{79} 90.95		
12	Br^{81} 2,605.82	2,606.02	2,605.95
	Br^{79} 06.22		
13	Br^{81} 20.63	20.83	20.81
	Br^{79} 21.03		
14	Br^{81} 34.92	35.13	35.03
	Br^{79} 35.33		
15	Br^{81} 48.71	48.92	48.85
	Br^{79} 49.13		
16	Br^{81} 61.99	62.19	62.13
	Br^{79} 62.39		
17	Br^{81} 74.76	74.97	
	Br^{79} 75.19		
18	Br^{81} 87.00	87.20	
	Br^{79} 87.41		
19	Br^{81} 98.68	98.90	
	Br^{79} 99.11		
20	Br^{81} 2,709.86	2,710.07	
	Br^{79} 10.29		
21	Br^{81} 20.48	20.68	
	Br^{79} 20.89		
22	Br^{81} 30.51	30.73	
	Br^{79} 30.95		
23	Br^{81} 40.02	40.24	
	Br^{79} 40.46		
24	Br^{81} 48.93	49.16	
	Br^{79} 49.39		

peak (near 1-cm^{-1} half-width), its frequency is given well enough by the component average. In table 8, the high resolution average of components is the recommended value for single peak use. Calculated values were also determined for the high resolution results and the values given in the first column of table 8 are believed to be accurate to within ±0.02-cm^{-1} absolute.

5.10. HCl Fundamental

The spectrum illustrated in figure 9 was recorded under low resolution and the entire band shown in this way for the sake of compression. Figure 8–B shows 3 lines of the band under high resolution. The band was measured on both instruments in this laboratory and results are compared with values reported by Mills, Thompson, and Williams [28] (see table 9). Molecular constants were obtained from the high resolution observations and calculated line frequencies agree well with the observed. In general, the high resolution results of this work fall between the low resolution values and those of Mills, Thompson, and Williams. The high resolution work does not, however, represent precision measurement, since the lines were measured at medium-fast scan in order to appropriately cover this extremely wide band in reasonable time. The observed values given in the table for the high resolution work are to be preferred and represent the best possible set. These values should be good to about ±0.02-cm^{-1} absolute. (Future precision measurements are contemplated for this band.)

5.11. Methane, ν_3 Band

The R branch of this band and some of the lower-J lines of the P branch are fairly suitable for providing calibration points in this region. However, care should be exercised to the extent of staying within the bounds of the resolution illustrated in figure 10.

TABLE 9. *Absorption lines of* HCl *from 2,650 to 3,050 cm^{-1}*

Serial number	This work high resolution ν cm^{-1} (vac.) observed	This work high resolution ν cm^{-1} (vac.) calculated	This work low resolution ν cm^{-1} (vac.) observed	M., T., and W.[a] ν cm^{-1} (vac.) observed
		HCl^{35}		
0	2,651.98	2,651.98		.94
1	77.74	.75	.86	.77
2	2,703.02	2,703.02	.03	2.95
3	27.79	.79	.76	.75
4	52.05	.05	.15	.01
5	75.77	.77	.85	.77
6	98.95	.95	.96	9.00
7	2,821.58	2,821.57	.56	.59
8	43.63	.63	.60	.63
9	65.10	.10	.14	.14
10	2,906.25	2,906.25	.24	.25
11	25.91	.90	.89	.92
12	44.92	.92		.99
13	63.30	.30	.20	.35
14	81.02	.02		.05
15	98.07	.07		.05
16	3,014.44	3,014.44		.50
17	30.10	.11	.12	.12
18	45.07	.08	.02	.15
		HCl^{37}		
0	2,650.23	2,650.24		.17
1	75.96	.96		.98
2	2,701.20	2,701.19	.28	.15
3	25.93	.93	.95	.90
4	50.14	.14		.13
5	73.84	.83	.89	.82
6	96.98	.98		7.01
7	2,819.57	2,819.57		.56
8	41.59	.59		.56
9	63.02	.03		.06
10	2,904.12	2,904.12	.14	.07
11	23.74	.74	.79	.74
12	42.74	.73	.66	.79
13	61.08	.08	.06	.13
14	78.77	.77		.80
15	95.79	.79		.78
16	3,012.15	3,012.14	.14	.23
17	27.80	.79	.72	.84
18	42.74	.74	.68	.80

[a] Mills, Thompson and Williams[28].

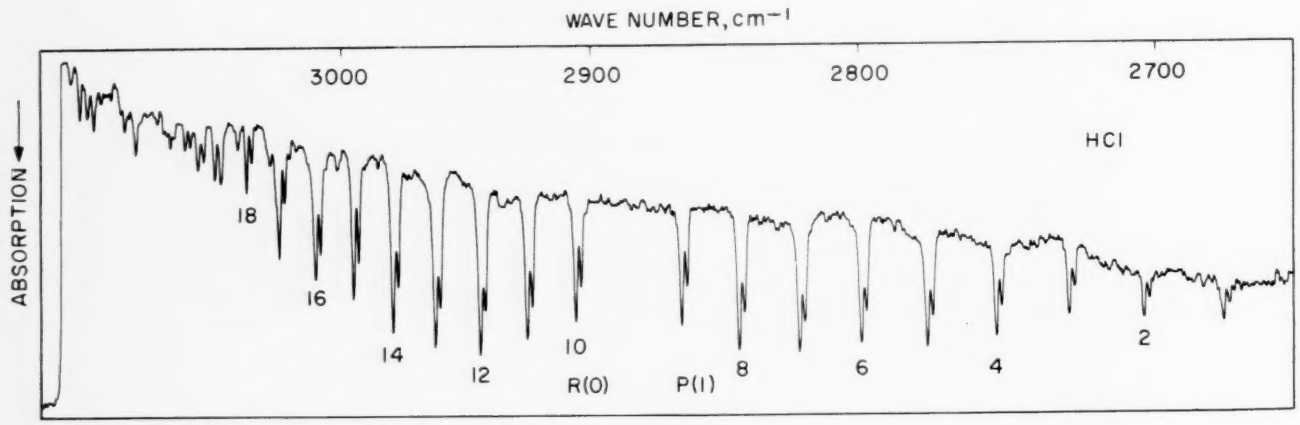

FIGURE 9. *Absorption band of* HCl *recorded in the second order of a 5,000 lines/in. grating with 20-cm pressure and 5-cm path.*
Spectral slit width about 1.0 cm^{-1}. Weak atmospheric water lines of the $2\nu_2$ band begin to appear at the high frequency end.

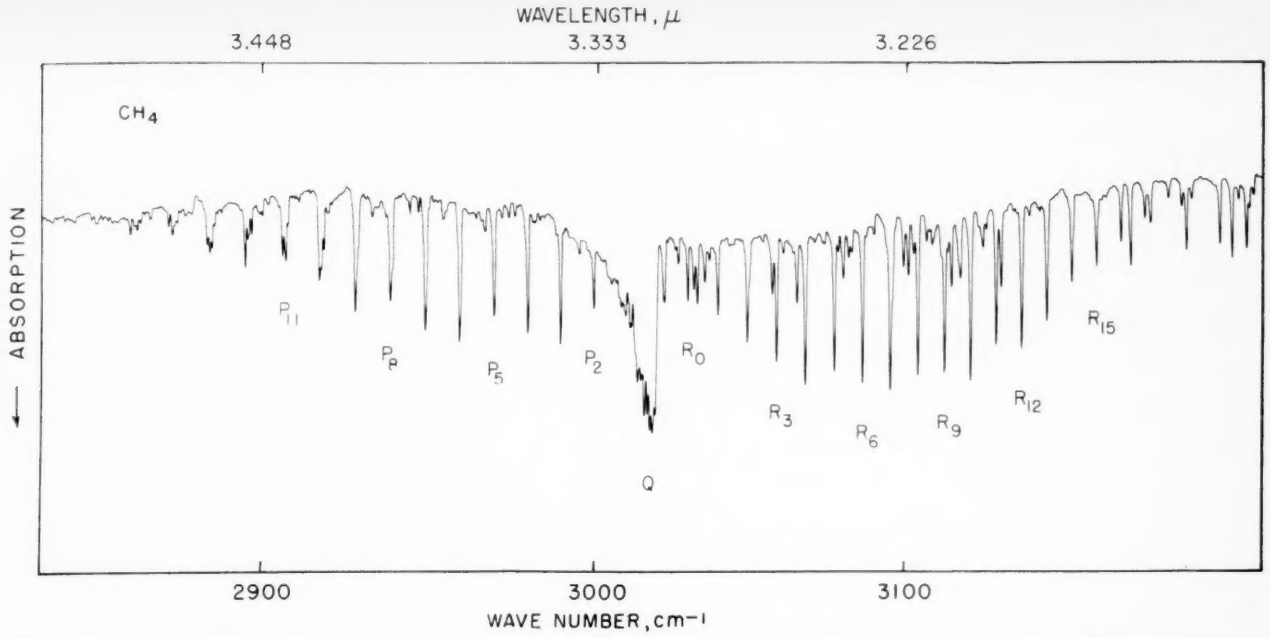

FIGURE 10. *The ν_2 fundamental of methane recorded with a 7,500 lines/in. grating with 10-cm pressure and 5-cm path.*
Spectral slit width about 0.9 cm^{-1}, certain weak lines occurring between methane lines are part of the $2\nu_2$ band of atmospheric water vapor.

Under higher resolution the lines begin to break up, P 4, for example, shows four components within 0.37 cm^{-1} and frequency allocation becomes difficult. The values are listed in table 10 and strongest components should be used where indicated.

5.12. Acetylene Bands Near 3,300 cm^{-1}

The spectrogram of figure 11 gives a rather interesting comparison of lines and peaks under considerably differing resolution. The scale on the lower panel, though close to that of the upper one differs somewhat and is indicated by the tie lines. The values listed in table 11 indicate the rather remarkable feature that even under considerably lower resolution single or symmetrical lines can still be accurately measured. The high resolution measurements were made with fringes and the grating circle was used for the lower resolution measurements. In two cases (lines 6 and 7; 20 and 21), two closely spaced and nearly equal intensity components were measured as a single peak and this value compared with the average of the two components. As in the case of HBr, the agreement is quite satisfactory. The results of this work are compared with values reported by Christensen, Eaton, Green, and Thompson (see ref. [23]).

TABLE 10. *Absorption lines of methane from 2,900 to 3,170 cm^{-1}*

Line number	Plyler, Blaine, and Nowak [a] ν cm^{-1} (vac.) observed	Line number	Plyler, Blaine, and Nowak [a] ν cm^{-1} (vac.) observed
P 12	[b] 2,895.18	R 0	3,028.84
11	[b] 2,906.72	1	38.58
10	[b] 16.36	2	48.25
9	26.86	3	57.79
8	37.34	4	67.30
7	47.92	5	76.74
6	58.20	6	86.02
5	68.67	7	95.22
4	79.00	8	3,104.36
3	88.27	9	13.42
2	99.10	10	22.46
		11	31.39
		12	40.20
		13	48.95
		14	57.61
		15	66.20

[a] Plyler, Blaine, and Nowak [11].
[b] Frequency of strongest component.

5.13. Water and Carbon Dioxide Bands Near 3,700 cm^{-1}

The spectrogram (fig. 12–A), illustrating the atmospheric absorption in this region, was recorded with the low resolution instrument so that results would approximate those attainable with small grating intruments. The indicated lines were measured under these conditions and in table 12–A the results are compared with the high resolution and high precision work of Plyler and Tidwell [29]. The agreement is satisfactory and indicates that even with lower resolution, good measurements in the order of 1 part in 100,000 can still be made. The higher resolution numbers are the recommended ones and if more frequent calibrating points are required, workers should make use of reference [29].

528863—60——4

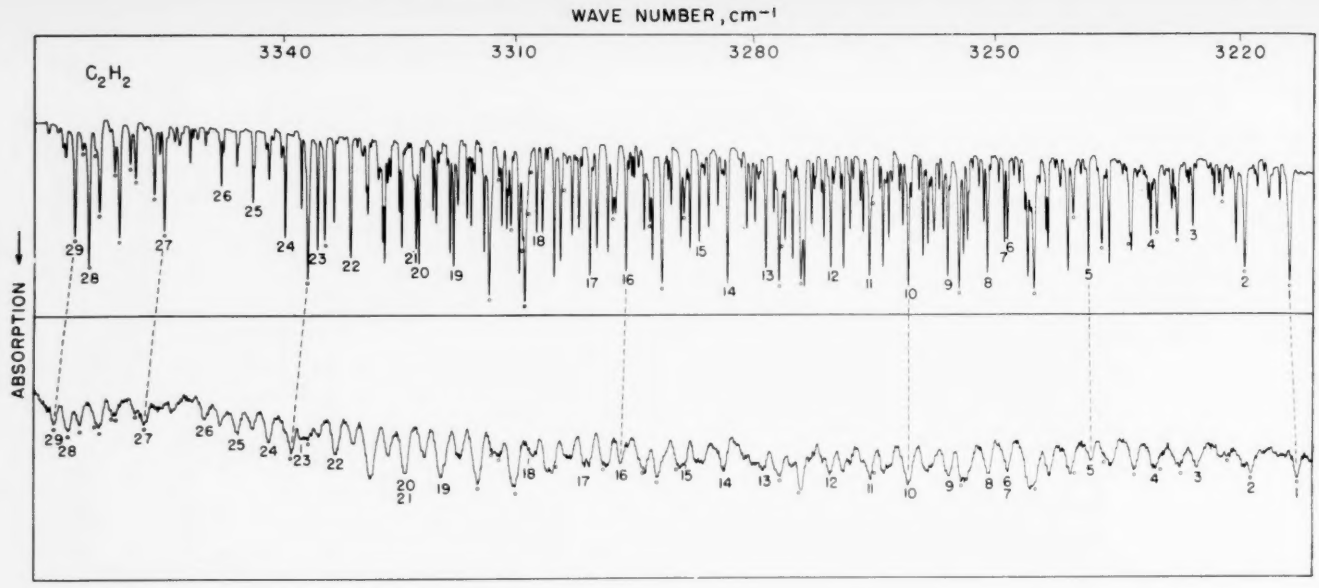

FIGURE 11. *The two absorption bands of acetylene near 3,300 cm⁻¹ compared under high and lower resolution.*

The upper spectrogram was recorded with a 10,000 lines/in. grating singly passed with 1.5-cm pressure and 5-cm path. The lower spectrogram was recorded in the second order of a 5,000 lines/in. grating with 4-cm pressure and 5-cm path. Spectral slit widths about 0.10 and 0.8 cm⁻¹, respectively. Atmospheric water lines of the $2\nu_2$ band are denoted by open circles.

TABLE 11. *Absorption bands of acetylene (2 bands) from 3,200 to 3,380 cm⁻¹*

Serial number	This work medium-high resolution ν cm⁻¹ (vac.) observed		This work low resolution ν cm⁻¹ (vac.) observed		C., E., G., and T.[b] medium resolution ν cm⁻¹ (vac.) observed	
2	3,219.42	(H_2O)				
3	25.63				.64	
4	30.72				.72	
5	38.31		.44		.29	
6	48.19	[a]48.38	48.41		.34	[a]48.40
7	48.56				.47	
8	50.71		.82	(slightly blended)	.65	
9	55.59				.56	
10	60.46		.60	(slightly blended)	.40	
11	65.29		.32		.26	
12	70.10				.04	
13	78.22				.20	
14	83.04		.14		2.93	
15	86.63				.48	
16	95.88		.80		.83	
17	3,300.46				.35	
18	07.27				.14	
19	17.92				.99	
20	22.41	[a]22.59	22.62		22.44	
21	22.77					
22	31.29		.31		.18	
23	35.59				.49	
24	39.83		.98		.72	
25	44.08		.01	(slightly blended)	3.93	
26	48.23		.21		.08	
27	55.74	(H_2O)				
28	65.78	(H_2O)	.86			
29	67.67	(H_2O)				

[a] Average of two components of nearly equal intensity.
[b] Christensen, Eaton, Green, and Thompson [23].

5.14. CO_2, 021, and 101 Bands

Plyler and Tidwell (see ref. [29]) report the precise measurement of many of these lines. Certain others, which could not be measured due to overlapping water lines, are not listed in table 12–B. Most of these lines are good to about ± 0.02 cm⁻¹. The two bands are illustrated in figure 12–B as recorded with a nitrogen-purged small grating instrument with CO_2 in a cell. (The spectrogram was recorded by Dr. Norman Jones, National Research Council, Ottawa, Canada.)

5.15. C_2H_2, $\nu_1+\nu_5$ Band

From the end of the P branch of the CO harmonic to the beginning of the μ_3 water vapor band there is a gap of about 100 cm⁻¹. There is a band of acetylene of medium intensity that falls in this region (4,039 to 4,130 cm⁻¹). This band is overlapped by four weaker bands and when measured with low pressure and high resolution many lines are observed [30]. When a pressure of 1 atm. is used in a 10-cm cell, the smaller bands are not observed and the P and R branches of the band stand out clearly. A number of the strong lines were measured under both high and low pressures and the values agreed closely. The numbers listed in table 13 are the results of the low pressure measurements. The spectrum is shown in figure 13.

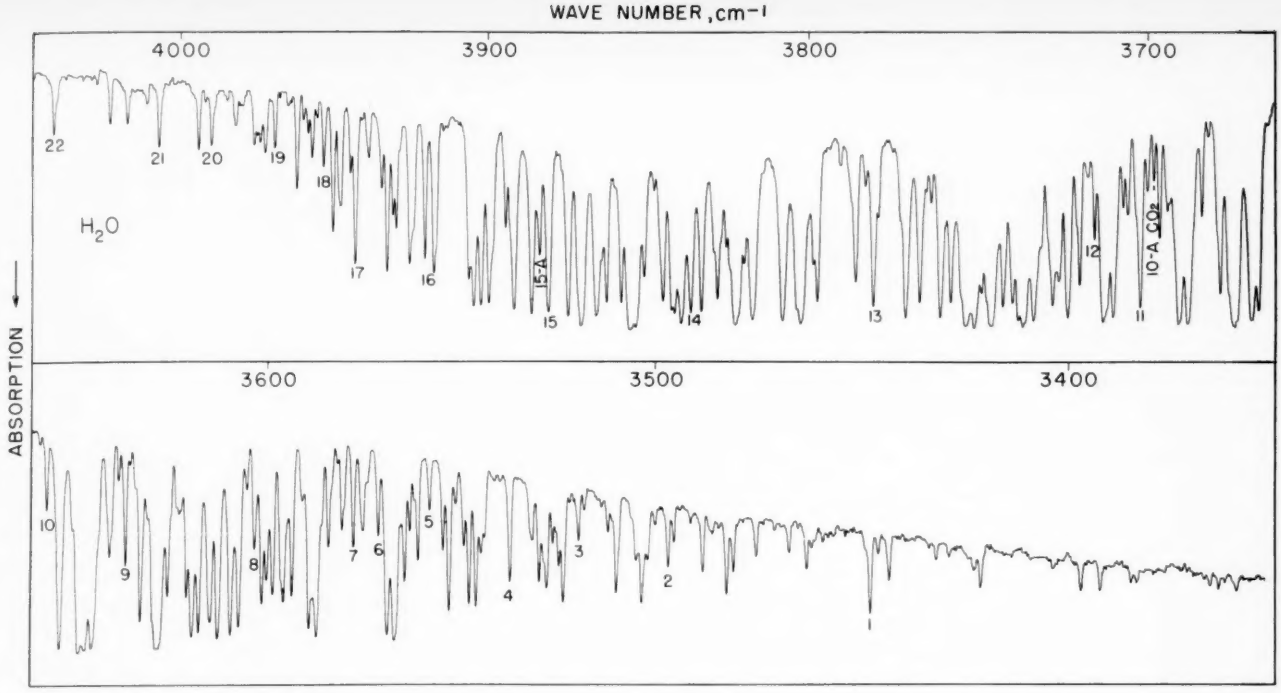

FIGURE 12–A. *Atmospheric absorption bands of H_2O and CO_2 in the 3,700-cm^{-1} region recorded under intermediate resolution in the second order of a 5,000 lines/in. grating.*

The path was 7 m with 48 percent humidity at 23° C. Spectral slit width about 0.7 cm^{-1}.

TABLE 12–A. *Absorption lines of water from 3,400 to 4,000 cm^{-1}*

Line serial number	High resolution Plyler and Tidwell [a] ν cm^{-1} (vac.) observed	Intermediate resolution this work ν cm^{-1} (vac.) observed
	3,397.20	
1	3,447.20 (7.03)	3,447.21
2	96.63	96.62
3	3,518.97	3,519.05
4	(2 components)	36.44 avg
5	----------	57.21
6	70.54	70.48
7	76.89	----------
	77.06 avg	77.02 avg
	77.23	
(8)	3,603.08	3,602.98 (complex)
9	----------	38.15
10	59.94	59.94
10–A(CO_2)	98.00	98.08
11	----------	3,701.90
12	3,714.81	3,714.82
13	----------	79.38
14	----------	3,835.06
15	----------	80.52
15–A	3,883.26	83.32
16	3,920.10	3,920.28
17	----------	42.86
18	53.11	53.22
19	69.15	69.16
20	90.72	90.74
21	4,008.59	4,008.59
22	44.90	----------

[a] Plyler and Tidwell [29].

TABLE 12–B. *Some precisely measured CO_2 lines of the 021 and 101 bands at 3,609 and 3,716 cm^{-1}*

Line number	Plyler and Tidwell [a] ν cm^{-1} (vac.) observed	Line number	Plyler and Tidwell [a] ν cm^{-1} (vac.) observed
	021 Band		
P 38	3,579.34	R 2	(3,615.25)
36	81.31	10	(21.17)
32	85.21	12	22.50
26	90.78	14	23.93
24	92.65	16	25.27
22	94.42	26	31.85
20	(96.22)	40	40.00
16	99.74		
14	3,601.40		
10	04.81		
8	06.48		
6	08.07		
	101 Band		
P 36	3,682.78	R 6	3,720.09
32	86.74	10	22.90
26	92.46	12	24.35
24	94.34	14	(25.72)
20	98.00	18	28.42
18	99.79	20	29.73
14	3,703.29	22	31.01
12	05.02	26	33.48
10	06.70		
8	08.38		

[a] Plyler and Tidwell [29].

Values in parentheses indicate lines which may be overlapped by water lines.

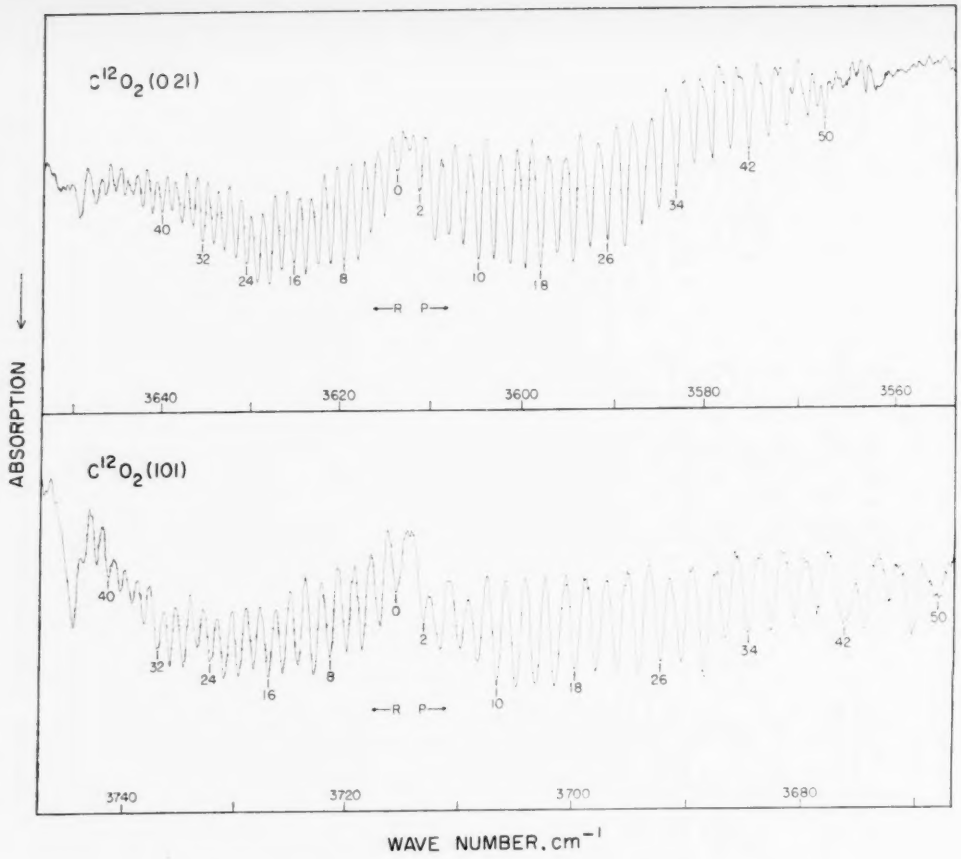

FIGURE 12–B. *The 021 and 101 bands of CO_2 recorded with a purged small grating instrument.*
The CO_2 was contained in a 10-cm cell at 25-cm pressure for both bands. Spectral slit width about 0.30 cm^{-1}.

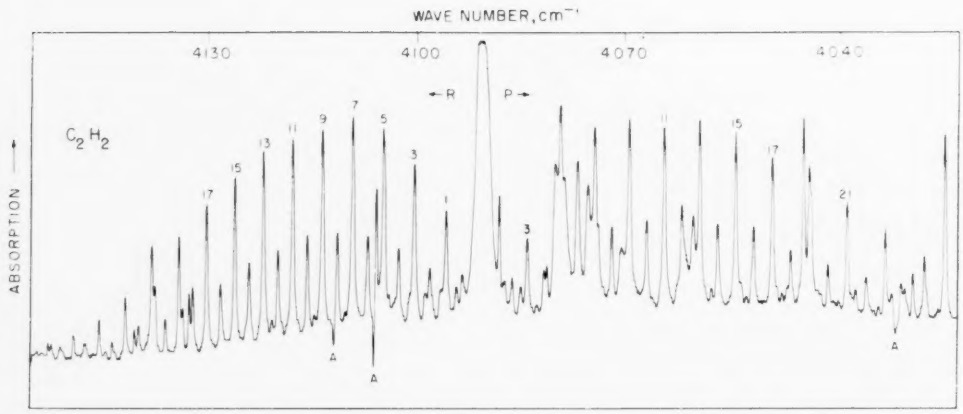

FIGURE 13. *The $\nu_1 + \nu_5$ band of acetylene recorded with a 15,000 lines/in. grating singly passed with 1-atm pressure and 10-cm path.*
Spectral slit width about 0.08 cm^{-1}.

TABLE 13. *Absorption lines of acetylene from 4,040 to 4,130 cm⁻¹*

Line number	Previous work this laboratory ν cm⁻¹ (vac.) observed	Line number	Previous work this laboratory ν cm⁻¹ (vac.) observed
P 3	4,084.14	*R* 17	4,130.10
11	64.58	15	26.91
15	54.52	13	22.63
17	49.36	11	18.30
21	38.95	9	13.94
		7	09.47
		5	04.98
		3	4,100.47
		1	4,095.84

5.16. CO Harmonic Band

The CO harmonic band at 2.34 μ has been measured very accurately by Rank and his colleagues (see ref. [14]) and also by Plyler, Allen, and Tidwell (see ref. [15]). This band is one of the few which have been measured in the infrared to such a precision that the reported frequencies are accurate to a few thousandths of a cm⁻¹. This spectrum was measured with a 60-cm cell and 20-cm pressure, but a 10-cm cell with 50-cm pressure is sufficient for observing forty lines of this band. The spectrum is shown in figure 14 and the frequencies are listed in table 14.

TABLE 14. *Absorption lines of the 2–0 harmonic band of* CO *from 4,100 to 4,340 cm⁻¹*

Line number	Plyler, Allen, and Tidwell [a] ν cm⁻¹ (vac.) observed	Rank et al.[b] ν cm⁻¹ (vac.) observed	Line number	Plyler, Allen, and Tidwell [a] ν cm⁻¹ (vac.) observed	Rank et al.[b] ν cm⁻¹ (vac.) observed
P 27	4,132.19	----------	*R* 0	4,263.842	.838
26	37.79	.770	1	67.548	.542
25	43.33	----------	2	71.182	.179
24	48.817	----------	3	74.750	.743
23	54.234	----------	4	78.235	.234
22	59.564	----------	5	81.655	.661
21	64.852	----------	6	85.013	.010
20	70.066	.058	7	88.298	.290
19	75.212	.204	8	91.512	.500
18	80.286	.285	9	94.639	----------
17	85.302	.298	10	97.703	----------
16	90.234	.242	11	4,300.712	----------
15	95.120	----------	12	03.614	----------
14	99.931	----------	13	06.482	----------
13	4,204.673	----------	14	09.262	.257
12	09.356	----------	15	11.969	962
11	13.962	----------	16	14.606	.597
10	18.504	----------	17	17.173	.161
9	22.974	954	18	19.665	.650
8	27.371	----------	19	22.085	.065
7	31.694	.685	20	24.425	----------
6	35.952	.949	21	26.699	----------
5	40.150	----------	22	28.878	----------
4	44.278	.267	23	31.022	----------
3	48.330	----------	24	33.057	.054
2	52.308	.307	25	----------	4,335.030
1	56.226	----------	26	----------	36.934
			27	----------	38.763
			28	----------	40.517
			29	----------	42.202

[a] Plyler, Allen, and Tidwell [15].
[b] Rank et al. [14].

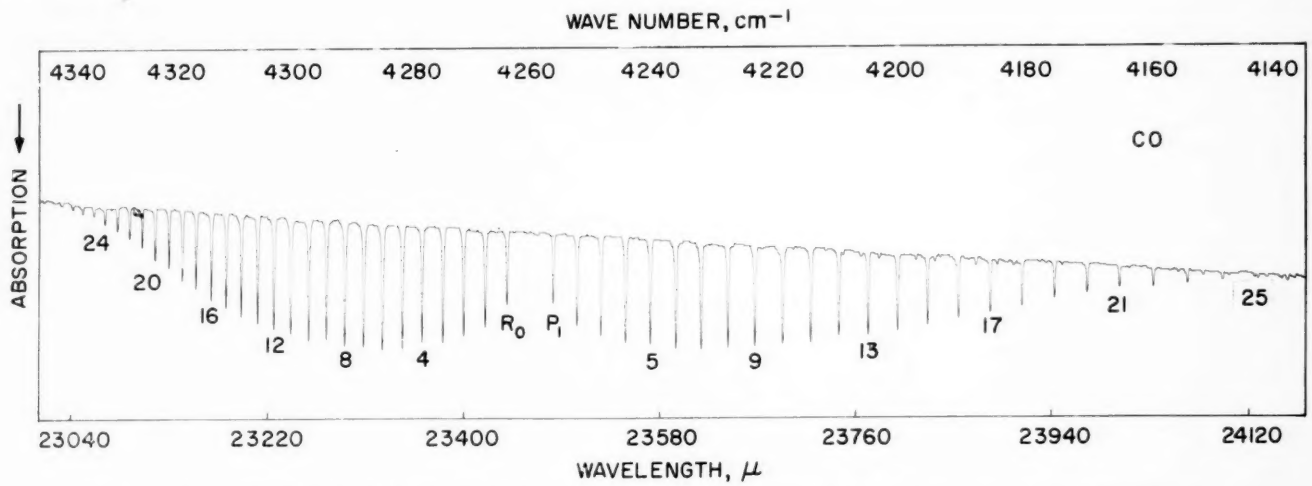

FIGURE 14. *The 2–0 band of* CO *recorded with a 15,000 lines/in. grating with 20-cm pressure and 60-cm path.*
Spectral slit width about 0.15 cm⁻¹.

5.17. N_2O, $2\nu_1$ Band and Hot Band

The $2\nu_1$ band of N_2O has been measured in the region from 2,520 to 2,580 cm⁻¹ and the results are shown in figure 15 and table 15. Thompson and Williams [31] had previously measured this band and their values are used to compare with the results obtained in this work. The lines which have been measured are noted by a dot on the spectrogram. There is an overlapping structure of weak lines and only those lines were measured which appeared in the open. This band can be resolved by a small grating instrument if a photoconducting cell is used as the detector and could be used as an alternate for HBr in this region. Also there are several regions where lines are closely grouped and the band can be used to check instrumental performance and resolution. The measurements of Thompson and Williams agree, on the average, to within ± 0.04 cm⁻¹ of the

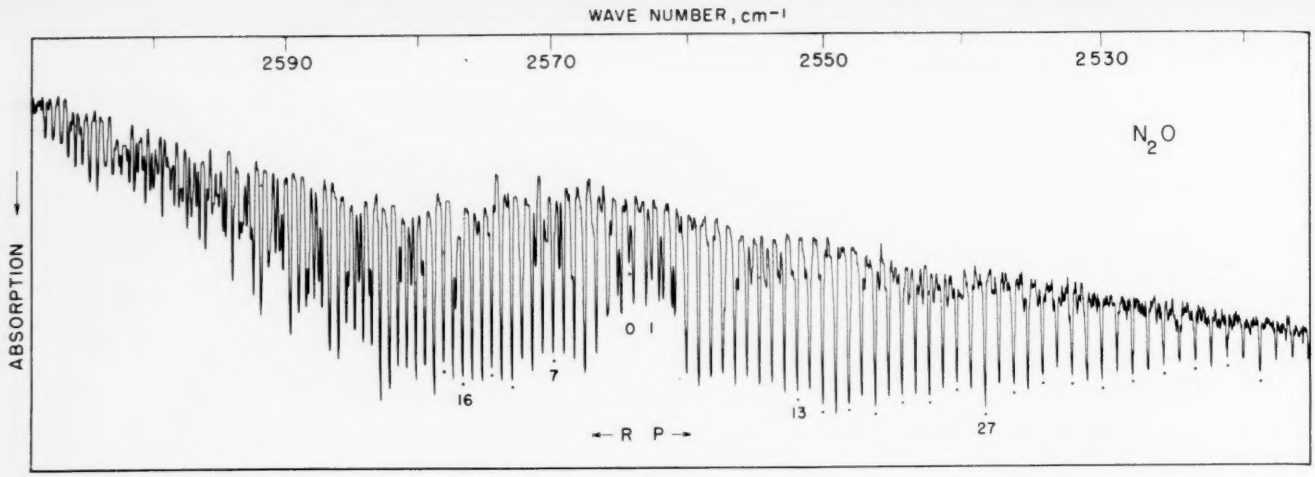

FIGURE 15. *The $2\nu_1$ band (2564 cm^{-1}) of N_2O together with the hot band ($2\nu_1+\nu_2-\nu_2$, 2577 cm^{-1}) recorded with a 10,000 lines/in. grating with 2-mm pressure and 6-m path.*

Spectral slit width about 0.08 cm^{-1}. The dots denote the measured and tabulated lines.

TABLE 15. *Absorption lines of N_2O from 2,520 to 2,580 cm^{-1}*

J	This work ν cm^{-1} (vac.) observed	Thompson and Williams [a] ν cm^{-1} (vac.) obs. laboratory
P 45	2,519.01	.05
43	21.27	.29
41	23.50	.52
39	25.71	.72
37	27.87	.88
35	30.03	.03
33	32.15	.17
31	34.25	.27
29	36.31	.35
27	38.37	.41
25	40.38	.42
23	42.38	.42
21	44.34	.38
19	46.27	.32
17	48.19	.23
15	50.07	.13
13	51.92	2.01 (1.97 calc.)
R 0	2,564.18	.24
7	69.82	.86
11	72.87	.94
13	74.38	.45
16	76.56	.59
18	77.99	8.04

[a] Thompson and Williams [31].

values in this work. There is a small shift in the direction of lower frequency of all the values of the present measurements. An average of the two sets of values would probably be correct to ± 0.03 cm^{-1}, which should be entirely adequate for calibrating medium resolution instruments.

5.18. NH_3, ν_4 Fundamental

This band is being included as an alternate to the 6-μ water band and should prove of some use to workers who wish to flush their instruments or use double-beam operation to study samples contained in cells. Dr. W. S. Benedict, of the Johns Hopkins University, has picked out of the band (in accordance with the resolution illustrated in fig. 16) some 19 single or not-too-complex absorption peaks and has determined the best possible frequencies from the higher resolution results of Garing and Nielsen (see ref. [24]) and unpublished results from the National Bureau of Standards Laboratory. The results of these two works agree to within about ± 0.02 cm^{-1}. The frequency assigned to certain absorption peaks which appear single in figure 16 but which actually consist of several components is, of course, no longer applicable if the peak is broken up into its components under slightly higher resolution. (The letter S in figure 16 indicates a single line.) No table accompanies this spectrogram but instead the acceptable values which are probably good to ± 0.02 cm^{-1} for single lines and off by as much as ± 0.2 cm^{-1} for some complex lines, have been printed on the illustration. For calibration purposes, the μ_2 water lines (see table 5) are considerably better than the lines of this band. (The spectrogram was recorded by Dr. Norman Jones, National Research Council, Ottawa, Canada.)

6. Polystyrene Film

In 1950 Plyler and Peters (see ref. [7]) measured the infrared absorption spectrum of polystyrene on a grating instrument and certain bands were suggested for use in calibrating prism instruments. Since that time, films of polystyrene have been widely used in many laboratories and it has been found very useful in checking the calibration of an instrument in certain regions to ascertain if there are any changes in the reading of the wavelength or frequency scale of the instrument. There is a question as to the suitability of polystyrene for a calibrating material as it is not completely stable and has a different absorption spectrum when it

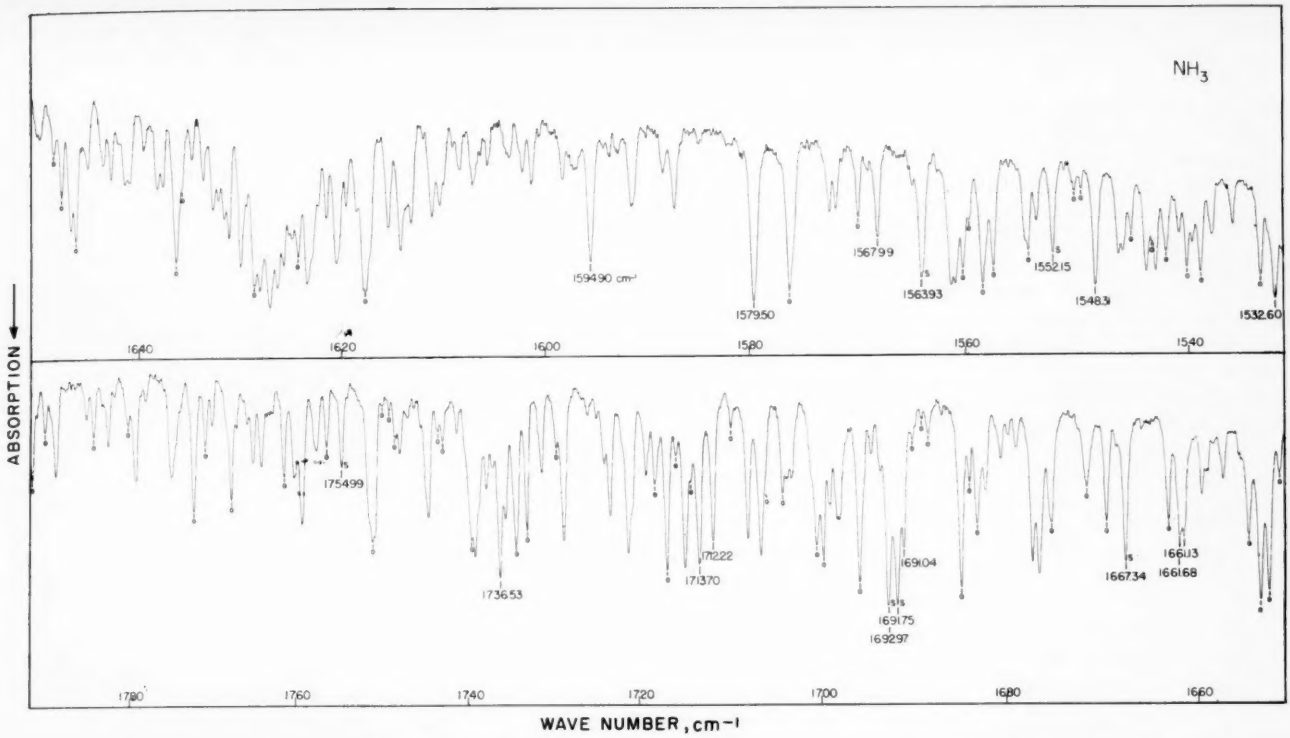

FIGURE 16. *The ν_4 band of NH_3 at 1628 cm^{-1} recorded with a nitrogen-purged small grating instrument.*
Certain strong lines of the ν_2 water band still appear. A gas pressure of 7.5 cm in a 10-cm cell was used. Spectral slit width about 0.50 cm^{-1}.

ages. Also different batches of the material may show differences in absorption. The variation in the absorption spectrum of different films can easily be demonstrated, but the strong bands are not appreciably changed in wavelength by age or the origin of the film. In this work, we checked a film which had been made ten years ago and it showed no appreciable shifts in the absorption bands. Eight bands from 6 to 14.4 μ have been remeasured and the results are compared with the previous measurements of 1950 and the additional measurements of Plyler, Blaine, and Nowak (see ref. [11]) in 1957. The spectrum is shown in figure 17 and the wavelengths and wave numbers in vacuum are listed in table 16. When the faces of the film are parallel, interference fringes appear but these usually occur

TABLE 16. *Polystyrene absorption bands*

Previous measurement wavelength (air) μ	New measurement this work wavelength (air)	This work cm^{-1} (vac.)
3.3026		
3.422		
3.507		
5.138		
5.343		
5.549		
6.238	6.2427	1,601.4$_s$
	6.3151	1,583.0$_s$
6.692		
	8.4615	1,181.5$_o$
8.662	8.6626	1,154.0$_s$
	9.3524	1,068.9$_s$
9.724	9.7226	1,028.2$_s$
11.035	11.028	906.5$_o$
	14.316	698.3$_s$

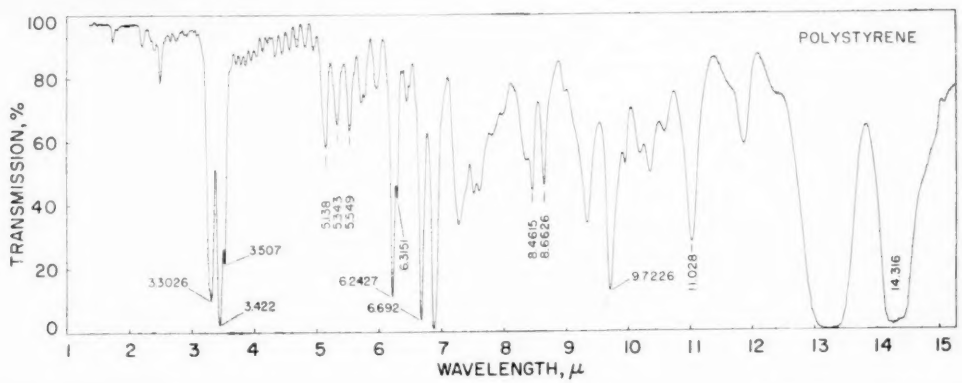

FIGURE 17. *Infrared absorption spectrum, from 2 to 15 μ, of a 50-μ film of polystyrene recorded with a rock-salt prism instrument.*

between 4 and 6 μ for a 50-μ film and do not change the position of the bands beyond 6 μ. The small band at 6.3151 μ, which is on the long wavelength side of the strong band at 6.24 μ, is completely resolved by a low resolution grating instrument and is not overlapped by atmospheric water lines. It should be useful for calibration in this region. The strong band at 14.316 μ was measured with a film of 8-μ thickness and with this film the maximum of absorption could be accurately determined. It is estimated that the bands listed in table 16 are accurate to $\pm 0.3 cm^{-1}$ and should be useful in calibrating low resolution instruments, but should not be considered as being of the same order of accuracy as the molecular vapor bands. In measuring the polystyrene bands, the center was determined near the ¾-absorption point for symmetrical bands and reference should be made to this point when making use of the numbers in table 16.

7. Summary

The rather "popular" ammonia band at 3 μ was not used in this work because of its resolution sensitiveness and also because of temperature and pressure effects. For example, there are 12 components in the P 8 "line" extending over 1.5 cm^{-1}. Under low resolution (see ref. [11]) the Q branch, which extends over 5.5 cm^{-1} and consists of hundreds of lines is probably good to 0.5 cm^{-1}.

The 16-μ coverage may be appropriately extended by making use of frequency values reported by Lakshmi, Rao, and Nielsen [32] for N_2O. In this work, we have checked Rao's measurements on the 15-μ CO_2 band and feel that if the same techniques were used on the N_2O measurements, then these numbers may be used. Considering the lower resolution used by the Japanese workers (see ref. [12]) on this band, the agreement with values reported in [32] above is quite good.

At the high frequency end, we have already given reference to the work of Rank and coworkers on HCN (see ref. [16]) and wish to include also the grating work on H_2O vapor at 1.9 μ and on CH_4 at 2.2 μ as given in reference [8].

The calibrating values given in this report should make it easier for infrared spectroscopists to obtain accurate measurements in the region from 2 to 16 μ. As further measurements are carried out in other laboratories, there will be more values for intercomparison and it should be possible to obtain calculated values for certain bands which would be more accurate than the observed values from any one laboratory. No recommended frequencies representing properly weighted averages of the work of several laboratories have been given, but this may be done at a later date when more data are available. It is hoped that spectroscopists will send new data of this type to the authors for wavelength standards so that it may be incorporated in a future report. It is also requested that any corrections or suggested changes be communicated to the authors.

8. References

[1] R. C. Lord and T. K. McCubbin, Jr., J. Opt. Soc. Am. **45,** 441 (1955).
[2] R. C. Lord and T. K. McCubbin, Jr., J. Opt. Soc. Am. **47,** 689 (1957).
[3] E. K. Plyler and N. Acquista, J. Research NBS **56,** 149 (1956) RP2660.
[4] E. K. Plyler and L. R. Blaine, J. Research NBS **60,** 55 (1958) RP2821.
[5] R. A. Oetjen, Chao-Lou Kao, and H. M. Randall, Rev. Sci. Instr. **13,** 515 (1942).
[6] D. S. McKinney and R. A. Friedel, J. Opt. Soc. Am. **38,** 222 (1948).
[7] E. K. Plyler and C. W. Peters, J. Research NBS **45,** 462 (1950) RP2159.
[8] E. K. Plyler, N. M. Gailar, and T. A. Wiggins, J. Research NBS **48,** 221 (1952) RP2309.
[9] N. Acquista and E. K. Plyler, J. Research NBS **49,** 13 (1952) RP2338.
[10] A. R. Downie, M. C. Magoon, T. Purcell, and B. Crawford, J. Opt. Soc. Am. **43,** 941 (1953).
[11] E. K. Plyler, L. R. Blaine, and M. Nowak, J. Research NBS **58,** 195 (1957) RP2752.
[12] S. Mizushima and colleagues, Tokyo University, Hongo, Tokyo, Japan. A report on the Perkin-Elmer grating spectrophotometer model 112–G. English translation by Perkin-Elmer Corp., Norwalk, Conn.
[13] E. K. Plyler, L. R. Blaine and W. S. Connor, J. Opt. Soc. Am. **45,** 102 (1955).
[14] D. H. Rank, A. H. Guenther, G. D. Saksena, J. N. Shearer and T. A. Wiggins, J. Opt. Soc. Am. **47,** 686 (1957).
[15] E. K. Plyler, H. C. Allen, Jr., and E. D. Tidwell, J. Research NBS **61,** 53 (1958) RP2883.
[16] D. H. Rank, A. H. Guenther, J. N. Shearer, and T. A. Wiggins, J. Opt. Soc. Am. **47,** 148 (1957).
[17] E. K. Plyler, L. R. Blaine, and E. D. Tidwell, J. Research NBS **55,** 279 (1955) RP2630.
[18] This extremely precise circle was ruled and calibrated by Mr. Benjamin Page of this Bureau.
[19] E. K. Plyler and L. R. Blaine, J. Research NBS **62,** 7 (1959) RP2922.
[20] R. Penndorf, J. Opt. Soc. Am. **47,** 176 (1957).
[21–A] K. Rossman, K. N. Rao, and H. H. Nielsen, J. Chem. Phys. **24,** 103 (1956).
[21–B] K. Rossman, W. L. France, K. N. Rao, and H. H. Nielsen, J. Chem. Phys. **24,** 1007 (1956).
[22] K. N. Rao, L. R. Ryan, and H. H. Nielsen, J. Opt. Soc. Am. **49,** 216 (1959).
[23] M. T. Christensen, D. R. Eaton, B. A. Green, and H. W. Thompson, Proc. Roy. Soc. **238,** 15 (1956).
[24] J. S. Garing, Dissertation Abstracts **18,** 839 (1958) Ann Arbor, Mich. (Abstracts of some U.S. theses issued commercially. This work may appear in a future issue of J. Mol. Spectroscopy.)
[25] F. W. Dalby and H. H. Nielsen, J. Chem. Phys. **25,** 934 (1956).
[26] E. K. Plyler, L. R. Blaine, and E. D. Tidwell, J. Research NBS **55,** 183 (1955) RP2617.
[27] C. P. Courtoy, Canad. J. Phys. **35,** 608 (1957).
[28] I. M. Mills, H. W. Thompson, and R. L. Williams, Proc. Roy. Soc. **218,** 29 (1953).
[29] E. K. Plyler and E. D. Tidwell, Extrait des Memories in 8 de la Societe Royale des Sciences de Liege Quatrieme Serie Tome XVIII, 426 (1956).
[30] H. C. Allen, Jr., E. D. Tidwell, and E. K. Plyler, J. Research NBS **57,** 213 (1956) RP2711.
[31] H. W. Thompson and R. L. Williams, Proc, Roy. Soc. **220,** 435 (1953).
[32] K. Lakshmi, K. N. Rao, and H. H. Nielsen, J. Chem. Phys. **24,** 811 (1956).
[33] H. M. Mould, W. C. Price, and G. R. Wilkinson, Spectrochim. Acta, In press (June 1959).

Washington, D.C. (Paper 64A1–27)

JOURNAL OF RESEARCH of the National Bureau of Standards—A. Physics and Chemistry
Vol. 64A, No. 1, January–February 1960

Combustion Calorimetry with Fluorine: Constant Pressure Flame Calorimetry [1]

G. T. Armstrong and R. S. Jessup

(September 25, 1959)

Instruments and methods have been developed and are described for the measurement of heats of reaction between fluorine and other gaseous materials. Verification of the amount of reaction of hydrogenous materials is possible. The estimated accuracy of measurements is about 0.3 percent. Lack of certainty of the magnitude of corrections to be applied for hydrogen fluoride nonideality is an important factor. The heat of formation of hydrogen fluoride is found to be -64.4 ± 0.25 kcal/mole on the basis of the reaction of fluorine with ammonia.

1. Introduction

For the determination of the heat of formation of a compound from its elements, the study of suitable reactions involving directly each of the individual elements is essential. In some cases the heat of formation of a given substance may be obtained by measuring the heat of a single reaction, for example,

$$C(c, \text{graphite}) + O_2(g) \rightarrow CO_2(g).$$

In general, however, it is necessary to combine the heats of several reactions, as for example

$$CO(g) + \tfrac{1}{2}O_2(g) \rightarrow CO_2(g)$$

$$\frac{C(c, \text{graphite}) + O_2(g) \rightarrow CO_2(g)}{C(c, \text{graphite}) + \tfrac{1}{2}O_2(g) \rightarrow CO(g)}.$$

Since the measured heat of each reaction used in calculating the heat of formation of a given compound may be subject to unknown experimental error, confirmation of the result by essentially different procedures; i.e., by combination of the heats of different sets of reactions permits greater confidence to be placed in the value obtained. Such confirmation is especially valuable in dealing with a group of compounds for which satisfactory procedures for measurements of heats of reaction have not been established, as they have been, for example, for combustion in oxygen of carbon-hydrogen-oxygen compounds.

Fluorine compounds furnish an example of such a group. In this group many of the methods of measurement of heats of reaction are subject to great experimental difficulties, and consequently, the values obtained for the heats of such reactions are subject to relatively large uncertainties. This is particularly true for reactions involving elemental fluorine. The development of valid procedures for accurate determination of heats of reaction involving elemental fluorine, therefore, promises valuable improvements in the reliability of heats of formation of fluorine-containing compounds. The potential usefulness of such procedures is augmented by the fact that fluorine, the most active nonmetal, reacts vigorously with most elements and with very many compounds, and thus the development of such procedures would open a wide area of possible reaction study. Finally, fluorine, as a monovalent element forms some compounds differing considerably in physical characteristics from the corresponding oxygen compounds, and thus opens up avenues of approach to compounds accessible only with difficulty by the use of oxygen.

The development of procedures for the direct utilization of fluorine as an oxidizer in combustion calorimetry has been retarded by certain obvious difficulties: the difficulty of finding suitable containers for the reaction processes, so as to avoid side reactions with the apparatus itself; the difficulty of obtaining pure fluorine; the difficulty of handling fluorine safely because of its toxicity and its corrosive effects on equipment. Despite these difficulties a limited number of thermal studies of reactions have been carried out with elemental fluorine, which have provided the present basis of the thermochemistry of fluorine compounds. See for example, studies of the reaction of fluorine with hydrogen by von Wartenberg and Fitzner [1],[2] von Wartenberg and Schütza [2], Ruff and Menzel [3]; and the reaction of fluorine with carbon by von Wartenberg and Schütte [4]. With the exception of the latter difficult and, as was shown later, not very accurate experiment on the combustion of charcoal, all of the experiments mentioned involved fluorine as the minor constituent, a procedure which avoids part of the difficulties mentioned above but severely limits the general applicability of the reactions. Thus for example, the study of the combustion of hydrocarbons by this process would be very difficult because of the

[1] The work described here was largely carried out under the sponsorship of the Ordnance Corps, Department of the Army, and the Wright Air Development Center, Department of the Air Force under contracts D of A 599-01-ORD-004, AF 33(616)-53-15, and AF 33(616)-56-20.

[2] Figures in brackets indicate the literature references at the end of this paper.

multiplicity of products. At the same time, impurities in the fluorine would react where possible, whereas they would be excluded by their lesser reactivity from reaction in an excess of fluorine.

A considerable improvement in technique and materials for handling fluorine has occurred since those pioneering investigations, made under great difficulty, so that the development of accurate methods for reaction calorimetry of fluorine is now possible and practical, either by constant-volume bomb or constant-pressure flame processes. A series of research tasks carried out at NBS during the course of several years demonstrates the feasibility, in particular, of the constant-pressure flame calorimeter employing fluorine as the oxidizing atmosphere, indicates specific aspects of some problems encountered, and delineates procedures which appear to have general applicability in the solution of these problems. The procedures are discussed in detail in later sections of this paper. It is not claimed by any means that flame combustion calorimetry with fluorine can at present give results of accuracy comparable with the oxygen flame calorimeter in systems which have been most carefully studied. The accuracy of the fluorine flame calorimeter is of the order of 0.3 percent, compared to 0.01 percent under the best circumstances for the oxygen flame calorimeter [5]. The difference should not be taken as an indication of the relative ultimate accuracy obtainable, but rather of the present relative states of development of experimental techniques for handling the reactions involved.

Some general features of fluorine combustion systems may be pointed out, providing a key to the methods which have been adopted. Hydrogenous materials and some other substances generally ignite spontaneously at room temperature in an atmosphere of fluorine. This hypergolic behavior renders initiation of reaction easy except for those substances having a long induction period (notably hydrogen itself) which may detonate because of appreciable premixing before ignition unless an ignition device is provided. On the other hand, the premixing of fuel and oxidizer is not feasible, and so a diffusion flame must be used, with some resulting problems in burner design to achieve complete combustion. The flame once initiated may be expected to continue to burn in excess fluorine even when the concentration of fuel in the entering gases is extremely small, allowing a thorough flushing of the fuel flow lines, and also permitting extension of the method to the combustion of volatile liquids which may be vaporized into a gas stream for admittance to the burner. Hydrogen, as a constituent of a fuel, rapidly and completely combines with fluorine to form hydrogen fluoride, which can readily be quantitatively absorbed and weighed to obtain a confirmation of the amount of reaction. Some specific problems also arise in the interpretation of heat measurements because of the extreme nonideality of hydrogen fluoride gas.

In the discussion which follows are given details of instruments and methods which have been used in studies of fluorine flame calorimetry at the National Bureau of Standards, a discussion of the problem of the nonideality of hydrogen fluoride, and comments on the findings of studies of the combustion in several particular systems.

2. Instruments and Methods

The calorimetric method used resembles in many respects the procedure described by Rossini [5] for the combustion of hydrogen and other gases in oxygen. In brief outline the process is as follows: a weighed sample of fuel is introduced at a uniform rate into a burner in which is flowing a continuous stream of fluorine in excess. The burner and the combustion chamber of which it forms a part, are submerged in a water-filled, weighed, well-stirred calorimeter inside a constant temperature enclosure ("jacket"), from which it is insulated by an airspace. Hydrogen fluoride (if formed) and perhaps other products are collected and their amounts determined. The temperature rise of the calorimeter, the energy-equivalent of the calorimeter, and the quantity of reaction determined from the measured quantities of reactants and products, together with certain corrections, are used for the calculation of the heat of reaction for unit quantity of reactant.

2.1. Calorimeter and Burner

A diagram of the burner and combustion chamber used in the calorimetric work is shown in figure 1.

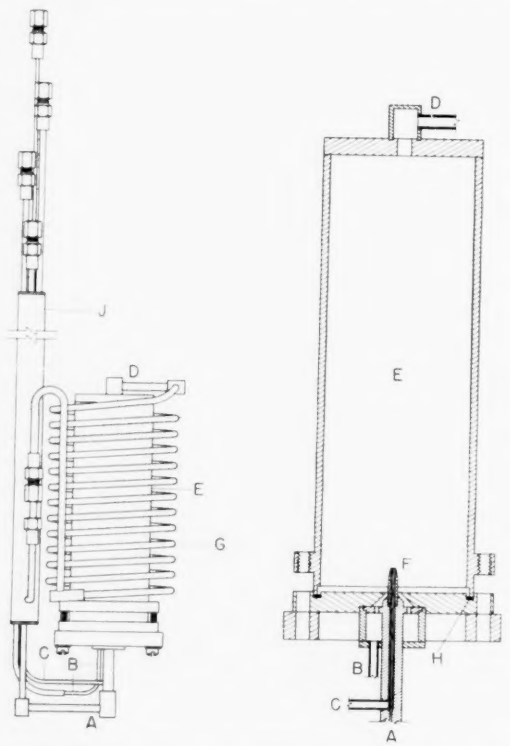

FIGURE 1. *Burner for fluorine flame calorimetry.*

A, B, C, fuel, fluorine, and helium flow lines; *D,* combustion chamber exit; *E,* burner chamber; *F,* burner tip; *G,* monel coil; *H,* Teflon gasket; *J,* heat interchanger for incoming and outgoing gases.

The gases entering the calorimeter pass through the interchanger J and are then brought to the burner F through concentric openings. Fuel enters through copper tube A. Fluorine in tube B enters the combustion chamber E through an orifice in the base plate. In the combustion of hydrocarbons in fluorine in a Monel or copper burner, carbon formation is very considerable if the flame is in contact with the metal [6]. An annular stream of helium is therefore introduced through tube C surrounding the fuel orifice in order to prevent such contact and inhibit carbon formation. The gases leave the combustion chamber at D through a Monel tube wound in a coil G from which they pass to the interchanger J again and are brought to the temperature of the entering gases before leaving the calorimeter. The combustion chamber and its base plate are made of copper. A Teflon gasket H seals the joint between the combustion chamber body and base and permits disassembly of the chamber for inspection and cleaning.

An exploratory burner similar in general outline to the above but differing in details is used for preliminary studies. The combustion chamber of the exploratory burner has a replaceable glass window through which the flame can be observed for short periods of time and has two electrodes for ignition of the flame when necessary. If ignition of the flame by spark or hot wire is necessary, it should be anticipated that any fine wires used in the igniter will burn back to their contacts with a massive metal surface.

For calorimetric work the combustion chamber and most of the interchanger are immersed in the stirred water of a calorimeter similar to that described by Dickinson [7]. The calorimeter is in an airspace submerged in a well-stirred constant-temperature water jacket. The water jacket is kept isothermal to a few thousandths of a degree by an electronic thermoregulator having a temperature-sensitive resistor as a sensing element. Temperatures are measured by a platinum resistance thermometer, immersed in the water surrounding the burner. Temperatures can be read reproducibly to 0.0001° C, but in these experiments the errors from other sources make temperature differences less than 0.001° C insignificant.

2.2. Gas Flow System

A typical diagram of gas flow lines of the combustion system is shown in figure 2, as used for a study of the combustion of methane in oxygen-fluorine mixtures [8]. Flow lines for other combustion systems may be similar but are adapted to the particular properties of the gases to be handled. Where oxygen is not desired in the combustion the specific flow lines required to introduce it are omitted. Gas supplies shown in the figure are fluorine, A; helium, B and D; oxygen, C; and fuel, E. Flow rates of helium, fluorine, oxygen, and other gases drawn from large tanks are regulated by small mechanical regulators as indicated at J and K which act to keep constant pressure differentials across valves immediately following the regulators. Fluorine is metered by a calibrated orifice meter L using Kel-F No. 1 oil as an indicating liquid. Oxygen and helium are metered by float-type flowmeters M and N. Metering and flow rate control are relatively simple for these gases because the tank pressure does not change very much during a run. The fuel, however, is drawn from a small sample bulb suitable for weighing. If it is present as a gas, a large fraction, perhaps 2/3 is drawn from the bulb in each experiment. For the most careful work it would be desirable to have the rate of temperature rise, and therefore, the rate of fuel flow constant during the combustion period. However, the large changes of pressure make the problem of obtaining constant flow rate somewhat difficult. A suitable flow rate controller had not been satisfactorily developed in time to use for the experiments thus far described, so that some sacrifice of flow rate constancy was made. In the case of a condensable gas such as ammonia, fairly good pressure and hence flow regulation is obtained by keeping the fuel as a liquid at constant temperature. Provision for a flow regulator for the fuel is shown at P. However, in the experiments thus far performed a needle valve is at P. In addition to separating the flame from the burner, helium is also used to purge the lines. Tank B is used to clear fluorine from the flow system as a whole in preparation for opening; tank D is used to carry all fuel released from bulb E into the burner for combustion. To this end, the fuel flow lines are made of small diameter tubing and connecting components are designed to minimize entrapment of gas. To reduce introduction of impurities into the burner to a minimum, fluorine passes through an NaF trap F which removes HF. In most of the experiments a similar trap (not shown) was immersed in a dry ice-alcohol bath immediately following trap L to remove Kel-F vapors which may be carried from the flowmeter. A drying tube G containing calcium sulfate is used to dry oxygen.

The calorimeter is shown without detail at R. A trap U in the flow line immediately following the calorimeter is packed with sodium fluoride pellets prepared in an active form for absorbing hydrogen fluoride by heating sodium bifluoride pellets to approximately 400° C in a stream of nitrogen. Trap U can be reactivated several times before refilling is required. This trap quantitatively absorbs hydrogen fluoride which is determined by weighing. To reduce collection of unwanted materials, gases flowing through the calorimeter bypass this trap through valve T except during the combustion reaction and subsequent flushing of the burner chamber.

A tee in the flow line immediately following the sodium fluoride trap U permits attachment of an evacuated glass bulb V, containing a little mercury, for collecting a sample of product gases during a run. Beyond the tee the gases pass through a bubbler W of glass containing Kel–F oil. The purpose of the bubbler is to prevent possible suction of outside gases into the sample bulb when drawing a sample of combustion products. The gases finally pass into a fluorine absorbing tower X of Monel tubing with a welded Monel bottom, packed with

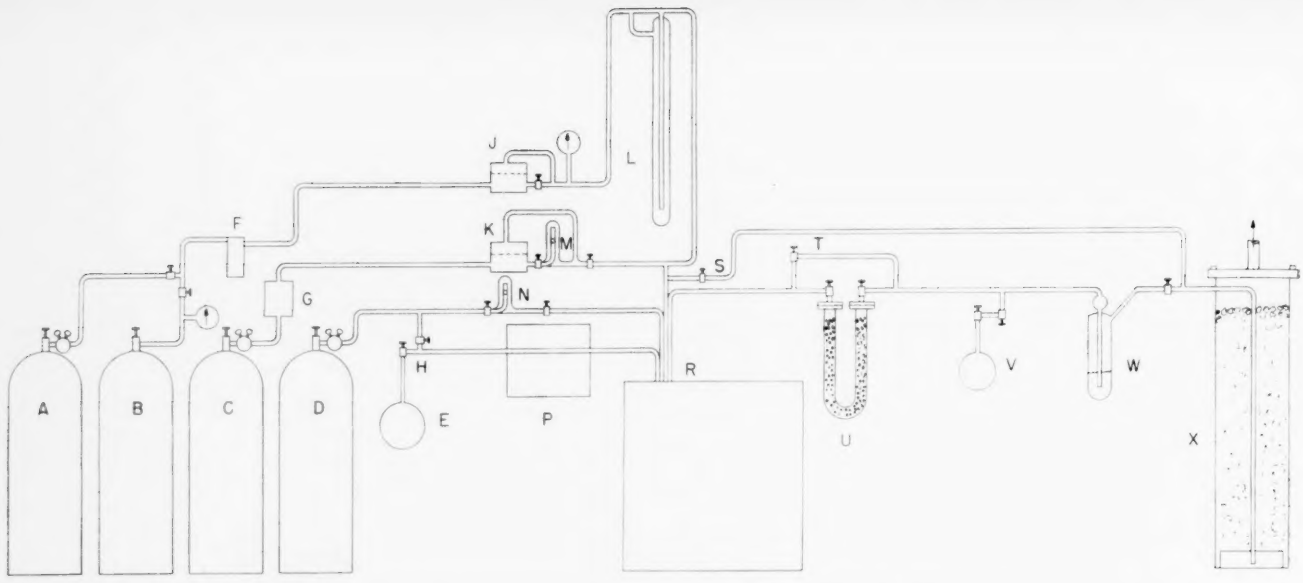

FIGURE 2. *Schematic flow diagram of gases in fluorine flame calorimetry.*

A, fluorine; *B*, *C*, helium; *D*, oxygen; *E*, fuel; *F*, hydrogen fluoride trap; *G*, drying tube; *H*, connection for purging fuel lines; *J*, *K*, mechanical flow regulators; *L*, orifice-type flowmeter for fluorine; *M*, *N*, float-type flowmeters; *P*, fuel flow regulator; *R*, calorimeter; *S*, *T*, fluorine bypass valves; *U*, hydrogen fluoride collector; *V*, gas product sample collector; *W*, bubbler; *X*, fluorine absorbing tower.

granular soda-lime. The gases pass upward through the packing. The soda-lime tower becomes hot to the touch during an experiment, the position of the hot spot serving to indicate the degree of exhaustion of the packing. The effluent gases are released into a laboratory hood, but no odor of fluorine is ordinarily detected from this source. A bypass is provided from directly before the calorimeter to the soda-lime absorber, valve *S*, permitting fluorine to be diverted from the calorimeter and traps. This precaution was found to be desirable to permit quick cleaning up of the system in case of line blockages, which were not infrequent.

The flow lines may be of copper but are preferably of heavy-wall Monel tubing, despite the greater difficulty of bending the latter. Connections are silver soldered where solder is necessary. A commercial Monel compression-type fitting and commercial Monel valves with Teflon packing have been found satisfactory in some flow lines involving fluorine. Where small valve volume is desirable as in the lines through which fuel and products flow, Monel or stainless steel valves [9] of a design due to H. F. Stimson of NBS have been found satisfactory. Connections to these valves and in other places where easy disassembly is desirable are made with small cone fittings.

2.3. Analysis of Fluorine

Because of the difficulty of obtaining very pure fluorine, analysis is desirable in order to be sure whether any factor modifying the experiment is present. For the accuracy required here fluorine of reasonably good (97 to 99 percent) purity can be quickly analyzed by absorption in mercury and measurement of the residual pressure of nonreactive gases [10, 11]. For this purpose a 50-ml glass bulb (fig. 3), fitted with a Monel valve, is used as a sample holder and absorption vessel. In preparation for analysis the bulb is evacuated to a pressure below 0.01-mm Hg, 1 or 2 ml of mercury are drawn into the bulb, and it is again evacuated and heated to drive off residual gases and water vapor. It is then filled to 1-atm pressure with the gas to be analyzed.

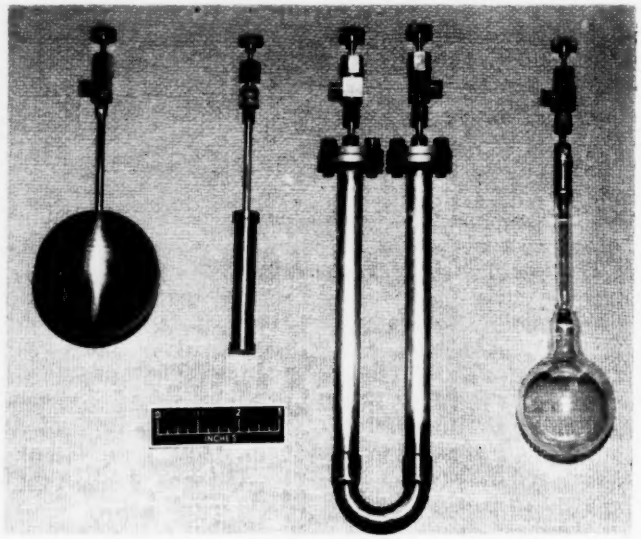

FIGURE 3. *Vessels used in fluorine flame calorimetry.*

Left to right: Monel fuel container for noncondensable gases, stainless steel fuel container for condensable gases, hydrogen fluoride collector, bulb for fluorine analysis.

Because of surface film formation, no appreciable absorption of fluorine by mercury occurs so that the bulb is readily filled. With the valve closed and continuous violent shaking to break the surface film absorption is complete in 10 to 15 min. with evolution of considerable heat. The end of the reaction is identified by the cooling of the bulb and by a sudden change in appearance of the fluorine film on the mercury from a yellowish or slightly iridescent texture to a dull gray. The residual pressure is measured by an oil manometer as shown in figure 4. The reading of the manometer is corrected for the increase in volume of the gas when admitted to the evacuated manometer arm. By this procedure determination of total impurities up to several percent is possible, though its accuracy is probably limited by the adsorption of some gas in the surface film of mercuric fluoride, and perhaps by the reaction of oxygen difluoride and nitrogen trifluoride under the conditions of the experiment. The reproducibility in a short series of measurements of impurities at the 3-percent level is approximately ± 0.05 percent.

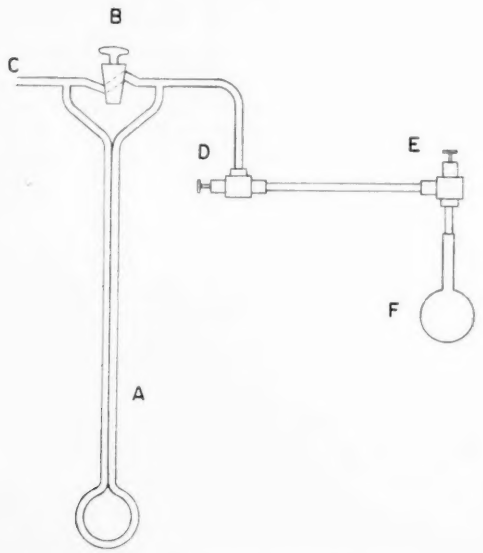

FIGURE 4. *Fluorine impurity tester.*

A, oil filled manometer; *B*, valve; *C*, vacuum source; *D*, *E*, metal valves; *F*, fluorine analysis bulb.

When analyzed by this method commercia fluorine shows total impurities of 1 to 3 percent Analysis of the residual gas by mass spectrometer shows it to consist principally of tetrafluoromethane, oxygen, and nitrogen. Hydrogen fluoride is presumed to be present in the fluorine as received, but passage of the fluorine through a sodium fluoride trap is routinely practiced before use, so no analysis was made for this substance. If the sodium fluoride trap is immersed in liquid oxygen, the tetrafluoromethane is removed, nitrogen and oxygen are reduced in amount, and their relative proportions change.

2.4. Weighing

Weighing of several types of rather bulky containers is necessary during the experiments. A container of nearly equal volume and weight is used as a tare in order to reduce air buoyancy corrections. Sample bulbs for noncondensable gases are spun aluminum or stamped Monel spheres of 0.015-in. to 0.020-in. wall thickness and 3-in. diam, fitted with a 3-in. long tubular neck of the same material as the bulb to permit possible refrigeration, and closed with a small brass valve (see fig. 3). These spheres under a gage pressure of 140 to 150 psi contain up to 0.1 mole of usable gas and weigh about 70 or 140 g depending on the material. Although aluminum bulbs are lighter in weight the difficulty of obtaining aluminum welds free from leaks makes Monel more desirable. Monel also is preferable because of its greater strength. In the aluminum bulbs the joint from aluminum to the brass valve was made successfully by first coating each metal with its appropriate solder, and then joining and finishing with a fillet of aluminum solder.

Condensable gases such as ammonia are retained as liquids in cylinders of heavier wall made of stainless steel and fitted with a similar valve of stainless steel (see fig. 3).

The weighing tube for hydrogen fluoride is a U-tube of Monel and copper, closed at the ends with bolted Monel flanges sealed with Teflon gaskets. The ends are fitted with Monel valves. The U-tube is filled with helium at 1-atm pressure before weighing each time.

2.5. Conduct of an Experiment

An experiment is initiated in a way customary in combustion calorimetry with the calorimeter temperature preset at about 3 deg below the jacket temperature. The observations of temperature of the calorimeter at given times are divided into three periods: an initial period in which changes in temperature are due entirely to thermal leakage and heat of stirring, a middle period in which the principal part of the temperature rise results from the heat produced by the combustion reaction, and a final period in which the temperature change is again due entirely to thermal leakage and heat of stirring. The lengths of the initial and final periods are at least 10 min each, and during these periods all gases but the fuel are flowing in the system. The middle period is started by introducing fuel into the burner. Fuels containing hydrogen generally ignite spontaneously, and the rate of temperature rise due to the reaction can be made nearly constant by keeping the fuel flow rate constant. To conclude combustion the flow of fuel is shut off and replaced by helium flow to purge the line between the fuel sample weighing bulb and burner and thereby cause the combustion of all fuel leaving this bulb. After combustion ceases the rate of temperature rise drops rapidly. The end of the middle period and beginning of the final period take place when the rate of temperature rise diminishes to a constant value.

Time-temperature readings are made at intervals of 1 min during the initial and final periods and at intervals of 0.1° C during the middle period. The time-temperature data are used to correct the observed temperature rise of the calorimeter for heat of stirring and thermal leakage (including heat introduced or removed by the flowing gases) as explained later.

After the final drift period, fluorine is purged from the system by helium, leaving the hydrogen fluoride absorption tube filled with helium for weighing. Figure 5, a characteristic time-resistance plot for a fluorine combustion experiment, shows that no obvious anomalous effects occur to disturb the reliability of the measurement of temperature rise.

For work of the accuracy of these experiments the corrected temperature rise is determined by graphically finding a time t_m which causes areas *bcd* and *def* to be equal. The difference between the extrapolated initial and final drift period resistances at t_m is the desired corrected temperature rise [7]. For more accurate work a numerical integration procedure can be used for determining the thermal leakage and the corrected temperature rise [5].

Fuel sample bulb and sodium fluoride trap are weighed before and after the experiment. At some time during the actual combustion, the glass sample bulb is filled with a sample of gaseous products for later analysis if desired. After collection of such a sample, the bulb is first shaken to promote the absorption of fluorine by the mercury. The residual gas is then analyzed by a mass spectrometer.

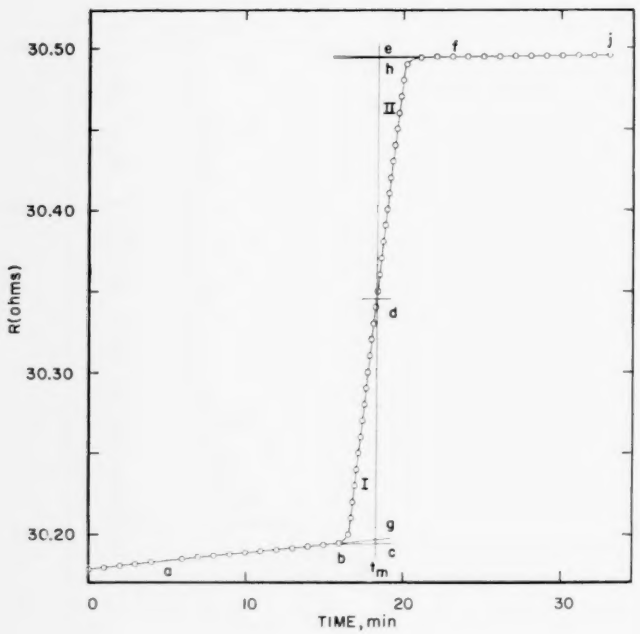

FIGURE 5. *Time-resistance plot for combustion experiment.*
Area *bcd* (I) equals area *def* (II). Corrected resistance rise is $R_A - R_E$.

3. Calibrations, Corrections, and Measurements

3.1. Calibration

The calorimeter may be calibrated electrically or by means of a chemical reaction of known heat, depending upon the immediate circumstances. The former method is more precise and was used in a study of the methane-fluorine combustion [6]. Satisfactory calibration can be obtained using a four-terminal constantan heating element sheathed in copper, with its leads in close thermal contact with both calorimeter and jacket and with the potential leads attached to the current leads at points halfway between jacket and the point of emergence of the current leads from the calorimeter water. The method of making electrical calibrations has been adequately described by Coops, Jessup, and van Nes [12] and by Rossini [5].

As the result of four determinations, an energy equivalent of 14806.7 j/°C was determined with a standard deviation of the mean of 1.4 j/°C (0.009 percent). The calibration results are shown in table 1, in which I is the heater current, E is the heater voltage, ΔR_c is the corrected resistance thermometer change, Δt the corrected temperature rise, and E_s is the energy equivalent of the calorimeter. The calorimeter to which this calibration applies includes the calorimeter can containing a weighed amount of water, lid, electrical heater, stirrer, thermometer, and the burner assembly, with flow lines attached and filled with stationary air. The calibration was assumed to be the same with stationary air and flowing gases in the burner.

TABLE 1. *Electrical calibration of the calorimeter*

Run	Time	I	E	Q	ΔR_c	Δt	E_s
	sec	*amp*	*v*	*j*	*Ohm*	*deg C*	*j/deg C*
1	660.00	2.63371	25.6401	44568.9	0.303295	3.00924	14810.7
2	660.00	2.63181	25.5966	44461.2	.302289	3.00279	14806.6
3	660.00	2.65606	25.8362	45290.9	.308391	3.05883	14806.5
4	660.00	2.65022	25.7808	45094.4	.306762	3.04628	14803.1
Mean							14806.7±1.4 (0.009%)

On the basis of later discussions of the combustion of methane and of ammonia, a nonelectrical calibration of the calorimeter can be made with somewhat less precision using either of these reactions. An indication of the precision to be achieved is shown by the standard deviation of the mean heat of formation of HF found as the result of four experiments with ammonia shown in column 7 or column 11 of table 5, or by the standard deviation of the mean calorimeter constant $\Delta R_c/m$ found in a slightly different calorimeter setup as the result of seven combustion reactions with methane shown in table 4. In table 4 ΔR_c is the corrected temperature rise of the calorimeter caused by burning $m(CH_4)$ grams of methane. The standard deviation of the mean $\Delta R_c/m$ is 0.32 percent. This estimate of the uncertainty in the calorimeter constant includes both

variations among experiments and also uncertainties in the amount of reaction for each experiment as calculated on the basis of observed mass of methane passed through the burner and calculated mass of methane determined from the gain in weight of the hydrogen fluoride absorber.

3.2. Correction for Non-Ideality of Hydrogen Fluoride

In a combustion experiment the thermal corrections to the observed heat for gas non-ideality are small for fluorine and for helium. For other gases entering the reaction such thermal effects must be examined carefully. In measurements of reactions involving gaseous hydrogen fluoride, large corrections may be necessary to reduce the results of such measurements to the basis of the ideal gas state; i.e., the standard state of unit fugacity for this gas. Unfortunately, the magnitude of these corrections is subject to considerable uncertainty because of discrepancies between the PVT data reported for hydrogen fluoride by various observers [13, 14, 15].

The magnitude of the uncertainty in the correction may be seen by comparing values of (H°–H), the enthalpy of the ideal gas less that of the real gas, as calculated from the data of the two most recent and most extensive investigations of the PVT relation of hydrogen fluoride in the pressure range of interest; namely, those of Long, Hildebrand, and Morrell [14] and of Strohmeier and Briegleb [15(a)].

The large deviations of hydrogen fluoride from ideality have been attributed to the formation of polymers as a result of hydrogen bonding, and two models of the gas have been proposed on this basis. Long, Hildebrand, and Morrell [14] found that their data could be represented fairly well by assuming that the gas is largely a mixture of HF and $(HF)_6$, the latter being assumed to be cyclic in structure. The heat of polymerization at a temperature of 305° K and pressure of 0.3 atm, a typical concentration of hydrogen fluoride in the combustion products, as calculated on the basis of this model is entirely negligible in comparison with the measured heat of fluorination of methane, for instance. It will be seen from figure 6, however, that the values of the association factor, $Z=RT/PV$, calculated for this model (curve L) fall considerably below the experimental values at low pressures, so that the model does not give a correct representation of the PVT data at low pressures. This fact was observed by Long et al. [14], who suggested that under conditions in which the association factor is less than 1.3 lower polymers play an appreciable role.

The other model of hydrogen fluoride, originally proposed by Briegleb [16], assumes that the gas is a mixture of polymers $(HF)_n$ in which n assumes an indefinite number of integral values. Evidence favoring this model includes electron diffraction data [17] which indicate the presence of chain polymers, and measurements of the dielectric constant of the gas [18] which show that its dipole moment increases with pressure, contrary to what would be expected if the polymer exists solely in the ring form.

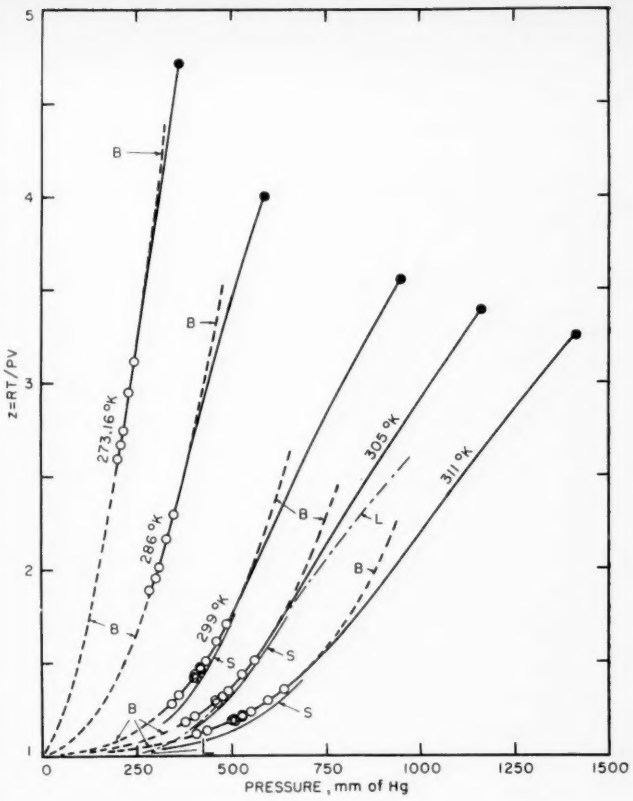

FIGURE 6. *Values of association factor for gaseous* HF.

Open circles, data of reference [14]. Solid circles, data of reference [24]. Solid curves drawn through experimental points. Curves B calculated as described in text from data of reference [14]. Curve L calculated from data of reference [14], assuming only monomer and hexamer molecules present. Curves S represent experimental data of reference [15(a)].

Considering all the data available, it appears probable that both linear and cyclic polymers are present in the gas phase. However, because only the low pressure region is of interest in this work, a model similar to that of Briegleb has been assumed in making calculations of (H°–H). Using this model and the experimental association factors of Long, Hildebrand, and Morrell [14], equilibrium constants for the polymerization reactions

$$2HF \longrightarrow (HF)_2$$

and

$$(HF)_n + HF \longrightarrow (HF)_{n+1} \qquad (n=2, 3, \ldots)$$

were derived on the assumption that the equilibrium constant $k_{n,n+1}$ for the second reaction is independent of n, and the further assumption that deviations from ideality are due entirely to polymerization. The equilibrium constants obtained from the experimental data are compared in table 2 with values calculated from the following empirical equations

$$-R \ln k_{1,2} = -\frac{15488.5}{T} + 55.2631,$$

$$-R \ln k_{n,n+1} = -\frac{1329.6}{T - 169.92} + 9.6588, \quad (n > 1),$$

where R is in cal/mole deg K and pressures are expressed in atm.

TABLE 2. *Observed and calculated values of equilibrium constants derived from data of reference [14]*

Temperature	k_{12}		$k_{n,n+1}$	
° K	*obs.*	*calc.*	*obs.*	*calc.*
311	0.0764	0.0641	0.862	0.889
305	.1050	.1049	1.100	1.097
299	.1748	.1751	1.375	1.381
286	.5730	.5927	2.477	2.469
273.15	2.0620	2.0619	5.050	5.056

The equilibrium constants were used to calculate values of the association factor and the results of these calculations are shown by the curves marked B in figure 6. In the pressure ranges covered by the experimental data of Long, Hildebrand, and Morrell these curves are seen to be practically identical with the solid curve drawn through the open circles representing their data and the solid circles representing the data of Jarry and Davis [19] at saturation pressure. Between these two sets of points, however, the curves B begin to diverge from the experimental curves. Nevertheless the curves B seem to give a satisfactory interpolation between the pressures covered by Long, Hildebrand, and Morrell and zero pressure, where the gas is presumed to be ideal and monomeric. It will be seen that the curve B for $T=305°$ K fits the experimental points of Long, Hildebrand, and Morrell at low pressures better than does their curve L derived on the basis that only monomer and hexamer are present.

Using the temperature coefficients of the equilibrium constants, the heats of the polymerization reactions were calculated, and these together with the association factors were then used to calculate values of (H°–H) per mole of HF.

The data of Strohmeier and Briegleb [15(a)] have also been used to calculate values of (H°–H), using the equilibrium constants and their temperature coefficients reported by Briegleb and Strohmeier [15(b)] for the reactions

$$n\mathrm{HF}(g) = (\mathrm{HF})_n(g) \qquad (n=2, 3, \ldots).$$

The association factors calculated from these equilibrium constants have been shown by Briegleb and Strohmeier (15(b)] to be in very good agreement (about 0.1 percent) with their experimental values. The curves calculated by Briegleb and Strohmeier to represent association factor versus pressure (experimental points not shown) for the three isotherms covered both by Long, Hildebrand, and Morrell, and by Strohmeier and Briegleb are those marked S in figure 6. The two sets of curves differ systematically by considerably more than would be expected from the precision of the two sets of measurements.

Values of (H°–H) calculated from both sets of data are given in table 3 and are shown graphically in figure 7. The values based on the data of Long, Hildebrand, and Morrell at temperatures above 38° C represent extrapolations beyond the range of their experimental data. The values calculated from the data of Long, Hildebrand, and Morrell are higher by a factor of two to three than those calculated from the data of Strohmeier and Briegleb.

TABLE 3. *Enthalpy differences (H°–H) for hydrogen fluoride gas*

	H°–H kj/mole					H°–H kcal/mole				
	a. Calculated to fit the data of Long, Hidebrand, and Morrell									
P atm \ T deg C	26	32	38	50		26	32	38	50	
0.1	1.32	0.77	0.46	0.18		0.316	0.185	0.110	0.043	
.2	3.10	1.78	1.05	.38		.742	.426	.250	.091	
.3	5.49	3.10	1.77	.63		1.312	.740	.424	.150	
.4	8.43	4.80	2.71	.91		2.015	1.146	.647	.218	
.5	11.89	6.95	3.89	1.26		2.842	1.660	.930	.300	
	b. Calculated to fit the data of Strohmeier and Briegleb									
P atm \ T deg C	26	32	38	44	56	26	32	38	44	56
0.1	0.41	0.32	0.25	0.19	0.12	0.098	0.076	0.059	0.046	0.028
.2	.97	.70	.53	.40	.24	.232	.167	.126	.096	.058
.3	1.81	1.23	.86	.63	.37	.432	.293	.205	.150	.088
.4	.....	2.11	1.31	.90	.50	.....	.502	.314	.216	.120
.5	.....	.....	2.02	1.25	.66	.....	.....	.483	.299	.158

As an indication of the possible effect of these discrepancies we may consider the measurements of Jessup, McCoskey, and Nelson [6] who determined the heat of formation of CF_4 from the measured heat of reaction of methane and fluorine combined with values for the heats of formation of methane and hydrogen fluoride. Under the conditions of their experiment the correction for the gas imperfection of HF calculated from the data of Long, Hildebrand, and Morrell, was 2.1 kj (0.5 kcal) per mole of HF, or 8.4 kj (2.0 kcal) per mole of CF_4. If the data of Strohmeier and Briegleb had been used, the correction would have been only 3.3 kj (0.8 kcal) per mole of CF_4, so that the value obtained for the heat of formation of CF_4 would have been different by 5.1 kj (1.2 kcal) per mole.

In view of the discrepancies between the data reported in reference [14] and [15], further experimental work on the gas imperfections of hydrogen fluoride would be very desirable.[3] Such work might include further PVT measurements, throttling experiments, or calorimetric experiments similar to those reported by Rossini and Frandsen [20].

[3] At least two investigations of the PVT relation of HF are known to be in progress, but cover a pressure range much higher than that of interest in most calorimetric measurements.

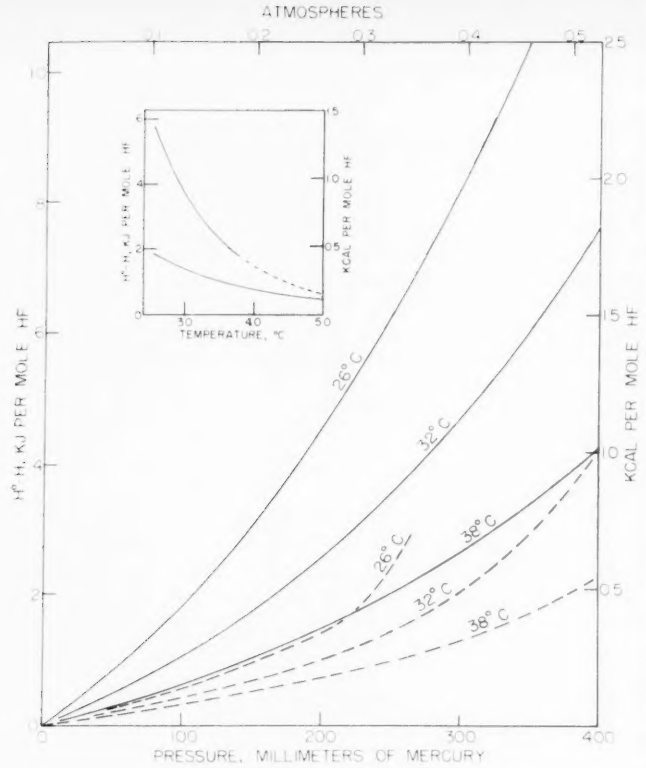

FIGURE 7. *Change in enthalpy with pressure for hydrogen fluoride at 26°, 32°, and 38° C.*

Solid curves calculated as described in text from data of reference [14]. Dashed curves calculated from data of reference [15(a), 15(b)].
Insert: Isobar at 0.3 atm calculated from data of reference [14] (upper curve) and from data of reference [15(a), 15(b)] (lower curve).

Until the PVT behavior is known with greater certainty in the low pressure region at temperatures near 25° C, the problem of corrections to calorimetric data can be avoided by making measurements at higher temperatures. The work of Wartenberg and Fitzner [1] at 100° C, for example, does not suffer from any such uncertainty because the enthalpy corrections are negligible for hydrogen fluoride at that temperature. It will also be seen by reference to the 0.3-atm isobar in figure 7 (insert) that in the neighborhood at 50° C the differences between the experimental data become negligible in this isobar which is typical. In some experiments at NBS measurements have been made at 50° C taking advantage of this fact.

3.3. Measurement of Amount of Reaction

The amount of fuel entering the calorimeter is readily determined by weighing the container before and after the experiment. The early measurements in the fluorine flame calorimeter suffered from lack of confirmation that the entering fuel was completely burned. The vapor pressure of HF over the compound NaF·HF is very small at room temperature (about 0.01-mm Hg [21]). The use of an absorbing tube to collect for weighing the hydrogen fluoride resulting from the combustion of hydrogenous fuels is thus an obvious technique for verifying the completeness of reaction, and has been used throughout these experiments. This absorbent has also been used by Wartenberg and Schutza [2], though not in the same manner as here. They may not have encountered the same difficulties because of the use of hydrogen as the gas in excess rather than fluorine. In none of the early experiments in this laboratory, either in the combustion of methane or of ammonia, was consistent correlation found between weight of fuel and weight of hydrogen fluoride formed. The most general behavior was for the weight of hydrogen fluoride to be rather erratically too high.

The excess weight gain was traced (a) to impurities (HF and perhaps some CF_4) in the fluorine supply, and (b) to additional impurities (presumably HF) acquired by the fluorine first passing through the combustion chamber. Impurities in the fluorine supply may be removed by allowing the fluorine to pass through a sodium fluoride trap immersed in a dry-ice-alcohol bath just before entering the calorimeter. Collection and weighing of the added impurities acquired by the fluoride in its passage through the combustion chamber may be avoided by diverting the fluorine through a valve bypassing the hydrogen fluoride weighing tube until time for introduction of the fuel. Evidence for the nature of the impurities to be avoided in this way is as follows. After a combustion reaction, the inner surface of the copper combustion chamber has a brick-red color on first opening for inspection. On standing, the red color changes to white, a behavior which is attributed to the hydrolysis of red cuprous fluoride by moisture in the air. In preparing for the fore-period drift measurements, the first introduction of fluorine always causes a sharp increase in the drift rate, which disappears after a few minutes leaving the drift rate approximately the same as in the absence of fluorine. By blank experiments in which the calorimeter was not opened to the air it was found that increases in the weight of the hydrogen fluoride weighing tube cease a few minutes after the first introduction of fluorine. The gain in weight could thus be attributed to gases formed by interaction of fluorine with substances on the surfaces of the combustion chamber.

Table 4a shows a typical series of weighings in calorimetric experiments with methane, using experiments in which no carbon formation was observed, and in which all of the gases used in the experiment passed through the hydrogen fluoride weighing tube. In this table $m(CH_4)$ is the weighed mass of methane passed through the burner, and $m'(CH_4)$ is the mass of methane calculated on the basis of the weight of hydrogen fluoride collected. The mean difference is 2.1 percent. In the first three columns of table 4b are shown data for a series of experiments in which gases were collected in the hydrogen fluoride weighing tube only after the initial drift period was nearly complete. In these experiments the mean difference between $m(CH_4)$ and $m'(CH_4)$ without regard for sign is 0.13 percent, a

significant improvement over the preceding series of experiments.

By these experiments it has thus been shown possible to confirm the amount of reaction of a hydrogenous fuel with reasonable accuracy by relatively simple precautions in the conduct of an experiment. Some uncertainty remains because of the present inability to collect other product gases for weighing or analysis, and a sampling technique must be resorted to for the indication of side reactions. In the specific instances of the combustion of methane and ammonia the reactions have been found to be simple and not accompanied by measurable amounts of side reactions.

TABLE 4. *Consistency of weighings and reproducibility of heat measurement in the combustion of methane by fluorine*

a. All gases pass through hydrogen fluoride trap

$m(CH_4)$	$m'(CH_4)$	$m(CH_4)-m'(CH_4)$	Difference
g	*g*	*g*	%
0.4139	0.4215	−0.0076	−1.8
.4020	.4075	−.0055	−1.4
.4020	.4173	−.0153	−3.8
.4074	.4129	−.0055	−1.3

b. Fore-period gases do not pass through hydrogen fluoride trap

$m(CH_4)$	$m'(CH_4)$	Difference	ΔR_c	$\frac{\Delta R_c}{m(CH_4)}$	$\frac{\Delta R_c}{m'(CH_4)}$	t
g	*g*	%	*Ohm*	*Ohm/g*	*Ohm/g*	°*C*
0.3923	0.3925	−0.05	0.31090	0.7925	0.7921	49.75
.3940	.3938	+.05	.31362	.7960	.7964	49.77
.4053	.4068	−.37	.31964	.7887	.7857	49.72
.3987	.3986	+.02	.31558	.7915	.7917	49.71
.4031	.4036	−.12	.32130	.7971	.7961	49.72
.4138	.4131	+.17	.32851	.7939	.7952	49.69
.4335	.4341	−.15	.33745	.7784	.7773	49.86
Mean		±0.13		0.7912	0.7906	

Mean: $\Delta R_c/m$, $\Delta R_c/m' = 0.7909 \pm 0.0025$

4. Heat of Reaction of Ammonia With Fluorine

The combustion of ammonia in fluorine was found to proceed without the formation of any fluorides of nitrogen when carried out in the burners described, contrary to the experience of Ruff and Hanke [22]. Absence of compounds of nitrogen and fluorine in the product gases was determined by mass spectrometer. The only reaction observed was that shown by eq (1)

$$NH_3 + \tfrac{3}{4} F_2 \longrightarrow 3HF + \tfrac{1}{2} N_2 \qquad (1)$$

The results of four combustion reactions carried out between 30 and 32° C are shown in table 5. The amount of reaction was based on the weight of ammonia burned (col. (1)) because the collection of HF was not under control in these experiments. The observed heat of reaction is shown in column (2); the partial pressure of hydrogen fluoride in the effluent gases, determined by the proportions of materials introduced is shown in column (3). Column (4) shows the correction for non-ideality of hydrogen fluoride calculated on the basis of the data of Long et al. by application of which are calculated the standard heat of reaction, column (5), and the standard heat of formation of hydrogen fluoride, column (6). Column (8) shows the correction for non-ideality of hydrogen fluoride calculated on the basis of the data of Strohmeier and Briegleb, by application of which are calculated the standard heat of reaction shown in column (9) and the standard heat of formation of hydrogen fluoride, column (10). Columns (7) and (11) give the deviation from the mean, δ, of the individual results in columns (6) and (10), respectively. In the above calculations a correction of −0.13 kj/mole is made for the difference $\Delta H^\circ_{25} - \Delta H^\circ_{32}$. The heat of formation of ammonia is well established and was taken as −46.19 kj/mole = −11.04 kcal/mole [23]. The mean heat of formation of HF in column (6) is -268.7 ± 0.5 kj/mole $= -64.22 \pm 0.13$ kcal/mole, in which the uncertainty given is the standard deviation of the mean. This may be compared with −64.2 kcal/mole found in reference [23], which is an average based on values of −63.8 kcal/mole calculated by Ruff and Menzel [3] from the experimental work of Wartenberg and Fitzner [1], −64.2 kcal/mole calculated by Ruff and Menzel from the experimental work of Ruff and Laass [24], and -64.45 ± 0.1 kcal/mole reported by Wartenberg and Schutza [2].

However, the average value of column (10) is -270.4 ± 0.3 kj/mole $= -64.63 \pm 0.07$ kcal/mole. The scatter is less in this calculation than in the preceed-

TABLE 5. *Combustion of ammonia in fluorine*

(1) $m(NH_3)$	(2) ΔH_{32} obs	(3) $p(HF)$	(4) $q(HF)(1)$	(5) $\Delta H°_{25}(1)$	(6) $\Delta H°_{f_{25}}(HF)(1)$	(7) $\delta(1)$	(8) $q(HF)(2)$	(9) $\Delta H°_{25}(2)$	(10) $\Delta H°_{f_{25}}(HF)(2)$	(11) $\delta(2)$
g	*kj/mole* NH_3	*atm*	*kj/mole* NH_3	*kj/mole*	*kj/mole*	*kj/mole*	*kj/mole* NH_3	*kj/mole*	*kj/mole*	*kj/mole*
0.933	−765.7	0.11	2.4	−763.4	−269.9	+1.2	1.0	−764.8	−270.3	−0.1
.8273	−767.6	.31	11.7	−756.0	−267.4	−1.3	4.3	−763.4	−269.9	−.5
.9232	−772.4	.35	14.2	−758.3	−268.2	−.5	5.2	−767.3	−271.2	+.8
.5430	−766.3	.18	5.1	−761.3	−269.2	+.5	2.0	−764.4	−270.2	−.2
Mean (kj/mole)				−759.7	−268.7	±0.55[a]		−765.0	−270.4	±0.28[a]
Mean (kcal/mole)				−181.6	−64.22	±0.13[a]		−182.8	−64.63	±0.07[a]

[a] Standard deviation of the mean.

ing one, but it is obvious that the principal source of uncertainty is in the amount of correction to be applied for non-ideality of hydrogen fluoride. The mean of all the calculated values gives $\Delta H°_{f_{25}}$ (HF) = -269.6 ± 1.1 kj/mole = -64.4 ± 0.25 kcal/mole, as the best value which can be derived from the data presented here.

It might be noted that several values [6, 25, 26] for the heat of formation of carbon tetrafluoride are based in part on the value −64.2 kcal/mole for the heat of formation of HF. A more negative value for the heat of formation of hydrogen fluoride would tend to bring closer together the values for heat of formation found on the basis of oxygen bomb calorimetry [25, 26] on the one hand and by fluorine flame calorimetry [6] on the other hand.

5. References

[1] H. von Wartenberg and O. Fitzner, Z. anorg. u. allgem. Chem. **151,** 313 (1926).
[2] H. von Wartenberg and H. Schütza, Z. anorg. u. allgem. Chem. **206,** 65 (1932).
[3] O. Ruff and W. Menzel, Z. anorg. u. allgem. Chem. **198,** 375 (1931).
[4] H. von Wartenberg and R. Schütte, Z. anorg. u. allgem. Chem. **211,** 222 (1933).
[5] F. D. Rossini, editor, Experimental thermochemistry, ch. 4 (Interscience Publishers, Inc., New York, N.Y., 1956).
[6] R. S. Jessup, R. E. McCoskey, and R. A. Nelson, J. Am. Chem. Soc. **77,** 244 (1955).
[7] H. C. Dickinson, Bul. BS **11,** 189 (1914).
[8] G. T. Armstrong, C. F. Coyle, and L. A. Krieger (in preparation).
[9] A. R. Glasgow, Jr., and G. S. Ross, Sr., Anal. Chem. **26,** 2003 (1954).
[10] L. A. Bigelow, Chem. Revs. **40,** 110 (1947).
[11] H. Schmitz and H. J. Schumacher, Z. anorg. u. allgem. Chem. **245,** 221 (1940).
[12] J. Coops, R. S. Jessup, and K. van Nes, Experimental thermochemistry, ch. 3 (Interscience Publishers, Inc., New York, N.Y., 1956).
[13] K. Friedenhagen, Z. anorg. u. allgem. Chem. **218,** 161 (1934).
[14] R. L. Long, J. H. Hildebrand, and W. E. Morrell, J. Am. Chem. Soc. **65,** 182 (1943).
[15] (a) W. Strohmeier and G. Briegleb, Z. Elektrochem. **57,** 662 (1953).
(b) G. Briegleb and W. Strohmeier, Z. Elektrochem. **57,** 668 (1953).
[16] G. Briegleb, Z. physik. Chem. [**B**]**51,** 9 (1941).
[17] S. H. Bauer, J. Y. Beach, and J. H. Simons, J. Am. Chem. Soc. **61,** 19 (1939).
[18] R. A. Oriani and C. P. Smyth, J. Am. Chem. Soc. **70,** 125 (1948).
[19] R. L. Jarry and W. Davis, Jr., J. Phys. Chem. **57,** 600 (1953).
[20] F. D. Rossini and M. Frandsen, BS J. Research **9,** 733 (1932) RP503; see also E. W. Washburn, BS J. Research **9,** 521 (1932) RP487.
[21] R. C. Downing, Purification and compression of fluorine, Ch. 8, p. 162, C. Slesser and S. R. Schram, editors, Preparation, properties and technology of fluorine and organic fluoro compounds, Nat. Nuclear Energy Serv. **VII–1** (McGraw-Hill Book Co., New York, N.Y., 1951).
[22] O. Ruff and E. Hanke, Z. anorg. u. allgem. Chem. **197,** 395 (1931).
[23] F. D. Rossini, D. D. Wagman, W. H. Evans, S. Levine, and I. Jaffee, Selected values of chemical thermodynamic properties, NBS Circ. 500 (1952).
[24] O. Ruff and F. Laass, Z. anorg. u. allgem. Chem. **183,** 217 (1929).
[25] D. W. Scott, W. D. Good and G. Waddington, J. Am. Chem. Soc. **77,** 245 (1955).
[26] C. A. Neugebauer and J. L. Margrave, J. Phys. Chem. **60,** 1318 (1956).

WASHINGTON, D.C. (Paper 64A1–28)

JOURNAL OF RESEARCH of the National Bureau of Standards—A. Physics and Chemistry
Vol. 64A, No. 1, January–February 1960

Pits in Metals Caused by Collision With Liquid Drops and Rigid Steel Spheres

Olive G. Engel

(September 24, 1959)

A pit-depth-versus-velocity equation developed earlier was tested further with experimental data obtained using target plates of electrolytic tough pitch copper, 1100–O aluminum, and 2024–O aluminum, the static strength properties of which were measured by testing tensile specimens. The projectiles used to produce the pits were mercury drops, waterdrops, and steel spheres. It was found that the numerical constants in the equation for projectiles that flow during and as a result of the collision are different from those for projectiles that do not flow (hardened steel spheres). Curves calculated using the equation were found to be in acceptable agreement with experimental pit-depth-versus-velocity data for collisions of the indicated projectiles with target plates of the three metals used with the exception of the case of steel-sphere impingement against 2024–O aluminum alloy. In this case work-hardening of the target metal seems to foster a mode of pit formation that was not considered in the development of the pit-depth-versus-velocity equation.

1. Introduction

Collisions between liquids and solids in all of the possible projectile-target combinations in which they can occur have been topics for research. Some of these are: solid-against-solid collisions (artillery experiments), solid-against-liquid collisions (water-entry problems), liquid-against-solid collisions (high-speed rain-erosion research), and liquid-against-liquid collisions (impact of solids at meteor velocities). Work has been done at the National Bureau of Standards toward developing an equation that will give pit depth as a function of impingement velocity for collisions of target plates of the soft and medium hard metals with drops of liquids [1].[1]

The model on which the equation is based is the movement of the core of metal of the target plate immediately under the collision area with respect to the remainder of the plate. In order that the core of metal through the target plate under the collision area may be free to move, the side of the plate opposite to that on which the collision occurs must be a free surface. In addition to this condition on the target plate, it must not be so thin that it bends as a whole under the collision, or so thick that the spread of the compressional wave that passes through it as a result of the collision is appreciable.

In the development of this pit-depth-versus-velocity equation, such characteristic fluid-flow parameters as the Weber number and the Reynolds number were neglected. The equation should, therefore, apply equally well to pits caused by collisions of solid spheres with target plates of the soft and medium hard metals.

In the case of collisions of solid-sphere projectiles that flow like a liquid drop during and as a result of the collision, the equation should apply without modification even of the numerical constants. It has been found that the equation does produce curves that fit pit-depth-versus-velocity data for high-speed collisions of soft ductile metal spheres against targets of the same metals [1].

For the case of collisions of hardened steel spheres, the numerical constants in the equation will be different. These spheres do not flow during the collision; none of the collision energy is lost in the flow of the projectile and, therefore, a larger amount of it is used in forming the pit.

Pit-depth-versus-velocity data [2] for high-speed collision of liquid drops with metal plates were used to evaluate the numerical constants in the equation and to test the equation. These data were of a preliminary nature. The yield strength and the speed of sound of the metals used for the target plates were not determined by experiment. The speed of sound in this case is the speed of irrotational waves in an infinite medium.

It is important to know the static yield strength of the target metal. Although it is the dynamic yield strength that must be used in the equation, in most cases the dynamic yield strength may be expected to vary in the same direction that the static yield strength varies for different heat-treatment states of a given metal. Different sets of pit-depth-versus-velocity data will not, in general, be comparable unless the static yield strength of the metal target plates that are used is essentially the same. Furthermore, the static yield strength can be used to calculate the dynamic yield strength in the case of the duralumins [2] and closely related aluminum alloys.

The work described in this paper is an effort to test the equation further by determining the depth of pits that result from impingement of waterdrops, mercury drops, and rigid steel spheres against target

[1] Figures in brackets indicate the literature references at the end of this paper.

[2] These data were obtained at Convair, Division of General Dynamics Corp., in San Diego, Calif. See reference [1].

plates of 1100–O aluminum, 2024–O aluminum, and annealed electrolytic tough pitch copper, the static yield strengths of which have been determined by experiment. The work described was conducted under the sponsorship of the Materials Laboratory, Directorate of Laboratories, Wright Air Development Center. The experimental work was done at Convair, Division of General Dynamics Corp., in San Diego, Calif., and at the U.S. Naval Research Laboratory in Washington, D.C.

2. Materials

2.1. Preparation of the Target Plates

Plates of the metals were obtained in 2.5-cm (1-in.) thickness so that 15.2- by -15.2-cm (6- by -6-in.) target plates cut from them for use in experiments involving impingement of 0.5556-cm- ($\frac{7}{32}$-in.-), 0.7938-cm- ($\frac{5}{16}$-in.-), and 1.270-cm- ($\frac{1}{2}$-in.-) diam steel spheres, would be approximately 2 to 4.5 sphere diameters thick. Tensile specimens for determining the static yield strength and small 0.317-cm- ($\frac{1}{8}$-in.-) thick target plates for use in experiments involving collision with 0.1-cm and 0.2-cm drops of mercury and water were machined from some of this material.

The 1100–O aluminum was obtained from the Davenport Works of the Aluminum Co. of America in Riverdale, Iowa. The material was furnished in mill finish and was as scratch-free as was commercially feasible. For the annealing process the objects were placed in the furnace while it was cold. The furnace temperature was then brought up to 343° C (650° F) and was held at 343° C (650° F) for 4.5 hr in the case of the large target plates and the tensile specimens and for about 2 hr in the case of the small target plates. The furnace was then turned off and the objects were allowed to cool with the furnace. The tensile specimens were suspended in the vertical position during the annealing process to prevent sagging.

The 2024–O aluminum was obtained as 2024–T4 aluminum at the U.S. Naval Research Laboratory in Washington, D.C. For the annealing process the tensile specimens and the target plates of this aluminum alloy were put into the furnace after it had been raised to a temperature of 399° C (750° F). They were heated at 399° C (750° F) for 4 hr, cooled to 166° C (350° F) at a rate of 25.5° C (46° F) per hour, and then removed from the furnace.

The electrolytic tough pitch copper was obtained from the American Brass Co. For annealing, the objects were placed in the furnace after it had attained a temperature of 427° C (800° F). The large target plates were kept in the hot furnace for approximately 1 hr, the small target plates for about 40 min, and the tensile specimens for about 30 min. The objects were in each case removed from the furnace at the end of the specified time and were air cooled. The copper oxide that formed was removed from the target plates by pickling in dilute acid and by gentle abrasion.

2.2. Static Tensile Properties of the Metals

The tensile specimens were standard ASTM test specimens having 1.283-cm (0.505-in.) diameter in accordance with ASTM designation E 8–54 T. They were tested in a standard testing machine in the NBS Engineering Mechanics Section using autographic recording equipment. The data obtained were yield strength (0.2 percent offset), tensile strength, and elongation in 5.1 cm (2 in.). The test results are given in table 1.

TABLE 1. *Static tensile properties of the metals*

Metal	Yield strength		Tensile strength		Elongation
	$10^8 d/cm^2$	*psi*	$10^8 d/cm^2$	*psi*	%
1100–O aluminum	1.83	2,650	7.83	11,350	41.6
1100–O aluminum	1.79	2,600	7.65	11,100	41.5
2024–O aluminum	8.69	12,600	19.6	28,400	17.5
2024–O aluminum	8.76	12,700	20.0	29,000	17.5
2024–O aluminum	8.69	12,600	20.7	30,000	18.0
2024–O aluminum	8.69	12,600	20.9	30,300	18.5
Annealed copper	2.90	4,200	21.2	30,800	50.0
Annealed copper	2.96	4,300	21.4	31,000	49.0
Annealed copper	2.55	3,700	21.5	31,200	54.0
Annealed copper	2.55	3,700	21.4	31,100	53.0

3. Liquid-Against-Solid Collisions

The small target plates of 1100–O aluminum, 2024–O aluminum, and annealed electrolytic tough pitch copper were sent to Convair, Division of General Dynamics Corp., in San Diego, Calif., to be fired into drops of mercury (0.1 cm and 0.2 cm in diam) and drops of water (0.2 cm in diam) at high speed. When the tests were made, the 1100–O aluminum targets were not fired because they were too thin.

The mercury drops used in the firings were individually weighed on an analytical balance, and the diameters of the drops were calculated. The actual diameters of the mercury drops and waterdrops varied in most cases by less than ± 10 percent of the nominal size. The depths of the pits produced were measured at Convair using an optical micrometer; the depth measurements were reported to be good to ± 0.0013 cm (± 0.0005 in.).

The theoretical curves for the collisions of liquid drops against solid targets were obtained using the equations [1]

$$\delta' = \frac{7.2dz}{c(z+z')}\,[V - V_i] \tag{1}$$

and

$$V_i = \frac{19E'(z+z')}{(\rho c' z'^3)^{\frac{1}{2}}} \tag{2}$$

in which δ' is pit depth, d is drop diameter, c is the speed of sound as defined previously, ρ is the density, z is the acoustic impedance ($z=c\rho$), E' is the dynamic compressive yield strength of the target metal, V_i is the smallest impingement velocity at which a permanent pit is made, and V is the impingement velocity. Primed quantities refer to the material of the target

TABLE 2. *Constants of the materials of projectiles and targets*

Constant	Projectile			Target		
	Water	Mercury	Steel	1100–O Aluminum	2024–O Aluminum	Copper electrolytic
Sound speed, c ..... cm/sec	[a] 1.497 ×10 [5]	[a] 1.451×10 [5]	[b] 5.786×10 [5]	[b] 6.318×10 [5]	[b] 6.370×10 [5]	[b] 4.691×10 [5]
Density, ρ ..... g/cm [3]	[c] 0.99707	[c] 13.546	[d] 7.859	[e] 2.713	[e] 2.768	[e] 8.92
Acoustic impedance [f], z ..... g/cm [2] sec	0.1493×10 [6]	1.966×10 [6]	4.547×10 [6]	1.714×10 [6]	1.763×10 [6]	4.184×10 [6]
Dynamic yield strength, E' ..... dynes/cm [2]				[g] 7.239×10 [8]	[g] 2.350×10 [9]	[b] 2.394×10 [9]

[a] Data from Bergmann [3].
[b] Measured in NBS Sound Section by C. E. Tschiegg.
[c] Data from Handbook of Chemistry and Physics.
[d] Data from Metals Handbook.
[e] Data from Aluminum Co. of America.
[f] Acoustic impedance is the product of sound speed and density, $z=c\rho$.
[g] Dynamic yield strengths of the aluminum alloys were calculated from estimates of Whiffin, communicated by letter, for the ratio of the dynamic to the static yield strength.
[h] Dynamic yield strength of copper is that given by Whiffin [2].

plate and unprimed quantities refer to the material of the liquid drop. All quantities are in cgs units. Values of these quantities for the materials used for projectiles and targets are listed in table 2.

The development of eqs (1) and (2) has been given previously [1]. The conditions for valid use of these equations were discussed in section 1.

3.1. Collisions Between Metal Target Plates and Mercury Drops

The experimental pit depths for collisions of 0.1- and 0.2-cm mercury drops against target plates of annealed electrolytic tough pitch copper are listed in table 3. They are plotted in figure 1 along with theoretical curves calculated using eqs (1) and (2) and the data in table 2. The theoretical curves are in relatively good agreement with the experimental points. The effect of the change in drop size is properly accounted for by the theoretical equations. Curve A, calculated for the 0.1-cm drop size, is in better agreement with the observed depths produced by collision with 0.1-cm drops than curve B, calculated for the 0.2-cm drop size, is with the observed depths produced by collision with 0.2-cm drops. The assumption of spherical drops used in calculating drop diameters from the weight of the mercury drops can be expected to be more accurate for the smaller drop size. In this connection, it is noteworthy that there is more scatter in the experimental data for the 0.2-cm drop size.

TABLE 3. *Experimental data [a] for collisions of mercury drops of two sizes with annealed electrolytic tough pitch copper*

0.1-cm drops			0.2-cm drops		
Collision velocity	Drop diameter	Pit depth	Collision velocity	Drop diameter	Pit depth
10^4 *cm/sec*	*cm*	*cm*	10^4 *cm/sec*	*cm*	*cm*
1.965	0.0946	$.009_1$	1.773	0.2027	0.029_2
1.965	.0913	$.010_2$	2.402	.2002	$.047_8$
1.965	.1005	$.014_0$	2.542	.2064	$.066_0$
1.965	.0966	$.016_2$	2.716	.1989	$.059_7$
1.978	.1041	$.016_3$	2.779	.1953	$.058_7$
2.432	.0976	$.021_4$	2.841	.2030	$.064_0$
2.829	.1037	$.029_5$	2.850	.2113	$.074_7$
3.246	.1054	$.039_1$	2.865	.2012	$.065_5$
3.706	.1102	$.044_4$	2.865	.2012	$.067_8$
3.761	.0981	$.043_7$	2.890	.2004	$.065_0$
3.944	.1070	$.051_3$	2.984	.1991	$.077_0$
4.401	.1045	$.058_7$	3.225	.2032	$.082_3$
4.724	.0991	$.061_5$	3.310	.1889	$.076_7$
5.038	.0951	$.059_9$	3.313	.1951	$.076_8$
5.371	.0890	$.064_5$	3.438	.2006	$.073_7$
5.779	.0956	$.074_2$	3.575	.1972	$.094_7$
6.126	.1045	$.083_6$	3.663	.2032	$.131_8$
6.486	.0951	$.084_6$	3.697	.1997	$.083_4$
6.772	.1041	$.097_3$	3.986	.2011	$.123_2$
7.090	.0991	$.093_0$	4.084	.2006	$.107_3$
7.388	.1010	$.093_2$	4.096	.2004	$.110_7$
7.526	.0991	$.097_0$	4.322	.2048	$.122_7$
8.074	.0935	$.097_0$	4.401	.2003	$.123_2$
8.409	.1065	$.116_8$	4.450	.2025	$.123_4$
8.708	.1019	$.113_8$	4.862	.1990	$.135_1$
9.832	.1028	$.138_9$	5.919	.2099	$.191_1$
10.50	.1036	$.130_3$	6.969	.2046	$.179_2$
			6.315	.2018	$.177_5$
			6.410	.1995	$.169_9$
			6.461	.1990	$.199_9$

[a] See footnote 2.

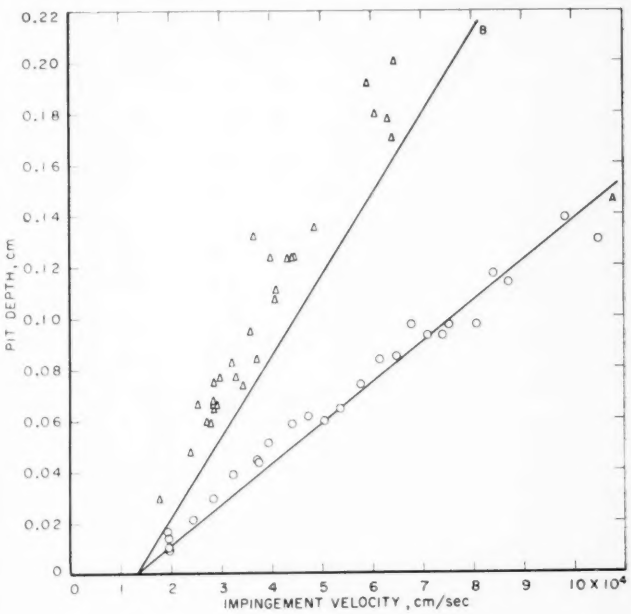

FIGURE 1. *Collisions of mercury drops of two sizes against annealed electrolytic tough pitch copper.*

Curve A, calculated using eqs (1) and (2) for 0.1-cm drops;
⊙, observed depth produced by collision with 0.1-cm drops;
Curve B, calculated using eqs (1) and (2) for 0.2-cm drops;
△, observed depth produced by collision with 0.2-cm drops.

On the other hand, if the calculated intercept velocity, V_i, had been a little smaller, the fit would have been better. The dynamic compressive yield strength reported by Whiffin [2] for electrolytic copper was used for E' in computing V_i for the theoretical curves (see table 2). It is not known if the electrolytic copper for which Whiffin [2] obtained the dynamic compressive yield strength was equivalent to the electrolytic tough pitch copper that was used for the target plates. Whiffin [2] did not report the static yield strength of the electrolytic copper that he used; he described it as being normally very soft and giving no definite indication of yield strength in static compression tests. No formula exists for copper by means of which the dynamic compressive yield strength can be calculated from the static yield strength; however, the latter provides a means of identification that can be reproduced by others.

The experimental pit depths for collisions of 0.1- and 0.2-cm mercury drops with target plates of 2024–O aluminum are listed in table 4. They are plotted in figure 2 with the theoretical curves calculated using eqs (1) and (2) and the data in table 2. The theoretical curves are in reasonably good agreement with the experimental points. As was found to be true in figure 1, the effect of the change in drop size is properly accounted for by the theoretical equations. As in the case of the copper targets,

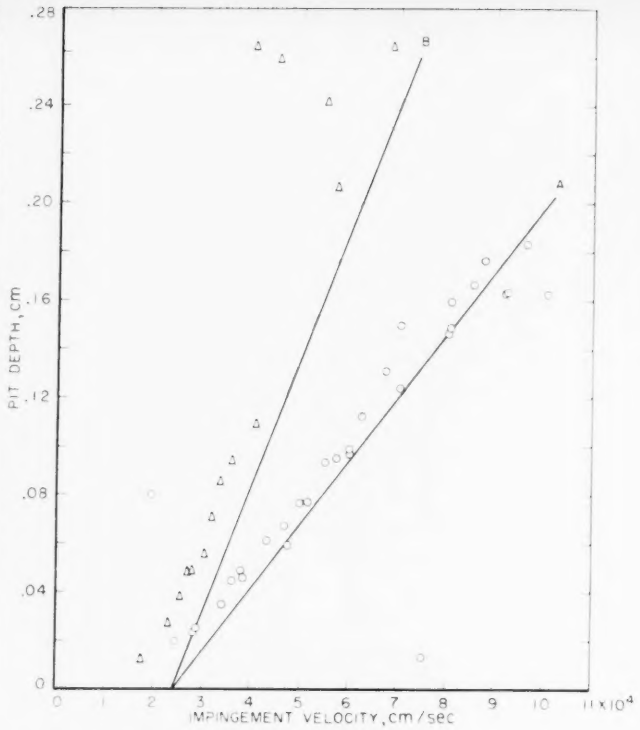

FIGURE 2. *Collisions of mercury drops of two sizes against 2024–O aluminum*

Curve A, calculated using eqs (1) and (2) for 0.1-cm drops; ⊙, observed depth produced by collision with 0.1-cm drops; Curve B, calculated using eqs (1) and (2) for 0.2-cm drops; △, observed depth produced by collision with 0.2-cm drops.

TABLE 4. *Experimental data[a] for collisions of mercury drops of two sizes with 2024–O aluminum*

0.1-cm drops			0.2-cm drops		
Collision velocity	Drop diameter	Pit depth	Collision velocity	Drop diameter	Pit depth
10^4 *cm/sec*	*cm*	*cm*	10^4 *cm/sec*	*cm*	*cm*
1.966	0.1022	0.080$_6$	1.759	0.19514	0.012$_4$
2.454	.0956	.020$_1$	2.316	.19175	.027$_2$
2.816	.0940	.023$_4$	2.554	.1998	.038$_1$
2.890	.1032	.025$_6$	2.682	.20122	.048$_4$
3.413	.0976	.035$_5$	2.789	.1969	.049$_0$
3.627	.0966	.044$_2$	3.048	.1984	.055$_9$
3.797	.1037	.049$_6$	3.200	.2017	.071$_1$
3.822	.0996	.046$_1$	3.377	.19672	.085$_6$
4.322	.1037	.061$_3$	3.596	.20330	.094$_4$
4.669	.1009	.067$_6$	4.008	.2047	.264$_2$
4.745	.0946	.059$_4$	4.084	.2031	.109$_5$
4.995	.1041	.076$_2$	4.517	.2010	.259$_1$
5.145	.1000	.077$_2$	5.489	.20572	.241$_5$
5.517	.1058	.093$_7$	5.727	.2000	.206$_5$
5.752	.1014	.095$_5$	6.834	.1982	.264$_7$
6.004	.0971	.099$_1$			
6.066	.0961	.095$_8$			
6.251	.1032	.112$_5$			
6.736	.1028	.130$_8$			
7.047	.0971	.124$_1$			
7.047	.0971	.149$_9$			
7.525	.1032	.013$_3$			
8.019	.1028	.146$_5$			
8.071	.1037	.159$_8$			
8.074	.1014	.148$_8$			
8.525	.1023	.166$_5$			
8.772	.1045	.176$_3$			
9.195	.0946	.162$_7$			
9.229	.0966	.163$_6$			
9.623	.1019	.182$_9$			
10.06	.0956	.162$_8$			

[a] See footnote 2.

curve A, calculated for the 0.1-cm drop size, is in better agreement with the observed depths produced by collision with 0.1-cm drops than curve B, calculated for the 0.2-cm drop size, is with the observed depths produced by collision with 0.2-cm drops. There is quite a bit of scatter in the experimental points for both drop sizes.

As in the case of the pit-depth-versus-velocity data for copper, there would be better agreement between the theoretical curves and the empirical data if the calculated intercept velocity, V_i, were smaller. In the case of the 2024–O aluminum, the dynamic yield strength used for E' in computing V_i was calculated from the measured static yield strength (see table 2) and should be fairly reliable.

The numerical constants used in eqs (1) and(2) were originally chosen [1] using pit-depth-versus-velocity data (see footnote 2) for metals whose static yield strength and whose sound speed in infinite medium were not measured experimentally. It may be found necessary to change the constants in the equations to some extent when more pit-depth-versus-velocity data become available using targets of metals for which these quantities have been measured.

Although eq (2) appears to be the most acceptable expression for the intercept velocity on the basis of the available experimental data for collisions of

liquid drops against solids [1], it is possible that, when more data are obtained and the problem is studied further, it may be found necessary to modify it.

3.2. Collisions Between Metal Target Plates and Waterdrops

The experimental pit depths for collisions of 0.2-cm waterdrops against target plates of annealed electrolytic tough pitch copper are listed in table 5. They are plotted in figure 3 with the theoretical curve calculated using eq (1) and (2) and the data in table 2. The theoretical curve is in acceptable agreement both as to slope and intercept with the experimental data. There is, unfortunately, a large amount of scatter in the experimental data which reduces their effectiveness as a check of the theoretical equations.

TABLE 5. *Experimental data[a] for collisions of 0.2-cm waterdrops with annealed electrolytic tough pitch copper*

Collision velocity	Pit depth
10^4 *cm/sec*	*cm*
4.593	0.003_3
4.983	$.005_1$
5.297	$.009_1$
5.486	$.003_5$
6.111	$.010_4$
6.584	$.009_9$
6.660	$.006_1$
7.041	$.013_6$
7.041	$.019_2$
8.839	$.017_0$

[a] See footnote 2.

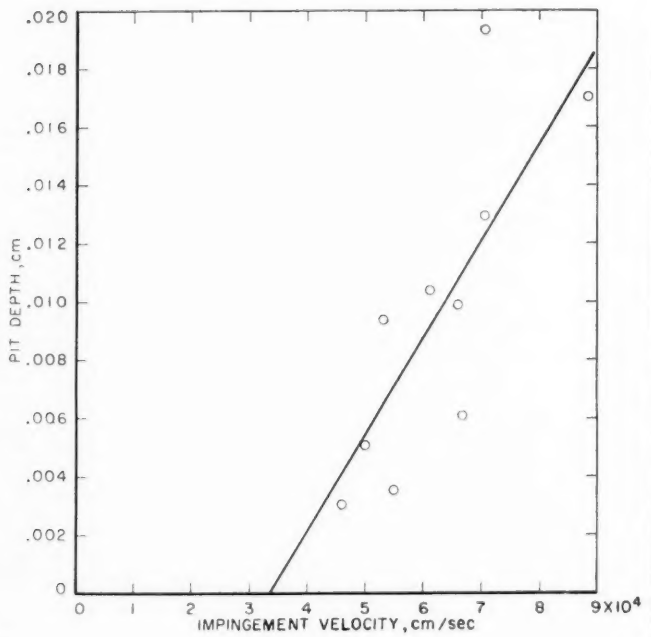

FIGURE 3. *Collisions of 0.2-cm waterdrops against annealed electrolytic tough pitch copper*

———, calculated using eqs (1) and (2) for 0.2-cm drops; ⊙, observed depth produced by collision with 0.2-cm drops.

The experimental pit depths for collisions of 0.2-cm waterdrops against target plates of 2024–O aluminum are listed in table 6. They are plotted in figure 4 with the theoretical curve calculated using eqs (1) and (2) and the data of table 2. The theoretical curve is a good fit for the experimental data both as to slope and intercept. This is more significant than the extent of agreement found between the theoretical curve and the experimental data in figure 3 because there is considerably less scatter in these data than in those obtained with the copper targets.

The agreement found between the theoretical curves and the experimental data in figures 3 and 4 is an indication that eqs (1) and (2) may be reliable

TABLE 6. *Experimental data[a] for collisions of 0.2-cm waterdrops with 2024–O aluminum*

Collision velocity	Pit depth
10^4 *cm/sec*	*cm*
4.581	0.002_3
4.581	$.002_5$
4.852	$.005_3$
5.456	$.004_6$
6.370	$.010_7$
6.584	$.011_7$
7.224	$.014_7$
7.498	$.020_6$

[a] See footnote 2.

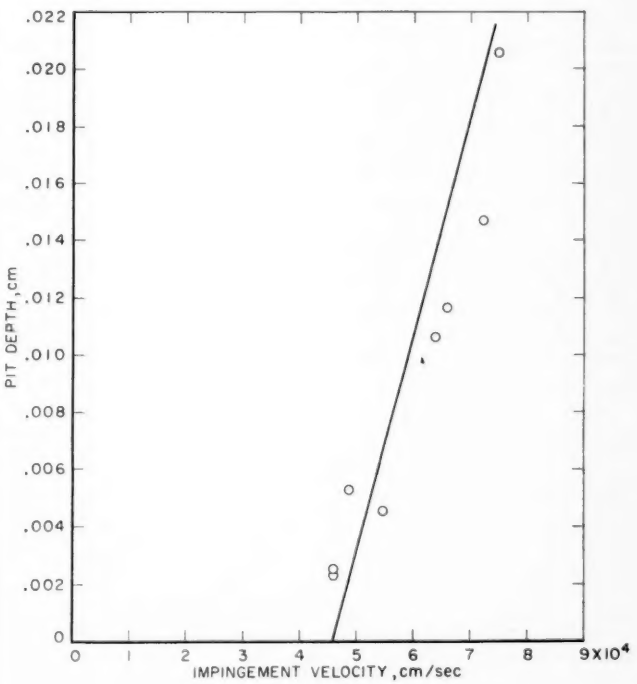

FIGURE 4. *Collisions of 0.2-cm waterdrops against* 2024–O *aluminum.*

———, calculated using eqs (1) and (2) for 0.2-cm drops; ⊙, observed depth produced by collision with 0.2-cm drops.

in their present form for calculating the depths of pits formed in the soft and medium hard metals as a result of collision with liquid drops. Although the speed of sound in mercury is nearly identical with the speed of sound in water, the density, and, therefore, the acoustic impedance, of mercury is very much higher than that of water. Further test of the equations should be made, however, using drops of a liquid that has a sound speed different from that of mercury or water.

4. Solid-Against-Solid Collisions

Because the pit-depth-versus-velocity equation developed [1] for collisions of target plates of the soft and medium hard metals with liquid drops ignored such characteristic fluid-flow parameters as the Weber number and the Reynolds number, it should apply equally well to pits produced by collision of solid spheres with target plates of the same types of metals. The equation may, in fact, be substantiated further with data of this kind. To explore this possibility, 2.5-cm- (1-in.-) thick plates of 1100–O aluminum, 2024–O aluminum, and annealed electrolytic tough pitch copper were used as targets for steel sphere impingement. The test firings were made at the U.S. Naval Research Laboratory in Washington, D.C., under the direction of Mr. Wilfred J. Ferguson and Mr. Harry O. Ewing. Most of the shots were made using a target mounting in which the plate was given edge support only. In this form of mounting the rear face of the target plate was a free surface. These data are presented and discussed in sections 4.1, 4.2, and 4.3. One set of data was obtained for collisions of steel spheres against 2024–O aluminum target plates backed with a 12.7-by-15.2-cm (5-by-6-in.) steel supporting block 7.6-cm (3-in.) thick. In this form of mounting the rear face of the target plate was not a free surface. These data are presented and discussed in section 4.4.

The velocity measurements were made using a Potter chronograph. The base length was 30.5 cm (12 in.). The chronograph was started and stopped by breaking conducting grids. The distance from the midpoint of the base length to the target face was 58.4 cm (23 in.); the velocity measurements were not corrected for deceleration of the steel spheres during transit over this distance.

The steel spheres were SKF Grade 1 and had an approximate hardness of 60 on the Rockwell C scale. These spheres have a high order of accuracy in dimensions because they are made for ball bearings. Three sphere sizes were used for the firings: 0.5556-cm ($\frac{7}{32}$-in.), 0.7938-cm ($\frac{5}{16}$-in.), and 1.270-cm ($\frac{1}{2}$-in.) diameter.

The depths of the pits produced by impingement of the steel spheres against target plates of the three metals were measured using an Ames dial gauge graduated in mils. Each depth measurement is the difference between the dial reading at the pit bottom and an average of four dial readings taken on the surface of the target plate around the mouth of the crater.

4.1. Collisions of Steel Spheres With Target Plates of 1100–O Aluminum

The velocities at which the shots were made and the depths of the pits produced in the 1100–O aluminum plates are given in table 7 for the three sizes of steel spheres used.

The pit-depth-versus-velocity curve for collisions of steel spheres with 1100–O aluminum was first calculated according to the equations that were developed for collisions between metal target plates and liquid drops. Although the experimental pit-depth-versus-velocity data were found to lie along straight lines, the slope of the lines was found to be much steeper than that of the lines given by the pit-depth-versus-velocity equation for collision of liquid drops against target plates of the soft and medium hard metals. This is to be expected because in the case of the very hard steel-sphere projectiles most of the collision energy is used in forming the pits, whereas in the case of projectiles that flow during and as a result of the collision, part of the collision energy is used in the flow of the projectile.

TABLE 7. *Experimental data* [a] *for collisions of steel spheres of three sizes with 1100–O aluminum*

Sphere diameter 0.5556 cm (7/32 in.)		Sphere diameter 0.7938 cm (5/16 in.)		Sphere diameter 1.270 cm (1/2 in.)	
Velocity	Pit depth	Velocity	Pit depth	Velocity	Pit depth
10^3 *cm/sec*	*cm*	10^3 *cm/sec*	*cm*	10^3 *cm/sec*	*cm*
0.9784	0.10$_5$	0.7163	0.11$_0$	0.887	0.22$_4$
1.018	.10$_4$	.9723	.14$_8$	1.055	.27$_2$
1.049	.10$_7$	1.265	.19$_2$	1.295	.32$_6$
1.411	.14$_8$	1.414	.21$_2$	1.558	.37$_5$
1.457	.15$_1$	1.490	.22$_4$	1.609	.39$_2$
1.704	.18$_0$	1.506	.23$_4$	1.759	.44$_8$
1.871	.19$_9$	1.530	.23$_4$	1.807	.46$_0$
2.140	.22$_6$	1.646	.25$_3$	2.009	.52$_0$
2.146	.23$_1$	1.661	.25$_6$	2.082	.55$_6$
2.576	.29$_1$	1.783	.27$_6$	2.121	.60$_8$
2.865	.34$_4$	1.789	.27$_5$	2.128	.55$_4$
3.103	.37$_1$	1.862	.29$_6$	2.414	.65$_9$
		1.993	.31$_7$		
		2.137	.34$_1$		
		2.423	.37$_8$		

[a] These data were obtained at the U.S. Naval Research Laboratory, Washington, D.C.

To fit the experimental data, it was found by trial that it was necessary to increase the numerical constant in the expression for pit depth to 17.5 and to reduce the numerical constant in the expression for the intercept velocity to 1. With these changes, the pit-depth-versus-velocity equation for collisions of projectiles that neither flow nor undergo appreciable permanent yield with targets of the soft and medium hard metals is

$$\delta' = [17.5\ d\ z/c(z+z')]\cdot[V - V_i] \tag{3}$$

where

$$V_i = E'\ (z+z')/(\rho c' z'^3)^{\frac{1}{2}} \tag{4}$$

The theoretical pit-depth-versus-velocity curves, calculated using eqs (3) and (4) and the data in table 2, for collisions of steel spheres of three sizes against

1100–O aluminum target plates are shown with the experimentally determined points in figure 5. The experimental points lie along the theoretical curves. In particular, it can be seen that the effect of a change in sphere size is properly accounted for by the equations.

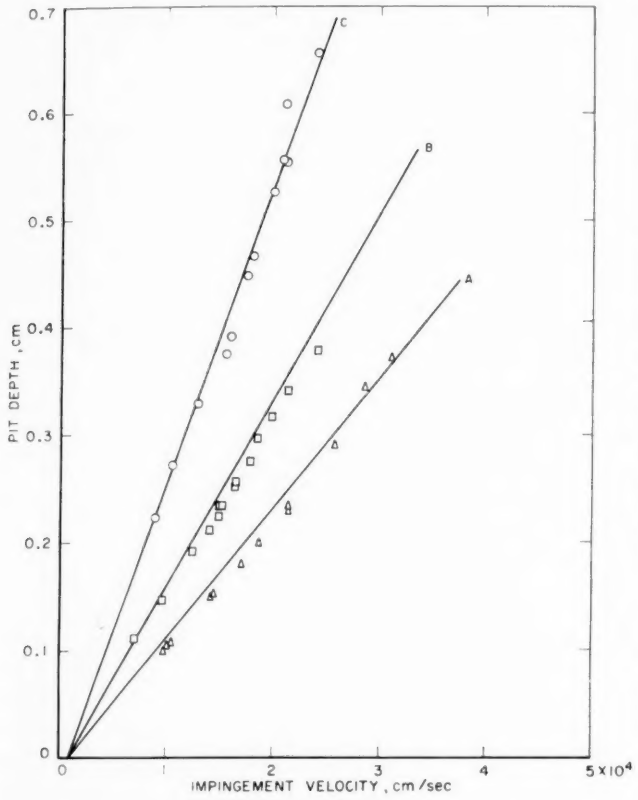

FIGURE 5. *Collisions of steel spheres of three sizes against 1100–O aluminum.*

Curve A, calculated using eqs (3) and (4) for 0.5556-cm (7/32-in.) spheres; △, observed depth produced by collision with 0.5556-cm (7/32-in.) spheres; Curve B, calculated using eqs (3) and (4) for 0.7938-cm (5/16-in.) spheres; ⊡, observed depth produced by collision with 0.7938-cm (5/16-in.) spheres; Curve C, calculated using eqs (3) and (4) for 1.270-cm (1/2-in.) spheres; ⊙, observed depth produced by collision with 1.270-cm (1/2-in.) spheres.

4.2. Collisions of Steel Spheres With Target Plates of Annealed Electrolytic Tough Pitch Copper

The velocity at which the shots were made and the depth of the pits produced with three sizes of steel spheres against 2.5-cm-(1-in.-) thick plates of annealed electrolytic tough pitch copper are given in table 8. Theoretical pit-depth-versus-velocity curves, calculated using eq (3) and (4) and the data in table 2, are shown with the experimentally determined points in figure 6. There is quite a bit of scatter in the experimental data for the 1.270-cm-(1/2-in.-) diam steel spheres. Nevertheless, there is, in general, good agreement between the theoretical curves and the observed points. The effect of a change in sphere size is properly accounted for by the equations.

TABLE 8. *Experimental data* [a] *for collisions of steel spheres of three sizes with annealed electrolytic tough pitch copper*

Sphere diameter 0.5556 cm (7/32 in.)		Sphere diameter 0.7938 cm (5/16 in.)		Sphere diameter 1.270 cm (1/2 in.)	
Velocity	Pit depth	Velocity	Pit depth	Velocity	Pit depth
10^4 *cm/sec*	*cm*	10^4 *cm/sec*	*cm*	10^4 *cm/sec*	*cm*
1.100	0.08$_7$	0.7803	0.09$_0$	0.4084	0.08$_3$
1.372	.10$_3$	.9388	.10$_9$	.4389	.09$_2$
1.500	.15$_4$	1.119	.12$_4$	.9601	.18$_4$
1.878	.13$_8$	1.283	.14$_5$	1.353	.24$_0$
1.981	.14$_3$	1.588	.17$_3$	1.411	.24$_9$
2.121	.15$_6$	1.740	.18$_8$	1.426	.25$_0$
2.124	.15$_9$	2.280	.24$_9$	1.451	.30$_9$
2.158	.16$_7$	2.377	.26$_2$	1.868	.30$_1$
2.225	.16$_6$	2.457	.27$_4$	1.966	.35$_4$
2.234	.16$_8$			2.036	.36$_9$
2.256	.17$_0$			2.060	.37$_7$
2.271	.17$_2$			2.134	.42$_5$
2.316	.17$_6$			2.204	.39$_5$
2.646	.20$_2$			2.216	.40$_0$
2.685	.20$_6$			2.694	.57$_3$
2.960	.23$_3$			2.704	.38$_8$
3.560	.28$_9$			3.066	.58$_0$
				3.109	.49$_5$
				3.225	.62$_2$
				3.432	.63$_8$

[a] These data were obtained at the U.S. Naval Research Laboratory, Washton, D.C.

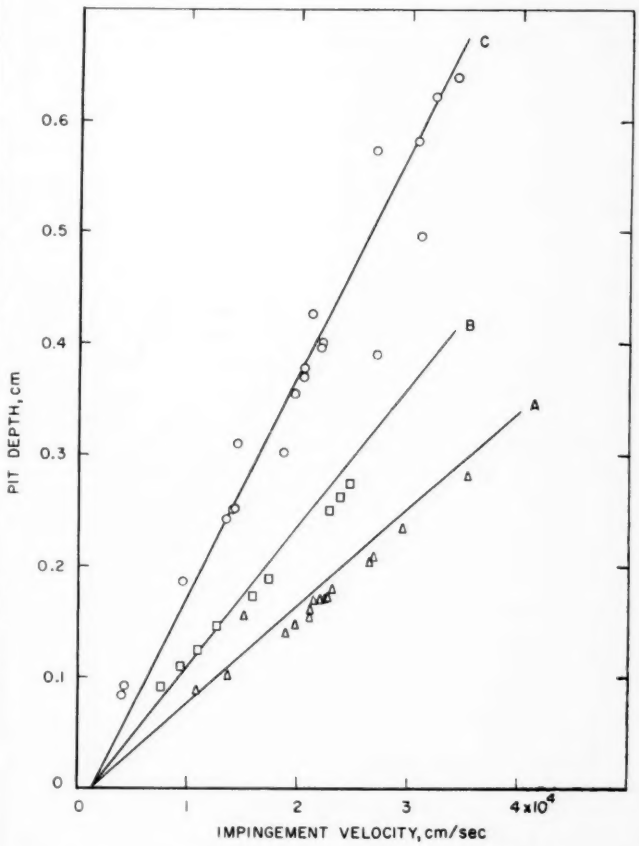

FIGURE 6. *Collisions of steel spheres of three sizes against annealed electrolytic tough pitch copper.*

Curve A, calculated using eqs (3) and (4) for 0.5556-cm (7/32-in.) spheres; △, observed depth produced by collision with 0.5556-cm (7/32-in.) spheres; Curve B, calculated using eqs (3) and (4) for 0.7938-cm (5/16-in.) spheres; ⊡, observed depth produced by collision with 0.7938-cm (5/16-in.) spheres; Curve C, calculated using eqs (3) and (4) for 1.270-cm (1/2-in.) spheres; ⊙, observed depth produced by collision with 1.270-cm (1/2-in.) spheres

4.3. Collisions of Steel Spheres With Target Plates of 2024–O Aluminum

The velocity at which shots with three sphere sizes were made against plates of 2024–O aluminum and the depths of the pits that were produced by the shots are given in table 9. Theoretical pit-depth-versus-velocity curves calculated using eq (3) and (4) and the data in table 2 are shown with the experimental data in figure 7. For each sphere size used, the experimental points lie below the theoretical curve.

TABLE 9. *Experimental data* [a] *for collisions of steel spheres of three sizes with* 2024–O *aluminum*

Sphere diameter 0.5556 cm (7/32 in.)		Sphere diameter 0.7938 cm (5/16 in.)		Sphere diameter 1.270 cm (1/2 in.)	
Velocity	Pit depth	Velocity	Pit depth	Velocity	Pit depth
10^4 *cm/sec*	*cm*	10^4 *cm/sec*	*cm*	10^4 *cm/sec*	*cm*
1.113	0.07½	0.7894	0.08½	0.5578	0.19½
1.451	.10½	1.067	.10½	.5822	.17½
1.542	.10½	1.305	.14½	1.207	.33½
1.981	.13½	1.698	.17½	1.326	.26½
2.173	.15½	1.771	.18½	1.460	.24½
2.274	.18½	1.832	.18½	2.039	.34½
2.368	.16½	2.856	.34½	2.722	.48½
2.448	.17½			2.780	.49½
2.701	.19½			2.786	.49½
				3.301	.67½
				3.484	.39½
				3.518	.62½
				3.658	.60½

[a] These data were obtained at the U.S. Naval Research Laboratory, Washington, D.C.

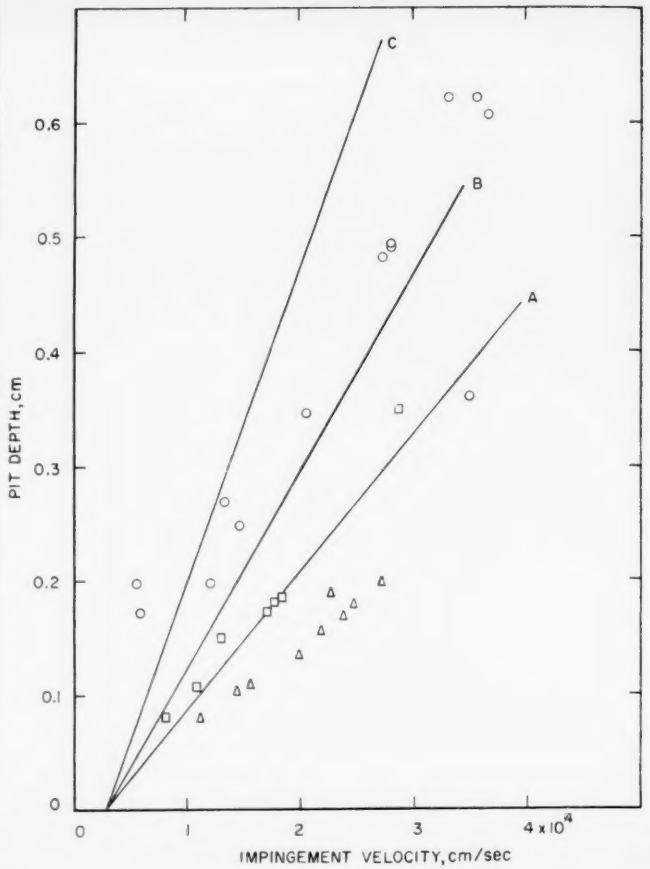

FIGURE 7. *Collisions of steel spheres of three sizes against* 2024–O *aluminum.*

Curve A, calculated using eqs (3) and (4) for 0.5556-cm (7/32-in.) spheres; △, observed depth produced by collision with 0.5556-cm (7/32-in.) spheres; Curve B, calculated using eqs (3) and (4) for 0.7938-cm (5/16-in.) spheres; □, observed depth produced by collision with 0.7938-cm (5/16-in.) spheres; Curve C, calculated using eqs (3) and (4) for 1.270-cm (1/2-in.) spheres; ⊙, observed depth produced by collision with 1.270-cm (1/2-in.) spheres.

Four possible reasons for this discrepancy were explored. (1) In steel-sphere collisions with materials as strong as 2024–O aluminum the steel sphere may be permanently deformed and in this way part of the collision energy may be diverted from pit formation, whereas in the case of the very soft metals all of the collision energy may go into pit formation. (2) In view of the fact that heat-treated 2024 aluminum is subject to spalling, energy may be diverted from pit formation into crack formation, although this is unlikely in the case of the annealed metal. (3) Sound is attenuated to different degrees in the target metals used. (4) The target metals that were used work-harden by different amounts.

To check the first possibility, two 1.270-cm-(½-in.-) diam steel spheres that were fired against target plates of annealed copper and 2024–O aluminum, respectively, were recovered. The sphere that struck the copper target plate had a collision velocity of 3.432×10^4 cm/sec (1,126 ft/sec) and the sphere that struck the 2024–O aluminum target plate had a collision velocity of 3.650×10^4 cm/sec (1,200 ft/sec). These spheres were examined with a microinterferometer in the NBS Engineering Metrology Section. It was found that the diameter measured through the impact area of the sphere shot into copper was 0.0025 cm (0.0010 in.) smaller than diameters measured outside of the impact area and that the diameter measured through the impact area of the sphere that was shot into 2024–O aluminum was 0.00020 cm (0.00008 in.) smaller than diameters measured outside of the impact area. On the basis of this evidence it cannot be concluded that a larger percentage of the impact energy is absorbed by a steel sphere on colliding with 2024–O aluminum than on colliding with annealed copper. In fact, the reverse is the case. Deformation of the steel sphere is not the cause of the divergence of the 2024–O aluminum experimental pit-depth-versus-velocity data from the theoretical curves.

Cross-sectional cuts of the pits produced by these spheres were mounted in epoxy plastic in the NBS Mechanical Metallurgy Section (see fig. 8). They were given a high polish and examined with a microscope for evidence of crack formation. No evidence of crack formation was found. The cross section of the pit in 2024–O aluminum was then etched in an effort to accentuate any cracks if they existed, but no cracks were found. Crack formation in the tar-

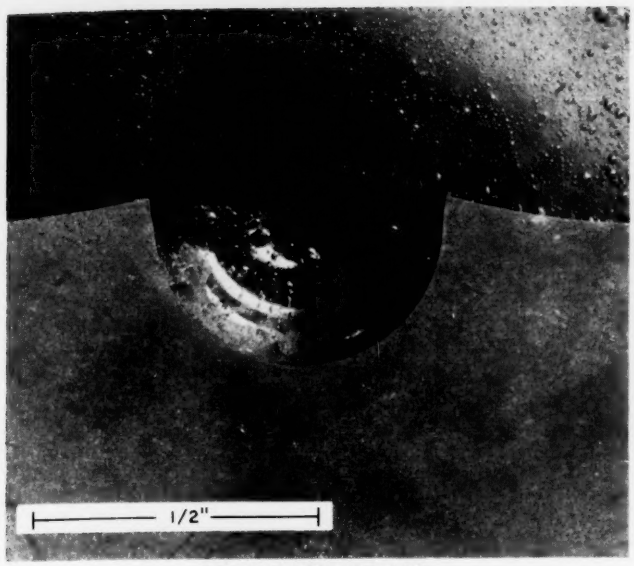

PIT IN ALUMINUM ALLOY

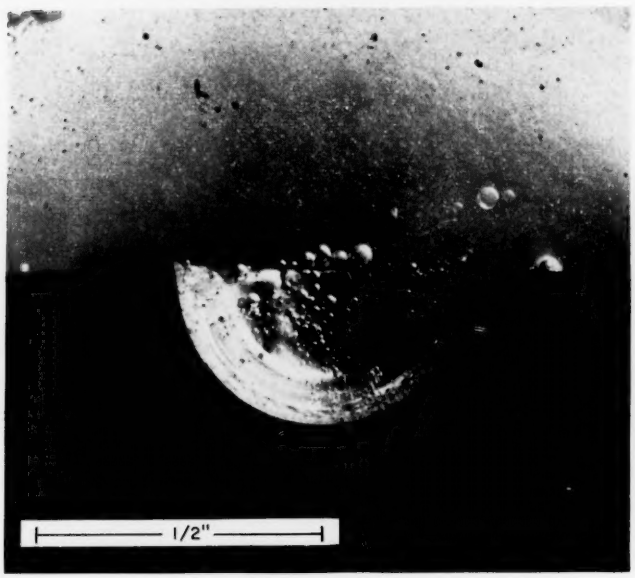

PIT IN COPPER

FIGURE 8. *Cross sections of pits produced by collision of a 1.270-cm (½-in.) steel sphere with annealed electrolytic tough pitch copper and with* 2024–O *aluminum.*

get is, therefore, not the cause of the divergence of the 2024–O aluminum experimental pit-depth-versus-velocity data from the theoretical curves.

It was then thought that the compressional wave caused by the collision may have reflected as a tension wave from the free reverse surface of the 2024–O aluminum target plate and may have returned to the collision surface with the effect of filling in the pits. This possibility is in agreement with the fact that attenuation of sound is greater in 1100–O aluminum and in annealed copper than it is in 2024–O aluminum.

To test this possibility a 1.59-cm-(⅝-in.-) thick plate of 1100 aluminum was cut to fit one of the 2.5-cm (1-in.-) thick target plates of 2024–O aluminum and was annealed under the same conditions as those that were used for the 1100–O aluminum targets. The contact surfaces between the two plates were machine ground and polished until, when they were pressed together, one plate was able to lift the other. They were tightly clamped together and 11 test firings were made against the combination target plate. The reverse (1100–O aluminum) face of the combination target plate was maintained as a free surface during the firings. Steel spheres 0.7938 cm (5/16 in.) in diameter were used for the shots.

It was hoped that if the compressional waves produced by the collisions had been returning to the collision surface as tension waves, they would now be prevented from doing this by attenuation on transit through the 1100–O aluminum. However, when the measured pit depths were plotted against the impingement velocity, it was found that the points were in complete agreement with those obtained without the 1100–O aluminum backing plate. The pit-depth-versus-velocity data are given in table 10. Apparently the return of the reflected tension wave to the collision surface is unable to explain the divergence of the 2024–O aluminum pit-depth-versus-velocity data from the theoretical curves. It is possible, however, that the degree of contact that was attained between the 2024–O aluminum target plate and 1100–O aluminum backing plate may not have been sufficient to ensure transmission of the elastic waves.

TABLE 10. *Experimental data*[a] *for collisions of* 5/16*-in. steel spheres with a* 2024–O *aluminum and* 1100–O *aluminum combination target*

Collision velocity	Pit depth
10^4 *cm/sec*	*cm*
0.9601	0.09$_6$
1.261	.12$_0$
1.478	.14$_9$
1.646	.16$_6$
1.890	.19$_3$
2.103	.22$_2$
2.603	.28$_0$
2.734	.29$_7$
2.841	.29$_4$
3.203	.36$_6$
3.755	.45$_3$

[a] These data were obtained at the U.S. Naval Research Laboratory, Washington, D.C.

The explanation was finally sought in the work-hardening properties of the three target metals. When a rigid sphere impinges against a metal target plate, shear stresses exist around the cylinder of target metal that is set in motion as a result of the collision, as indicated by the arrows marked τ_A in figure 9. Shear stresses also exist in the target metal around the point of impingement as indicated by the arrows marked τ_B in figure 9. It seems reason-

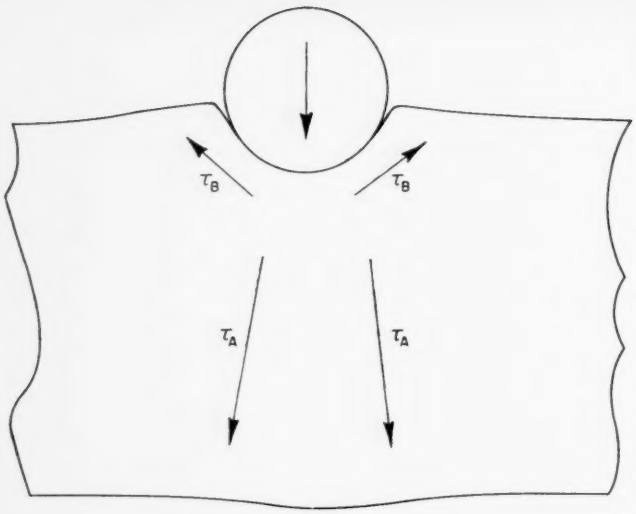

FIGURE 9. *Shear stresses produced in a metal plate by an impinging steel sphere.*

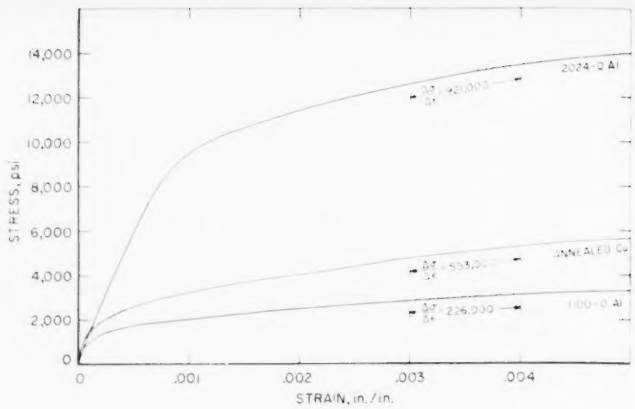

FIGURE 10. *Stress-strain curves for* 1100–O *aluminum,* 2024–O *aluminum, and annealed electrolytic tough pitch copper.*

able that, if the metal does not work-harden readily, or if the τ_B-shear stress is small, most of the plastic flow that takes place will occur as a result of the shear stress τ_A that exists below the collision area. If, however, the metal work-hardens extensively while this process is initiated, then flow as a result of the shear stress τ_A will be inhibited. In this case flow will occur as a result of the shear stress τ_B, if the τ_B-shear stress is appreciable, and the surface of the metal will be raised in a ring around the mouth of the pit that forms as a result of the collision.

It can be seen by laying a straight edge across the mouths of the crater cross sections shown in figure 8 that there is a considerable elevation of the target metal around the crater in the case of the 2024–O aluminum. Visual inspection of the target plates revealed that there was some rising of metal around the craters, especially in the case of the largest sphere size, for each of the target metals used. It appeared, however, to have occurred to a somewhat greater degree in the case of the 2024–O aluminum than in the case of the 1100–O aluminum or of the annealed electrolytic tough pitch copper.

Equations (1), (2), (3), and (4) were developed on the assumption that the principal movement that occurs as a result of a liquid-drop or of a steel-sphere collision with a metal target plate is that of the core of metal under the collision area [1]. If any other flow process (such as that resulting from the shear stress τ_B) becomes appreciable in a specific target metal, these equations cannot be expected to apply to pits formed in that metal.

The tensile stress-strain curves (fig. 10) provide a means of comparing the work-hardening properties of the 1100–O aluminum, annealed electrolytic tough pitch copper, and 2024–O aluminum used in the collision experiments. Work-hardening of metals may be evaluated by the tangent modulus [4]. The tangent moduli for the three metals in the range of strain from 0.003 to 0.004 are 1.56×10^{10} d/cm^2 (226,000 psi), 3.81×10^{10} d/cm^2 (553,000 psi), and 6.35×10^{10} d/cm^2 (921,000 psi), respectively. These data suggest that the 2024–O aluminum work-hardens much more than does the annealed electrolytic tough pitch copper or the 1100–O aluminum. Copper is the main alloying element in 2024 aluminum. Thomas and Nutting [5] have also found that aluminum-copper alloys that were given a 4-hr soak at 535° C (995° F) followed by water quenching work-hardened more than pure aluminum that was annealed for 3 hr at 600° C (1,112° F).

The work-hardening behavior of the three metals is in agreement with the fact that the pit-depth-versus-velocity data for 1100–O aluminum and for annealed electrolytic tough pitch copper are well fitted by the theoretical curves calculated using eq (3) and (4), whereas those for 2024–O aluminum are not. It is possible that the plastic yield that occurs in 1100–O aluminum and in annealed electrolytic tough pitch copper as a result of impingement of steel spheres may be caused almost entirely by the shear stress τ_A, whereas the plastic yield that occurs in 2024–O aluminum as a result of impingement of steel spheres may be caused both by the shear stress τ_A and the shear stress τ_B.

For mercury-drop and waterdrop impingement the pit-depth-versus-velocity data for 2024–O aluminum were well fitted by the theoretical curves calculated with use of eqs (1) and (2) (see fig. 2 and 4). This is not a contradiction because it is likely that the τ_B-shear stress is smaller for the case of projectiles that flow during and as a result of the collision than for the case of projectiles that do not flow.

More data, using steel-sphere projectiles and target metals that have different work-hardening properties, are needed to prove whether or not this explanation is correct.

4.4. Collisions of Steel Spheres With Target Plates of 2024–O Aluminum That Were Backed With a Heavy Steel Supporting Block

It has been pointed out that eqs (1), (2), (3), and (4) only apply to the case in which the target plate has edge support during the firings; the reverse side of the target plate must be a free surface. This is because the model on which eqs (1), (2), (3), and (4) are based involves the movement of the core of target material under the collision area with respect to the remainder of the target plate [1]. If the target plate is backed by a heavy metal plate or block, the reverse face of the target plate is not a free surface, the core of material under the collision area is not free to move with respect to the remainder of the target plate, and eqs (1), (2), (3), and (4) do not apply.

Pit-depth-versus-velocity data were obtained for collisions of steel spheres of three sizes against 2.5-cm (1-in.-) thick target plates of 2024–O aluminum backed with a 12.7-by-15.2-cm (5-by-6-in.) steel supporting block 7.6-cm (3-in.) thick. These data are of no value as far as substantiation of eqs (1), (2), (3), and (4) is concerned. They are presented to show how the pit-depth-versus-velocity curve differs for the two modes of support of the target plate during the firings. These data are listed in table 11 and are plotted in figure 11 where best-fit curves have been drawn through the data for each size of steel sphere used. It can be seen from figures 7 and 11 that when the reverse side of the target plate is a free surface, the pit-depth-versus-velocity curve is a straight line, but that when the reverse side of the target plate is not a free surface (use of a backing plate or block), the pit-depth-versus-velocity curve is not a straight line.

For the case that the reverse face of the target plate is a free surface, the projectile is stopped by resistance to the movement of the core of metal under the contact area. For the case that the reverse face of the target plate is not a free surface, the projectile is stopped by resistance to extrusion of metal around the crater.

TABLE 11. *Experimental data* [a] *for collisions of steel spheres of three sizes with* 2024–O *aluminum backed with a steel supporting block*

Sphere diameter 0.5556 cm (7/32 in.)		Sphere diameter 0.7938 cm (5/16 in.)		Sphere diameter 1.270 cm (1/2 in.)	
Velocity	Pit depth	Velocity	Pit depth	Velocity	Pit depth
10^4 *cm/sec*	*cm*	10^4 *cm/sec*	*cm*	10^4 *cm/sec*	*cm*
1.106	0.74	0.6035	0.09	0.9753	0.16
1.192	.08	1.012	.11	.9845	.16
1.295	.08	1.186	.14	1.341	.23
1.548	.10	1.247	.12	1.664	.28
1.844	.12	1.356	.11	1.966	.33
2.027	.14	1.369	.13	2.094	.37
2.115	.14	1.384	.13	2.143	.37
2.208	.16	1.384	.13	2.146	.37
2.408	.17	1.417	.13	2.502	.43
2.438	.17	1.436	.14	2.697	.51
2.502	.18	1.481	.13	2.780	.49
2.609	.18	1.503	.14	3.283	.61
2.615	.19	1.622	.15	4.331	.46
2.615	.18	1.786	.17		
2.688	.19	1.823	.18		
3.036	.23	1.939	.19		
3.216	.25	2.057	.21		
		2.216	.23		
		2.640	.28		
		3.255	.37		
		3.572	.41		
		4.209	.52		
		4.846	.64		

[a] These data were obtained at the U.S. Naval Research Laboratory, Washington, D.C.

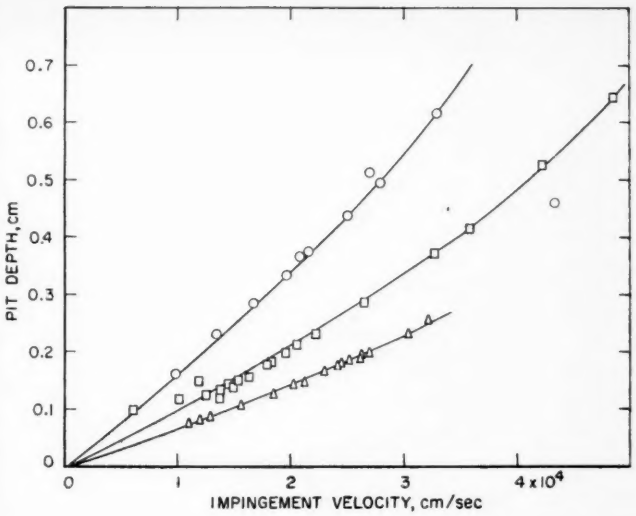

FIGURE 11. *Best-fit curves for collisions of steel spheres against* 2024–O *aluminum targets backed with a heavy steel supporting block.*

△, observed depth produced by collision with 0.5556-cm (7/32-in.) spheres; □, observed depth produced by collision with 0.7938-cm (5/16-in.) spheres; ⊙, observed depth produced by collision with 1.270-cm (1/2-in.) spheres.

5. Liquid-Against-Liquid Collisions

Very little study has been made of collisions that occur when liquid drops collide with a target liquid. It was postulated by Öpik [6] nearly 25 years ago, later by Pack and Evans [7], and recently by others [8] that at extremely high impingement velocities solid targets and projectiles will behave as though they were liquids. Öpik stated, "The 'aerodynamic' pressure at the penetration of a meteor into rock is of the order of 10^7–10^8 atmospheres, or more than 1,000 times the plastic limit of steel; no doubt all solid materials under such pressures must behave like liquids; thus the problem of meteor impact is the case of the impact of a liquid drop of given density δ into a liquid medium of density ρ."

It has been found that when solid-sphere projectiles made of the soft ductile metals are fired at sufficiently high impingement velocities against targets of the same metal, they flow like liquids during and as a result of the collision. Pit depth for such solid-against-solid collisions has been found [1] to be given by eqs (1) and (2) which apply to collisions of liquid drops against metal plates.

If the impingement velocity is increased further, it is reasonable to suppose that the behavior predicted by Öpik [6] will eventually be found; the target as well as the projectile will liquefy during the collision. For such collisions that occur at meteor velocities Öpik [6] found that the impingement velocity has only a small effect upon the depth of penetration. If this is the case, the pit-depth-versus-velocity curve for such collisions should run *almost* parallel to the velocity axis. The penetration formula developed by Pack and Evans [7] has no velocity dependence.

It appears that the straight-line, low-velocity, liquid-against-solid, and solid-against-solid pit-depth-versus-velocity curves for collisions of liquid drops and rigid steel spheres with metal plates must approach the high-speed liquid-against-liquid curve in some way when very high impingement velocities are reached. This is represented schematically in figure 12 where dashed lines have been used to indicate projected types of behavior.

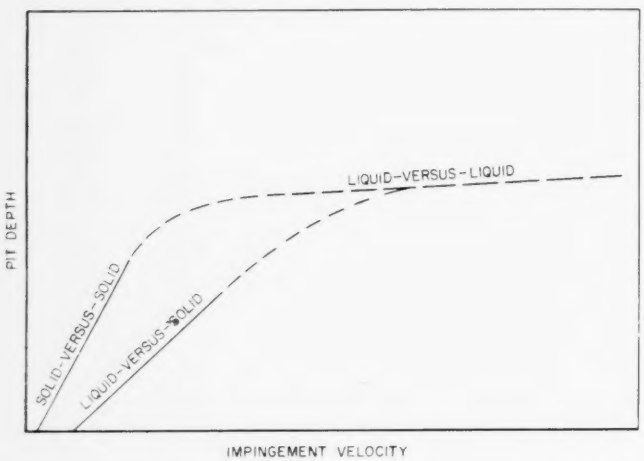

FIGURE 12. *Schematic relation between various types of projectile-target collisions.*

Equations (1), (2), (3), and (4) will not apply either in the transition regions or in the velocity range of high-speed liquid-against-liquid collisions. An analysis of liquid-against-liquid collisions is in progress.

6. References

[1] Olive Engel, Pits in metals caused by collision with liquid drops and soft metal spheres, NBS Journal of Research **62,** 229 (1959) RP2958.

[2] A. C. Whiffin, The use of flat-ended projectiles for determining dynamic yield stress, Proc. Roy Soc. (London) [A] **194,** 300 (1948).

[3] L. Bergmann, *Der Ultraschall*, S. Hirzel Verlag, Stuttgart, 1954.

[4] John M. Lessells, *Strength and resistance of metals* (John Wiley and Sons, Inc., New York, N.Y., 1954).

[5] G. Thomas and J. Nutting, The plastic deformation of aluminum and aluminum alloys, J. Inst. Metals **85,** 1 (1956).

[6] Ernst Öpik, Researches on the physical theory of meteor phenomena I, Toimetused, Acta et Commentationes, Universitatis Tartuensis, XXX, [A] 4 (1936) (Tartu, Estonia).

[7] D. C. Pack and W. M. Evans, Penetration of high-velocity ("Munroe") jets I and II, Proc. Phys. Soc. (London), LXIV B, 298, 303 (1951).

[8] See, for example, Proc. of Third Symposium on Hypervelocity Impact, Vol. I (Armour Research Foundation of Illinois Inst. Technol., Chicago, Ill., Feb., 1959).

WASHINGTON, D.C. (Paper 64A1–29)

JOURNAL OF RESEARCH of the National Bureau of Standards—A. Physics and Chemistry
Vol. 64A, No. 1, January–February 1960

Theory of Formation of Polymer Crystals with Folded Chains in Dilute Solution

John I. Lauritzen, Jr., and John D. Hoffman

(September 9, 1959)

A detailed interpretation of the kinetics of homogeneous nucleation and growth of crystals of a linear homopolymer from dilute solution is given. The probability of forming both nuclei with folded chains, and conventional bundlelike nuclei, from dilute solution is analyzed. It is predicted that at sufficiently high dilution, critical nuclei of length l_p^* will be formed from single polymer molecules by sharp folding of the chain backbone. The step height of the nucleus is given approximately by $l_p^* = 4\sigma_e/\Delta f$. Here σ_e is the free energy required to form a unit area of the loop-containing end surfaces, and Δf is the free energy difference per unit volume of crystal between the crystalline and solution states. The quantity Δf is approximately proportional to the degree of supercooling ΔT. The growth of these nuclei is then analyzed. After growth, the resulting crystal is flat and platelike, the loops formed by the chain folds being on the upper and lower surfaces. Kinetic factors determine that the distance between the flat surfaces in the grown crystal will vary over only a narrow range about a value that is in the vicinity of $l^* = 4\sigma_e/\Delta f$. (Neglecting effects due to edge free energies, the theoretical upper and lower limits are $l^* = 4\sigma_e/\Delta f$ and $l^* = 2\sigma_e/\Delta f$, respectively.) In some cases the predicted temperature dependence of the step height of the grown crystal, $l^* = \text{const.}/\Delta T$, may be modified by the existence of a constant term resulting from the presence of an edge free energy ϵ_p. A grown loop-type crystal is predicted to be stable in comparison with a bundlelike crystal of the same shape and volume in a sufficiently dilute solution. The logarithm of the nucleation rate is approximately proportional to $1/(\Delta T)^2$ near the melting point. The exponent n in the free growth rate law is predicted under various assumptions. To the extent that comparison is possible, the predictions given agree with the experimental results obtained by Keller and O'Connor and others on single crystals of unbranched polyethylene grown from dilute solution.

A survey is given of homogeneous nucleation in bulk polymers, where the conventional bundlelike nucleus containing segments from many different molecules is valid, and the essential results compared with those calculated for the dilute solution case.

The theory given for loop nuclei is both general and precise enough at the critical points to suggest that, on crystallization from sufficiently dilute solution, crystals of a definite step height are commonly to be expected for other crystallizable linear polymers than polyethylene, provided loop formation is sterically possible.

1. Introduction

Recently, a number of investigators [1, 2, 3, 4],[1] have prepared single crystals of high molecular weight linear polyethylene by precipitation from dilute solution through supercooling. As observed with an electron microscope, these crystals are shaped like flat parallelepipeds, and the X-ray studies of Keller [1, 2] show that the polymer chains are oriented perpendicular to the flat surfaces. The separation of the flat surfaces is nominally about 120A, and is sufficiently well defined to produce fourth-order reflections with low angle X-rays. The separation of the flat surfaces, which for convenience will be called the "step height," actually depends on the crystallization temperature, the step height being distinctly smaller at low crystallization temperatures than it is at high ones. Since the mean length of the polyethylene molecules is far in excess of 120A, Keller has proposed that the polymer molecules must be sharply folded in the crystals; the loops resulting from these folds form the two flat surfaces of the platelike crystals.

There appears to be no simple alternative to the initially somewhat startling proposal that the single crystals observed involve chain folding, and we believe that Keller's hypothesis may be accepted. Keller has indicated that the idea of chain folding in polymers is not entirely new, and refers to an earlier suggestion due to Storks [5].

The objective of this paper is to present a theoretical account of how polymer crystals with chain folds are formed in dilute solution, and why they have the properties they do. It will emerge that crystals with chain folds arise in dilute solution because a primary (homogeneous) nucleus of this type is on kinetic grounds the most likely to appear. Once such a nucleus is formed, it can be shown that the subsequent two-dimensional growth will closely follow the pattern established by the primary nucleus. Thus, the basic reasons such crystals form is to be found in the kinetics of nucleation and growth.

The situation is quite different for homogeneous nucleation in a highly crystallizable bulk polymer. First, the primary (homogeneous) nucleus in bulk polymers is thought to be formed by an alinement of segments of different polymer chains to form a

[1] Figures in brackets indicate the literature references at the end of this paper.

bundlelike nucleus without folds [6, 7], and second, the mean crystallite size in a semicrystalline bulk polymer that has not reached its equilibrium crystallite size distribution (a very difficultly achievable state by any account) is determined largely by the nature of impingements and chain entanglements, and possibly certain strain effects, together with the kinetics of nucleation and growth [6]. (The particular type of strain meant here is that which becomes increasingly great with radial growth.) Eventually, of course, the metastable distribution of crystallite sizes resulting from impingements will change as the impingements relax, and other mechanisms take place, and the equilibrium distribution with large crystallites will be slowly approached, but this does not alter the fact that impingements, entanglements, and possibly strain play an important, if not dominant, role in determining the crystallite size in bulk polymers as they are ordinarily found in the semicrystalline state. Impingements and entanglements, play no important role in impeding the crystallization in dilute solution.

In order to provide a clear development of the theory of crystallization of chain molecules from dilute solution, it is necessary first to bring out some general points connected with homogeneous nucleation theory. At the same time, it is advantageous to mention certain general features of homogeneously induced crystallization in bulk polymers.

2. Homogeneous Nucleation and Crystal Growth in Bulk Polymers

2.1. Homogeneous Nucleation in Bulk Polymers

According to Turnbull and Fisher [8], the equilibrium rate of homogeneous or primary nucleation in a supercooled bulk phase may be written as

$$I=\frac{NkT}{h}e^{-\Delta F^*_p/kT}e^{-\Delta\phi^*_p/kT} \tag{1}$$

where N is Avogadro's number, k Boltzmann's constant, h Planck's constant, T the absolute temperature, ΔF^*_p the free energy of activation of the supercooled-liquid—nucleus interface, and $\Delta\phi^*_p$ the free energy of formation of a primary (homogeneous) nucleus of critical size. In eq (1), I is in nuclei·mole^{-1}·sec^{-1}. The quantity $J=(kT/h)\exp[-\Delta F^*_p/kT]$, which is the jump rate in events per second at the interface, may be written as $(kT/h)\exp[\Delta S^*_p/k-\Delta H^*_p/kT]$, where ΔS^*_p is the entropy of activation, and ΔH^*_p the enthalpy of activation. For a polymer, it may be assumed that the smallest unit that may attach to the embryo or nucleus in an elementary process is a small segment of molecular weight M and length l_o. Hence we may write eq (1) in the form

$$I=I_0e^{-\Delta H^*_p/kT}e^{-\Delta\phi^*/kT} \tag{2}$$

where I_0 is $(NkT/hM\overline{V}_l)\exp(\Delta S^*_p/k)$, which has the units nuclei·cm^{-3}·sec^{-1}. The quantity $\overline{V}_l$ is the specific volume of the supercooled liquid at the temperature of crystallization. The main item of interest here is the form of $\Delta\phi^*_p$ for bulk polymers. The Turnbull-Fisher equation is derived on the assumption that many elementary steps are required to reach $\Delta\phi^*_p$.

In a bulk polymer, it is commonly assumed that the nucleus is bundlelike, and is formed through the alinement of segments of different polymer chains [6, 7]. This hypothesis certainly seems plausible for a bulk polymer, and can be used to give a detailed interpretation of the rate of injection of primary nuclei in a bulk polymer.

Two general types of bundlelike primary nuclei must be considered. The first of these is one where there is no minimum restriction on the length, or the number of segments contained in its cross-sectional area. Calculations for this nucleus yield results that are valid in a temperature range near the melting point, region A. The second is a nucleus where the length is restricted to l_0 (which is the length of a segment), but where the number of segments in the cross section is still unrestricted. Results obtained for this nucleus are valid in a temperature range, region B, that extends from somewhat below the melting point to a temperature that is considerably lower. A discussion of the properties of these two types of bundlelike nuclei has been given in an earlier publication [6], and what is given below is intended mainly as a summary. At still lower temperatures, region C type nucleation will prevail, and this will be brought into the discussion at the proper place.

Region A: Consider first the nucleus with unrestricted length and cross-sectional area. The model used is illustrated in figure 1*a*. For this nucleus, the free energy of formation may be written in a general way as

$$\Delta\phi_{p(A)}=2\nu a\sigma_e+C\sqrt{\nu a}l\sigma_s-\nu al\Delta f. \tag{3}$$

Here ν is the number of segments in the cross section of the nucleus, a the cross-sectional area of a segment, l the length of the nucleus, C a numerical constant that depends only on the shape of the cross section, and Δf the free energy difference per unit volume of crystal between the supercooled liquid and the crys-

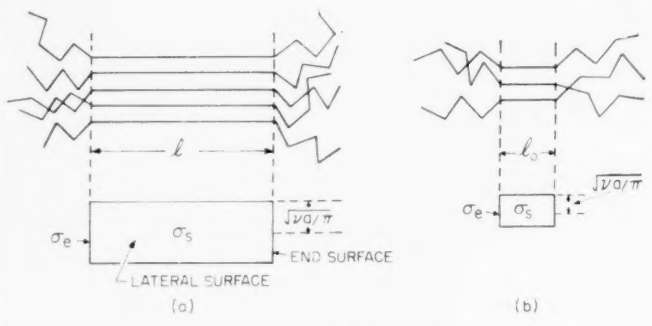

FIGURE 1. *Homogeneous bundlelike nucleus (bulk polymer).*

(a) Nucleus of length l and "radius" $\sqrt{\nu a/\pi}$ valid in region A, where there is no minimum restriction on l or ν.

(b) Nucleus of fixed length l_0 and "radius" $\sqrt{\nu a/\pi}$ valid in region B.

tal. The quantity va is the area of the end of the nucleus or embryo. The quantity σ_s is the work required to form a unit area of the lateral surface from the crystal, and σ_e is the corresponding work for the end of the crystallite. If at any given degree of supercooling ν and l are increased, $\Delta\phi_{p(A)}$ goes through a maximum where it has the value $\Delta\phi^*_{p(A)}$, and then falls rapidly through zero to strongly negative values, the latter implying increasing stability with increasing size. The critical values of l and va can readily be determined by setting $(\partial\Delta\phi_{p(A)}/\partial l)_{va}$ and $(\partial\Delta\phi_{p(A)}/\partial\sqrt{va})_l$ equal to zero. Thus,

$$l^*=\frac{4\sigma_e}{\Delta f}, \tag{4}$$

and

$$(va)^*=\frac{C^2\sigma_s^2}{(\Delta f)^2}. \tag{5}$$

Substitution of eqs (4) and (5) into (3) yields the result

$$\Delta\phi^*_{p(A)}=\frac{2C^2\sigma_s^2\sigma_e}{(\Delta f)^2}. \tag{6}$$

Thus, in region A, where both l and va are not subject to a minimum restriction, the rate of homogeneous nucleation is [2]

$$I_A=I_0e^{-\Delta H^*_p/kT}e^{-2C^2\sigma_s^2\sigma_e/(\Delta f)^2kT} \tag{7}$$

In this expression

$$C=2\pi^{\frac{1}{2}} \tag{8}$$

for a cylindrical nucleus, and

$$C=\frac{2}{\sqrt{\sin\psi}}\frac{x+y}{\sqrt{xy}} \tag{9}$$

for a nucleus where the cross section is a parallelogram with sides x and y, and apex angle ψ. The quantity $(va)^*$ is related to the square of the "radius" of the critical-sized nucleus.

For a strictly cylindrical nucleus, $r^*=[(va)^*/\pi]^{\frac{1}{2}}=2\sigma_s/\Delta f$, and $\Delta\phi^*_{p(A)}=8\pi\sigma_s^2\sigma_e/(\Delta f)^2$, results that have been given previously [6, 9]. The reaction path on the free energy surface described by eq (3) for the formation of the critical-sized nucleus is shown in figure 2. The critical-sized nucleus of length l^* and "radius" $[(va)/\pi]^{*\frac{1}{2}}$ is indicated by an asterisk, and the reaction path is designated by the heavy line $O-*-B$. The point $*$ is at a saddle point in the free energy surface. The embryo grows into a nucleus and thence into the stable region

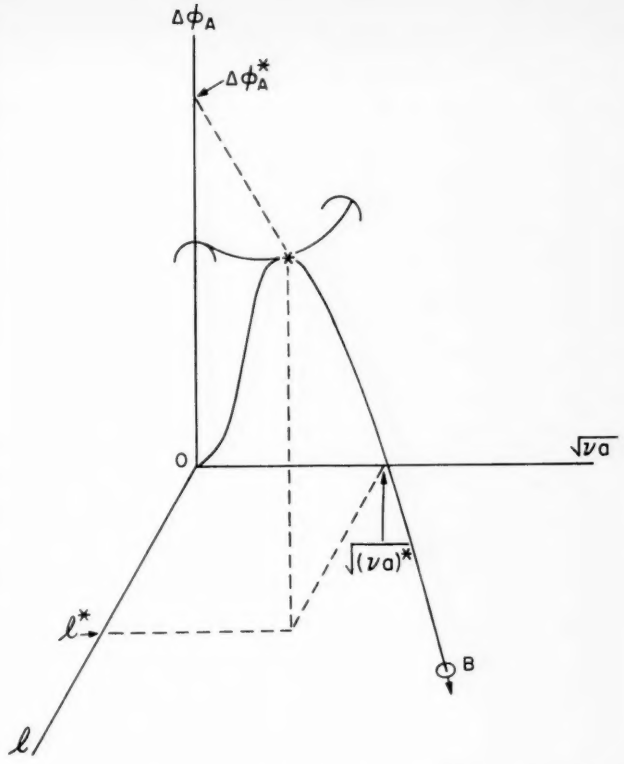

FIGURE 2. *Free energy surface for formation of a critical-sized homogeneous bundlelike nucleus for bulk polymers in region A.*

The reaction path is the heavy line $0-*-B$. The nucleus is of critical size at the saddle point marked $*$. The free energy surface for region B is similar, except that $l^*=l_0$.

(which is below the $l-[va]^{\frac{1}{2}}$ plane) by both lengthwise and "radial" growth.

Region B: For a bundlelike nucleus, it is necessary to recognize that σ_e might possibly be considerably smaller than σ_s. As one traces the environment of the various segments from the interior of the crystal out through the lateral surface into the liquid phase, a sharp and quite large drop in the degree of order will be noticed just at the crystal surface. Thus, the value of σ_s will correspond reasonably closely to the surface free energy for a nonpolymeric molecular crystal of the same chemical type, and will commonly lie in the range 5 to 25 erg·cm^{-2}. On the other hand, the drop in degree of order as one traverses a path from the center of the crystal out through the end will not be as sharp as in the case above. Because of this fact it seems plausible to suppose that σ_e will in some polymers be rather smaller than σ_s. However, σ_e cannot be zero, since this would imply no difference in free energy between the end of the crystallite or nucleus and the supercooled liquid.

The significance of the fact that σ_s may be considerably larger than σ_e for the bundlelike nucleus characteristic of primary nucleation in region A is that l^*, as given by eq (4), may, at some temperature T_c that is not too far below the melting point,

[2] Even if it is assumed that the nucleus is an ellipsoid of revolution, an expression for I_A similar to eq (7) is obtained. (See S. Matsuoka and B. Maxwell, Plastics Laboratory Technical Report 53E, Princeton University, 1959.) When the nucleus is large, i.e., at low supercooling, the ratio of the major and minor axes is determined by σ_s/σ_e. However, such a nucleus will tend to take on the shape of a disk or parallelepiped as the degree of supercooling is increased so that region B is approached. Thus, the overall behavior of I_A, including its temperature dependence and transition to region B, is unaffected by assumptions concerning the shape of the nucleus in region A.

fall close to the irreducible segment length, l_0. In this case, l must not be treated as a variable near and below T_c. Using the relation [10][3]

$$\Delta f = \frac{\Delta h_f T \Delta T}{T_m^2}, \tag{10}$$

where Δh_f is the heat of fusion at the equilibrium melting temperature, T_m, and $\Delta T = T_m - T$, where T is the isothermal crystallization temperature, it is found to a sufficient approximation that

$$\Delta T_c = \frac{4 T_m \sigma_e}{l_0 \Delta h_f}. \tag{11}$$

Here ΔT_c is the degree of supercooling that corresponds to the onset of region B. At lower temperatures, we must consider a primary nucleus with fixed length l_0, and variable va, as shown in figure 1b. In this case we have

$$\Delta \phi_{p(B)} = 2va\sigma_e + C\sqrt{va}\, l_0 \sigma_s - va\, l_0 \Delta f \tag{12}$$

which leads to

$$(va)^*_B = \left[\frac{C l_0 \sigma_s}{2(l_0 \Delta f - 2\sigma_e)}\right]^2 \tag{13}$$

and

$$\Delta \phi^*_{(B)} = \frac{C^2 l_0^2 \sigma_s^2}{4(l_0 \Delta f - 2\sigma_e)}. \tag{14}$$

In region B (or more precisely, from somewhat below T_c on down to considerably lower temperatures) the condition $l_0 \Delta f >> 2\sigma_e$ may be expected to hold. With this, eq (14) reduces to the simple form

$$\Delta \phi^*_{p(B)} \simeq \frac{C^2 l_0 \sigma_s^2}{4 \Delta f}, \tag{15}$$

and the rate of primary nucleation becomes

$$I_B = I_0 e^{-\Delta H^*_p / kT} e^{-C^2 l_0 \sigma_s^2 / 4 \Delta f kT}. \tag{16}$$

The values of C are the same as those given for region A; for the particular case of a strictly cylindrical nucleus, $\Delta \phi^*_{p(B)}$ is $\pi l_0 \sigma_s^2 / \Delta f$ [6].

Equations of the general form of (15) and (16) have sometimes been sharply criticized, apparently because of the incorrect belief that they could be derived only on the basis that $\sigma_e \equiv 0$, the latter being generally conceded to be impossible. However, the derivation sketched above makes it perfectly clear that eqs (15) and (16) hold if $l_0 \Delta f >> 2\sigma_e$, and there is no implication that $\sigma_e \equiv 0$ [6].

Region B type primary nucleation will prevail down to a temperature T_{cc} corresponding to a degree of supercooling of approximately

$$\Delta T_{cc} \simeq \frac{C \sigma_s T_m}{2 \Delta h_f \sqrt{(va)_0}}. \tag{17}$$

In the case that $\sigma_s >> \sigma_e$, ΔT_{cc} will be larger than ΔT_c, with the result that region B will cover a substantial range of temperature.

The free energy surface described by eq (12) has a saddle point at $l^* = l_0$ and $va = (va)^*$. Thus, both the embryo and nucleus always have a length l_0, but once of stable size, there is no inherent restriction on the addition of segments to increase the length. Lengthwise growth is in fact certain to occur [6]. Such a nucleus will increase in size by appropriate growth mechanisms until stopped by impingements or other factors (see sec. 2.2).

Region C: At crystallization temperatures below T_{cc}, the "radius" of the primary nucleus, $[(va)_0]^{1/2}$, will be close to the size of the unit cell, i.e., it will contain roughly 5 to 7 segments. While this radius is not irreducible in a strict sense, the small size of the stable nucleus below T_{cc} will lead to an excess number of nuclei owing to the fact that embryos of this size in the superheated state will be carried down in the supercooling process to the supercooled state. This will cause an enhanced rate of crystallization compared with region B or A. In the particular case where σ_e is larger than envisioned previously, and exceeds $l_0 C \sigma_s / 4[(va)_0]^{1/2}$, which is $l_0 \sigma_s / 2r_0$ for a cylindrical nucleus of radius r_0, region B will be absent, and the system will go directly from region A type homogeneous nucleation to that characteristic of region C.

Several important points concerning the nature of homogeneous nucleation in bulk polymers may now be emphasized. The first is that two types of temperature dependence are to be expected for the rate of nucleation. Sufficiently near the melting point, i.e., in region A,

$$\ln \frac{I_A}{I_0} = -\frac{\Delta H^*_p}{kT} - \frac{\alpha}{T^3 (\Delta T)^2}, \tag{18}$$

where the constant α is $2C^2 \sigma_s^2 \sigma_e T_m^4 \Delta h_f^2 k$. This is the same general form as is exhibited by nonpolymeric systems. At moderate to high degrees of supercooling, region B, the temperature dependence is

$$\ln \frac{I_B}{I_0} = -\frac{\Delta H^*_p}{kT} - \frac{\beta}{T^2 \Delta T}, \tag{19}$$

where the constant β is $C^2 l_0 \sigma_s^2 T_m^2 / 4 \Delta h_f k$. Equation (19) is a special result in that it reflects the segmental nature of the polymer chain, having been derived assuming l_0 was a constant. *In the special case where $\sigma_e \geqq l_0 \sigma_s / 2r_0$, region B will be absent, and the system will exhibit a temperature dependence of the form of eq (18) down to the $A \rightarrow C$ transition.* However, in some cases it is to be anticipated that σ_e will be sufficiently less than σ_s to cause region B to make its appearance. Region A will be large if $\sigma_e \sim \sigma_s$.

[3] The relation $\Delta f = \Delta h_f \Delta T / T_m$ is usually employed to give the free energy difference between the supercooled liquid and crystalline states. This expression is not as precise for a glass forming system as eq (10).

Both eqs (18) and (19) lead to a maximum in I/I_0 when plotted as a function of temperature. The terms $\exp[-\alpha/T^3(\Delta T)^2]$ and $\exp[-\beta/T^2\Delta T]$ lead to strongly negative temperature coefficients for the rate of injection of nuclei, but this effect is eventually overwhelmed by the term $\exp[-\Delta H_p^*/kT]$ that arises from the jump rate, and which has a positive temperature coefficient. Hence a maximum exists in I_A and I_B.

The second point is that there is nothing in the foregoing which suggests a highly uniform step height of the general character found in crystals formed from dilute solution. The only feature in the theory for bulk polymers that is even slightly suggestive of a pronounced step height, where the long axes of the polymer molecules are in the correct configuration with respect to the crystal surfaces, is the behavior of $l^*=4\sigma_e T_m^2/\Delta h_f T\Delta T$ in region A. However, an unacceptably large value of σ_e has to be introduced to cause l^* to be anywhere near as large as is observed for polymer crystals obtained from dilute solution. Furthermore, such a nucleus will certainly grow lengthwise, and it is very difficult to imagine why it would grow to a practically completely uniform length which would correspond to a step height. (More will be said of this later.)

The third point is that in a bulk polymer, the bundlelike nucleus, made up from segments of different polymer chains, is energetically the most favorable that can be conceived. Unless prevented by some factor not yet considered, this is the type of nucleus that should commonly appear in a bulk homopolymer. Then if no special strain effects interfere (say in the radial growth), such nuclei should grow both radially and lengthwise.

We turn now to some general considerations that have to do with the nature of the growth of the bundlelike primary nuclei, and the effects that cause such growth to cease in bulk polymers, or at least slow down to a marked extent. Once certain general features of the growth process in bulk polymers have been brought out, the discussion of primary nucleation and growth in dilute solution with chain folding can be given.

2.2. Crystal Growth, Bulk Rate Constants, and Impingements in Bulk Polymers

Two features of the growth process in bulk polymers are of interest here. The first is that the primary bundlelike nucleus without chain folding can, at least initially, grow radially and lengthwise. Each of these growth mechanisms is nucleation controlled sufficiently near the melting point. The second point is that the growing crystals will impinge on one another in such a manner as to essentially stop or markedly retard lengthwise and radial growth in a manner that can hardly lead to a highly uniform step height of the type found in dilute solution. In the special case where strain limits radial growth (see below), only the distribution of lengths will be impingement controlled, but this will still not correspond to an essentially fixed step height.

Consider first the types of growth that may occur, at least initially, for a bundlelike nucleus. Denote radial growth as $G_r=dr/dt$ (where in general $G_r\propto d[va]^{\frac{1}{2}}/dt$) and lengthwise growth as $G_l=dl/dt$. Further, define the free bulk growth rate as

$$\chi'=Z_n t^n \tag{20}$$

where χ' is the mass fraction crystallized, t the time, and n an exponent that depends on type of nucleation and the mode of growth. The free bulk growth rate is the rate at which the polymer would crystallize if the growing crystals were independent of one another. Values of n for various modes of growth with homogeneous initiation (i.e., primary nuclei born sporadically in time) are shown in table 1. The relationship between Z_n, I, G_l, and G_r are also shown.

TABLE 1. *Values of n and Z_n for various modes of growth of bundlelike nuclei (homogeneous nucleation)*

Mode of growth	n	Form of bulk rate constant [a]
One-dimensional	2	$Z_2\propto IG_l$
Two-dimensional	3	$Z_3\propto IG_r^2$
Three-dimensional [b]	4	$Z_4\propto IG_lG_r^2$

[a] In these expressions I may refer to either I_A or I_B.

[b] If branches develop, and $Z_4\propto IG_{spk.}^3$, where $G_{spk.}$ is the mean growth rate in the radial dimension.

The growth mechanism denoted by G_l is to be described by an expression of the general form

$$G_l=G_0 e^{-\Delta H_g^*/kT}e^{-\gamma/T^2\Delta T} \tag{20}$$

so that

$$\ln\frac{G_l}{G_0}=-\frac{\Delta H_g^*}{kT}-\frac{\gamma}{T^2\Delta T} \tag{21}$$

Here γ is a constant similar in character to β, and ΔH_g^* is the enthalpy of activation at the supercooled-liquid—growth-nucleus interface. The form of eq (20) arises from the fact that in the experimentally accessible region the growth nucleus is characterized by one fixed and temperature independent dimension of molecular size, usually a thickness of one molecule or segment length (circa 2.5 to 20A). However, the temperature dependence of the growth mechanism denoted by G_r may differ from that of G_l, since the secondary nucleus may be of a different nature. In general, both G_l and G_r will go through a maximum below the melting point, and will possess a strongly negative temperature dependence near the melting point. In the event that $\sigma_s>>\sigma_e$, the radial growth nucleus in the experimentally accessible region may have *two* fixed and temperature independent dimensions of molecular size. The radial growth nucleus will generally be easier to form than the lengthwise growth nucleus, so the condition $G_r>G_l$ is commonly to be anticipated. (See, however, remarks below concerning possible retardation of radial growth by strain.)

We must now ask what processes retard the free growth rate of the crystals in a bulk phase. Impingements and entanglements are certainly important factors [6]. The growing crystallites will run into each other, entanglements will occur in the vicinity of such "collisions", and this will tend to stop growth. The retardations due to impingements are relatively weak early in the crystallization, but gradually get stronger. The isotherms in this range, which is called "stage 1," will commonly be superposable simply by shifting the time scale [6]. Estimates of the free bulk growth rate constant, Z, may be obtained by analysis of stage 1 data. However, the system will approach a degree of crystallinity, well short of complete crystallization, where there is a massive degree of impingement (fig. 3). We refer to this as the pseudoequilibrium degree of crystallinity, χ_m. Detailed theoretical calculations due to Lauritzen [11], and certain experimental studies [6], fully justify the view that impingements will lead to the effect indicated. Near and above χ_m, the crystallization process is exceedingly slow. Other workers have called this "secondary crystallization" but for convenience we have termed it "stage 2." Relaxation of impingements and entanglements to form crystallites with greater length and radii is one of the principal crystallization processes in stage 2. The equilibrium degree of crystallinity is thus approached very slowly due to the intercession of a massive degree of impingement at χ_m.

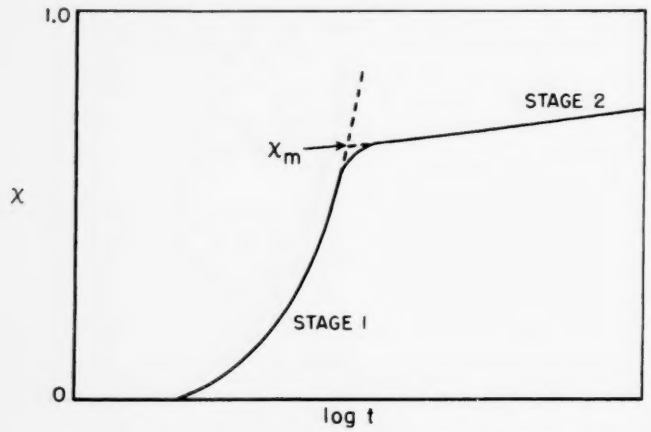

FIGURE 3. *Schematic diagram showing course of crystallization in a bulk polymer.*

χ is the mass fraction crystallized and t the time. Stage 1 strongly reflects the free growth rate $\chi' = Z_n t^n$. The pseudoequilibrium degree of crystallinity is denoted χ_m, and is the result of impingements and entanglements. Stage 2 slowly carries the crystallization beyond χ_m.

After the stage 2 mechanism has pursued its course for a sufficient time, the length and radius of a few of the crystallites will be large enough to melt quite close to the equilibrium melting temperature, T_m. In the vicinity of χ_m, the crystallites will often be rather small, and impingements will have set up a distribution of crystallite sizes. These effects will cause rather broad and low melting. The particular distribution that prevails at χ_m changes only very slowly toward the equilibrium one. Neither the distribution of radii and lengths resulting from impingements, nor even the true equilibrium one, is consistent with a uniform step height.

Another effect that may subdue growth of bundlelike nuclei is strain. Thus, while bundlelike *nuclei* may form easily, radial *growth* to large size may be hindered by the strain that results from the mismatch of the segments in the crystal with those in the "liquid" just outside the ends. Such a situation could be treated theoretically in terms of a σ_e value that increased with ν. The effect mentioned could conceivably severely restrict radial growth of bundlelike nuclei in some cases, causing a nearly constant crystallite radius to be observed. However, the stoppage of lengthwise growth will in such a case still be controlled by impingements, and not correspond to a step height of the type found in folded crystals.

Much of what has been said concerning the nature of impingements may be found in more detail in a previous article [6].

3. Homogeneously Induced Crystallization of Polymer From Dilute Solution

3.1. Preliminary Analysis of Homogeneous Nucleation From Dilute Solution

In order to set the stage for the detailed analysis to follow in subsequent sections, an elementary analysis of the problem of nuclei with chain folding is given first. This has the advantage of permitting an early emphasis on the simple physical picture involved, and has the virtue of clearly indicating just what points must be subjected to more searching analysis.

When a polymer is dissolved at high dilution in a relatively good solvent, the polymer molecules tend to be essentially isolated from each other. If the solution is supercooled, the polymer will tend to crystallize from the solution. The kinetics of this crystallization will be governed by the nucleation and growth process. Since the polymer molecules are essentially isolated from one another, the primary nucleus will tend to be formed, if at all possible, from a single polymer molecule. The formation of these nuclei is treated below and it will be shown that in sufficiently dilute solution these nuclei, characterized by chain folding, are kinetically favored over bundlelike nuclei containing segments from many molecules of the type discussed in the previous section for bulk phases. This treatment explains the main features of the single crystals obtained by Keller and others, and predicts other properties which should be capable of verification.

We shall outline in some detail the characteristics of the single crystals of polyethylene prepared from a dilute solution of xylene [1, 2]. These crystals, as revealed by electron micrographs, are flat parallelepipeds which are shown schematically in figure 4a. The step height, l^*, was measured by low angle X-ray scattering, and reflections up to the fourth order were observed. The step height increased from 90 to 140 A with increasing crystallization tem-

perature. The polymer chains lie approximately perpendicular to the two large flat faces of the crystal, i.e., parallel to the c-axis in figure 4a. The loops formed by the folding of the polymer molecules form the two flat surfaces of the crystal. In figure 4b the crystal is shown as viewed along the c-axis. The polymer chains intersect the plane normal to the c-axis at the corners and at the center of the rectangle. The planes determined by the two rows of carbon atoms in the zig-zag polymer chain backbone are shown as triple dashed lines. It has not been definitely determined which chains in figure 4b are connected by the loops, but Keller has indicated that it is sterically possible for the chains at P and Q in the figure to be connected by a loop containing three to five carbon atoms. The arrangement of the chains shown in figure 4b is essentially that given by Bunn [12].

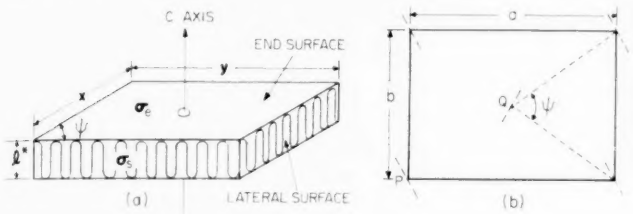

FIGURE 4. *Details of loop-type polyethylene crystals formed from dilute solution.*

(a) Polyethylene crystal with step height l^* showing orientation of chains. (b) View of unit cell along c-axis showing orientation of ribbonlike hydrocarbon chain - - -.

In the discussion of the nucleus with folds the following definitions are employed. First, $\boldsymbol{\nu}$ is taken to be the number of segments in the cross-sectional area of the nucleus or embryo, and $\mathbf{a}$ is the cross-sectional area of each segment. The area of the end of the nucleus is $\boldsymbol{\nu}\mathbf{a}$. The length of the nucleus or embryo is designated $\mathbf{l}_p$. All of these definitions are analogous to those used earlier for the bundlelike nucleus. Refer to the set of segments comprising the length of a nucleus or embryo, $\mathbf{l}_p$, as a *step element*; the step element length includes the (small) length involved in the folds at either end. The number of step elements in a nucleus is equal to $\boldsymbol{\nu}$, and the total number of folds is equal to $\boldsymbol{\nu}-1$.

We now introduce a particular model of the polyethylene crystal in order that we may have a specific picture in mind while calculating the properties of crystals formed by the folding of polymer chains. This model, which is essentially that suggested by Keller and O'Connor, is shown in figure 5. A single molecule forms the crystal through folding of its backbone as it progresses outward in a double spiral from a central position 0. (At a later stage in the development of the crystal, other molecules may, of course, participate.)

The above model of the nucleus with a double spiral is only one of several possibilities, but it still embodies the important general characteristics of nuclei with chain folding. These characteristics apply not only to polyethylene but also to any

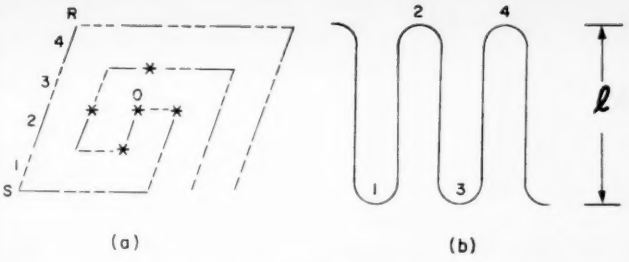

FIGURE 5. *Loops in homogeneous nucleus formed from dilute solution.*

(a) View of proposed loop nucleus along c-axis. Loop facing reader —, loop away from reader. The cross marks near 0 show one unit cell (Cf fig. 4b). (b) Cut through plane RS showing odd-numbered loops (down) and even-numbered loops (up).

polymer that can form such nuclei. First, it is possible to form nuclei from a single polymer molecule. Second, the crystals formed through chain folding possess sharp and definite boundaries between crystalline and noncrystalline regions. This is in contrast with the end surface of crystallites discussed in the section on bulk polymers. Third, a change in any reasonably short period of time [4] of the step height requires the melting (or dissolving) of the crystal and recrystallization with a new "step height". Fourth, if a molecule has formed an array of $\boldsymbol{\nu}$ step elements, the $\boldsymbol{\nu}+1$st step element may be added simply by the folding of a free end (or ends) of the polymer molecule. Fifth, when a polymer molecule forms an array of $\boldsymbol{\nu}$ parallel step elements there will be $\boldsymbol{\nu}-1$ folds in the nucleus. It is emphasized that all five of these items hold for either a double spiral model, a single spiral model (not shown), or any of a number of other configurations.

The rate of formation of nuclei constructed from a single polymer molecule through chain folding will be calculated by a procedure very similar to that used in section 2. Bold faced symbols are used for many of the quantities involved in order to clearly differentiate them from those pertaining to the conventional bundlelike nucleus described earlier. The free energy relative to the solution state of a primary nucleus composed of $\boldsymbol{\nu}$ step elements of length $\mathbf{l}$ may be written as

$$\boldsymbol{\Delta\phi}_p = 2\boldsymbol{\nu}\mathbf{a}\boldsymbol{\sigma}_e + C\sqrt{\boldsymbol{\nu}\mathbf{a}}\mathbf{l}\boldsymbol{\sigma}_s + 2C\sqrt{\boldsymbol{\nu}\mathbf{a}}\boldsymbol{\epsilon}_p - \boldsymbol{\nu}\mathbf{l}\boldsymbol{\Delta}\mathbf{f}, \quad (22)$$

where $\mathbf{a}$ is the cross-sectional area of a segment in the crystal, C is a numerical factor depending upon the shape of the nucleus, and $\boldsymbol{\Delta}\mathbf{f}$ is the free energy difference per unit volume of crystal between the polymer in the supercooled solution and the crystal. The quantity $\boldsymbol{\sigma}_s$ is the work required to form a unit area of the lateral surface from the crystal and $\boldsymbol{\sigma}_e$ the corresponding work for the end of the crystal. The quantity $\boldsymbol{\epsilon}_p$ is the work required to form a unit length of "edge" from the crystalline phase.

The relative size of $\boldsymbol{\sigma}_e$ and $\boldsymbol{\sigma}_s$ may be estimated from the following considerations. Both the lateral

[4] Over long periods of time, the step height will probably gradually increase in an isothermal process by lengthwise diffusion of segments. This point is treated more fully later.

and end surfaces of the nucleus with folds present an abrupt change from crystalline order with respect to the solution. In addition, on the end surface, an amount of work $\mathbf{q}$ kcal/mole of loops will be required to form a fold. When there are ν segments in the cross section of the nucleus, there will be $\nu-1$ folds, and area of the two ends is $2\,\nu\mathbf{a}$. Then we have

$$\sigma_e=\sigma_{eo}+\frac{\mathbf{q}(\nu-1)}{2\nu\mathbf{a}}\cong\sigma_{eo}+\frac{\mathbf{q}}{2\mathbf{a}}, \tag{23}$$

where σ_{eo} represents the (probably small) contribution to σ_e above that of fold formation. We should expect to find $\mathbf{q}$ with a value on the order of magnitude of 1 kcal/mole of loops.[5] In making this rough estimate, it was assumed that the principal contribution to $\mathbf{q}$ was the energy required to bring the part of the polymer chain in the folds (ca. five carbon atoms in the case of polyethylene) into the appropriate higher internal rotational states. If $\mathbf{a}=18\times10^{-16}$ cm^2, and $\mathbf{q}=1$ kcal/mole, $\mathbf{q}/2\mathbf{a}=20$ erg·cm^{-2}. We expect no really large difference between σ_s and σ_s, the lateral surface free energies of the nuclei with loops, and the bundlelike nuclei, respectively. The important differences in surface free energy between bundlelike nuclei, and nuclei with loops, can be summarized in the following way. For the bundlelike nucleus we have

$$\sigma_s\gtrsim\sigma_e, \tag{24}$$

where σ_s is a "normal" value, usually in the range 5 to 25 erg·cm^{-2}. For nuclei with loops, we have instead

$$\sigma_e>\sigma_s, \tag{25}$$

which is in sharp contrast to (24). Noting that σ_s will ordinarily have a "normal" value, we may effect the comparison between the loop and bundlelike types of primary nuclei by writing

$$\sigma_s\cong\sigma_s \tag{26}$$

and

$$\sigma_e>\sigma_e. \tag{27}$$

The quantity $\Delta\mathbf{f}$ in eq (22) may be approximated by [13]

$$\Delta\mathbf{f}=\Delta\mathbf{h}_f\cdot\frac{(\mathbf{T}_m-T)}{\mathbf{T}_m}=\frac{\Delta\mathbf{h}_f\Delta\mathbf{T}}{\mathbf{T}_m}, \tag{28}$$

where $\Delta\mathbf{h}_f$ is the heat of fusion per unit volume of crystal, and $\mathbf{T}_m$ is the equilibrium melting temperature of the crystal, both in the presence of large amounts of the solvent.

The presence of the edge energy term in eq (22) is not essential for the theory developed in this paper, and the general conclusions drawn about crystals with folds are independent of ϵ_p. Since the value of ϵ_p will depend on the detailed morphology of the crystals with folds, which is not treated in this paper, and for the reason that its inclusion at this juncture would not elucidate any essential points, it is set equal to zero in the remainder of this section. Nevertheless this term is included in eq (22) for completeness, and the consequences of ϵ_p possessing a nonnegligible value will be assessed later.

The energy surface described by eq (22) is shown in figure 6. It is formally similar to the energy surface for bundlelike nuclei. In both cases the most probable nucleation path passes through the saddle point. The difference between the two types of nuclei is that certain restrictions apply to the paths of nucleation on the surface for nuclei

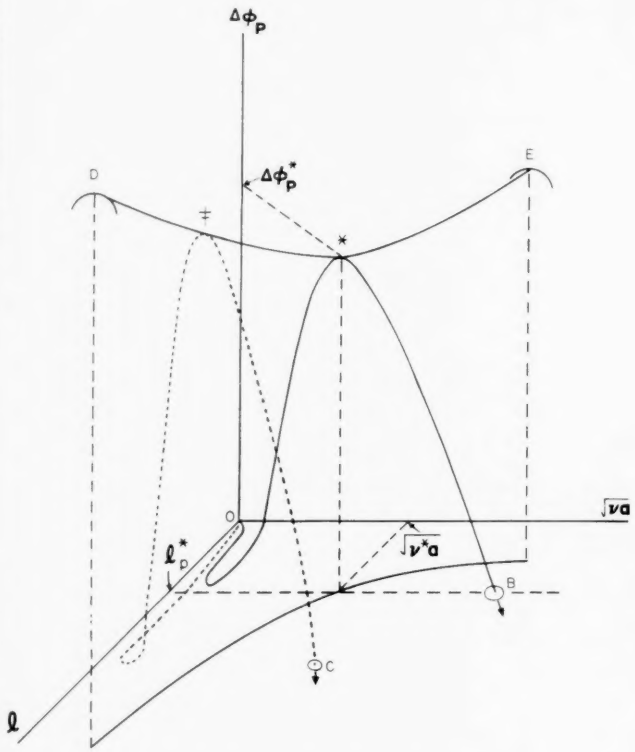

FIGURE 6. *Free energy surface for formation of critical-sized homogeneous nuclei with loops (dilute solution).*

The heavy line 0→*B* shows most probable reaction path; * is the saddle point across ridge D—E. The dotted line 0 · · · ‡ · · · *C* shows an other possible reaction path across ridge D—E, where $\Delta\phi_p^{\ddagger}>\Delta\phi_p^*$.

with loops that do not apply to bundlelike nuclei. For nuclei or embryos with folds, the elementary process is the addition or subtraction of a step element. Then the paths by which nuclei with folds are formed are characterized by a length that is invariant as the embryo or nucleus grows. Two paths of nucleation are shown in figure 6. One path passes through the saddle point, while the other path passes over a higher energy barrier. It will be shown subsequently that most of the nuclei formed will pass through or near the saddle point, and will therefore possess a length close to the value at the saddle point, $\mathbf{l}_p^*$. The coordinates of the saddle point may be found by calculating $(\partial\Delta\phi_p/\partial\mathbf{l})_\nu$

[5] The authors are indebted to Dr. C. W. Beckett for a helpful discussion concerning the probable value of $\mathbf{q}$.

and $(\partial \Delta \phi_p / \partial \nu \mathbf{a})_l$ from eq (22), and equating them to zero. It is found that

$$\mathbf{l}_p^* = \frac{4\sigma_e}{\Delta \mathbf{f}}, \tag{29}$$

and

$$\nu^* = \frac{\mathcal{C}^2 \sigma_s^2}{\mathbf{a}(\Delta \mathbf{f})^2}, \tag{30}$$

which lead in a straightforward manner to the result

$$\Delta \phi_p^* = \frac{2\mathcal{C}^2 \sigma_s^2 \sigma_e}{(\Delta \mathbf{f})^2}. \tag{31}$$

Already from eq (29) we can preceive the origin of a large nucleus length for nuclei with folds as compared with that for bundlelike nuclei. From this expression and $\Delta \mathbf{f} = \Delta \mathbf{h}_f \Delta \mathbf{T} / \mathbf{T}_m$, it is found for nuclei with folds that

$$\mathbf{l}_p^* = \frac{4\sigma_e \mathbf{T}_m}{\Delta \mathbf{h}_f \Delta \mathbf{T}}, \tag{32}$$

whereas from eq (4) and (10) we find, omitting the relatively unimportant factor T_m/T, that for bundlelike nuclei

$$l^* = \frac{4\sigma_e T_m}{\Delta h_f \Delta T}. \tag{33}$$

Since from eq (27), $\sigma_e > \sigma_e$, it is seen that $\mathbf{l}_p^*$ should generally be considerably larger than l^* under corresponding conditions of supercooling. As will be seen later, our estimate that $\sigma_e \sim 20$ erg·cm^{-2} leads to values of $\mathbf{l}^*$ in the vicinity of 100Å at a moderate degree of supercooling. The fundamental reason for the large value of $\mathbf{l}_p^*$ as compared to l^* is, of course, the work $\mathbf{q}$ required to form the fold.

On account of the relatively large value of σ_e compared to σ_e, it is to be anticipated that the nuclei formed in the experimentally accessible temperature range for dilute solutions will not ordinarily be subject to a minimal restriction of the type that causes the appearance of region B or C type nucleation in bulk polymers. Thus, our treatment of nuclei with chain folds is in some respects analogous to region A type nucleation in bulk polymers.

Equation (32) shows that $\mathbf{l}_p^*$ should increase as the crystallization temperature increases. Nuclei with lengths greater or less than $\mathbf{l}_p^*$ are improbable for kinetic reasons, as will be brought out subsequently.

It is seen that there is little difficulty in explaining why a nucleus with folds should have fairly large dimensions, corresponding in magnitude to the step height determined by Keller. The really critical issue is why this nucleus of length $\mathbf{l}_p^*$ does not continue to grow in the $\mathbf{l}$ dimension, but chooses instead to grow in the $\mathbf{x}$ and $\mathbf{y}$ dimensions. This question will be pursued in considerable detail later, but it is considered fitting at this juncture to mention the general nature of the arguments showing that the crystal will maintain a length $\mathbf{l}^*$ that is close to $\mathbf{l}_p^*$ as it grows. The presence of the folds on the end surfaces prevents rapid growth of the nucleus or embryo in the $\mathbf{l}$ direction of the simple type that can readily occur for a bundlelike nucleus in its l direction. The problem then becomes that of assessing the relative growth rates in the $\mathbf{l}$ direction, and on the lateral surfaces, for the loop type nucleus. Consider first what happens after a critical-sized nucleus with folds is formed. Since there will likely be very few other polymer molecules close by, the molecule already involved in the nucleus will continue to "crystallize," forming a primary crystallite containing one molecule. It can be demonstrated that the primary crystallite which on a kinetic basis has the highest probability of formation will in fact possess a length that is close to $\mathbf{l}_p^*$. It is, for example, highly improbable on energetic grounds that a new loop will protrude far above the plane of loops already established. The same is true of the set of new loops in a larger body. A quite similar argument applies to the growth of the crystallite when another polymer molecule enters the picture. Again the energetically least expensive growth nucleus contains a loop, and has a length $\mathbf{l}^*$ that is close to $\mathbf{l}_p^*$. Growth on the two primary crystallite faces containing the loops is not impossible, but will be subdued by the circumstance that a secondary or growth nucleus on this surface is nearly as difficult to form as the original primary nucleus. Considerable attention will be paid to the possible variation of the step height as the crystal grows, and this will be shown to be small. The relatively narrow distribution of step heights around the mean value of the step height is related to the nature of the saddle point in the free energy surface describing the rate of nucleation and growth.

In appendix 5.1 it is shown that to good approximation the number of stable nuclei formed isothermally per unit volume of solution per unit time is

$$\boldsymbol{I} = \frac{kT}{h} \mathbf{n}_0 e^{-\Delta \mathbf{F}_p^*/kT} e^{-\Delta \boldsymbol{\phi}_p^*/kT} \tag{34}$$

where $\mathbf{n}_0$ is the number of polymer molecules per unit volume of solution and $\Delta \mathbf{F}_p^*$ is the free energy of activation for a polymer molecule forming an additional step element. The approximate temperature dependence of $\Delta \boldsymbol{\phi}_p^*$ can be obtained from eqs (28) and (31):

$$\Delta \boldsymbol{\phi}_p^* = \frac{2\mathcal{C}^2 \sigma_s^2 \sigma_e \mathbf{T}_m^2}{(\Delta \mathbf{h}_f)^2 (\Delta \mathbf{T})^2}. \tag{35}$$

Hence,

$$\ln \frac{\boldsymbol{I}}{\boldsymbol{I}_0} = -\frac{\Delta \mathbf{H}_p^*}{kT} - \frac{\boldsymbol{\alpha}}{T(\Delta \mathbf{T})^2}, \tag{36}$$

where $\boldsymbol{I}_0 = (kT/h)\mathbf{n}_0 \exp(\Delta \mathbf{S}_p^*/k)$, and $\boldsymbol{\alpha} = 2C^2 \sigma_s^2 \sigma_e \mathbf{T}_m^2 / (\Delta h_f)^2 k$. (Here we have set $\Delta \mathbf{F}_p^* = \Delta \mathbf{H}_p^* - T\Delta \mathbf{S}_p^*$.) Equation (36) is seen to be of the same form as eq (18) except for the relatively unimportant factor T_m^2/T^2. Thus the temperature dependence of the nucleation rate at moderate supercooling is predicted to be similar to that of bundlelike nuclei in a bulk polymer in region A.

At this point it is convenient to indicate qualitatively why the nucleus with chain folds described by eq (29–31) and eq (34–36) is the most probable in dilute solution. The basic reason for this behavior is as follows: The free energy required to form a critical bundlelike nucleus in a very dilute solution is greater than the free energy required to form a critical nucleus with loops. This happens because the selection of segments to form the bundlelike crystals requires *many* polymer molecules to be gathered together. This leads to an important change in the difference between the configurational entropy of the crystalline state and the solution state. The change in entropy increases the free energy required to form a critical bundlelike nucleus. This effect is absent or greatly reduced for nuclei with loops, since such nuclei can be formed with a *single* polymer molecule, or a very few polymer molecules. Then stable nuclei with loops are formed much more rapidly than stable bundlelike nuclei from a sufficiently dilute solution. To be more quantitative, it will be shown in section 3.2 that when polyethylene is dissolved in xylene, crystallization will proceed primarily by formation of stable nuclei with loops when $v_2 \lesssim 0.001$, where v_2 is the volume fraction of polymer. It should be pointed out that while diffusional effects in dilute solutions will tend to reduce the rate of formation of bundlelike nuclei even further, these effects are important only at very low concentrations, where the reduction in configurational entropy has already effectively eliminated the formation of bundlelike nuclei.

The above arguments, concerning the entropy contribution to the free energy required to form a critical nucleus from a dilute solution, also apply to the entropy contribution to the free energy of a grown crystal. It will be shown that a loop-type crystal is more stable than a bundlelike crystal of the same shape and volume in a sufficiently dilute solution.

Brief consideration will now be given to certain aspects of the overall kinetics of crystallization. When a stable nucleus is formed, the nucleus will continue to grow until the molecule is consumed, forming a primary crystallite. At exceedingly low concentrations, where the polymer molecules are very widely separated, and long-range diffusion important, it is possible that the crystallization might proceed mainly through formation of such primary crystallites.

Since the birth time of such a crystallite is essentially the time required to form the critical nucleus, the time required for complete growth being negligible in comparison, the process will in effect be equivalent to sporadic formation of objects (primary crystallites) that do not grow. In this case, n would be unity in the *free* growth rate expression

$$\chi' = Z_n t^n. \tag{37}$$

(Note that $n=1$ in this case is not to be interpreted in the customary manner as one-dimensional growth of objects born at $t=0$.) At more moderate concentrations, where the degree of crystallinity could be more readily measured, subsequent growth of each nucleus would proceed through secondary nucleation of other adjacent polymer molecules. This nucleation will occur principally on the lateral surfaces of the growing crystal, leading to growth of the **x** and **y** dimensions, because the energy of formation is much smaller for nucleation on the lateral surfaces than on the end surfaces, which contain the folds. The relationship between χ', and the actual mass fraction of polymer crystallized will be given in section 3.3. Then we expect the nuclei, which are born sporadically in time, to grow principally in a two-dimensional manner leading to an overall crystallization isotherm described by $n=3$. As the crystallization proceeds, n will drop in value due to diffusional effects and the consumption of polymeric material. The secondary nucleation mechanism will be discussed further in section 3.3.

3.2. Detailed Analysis of Homogeneous Nucleation Rate and Constancy of Step Height in the Primary Crystallite

In section 3.1. we have outlined in simplified form the principal features of homongeneous nucleation from dilute solution. In the present section we shall treat the nucleation process in greater detail with particular emphasis on the variation in step height of the nuclei. We shall at first discuss an ensemble of nuclei, each of which is characterized by a fixed step height **l**, where **l** may differ from $\mathbf{l}_p^*$. The objective is to calculate the distribution in step height in the stable nuclei formed in such a system. Later the assumption that each nucleus in the set has a fixed step height will be relaxed, and found not to alter the general findings (see also appendix 5.1.). In this calculation the edge energy $\boldsymbol{\epsilon}_p$ will be equated to zero. Its inclusion would not alter the results in an important manner, but would needlessly complicate the analysis at this stage.

Consider a primary nucleus that is composed of $\boldsymbol{\nu}$ step elements, all of length **l**. The energy of such a nucleus was given in eq (22) and is rewritten here with $\boldsymbol{\epsilon}_p=0$:

$$\boldsymbol{\Delta\phi}_p = 2\boldsymbol{\nu}\mathbf{a}\boldsymbol{\sigma}_e + 4\mathbf{l}\sqrt{\boldsymbol{\nu}\mathbf{a}}\,\boldsymbol{\sigma}_s - \boldsymbol{\nu}\mathbf{a}\mathbf{l}\boldsymbol{\Delta}\mathbf{f}. \tag{38}$$

The energy surface represented by this equation is plotted in figure 6. Under the present assumption, a nucleus of $\boldsymbol{\nu}$ step elements of length **l** can change by an elementary process only to nuclei of either $\boldsymbol{\nu}-1$ or $\boldsymbol{\nu}+1$ step elements of length **l**. A stable nucleus of length **l** must be formed through the progressive addition of step elements until the free energy, $\boldsymbol{\Delta\phi}_p$, is negative. Then the path of nucleation will be along the points

$$\boldsymbol{\nu}_m, \boldsymbol{\nu}_m+1, \boldsymbol{\nu}_m+2 \ldots, \tag{39}$$

where $\boldsymbol{\nu}_m$ is the minimum size of a nucleus. Two such paths are shown in figure 6, and will be discussed in more detail shortly

It should be noted that if an embryo is to become stable, it must possess a length, **l**, greater than a

certain minimum. This can be seen clearly if eq (38) is differentiated with respect to ν:

$$\frac{\partial \Delta\phi_p}{\partial \nu} = \frac{C\sigma_s \sqrt{a}\, l}{2\sqrt{\nu}} + a(2\sigma_e - l\Delta f). \tag{40}$$

It can be seen by inspection that the right hand side of eq (40) decreases monotonically with increasing ν for all positive ν. If the length of the embryo is so small that $l < 2\sigma_e/\Delta f$, then $\partial \Delta\phi_p/\partial \nu$ is always positive. The free energy of such embryos will increase indefinitely with the addition of step elements, and the embryos can never become stable. Then stable nuclei can be formed only when

$$l > \frac{2\sigma_e}{\Delta f} = \frac{1}{2} l_p^*. \tag{41}$$

When eq (41) is satisfied, $\partial \Delta\phi_p/\partial \nu$ decreases monotonically with ν from a positive value to a finite negative value. Under these circumstances the free energy of the embryos, $\Delta\phi_p$, increases with the addition of step elements until a maximum value, $\Delta\phi_p^*$, is reached when there are ν^* step elements. The free energy decreases monotonically as further step elements are added. Two such paths of nucleation are shown in figure 6.

The number of step elements in the embryo at the energy barrier can be calculated by equating $\partial \Delta\phi_p/\partial \nu$ to zero in eq (40):

$$\nu^* = \frac{(C\sigma_s l)^2}{4a(l\Delta f - 2\sigma_e)^2}. \tag{42}$$

The energy barrier is

$$\Delta\phi_p^* = \frac{(C\sigma_s l)^2}{4(l\Delta f - 2\sigma_e)}. \tag{43}$$

We have already seen that this energy barrier is a minimum when

$$l_p^* = \frac{4\sigma_e}{\Delta f}, \tag{44}$$

and that this minimum energy barrier is

$$\Delta\phi_p^* = \frac{2C^2\sigma_s^2\sigma_e}{(\Delta f)^2}. \tag{45}$$

With some algebraic manipulation of eqs (43), (44) and (45), we may write the energy barrier, $\Delta\phi_p^*$, as

$$\Delta\phi_p^* = \Delta\phi_p^* \left[1 + \frac{(l/l_p^* - 1)^2}{1 + 2(l/l_p^* - 1)} \right]. \tag{46}$$

This expression gives the value of the barrier hindering the formation of a stable nucleus composed of step elements of length l; these values of $\Delta\phi_p^*$ lie on the ridge D—E on the free energy surface shown in figure 6. Since the energy barrier to be surmounted is a minimum at $l = l_p^*$, where there is a saddle point in the ridge, it can be seen intuitively that the rate of formation of nuclei will be largest when the nuclei have lengths near this value.

The effect of deviations of length from l_p^* on the rate will now be established. In appendix 5.1., the rate of formation of these nuclei was calculated using the procedure of Turnbull and Fisher [8]. It was determined that the number of stable nuclei with lengths between l and $l + dl$ formed per unit time per unit volume of solution is

$$i(l)dl = \xi dl \frac{n_0 kT}{h} e^{-\Delta F_p^*/kT} e^{-\Delta\phi_p^*/kT} \tag{47}$$

where

$$\xi = \frac{a^2 \sqrt{2\sigma_e}}{l} \frac{(l\Delta f - 2\sigma_e)^{\frac{3}{2}}}{\pi (kT)^2}.$$

The value of ξ may be considered valid at best to within an order of magnitude. However, it varies slowly with l compared to the factor $\exp[-\Delta\phi_p^*/kT]$. Substitution of eq (46) into eq (47) leads to

$$i(l) = \xi \frac{n_0 kT}{h} \exp\left[-\frac{\Delta F_p^*}{kT} - \frac{\Delta\phi_p^*}{kT} \right] \times \exp\left\{ -\frac{\Delta\phi_p^*}{kT} \cdot \left[\frac{(l/l_p^* - 1)^2}{1 + 2(l/l_p^* - 1)} \right] \right\}. \tag{48}$$

This equation shows clearly that the nucleation rate is most rapid when $l = l_p^*$, and that the distribution in the lengths of the nuclei formed will become sharper as the height of the barrier at the saddle point, $\Delta\phi_p^*$, increases.

The derivation given above can be generalized further to include various step heights $l_1, l_2 \ldots$, for each individual nucleus, rather than just one. The general conclusion is that eq (48) is a reasonable measure of the variation in length of the stable nuclei formed. The fraction of stable nuclei with lengths between l_1 and l_2 can be calculated directly from eq (48):

$$f(l_2, l_1) = \frac{\int_{l_1}^{l_2} i(l)\, dl}{\int_{l_{p/2}^*}^{\infty} i(l)\, dl} = \frac{\int_{l_1}^{l_2} \exp\left\{ -\frac{\Delta\phi_p^*}{kT} \left[\frac{(l/l_p^* - 1)^2}{1 + 2(l/l_p^* - 1)} \right] \right\} dl}{\int_{l_{p/2}^*}^{\infty} \exp\left\{ -\frac{\Delta\phi_p^*}{kT} \left[\frac{(l/l_p^* - 1)^2}{1 + 2(l/l_p^* - 1)} \right] \right\} dl} \tag{49}$$

The lower limit of the integral in the denominator represents the smallest possible size of a stable nucleus. This expression will prove useful in estimating the percentage variation of l about its probable value, l_p^*.

The total nucleation rate is obtained by integration of eq (48). When $(\Delta\phi_p^*/kT) >> 1$, the number of stable nuclei formed per unit time per unit volume of solution is

$$I = \int_{l_{p/2}^*}^{\infty} i(l) dl = K \frac{n_0 kT}{h} e^{-\Delta F_p^*/kT} e^{-\Delta\phi_p^*/kT} \tag{50}$$

where $K=(2\boldsymbol{\sigma}_e)^{\frac{5}{2}}(\boldsymbol{\Delta f})\mathbf{a}^2/\boldsymbol{\pi}^{\frac{1}{2}}C\boldsymbol{\sigma}_s(kT)^{\frac{3}{2}}$. For most cases of interest, K is within an order of magnitude of unity, and following Turnbull and Fisher, we shall set K equal to unity. Then we have for the nucleation rate

$$\boldsymbol{I}=\frac{\mathbf{n}_0 kT}{h}\,e^{-\Delta\mathbf{F}_D^*/kT}e^{-\Delta\boldsymbol{\phi}_p^*/kT}. \tag{51}$$

Substitution of eqs (45) and (28) into eq (51) yields

$$\boldsymbol{I}=\frac{\mathbf{n}_0 kT}{h}\,e^{-\Delta\mathbf{F}_D^*/kT}\exp\left[-\frac{2C^2\boldsymbol{\sigma}_s^2\boldsymbol{\sigma}_e\mathbf{T}_m^2}{kT(\boldsymbol{\Delta h}_f)^2(\boldsymbol{\Delta T})^2}\right]. \tag{52}$$

(loop nuclei in dilute solution)

At temperatures near $\mathbf{T}_m$, it is clear that the last factor furnishes the principal temperature dependence of $\boldsymbol{I}$.

We turn now to some numerical values to illustrate the general characteristics of the nucleation of crystals with loops. Unfortunately, no complete set of experimental data is available, so we must be satisfied with estimates. Attention will be centered on the case of the crystallization of polyethylene from xylene at 90° C, for Keller and O'Connor [1] have measured the step height as formed under these conditions and found it to be about 140 A. It should be noted that xylene is a reasonably good solvent, so that there is no separation into two liquid phases at low concentrations. This condition must be satisfied for the theory given here to be applicable. An estimate on $\boldsymbol{\sigma}_e$ may be obtained by combining eq (28) and eq (29) so that

$$\boldsymbol{\sigma}_e=\tfrac{1}{4}\boldsymbol{\Delta h}_f\mathbf{l}_p^*(\boldsymbol{\Delta T}/\mathbf{T}_m), \tag{53}$$

where we have approximated the step height of the crystal by $\mathbf{l}_p^*$ in this equation. Quinn and Mandelkern [14] have measured the heat of fusion of polyethylene and have found it to be 67 cal·g^{-1}. From Bunn's X-ray data [12] on bulk crystalline polyethylene at room temperature, it may be estimated that the cross-sectional area of the chain segment is $18{\cdot}5\times10^{-16}$ cm^2, and that the volume of each $-CH_2CH_2-$ unit is 47×10^{-24} cm^3. (These values are adjusted to be correct at 90° C.) It is determined from these results that Δh_f, the heat of fusion per unit volume of crystal, is 2.8×10^9 erg·cm^{-3}. We will (somewhat arbitrarily) assume that this is the heat of fusion $\boldsymbol{\Delta h}_f$ in the presence of large quantities of solvent. It is then found that

$$\boldsymbol{\sigma}_e=980\left[\frac{\mathbf{T}_m-363}{\mathbf{T}_m}\right]\text{erg·cm}^{-2}. \tag{54}$$

The melting point of polyethylene crystals in very dilute solutions of xylene is difficult to estimate with confidence. A lower limit on $\mathbf{T}_m$ of 95° C may be calculated from the theory of the depression of the melting point of a polymer by diluent [15] with the interaction parameter $\chi_1=0$. The true value of $\mathbf{T}_m$ is very probably somewhat higher, since χ_1 almost certainly differs from zero. It is considered probable that $\mathbf{T}_m$ lies between 95° C and 120° C for this particular solvent. Then $\boldsymbol{\sigma}_e$ lies between 13 and 75 erg·cm^{-2}. A value of $\boldsymbol{\sigma}_e$ in this range seems reasonable, since it corresponds to an energy of loop formation of 0.7 to 4 kcal/mole of loops. We should expect polymers with stiffer chains to possess higher values of $\boldsymbol{\sigma}_e$ than polyethylene. In continuing the numerical analysis $\boldsymbol{\sigma}_e$ will be set equal to 30 erg·cm^{-2}. In eq (54) this implies $\mathbf{T}_m=374.5°$ K, and therefore $\boldsymbol{\Delta f}=1.17\times10^8$ erg·cm^{-3} at 90°C. To estimate the value of $\boldsymbol{\Delta\phi}_p^*/kT$ at this temperature, the shape constant C must be known. If it is assumed that the shape of the cross section of the nucleus is a parallelogram with an acute angle, $\psi=70°$, between the sides, $C=4.13$. Then from eq (45) or (31)

$$\frac{\boldsymbol{\Delta\phi}_p^*}{kT}=1.5\boldsymbol{\sigma}_s^2 \tag{55}$$

at $T=90°$ C. A reasonable value of $\boldsymbol{\sigma}_s$ might lie between 5 and 20 erg·cm^{-2} (Thomas and Stavely [16] have found $\sigma=20.4$ erg·cm^{-2} for benzene). Then $\boldsymbol{\Delta\phi}_p^*/kT$ must lie between 38 and 600.

Crystallization could not be observed if $\boldsymbol{\Delta\phi}_p^*/kT$ possessed a value of 600. For the particular case of crystallization from a 0.01 percent solution of polyethylene in xylene, $\boldsymbol{\Delta\phi}_p^*/kT$ must be well below 100. If $\boldsymbol{\sigma}_s$ lies between 5 and 6 erg·cm^{-2}, $\boldsymbol{\Delta\phi}_p^*/kT$ lies between about 40 and 50. In any case it is clear that the value of $\boldsymbol{\Delta\phi}_p^*/kT$ for slow but measurable crystallization processes is a large number. This is because $\boldsymbol{\sigma}_s^2\boldsymbol{\sigma}_e$ possesses large values for nuclei with folded chains. One might expect that $\boldsymbol{\sigma}_s^2\boldsymbol{\sigma}_e$ lies between 500 and 10,000 erg^3·cm^{-6} for most polymers where the nuclei involve chain folding. The quantity $\sigma_s^2\sigma_e$ relevant to the case of bundlelike nuclei in bulk is much smaller, values of 25 to 250 erg^3·cm^{-6} being reasonable.

The distribution in step heights of critical nuclei about $\mathbf{l}_p^*$ can be estimated from eq (49). If when polyethylene is crystallized from a 0.01 percent solution of xylene, $\mathbf{l}_p^*=140$ A and $\boldsymbol{\Delta\phi}_p^*/kT=50$, the evaluation of eq (49) shows that 73 percent of the critical sized nuclei have step heights between 126 and 157 A. This distribution is sufficiently narrow so that several orders of low angle X-ray scattering might be expected,[6] if the grown crystals possess this distribution. This is in satisfactory agreement with experiment.

These numerical values will be discussed further after the growth of the crystals through secondary nucleation of other polymer molecules has been investigated in the next section.

We now wish to show in some detail that the formation of bundlelike nuclei in sufficiently dilute solution is negligible compared to nucleation through chain folding. The nucleation rate of bundlelike

[6] It is quite possible that local rearrangements of the segments would cause the step elements in the nucleus to become even more uniform in a relatively short period of time.

nuclei of circular cross section in the presence of diluent, I_d, has been calculated by Mandelkern [13]. With appropriate changes in notation his result is

$$I_d = I_{0d} e^{-\Delta F_d^*/kT} \exp\left[-\frac{8\pi\sigma_{sd}^2\sigma_{ed}}{kT(\Delta f_d)^2}\right] \exp\left[\frac{4\pi\sigma_{sd}^2}{a(\Delta f_d)^2} \log_e v_2\right] \tag{56}$$

(bundlelike nuclei in dilute solution)

where ΔF_d^* is the activation energy required for transport across the nucleus-liquid interface, Δf_d is the bulk free energy difference per unit volume of crystal between the crystalline and solution states, σ_{sd} is the free energy required to build a unit area of the lateral surface from the bundlelike crystal in solution, and v_2 is the volume fraction of the polymer in the solution. σ_{ed} is a surface free energy corresponding to σ_e, the free energy required to build a unit area of end surface in the bulk polymer. σ_{ed} must be less than $\boldsymbol{\sigma}_e$, the energy required to form a unit area of a surface containing loops. The pre-exponential factor, I_{0d}, is not particularly sensitive to v_2, varying approximately as the first power of $\mathbf{n}_0$. It is to be expected that σ_{sd}, Δf_d, and a should have values very nearly equal to $\boldsymbol{\sigma}_s$, $\mathbf{\Delta f}$, and $\mathbf{a}$, the corresponding terms for nuclei with folds. Then the important dependence of I_d upon v_2 occurs in the last factor in eq (56). The last factor decreases very rapidly with decreasing v_2, and the nucleation rate for bundlelike nuclei is reduced correspondingly. Thus at sufficient dilution the nuclei with folds are the preferred type, as may be seen by comparing eq (52) with eq (56).

A more quantitative comparison can be made if eq (52) is divided by eq (56):

$$\frac{\boldsymbol{I}}{I_d} = \mathcal{C}_0 \exp\left\{-\frac{\mathbf{\Delta\phi}_p^*}{kT}\left[1 - \frac{4\pi\sigma_{ed}}{\mathcal{C}^2\boldsymbol{\sigma}_e} + \frac{2\pi kT}{\mathcal{C}^2\mathbf{a}\boldsymbol{\sigma}_e} \log_e v_2\right]\right\} \tag{57}$$

where $\mathcal{C}_0 = (\mathbf{n}_0 kT/hI_{0d}) \exp\left[-(\mathbf{\Delta F}_p^* - \Delta F_d^*)/kT\right]$. In eq (57) it has been assumed that $\mathbf{\Delta f} = \Delta f_d$, $\boldsymbol{\sigma}_s = \sigma_{sd}$, and $\mathbf{a} = a$. Here $\mathbf{\Delta\phi}_p^*$ is the energy required to form a critical nucleus with loops. When $\boldsymbol{I}/I_d \gg 1$, the stable nuclei formed are primarily those with loops. It is instructive to evaluate eq (57) for polyethylene crystallized from xylene. $\mathcal{C}_0$ is not very sensitive to either concentration or temperature and probably has a value between 10^{-10} and 1. We find $2\pi kT/\mathcal{C}^2\mathbf{a}\boldsymbol{\sigma}_e \simeq 1/3$, if $\boldsymbol{\sigma}_e$ is assigned the value of 30 erg·cm^{-2}. Then eq (57) becomes

$$(\boldsymbol{I}/I_d) = \mathcal{C}_0 \exp\left\{-(\mathbf{\Delta\phi}_p^*/kT)[1 + \tfrac{1}{3}\log_e v_2 - (4\pi\sigma_{ed}/\mathcal{C}^2\boldsymbol{\sigma}_e)]\right\} \tag{58}$$

It has been shown that $\mathbf{\Delta\phi}_p^*/kT$ is a large number. If $v_2 = 0.001$ and $\mathcal{C}_0 = 10^{-10}$, $\boldsymbol{I}/I_d$ lies between 10^{12} and 10^{35} as $\mathbf{\Delta\phi}_p^*/kT$ varies between 40 and 80. Thus in a 0.1 percent solution of polyethylene in xylene, crystallization should definitely occur through the formation of nuclei with loops. At concentrations near 10 percent $\boldsymbol{I}/I_d \ll 1$, and bundlelike nuclei will dominate the crystallization process. The transition between the two types of crystals occurs near $v_2 = 0.01$. Equations (57) and (58) must be applied with caution near this transition region for two reasons: (a) the nucleation rate for crystallites with loops was derived for very dilute solutions and is probably inaccurate at higher concentrations; (b) $\boldsymbol{I}$ and I_d are rates for extreme types of nucleation, and in the transition region the stable nuclei formed are probably partially bundlelike and partially formed through chain folding. Nevertheless eq (57) indicates that there is a fairly sharp value of the volume fraction of polymer, $v_{2(c)}$, such that when $v_2 > v_{2(c)}$ bundlelike nuclei are formed, and when $v_2 < v_{2(c)}$ nuclei with loops are formed. If there is some restraint on the radial growth of bundlelike nuclei, such as the type of strain mentioned earlier, stable bundlelike nuclei may be even more difficult to form than has been indicated, and $v_{2(c)}$ would have a higher value than that deduced from eq (58). Even without this, the important point remains that loop-type nuclei will predominate at low concentration.

In extremely dilute solution the preponderance of nuclei with loops over those that are bundlelike is enhanced even further by diffusional effects. Since at higher concentrations loop nuclei are already the most important in the system, we see no compelling need to give a detailed analysis of the effect of long range diffusion.

The above comparison naturally raises the question of why the configurational entropy contribution to the free energy of formation of a bundlelike nucleus is so much more sensitive to the concentration of the solution than is the corresponding term for a nucleus with folds. Qualitatively this can be answered as follows. In forming a critical bundlelike nucleus the segments of many molecules must be brought together. The entropy reduction in bringing together different polymer molecules in dilute solution is sensitively dependent upon the concentration. In forming a critical nucleus with folds from a single polymer molecule, the segments of this molecule must be brought together in an appropriate manner. There is a corresponding entropy contribution but this contribution does not depend upon the concentration of the solution. This qualitative explanation can be placed on a quantitative basis if a lattice model is used. The lattice model is not accurate for dilute solutions, but calculations based upon it should be roughly correct. It is found that the reduction in entropy due to the gathering of molecules in a bundlelike crystal is $-k \ln v_2$ *per segment* in the cross section of the crystal. This result yields an end surface energy of the form $\sigma_{ed} - (kT/2a) \log_e v_2$ and leads to eq (56). By analogy, for a crystal with folds, the reduction in entropy is $-k \ln v_2$ *per polymer molecule* contained in the nucleus. If a single polymer molecule is involved in the formation of a critical nucleus with folds this contribution need not be considered and eq (52) results. If many molecules are involved in the crystal the free energy contribution per unit area of surface of the crystal is $-(\mathbf{l}/L)(kT/2\mathbf{a})\log_e v_2$, where $\mathbf{l}$ is the step height of the crystal, and L is the mean length of the polymer molecules. This term is unimportant for high molec-

ular weight polymers. In any case since this "surface energy" term is proportional to the step height of the crystal, it will be included in the bulk free energy difference per unit volume of crystal, $\mathbf{\Delta f}$.

It has already been shown that for kinetic reasons almost all of the critical nuclei possess lengths very close to $\mathbf{l}_p^*=4\boldsymbol{\sigma}_e/\mathbf{\Delta f}$. The critical nucleus can often be formed from a single polymer molecule. After these nuclei are formed, the remainder of the polymer molecule forming the nucleus will "crystallize" onto the nucleus until a primary crystallite is formed by a single molecule, which has a crystalline volume $\mathbf{a}L$ where L is the length of the molecule. The distribution in step heights of this primary crystallite will now be briefly considered.

It will be assumed that the primary crystallite will be formed from the critical nucleus by the addition of step elements in the manner shown by figure 5a, so that the step elements are added in a monomolecular layer to the existing already "crystallized" nucleus. This monomolecular layer will be added to one side of the nucleus until a "corner" of the nucleus is reached. At this stage the step height may be maintained near $4\boldsymbol{\sigma}_e/\mathbf{\Delta f}$ although lower values may be attained. When the monomolecular layer of step elements reaches the "corner" of the nucleus, the next step element must be added so that it extends beyond the corner of the nucleus. This situation is shown schematically in figure 7a and 7b, where the additional step element is designated by A.

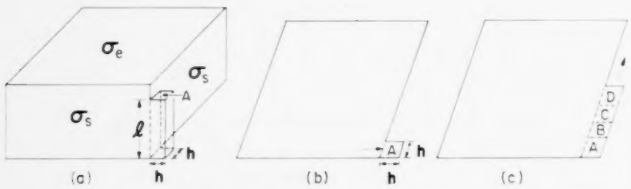

FIGURE 7. *The addition of step elements around a "corner" of a nucleus.*

(a) and (b): Perspective and a top view of the addition of a step element, A, to a nucleus. The step element A must be added in order that a monomolecular layer can be established along the face of the crystal. (c) Top view of the step elements B, C, D, . . . , that can be added to the crystal face after the first step element, A, has attached to the "corner" of the nucleus.

A monomolecular layer may then be added along the surface of the nucleus by the addition of step elements B, C, D, etc., as is shown in figure 7c. The calculation of the rate at which this monomolecular layer is deposited on the surface of the nucleus is complicated by two factors: (a) an accurate expression for the free energy of such a monomolecular layer is lacking, and; (b) the fundamental expression for the rate of crystallization of a monomolecular layer is somewhat different from the expression used for the primary crystallization.[7] The first complication will be avoided by using a purely geometric model for the free energy of the monomolecular layer. Thus each step element will be assumed to be a parallelepiped which has the surface energies appropriate to the bulk crystal. This model should yield answers that are qualitatively correct. Then if the step height of the added step elements A, B, C, D, . . ., is less than the step height of the nucleus, the free energy required to add $\boldsymbol{\nu}$ step elements around the corner of the nucleus is

$$\mathbf{\Delta\phi'}=2\mathbf{h}\boldsymbol{\sigma}_s\mathbf{l}+2\boldsymbol{\nu}\mathbf{a}\boldsymbol{\sigma}_e-\boldsymbol{\nu}\mathbf{al}\mathbf{\Delta f} \tag{59}$$

where $\mathbf{h}=(\mathbf{a}/\sin\boldsymbol{\psi})^{\frac{1}{2}}$ is the length of the side of the end surface of the step element. The usual method of finding the activation energy by setting $\partial\mathbf{\Delta\phi}/\partial\mathbf{l}=0$, $\partial\mathbf{\Delta\phi}/\partial\boldsymbol{\nu}\mathbf{a}=0$, and substituting into $\mathbf{\Delta\phi}$, is inapplicable in the case of monomolecular growth with $\boldsymbol{\nu}=1$, since the free energy surface does not have a saddle point that corresponds to a minimum activation energy. Hence we must examine the free energy ridge for $\boldsymbol{\nu}=1$ over which the system must pass in more detail.

The increment of energy required to add the step element at the corner of the nucleus is obtained by setting $\boldsymbol{\nu}=1$ in eq (59):

$$\mathbf{\Delta\phi'^{*}}=2\mathbf{h}\boldsymbol{\sigma}_s\mathbf{l}-\mathbf{a}(\mathbf{l}\mathbf{\Delta f}-2\boldsymbol{\sigma}_e). \tag{60}$$

At the degree of supercooling in the range of experimental interest, $2\mathbf{h}\boldsymbol{\sigma}_s>\mathbf{a}\mathbf{\Delta f}$, and therefore $\mathbf{\Delta\phi'^{*}}$ increases with increasing $\mathbf{l}$. Of course, if the length of the step element becomes larger than the nucleus, additional terms increase $\mathbf{\Delta\phi'^{*}}$ even more rapidly with $\mathbf{l}$. The addition of further step elements B, C, D, . . ., change the free energy by a constant amount

$$\mathbf{\Delta\phi}'_{\nu+1}-\mathbf{\Delta\phi}'_{\nu}=-E=-\mathbf{a}(\mathbf{l}\mathbf{\Delta f}-2\boldsymbol{\sigma}_e). \tag{61}$$

It is clear that the step element must have a length greater than $2\boldsymbol{\sigma}_e/\mathbf{\Delta f}$ or the resulting crystal is unstable.

The addition of the corner step element A requires an activation barrier $\mathbf{\Delta\phi'^{*}}$. Addition of further step elements of this length reduces the free energy by an amount E per step element. In appendix 5.2 it is shown that the equilibrium rate of deposition of monomolecular layers of step heights between $\mathbf{l}$ and $\mathbf{l}+d\mathbf{l}$ is

$$\mathbf{r}d\mathbf{l}=d\mathbf{l}\,\frac{C_1\mathbf{N}kT}{h}\,e^{-\mathbf{\Delta F}^*/kT}e^{-\mathbf{\Delta\phi'^{*}}/kT}\cdot\left\{\frac{2\sinh(E/2kT)}{1+2e^{-\mathbf{\Delta\phi'^{*}}/2kT}\sinh(E/2kT)}\right\} \tag{62}$$

where $\mathbf{\Delta F}^*$ is the activation energy of the elementary process of adding the step element, $\mathbf{N}$ is the number of primary nuclei which are growing, and C_1 is a normalization constant.

The rate of deposition of the monomolecular layer depends upon the step height, $\mathbf{l}$, of the layer. At $\mathbf{l}=2\boldsymbol{\sigma}_e/\mathbf{\Delta f}$ this rate is zero and as $\mathbf{l}$ increases the rate increases until a maximum is attained and then the rate decreases with a further increase of $\mathbf{l}$. It will be shown that the rate is appreciable in only a narrow range of values of $\mathbf{l}$.

[7] The Turnbull-Fisher theory is not applicable when the activated state is reached in one step, as in the present case of a monomolecular layer. The treatment of the nucleation rate in appendix 5.2 deals with the situation where the growth nucleus is formed in one step.

A numerical analysis shows that for the case in which we are interested, the rate in eq (62) can be approximated by

$$\mathbf{r}=2\frac{kT}{h}\mathbf{N}C_1{}^{-\Delta\mathbf{F}^*/kT}e^{-\Delta\boldsymbol{\phi}^*/kT}\sinh\left[\frac{E}{2kT}\right]$$

$$=2\frac{kT}{h}\mathbf{N}C_1e^{-\Delta\mathbf{F}^*/kT}e^{-\mathbf{l}(2\mathbf{h}\sigma_s-\mathbf{a}\Delta\mathbf{f})/kT}e^{-2\mathbf{a}\sigma_e/kT}$$

$$\sinh\left[\frac{\mathbf{a}(\mathbf{l}\Delta\mathbf{f}-2\boldsymbol{\sigma}_e)}{2kT}\right] \quad (63)$$

The mean length of the step height of this layer can be taken as

$$\bar{\mathbf{l}}=\frac{\int_{2\sigma_e/\Delta\mathbf{f}}^{\infty}\mathbf{l}\mathbf{r}\,d\mathbf{l}}{\int_{2\sigma_e/\Delta\mathbf{f}}^{\infty}\mathbf{r}\,d\mathbf{l}}=\frac{2\boldsymbol{\sigma}_e}{\Delta\mathbf{f}}+\left[\frac{2kT}{4\mathbf{h}\boldsymbol{\sigma}_s-3\mathbf{a}\Delta\mathbf{f}}+\frac{2kT}{4\mathbf{h}\boldsymbol{\sigma}_s-\mathbf{a}\Delta\mathbf{f}}\right]. \quad (64)$$

Similarly, the mean square deviation is

$$<(\mathbf{l}-\bar{\mathbf{l}})^2>=\frac{\int_{2\sigma_e/\Delta\mathbf{f}}^{\infty}(\mathbf{l}-\bar{\mathbf{l}})^2\mathbf{r}\,d\mathbf{l}}{\int_{2\sigma_e/\Delta\mathbf{f}}^{\infty}\mathbf{r}\,d\mathbf{l}}$$

$$=\left\{\frac{(2kT)^2}{(4\mathbf{h}\boldsymbol{\sigma}_s-3\mathbf{a}\Delta\mathbf{f})^2}+\frac{(2kT)^2}{(4\mathbf{h}\boldsymbol{\sigma}_s-\mathbf{a}\Delta\mathbf{f})^2}\right\}. \quad (65)$$

The square root of eq (65) can be used as a measure of the deviation of the step heights from the mean value, $\bar{\mathbf{l}}$.

When $\mathbf{h}\sigma_s>>\mathbf{a}\Delta\mathbf{f}$, eqs (64) and (65) become

$$\bar{\mathbf{l}}=\frac{2\boldsymbol{\sigma}_e}{\Delta\mathbf{f}}+\frac{kT}{\mathbf{h}\boldsymbol{\sigma}_s} \quad (66a)$$

and

$$<(\mathbf{l}-\bar{\mathbf{l}})^2>=\frac{1}{2}\left(\frac{kT}{\mathbf{h}\boldsymbol{\sigma}_s}\right)^2. \quad (66b)$$

Now if $\mathbf{h}=4.2$ Å, $\boldsymbol{\sigma}_s=6$ erg·cm^{-2}, and $T=363°$ K, then $kT/\mathbf{h}\boldsymbol{\sigma}_s$ is about 20 Å. The mean deviation about this average value is about 14 Å. Then when the monomolecular layer passes around the "corner" the length of the step height falls from $4\boldsymbol{\sigma}_e/\Delta\mathbf{f}$ to a value slightly greater than $2\boldsymbol{\sigma}_e/\Delta\mathbf{f}$. The distribution of step heights about this mean value is quite sharp. Every time the monomolecular layer reaches a "corner" this identical situation will be repeated. It might be expected that there is a tendency for the step height to increase, as the monomolecular layer is being crystallized along the side of a primary nucleus. An analysis of this process shows that the step height will remain near that given by eq (66a).

In summary, it can be said that if the edge energy $\boldsymbol{\epsilon}_p$ is negligible, the primary crystallite will have an interior section which has a step height $\mathbf{l}_p^*=4\boldsymbol{\sigma}_e/\Delta\mathbf{f}$, and the outer section will have a step height near $\bar{\mathbf{l}}=2\boldsymbol{\sigma}_e/\Delta\mathbf{f}+kT/\mathbf{h}\boldsymbol{\sigma}_s$. More will be said of this process in the next section. If the edge energy $\boldsymbol{\epsilon}_p$ is not negligible it will affect the growth of the critical nucelus into a primary crystallite. This effect will also be discussed in the next section.

3.3. Constancy of Step Height in Overall Growth Process and Volume Increase of a Folded Crystal Dilute Solution

When a primary crystal has been formed, it can grow by the addition of other polymer molecules upon it, one by one. This crystallization will proceed by the formation of a secondary nucleus by a single molecule upon the lateral surface of the crystal. This growth of the crystals is treated in this section with emphasis on two points. First we wish to demonstrate that the step height of the growing crystal has a tendency to remain at a constant value $\mathbf{l}^*$ for kinetic reasons. Second, it is desired to obtain appropriate expressions describing the volume rate of growth of these crystals.

Before we discuss growth through secondary nucleation on the lateral surfaces, our neglect of nucleation of the end surfaces must be justified. The end surface of the primary crystal is composed of loops formed by the folding of polymer molecules. The end surface of a secondary nucleus is also composed of folds. Thus there is a distinct boundary between the crystal and such a secondary nucleus. The effect of any affinity between the loops in the two end surfaces upon the free energy required to form a secondary nucleus is probably small. Then the free energy required to form a secondary nucleus upon the end surface of the crystal is almost as great as that required to form a primary nucleus. Some growth on the end surface will, of course, occur. However, by the arguments given above, the step height will be practically identical to that of the primary crystallite. Secondary growth of this type can lead to small patches of secondary growth on the primary crystallite, or in other cases to a distinct pyramidal appearance due to successive layers being formed. These effects should be subdued by forming crystals at very low concentration.

The free energy required to form a secondary nucleus upon the lateral surface of the crystal is considerably smaller than that required to form a primary nucleus. The volume growth of a crystal proceeds through the formation of a stable secondary nucleus on the growing (lateral) surface of the crystal followed by complete "crystallization" of the entire new molecule. The rate of addition of molecules to the crystal will be the average number of molecules in contact with the growing surface times the rate at which one of these molecules forms a stable nucleus, $\mathbf{p}_g$. The quantity, $\mathbf{p}_g$ can be calculated by the method of Turnbull and Fisher [8].

$$\mathbf{p}_g=\frac{kT}{h}e^{-\Delta\mathbf{F}^*/kT}e^{-\Delta\boldsymbol{\phi}_g^*/kT} \quad (67)$$

where $\Delta\boldsymbol{\phi}_g^*$ is the free energy required to form a secondary or growth nucleus of critical size. The

process of the formation of a fold by a molecule should be the same in primary and secondary nuclei, so that we anticipate $\Delta F_g^* = \Delta F_p^*$. This expression holds for growth where the activated state is reached through many successive elementary processes. Later, the case of growth through addition of a monomolecular layer will be considered, and eq (67) will be modified accordingly.

The free energy of secondary nuclei of critical size, $\Delta\phi_g^*$, will be considerably smaller than the corresponding energy for primary nuclei. The calculation of $\Delta\phi_g^*$ requires an accurate expression for the free energy of a secondary nucleus, $\Delta\phi_g$. We can obtain such an expression when the shape of the secondary nucleus is known and the number of segments in a cross-sectional area is large. It is probable that neither condition is satisfied for the secondary nucleus. We will, however, consider two extreme cases: (1) the cross section of the secondary nucleus has the same shape as that of the primary nucleus, and, (2) the secondary nucleus consists of a single layer of enfolded sections of a polymer molecule upon the surface of the crystal.

The former case where the shape of the cross section of the secondary and primary nuclei are the same is not likely to be correct, but it has the advantage that an accurate expression for its free energy may be written down explicitly. In figure 8, a secondary nucleus of this type is shown on the lateral surface of the larger primary crystal. The free energy required to form this nucleus is the difference between the free energy required to form the total crystalline region $P+S$ shown in figure 8, and the free energy required to form the crystal, P. If there are ν step elements in the secondary crystal, the free energy required to form the secondary nucleus is

$$\Delta\phi_g' = 2\nu a\sigma_e + \frac{C}{2}\sqrt{\nu a}\,\sigma_s l_p^* - \nu a l_p^* \Delta f. \tag{68}$$

The equation above applies to the case where both the crystal and the secondary nucleus possess the

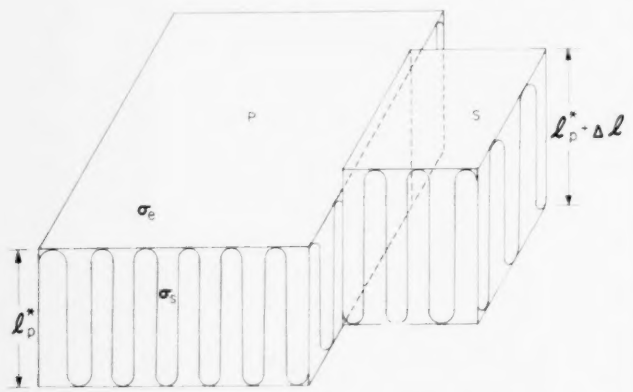

FIGURE 8. *Schematic diagram of primary crystal, P, with a hypothetical secondary nucleus of the same cross-sectional shape, S, upon lateral surface of the crystal.*

A secondary nucleus or embryo where $\Delta l \pm 0$ is shown in the text to be considerably less stable than one of length l_p^*.

critical length l_p^*. It should be noted that the secondary nucleus possesses only one-half as much lateral surface energy as a primary nucleus of the same size and shape. We easily find that

$$\Delta\phi_g^* = \frac{\Delta\phi_p^*}{4}. \tag{69}$$

Then the activation barrier of a secondary nucleus would be only one-quarter of that required to form a primary nucleus. If the height of the step elements in the secondary nucleus is allowed to be $l_p^* + \Delta l$, the free energy required to form such a secondary nucleus can be calculated by the usual methods. It is found that the energy barrier $\Delta\phi_g'^*$ which such a nucleus must surmount is

$$\Delta\phi_g'^* = \frac{1}{4}\Delta\phi_p^* + \frac{\Delta\phi_p^*}{2}\frac{(\Delta l)}{l_p^*} \text{ for } \Delta l \geq 0,$$
$$\Delta\phi_g'^* = \frac{1}{4}\Delta\phi_p^* + \frac{\Delta\phi_p^*}{4}\frac{(\Delta l)^2}{l_p^*(l_p^* + 2\Delta l)} \text{ for } \Delta l \leq 0. \tag{70}$$

The variation in lengths of secondary nuclei will thus be small, since we have seen that $\Delta\phi_p^*$ is large.

If the primary nucleus has a length l which is greater than l_p^*, the secondary nucleus will possess a length very close to l_p^*. It is clear that if the secondary nucleus has the same cross-sectional shape as the primary nucleus, the step height of the crystal will not increase as the latter body grows.

The activation barrier required to form a critical secondary nucleus of the same shape as the primary nucleus is large. It is therefore probable that the secondary nucleus of critical size is a *monomolecular* layer of step elements that lie along the growing crystal face. An accurate expression for the free energy of such a nucleus is not available, but the same assumptions that were used in the previous section may be applied here. The free energy required to nucleate on the growing crystal face is the same as that required for a monomolecular layer to turn a corner and grow on a new crystal face. Thus $\Delta\phi_g$ is identical to $\Delta\phi'$ in eq (59). From the results of the previous section concerning the formation of a primary crystallite it can be concluded that if the edge energy, ϵ, is negligible the crystal will grow with a constant step height, l^*, which is given approximately by

$$l^* = \frac{2\sigma_e}{\Delta f} + \frac{kT}{h\sigma_s}. \tag{71}$$

When the monomolecular layers have completely encircled the growing crystallite, it is improbable that additional layers will have step heights appreciably larger than l^* since such layers would extend above the growing crystal face and therefore would require more free energy to construct. Thus the distribution will be somewhat sharper than that implied by eq (65), and the step height may decrease slightly from the value given by eq (71). In any case the crystal will grow with a very narrow distri-

bution of step heights about $\mathbf{l}^*$, and the variation of step height should be approximately $1/2^{1/2}(kT/\mathbf{h}\sigma_s)$.

For this type of secondary nucleus, $\mathbf{p}_g$ is obtained by the integration of $(\mathbf{r}/\mathbf{N})d\mathbf{l}$ over all permissible values of $\mathbf{l}$. With a suitable choice of C_1 in eq (63) we have approximately

$$\mathbf{p}_g=\frac{kT}{h}\left(\frac{\mathbf{a}\Delta\mathbf{f}}{2\mathbf{h}\sigma_s}\right)\exp\left(-\frac{\Delta\mathbf{F}_g^*}{kT}\right)\exp\left\{-\frac{4\mathbf{h}\sigma_s\sigma_e}{kT\Delta\mathbf{f}}\right\}. \tag{72}$$

In this case log $\mathbf{p}_g$ varies approximately as $(\Delta\mathbf{T})^{-1}$ for moderate supercooling.

Price [19] has independently considered the growth of crystals with folds through nucleation of monomolecular layers.

At this point it is appropriate to discuss the possibility of an edge free energy affecting the growth process appreciably. An edge free energy in a monomolecular secondary nucleus can be considered to arise as follows. If the growing crystal has flat surfaces containing loops, the packing of the loops increases the stability of the crystal. If a monomolecular layer is placed upon the growing surface of the crystal, where the step height of the growing surface differs from that of the layer, the loops in the monomolecular layer cannot be as efficiently packed as if they coincided with the flat surfaces of the crystal. This will lead to an edge energy appearing in the expression for the free energy required to form this monomolecular layer

$$\Delta\phi_g''=2\mathbf{h}\sigma_s\mathbf{l}+2\nu\mathbf{a}\sigma_e+\nu\mathbf{h}\epsilon-\nu\mathbf{al}\Delta\mathbf{f} \tag{73}$$

where ϵ is the free energy required to form a unit length of "edge" in the monomolecular layer. The introduction of the parameter ϵ in eq (73) will not affect the general conclusions previously obtained, but will affect the quantitative results.

We are justified in considering this case since it will be shown in section 3.5. that it can be experimentally determined whether ϵ is negligible or not. Equation (73) applies to a layer where the step height of the monomolecular layer is less than that of the growing crystal surface.

The free energy required to form a monomolecular layer with a larger step height than the growing crystal surface requires the addition of a term $2\nu\mathbf{h}\sigma_s\Delta\mathbf{l}$ to eq (73), where $\Delta\mathbf{l}$ is the difference in step height. The free energy required to form a monomolecular layer with the same step height as the growing crystal surface is

$$\Delta\phi_g'''=2\mathbf{h}\sigma_s\mathbf{l}+2\nu\mathbf{a}\sigma_e-\nu\mathbf{al}\Delta\mathbf{f}, \tag{74}$$

i.e. no term in ϵ appears.

Inspection of eq (73) shows that when $\mathbf{l}<2\sigma_e/\Delta\mathbf{f}+\mathbf{h}\epsilon/\mathbf{a}\Delta\mathbf{f}$, $\Delta\phi_g''$ increases with increasing ν. This will hold true until the monomolecular layer extends around the entire crystal when a maximum free energy will be attained. Further additions of step elements would then reduce the free energy. The activation barrier would be very large particularly if the crystal were large. The formation of a stable nucleus with a step height less than $2\sigma_e/\Delta\mathbf{f}+\mathbf{h}\epsilon/\mathbf{a}\Delta\mathbf{f}$ would undoubtedly proceed through the formation of a differently shaped nucleus, but would in any case require a very large activation barrier. We see therefore that we need only consider the case

$$\mathbf{l}>\frac{2\sigma_e}{\Delta f}+\frac{\mathbf{h}\epsilon}{\mathbf{a}\Delta\mathbf{f}}. \tag{75}$$

Inspection of eq (73) shows that it is identical to eq (59) if σ_e in the former equation is replaced by $(\sigma_e+\mathbf{h}\epsilon/2\mathbf{a})$ in the latter. It is therefore unnecessary to repeat the calculations, and the step height of the monomoleuclar layer will be

$$\mathbf{l}^*=\frac{2\sigma_e}{\Delta\mathbf{f}}+\frac{\mathbf{h}\epsilon}{\mathbf{a}\Delta\mathbf{f}}+\frac{kT}{\mathbf{h}\sigma_s}. \tag{76}$$

After the step height given by eq (76) is established, additional monomolecular layers of this step height will require the free energy given by eq (74), while any deviation from this value will require a free energy that includes the edge free energy. Then the distribution in step heights will be sharper than that calculated previously.

We have not considered explicitly the case where the monomolecular layer has a step height greater than the growing crystal face, but it can be shown that the rate of deposition of such a layer is negligible, if there is an appreciable increase in step height. Thus while the step height of the primary critical nucleus may persist for a time, it is expected that as the crystal grows the step height will be reduced to $\mathbf{l}^*$ as given by eq (76) and the grown crystal will possess the step height $\mathbf{l}^*$.

The above remarks apply when the edge free energy, ϵ, is not so large that the right hand side of eq (76) is larger than $\mathbf{l}_p^*$, the step height of the critical nucleus. If, however, the value of $\mathbf{l}^*$ as given by eq (76) is larger than $\mathbf{l}_p^*$, then the grown crystal will have a step height $\mathbf{l}_p^*$, characteristic of the homogeneously formed critical nucleus.

It should be mentioned that if the edge free energy in the primary nucleus, ϵ_p, is included in our calculations it is found that

$$\mathbf{l}_p^*=\frac{4\sigma_e}{\Delta\mathbf{f}}+\frac{2C\epsilon_p}{\sigma_s}. \tag{77}$$

It must be understood that ϵ_p and ϵ are in general different and in fact it is likely that ϵ is appreciably larger than ϵ_p. Similarly, the free energy required to form a critical nucleus is

$$\Delta\phi_p^*=\frac{2C^2\sigma_s^2\sigma_e}{(\Delta\mathbf{f})^2}+\frac{2C^2\sigma_s\epsilon_p}{(\Delta\mathbf{f})}. \tag{78}$$

It may be stated in summary that, independent of the value of ϵ, the grown crystal will have a step height that is quite uniform due to kinetic factors that arise from the nature of the saddle point in the

free energy surface of forming stable growth nuclei. However, the step height of the grown crystal will be numerically different for different values of ϵ: (I) If ϵ is negligibly small the step height of the grown crystal is given by eq (71). (II) If ϵ has a moderate value the step height of the grown crystal is given by eq (76). (III) If ϵ is very large the step height of the grown crystal is equal to that of the primary nucleus, and is given by eq (77). Case I can be distinguished from II and III by a determination of the melting point of these crystals that will be described in section 3.5. Cases II and III may be distinguished by an accurate measurement of the melting point of the crystals combined with an accurate measurement of the variation of step height with the temperature of crystallization.

In order that the overall kinetics of crystallization can be calculated, it is necessary to calculate $\mathbf{v}_c(t, \tau)$, the volume at time t of a crystal that was nucleated at time τ. The volume growth in a crystal proceeds through the formation of a stable secondary nucleus on the growing (lateral) surface followed by the "crystallization" of the entire new molecule. The rate of addition of molecules to the crystal will equal the product of the average number of molecules in contact with the growing surface, $\boldsymbol{\rho}$, and the rate at which one of these molecules forms a stable nucleus, $\mathbf{p}_g$. Then the rate of volume increase of the crystal will be.

$$\frac{d\mathbf{v}_c}{dt}=\mathbf{a}L\boldsymbol{\rho}\mathbf{p}_g \tag{79}$$

where $\mathbf{a}L$ is the average crystalline volume of a polymer molecule. In section 2, the growth rate of the linear dimensions of a polymer crystal in a bulk phase was nucleation controlled and independent of time, unless impingements or chain entanglements between different crystals occurred. Impingements can be neglected in the growth of crystals in dilute solution. However, the growth rates are determined by both diffusion and nucleation processes, and are not in general independent of time for the loop nucleus. The number of polymer molecules per unit volume of the solution at the growing surface of the crystal, $\mathbf{n}(t, \tau)$, will depend upon diffusion processes and the consumption of polymer molecules. Nevertheless, since only a rough estimate of the growth rate will be attempted, it will be assumed that

$$\mathbf{n}(t, \tau)=\mathbf{n}_0. \tag{80}$$

We can estimate $\boldsymbol{\rho}$ by assuming that every polymer molecule that approaches the edge of the crystal by a distance closer than one-half its mean end-to-end distance in solution, $\boldsymbol{\lambda}$, can form a secondary nucleus. Then, if $\boldsymbol{\lambda}\gg\mathbf{l}^*$,

$$\boldsymbol{\rho}=P(\pi\boldsymbol{\lambda}^2)\mathbf{n}_0 \tag{81}$$

where P is the perimeter of the crystal and $\mathbf{n}_0$ is taken as the average number of polymer molecules per unit volume at the growing surface of the crystal.

It is assumed that the shape of the cross section of the crystal is a parallelogram with an acute angle between two sides, $\psi=70°$. Experimental values of $\psi=66°$ to $74°$ have been found by Till [3] for linear polyethylene crystals obtained from dilute solution. This is approximately the shape of the single crystals of polyethylene obtained by Keller [1]. It is also assumed that all four sides of the parallelogram have the same length, $\mathbf{X}$, i.e., $\mathbf{X}=\mathbf{x}=\mathbf{y}$. This assumption simplifies the following calculations, and is a consequence of the double spiral model used (it is clear for figs. 4b and 5a that $\mathbf{x}=\mathbf{y}$). Many other models also would lead to the same result. Then the volume of the growing crystal is

$$\mathbf{v}_c=\mathbf{l}^*\mathbf{X}^2\sin\psi. \tag{82}$$

The perimeter of the growing crystal is

$$P=4\mathbf{X}. \tag{83}$$

Combining eqs (79), (81), and (83),

$$\frac{d\mathbf{v}_c}{dt}=4\pi\boldsymbol{\lambda}^2\mathbf{a}L\mathbf{p}_g\mathbf{X}\mathbf{n}_0. \tag{84}$$

Integration of eq (84) gives immediately

$$\mathbf{v}_c(t, \tau)=\mathbf{a}L+4\pi\boldsymbol{\lambda}^2\mathbf{a}\mathbf{L}\mathbf{p}_g\mathbf{n}_0\int_\tau^t \mathbf{X}dt'. \tag{85}$$

Substitution of eq (82) into eq (84) yields after some manipulation

$$\mathbf{G}=\frac{d\mathbf{X}}{dt}=\frac{2\pi\boldsymbol{\lambda}^2\mathbf{a}L}{\mathbf{l}^*\sin\psi}\mathbf{p}_g\mathbf{n}_0. \tag{86}$$

Under the approximations employed above, the growth rate, $\mathbf{G}$, of the sides of the crystal is independent of the time. Integration of eq (85) yields

$$\mathbf{X}(t,\tau)=\frac{2\pi\boldsymbol{\lambda}^2\mathbf{a}L}{\mathbf{l}^*\sin\psi}\mathbf{p}_g\mathbf{n}_0(t-\tau) \tag{87}$$

where $\mathbf{X}(\tau,\tau)$ has been equated to zero.

Substituting eq (87) into eq (85) it is found that

$$\mathbf{v}_c(t,\tau)=\mathbf{a}L+\frac{8\pi^2\boldsymbol{\lambda}^4(\mathbf{a}L)^2(\mathbf{p}_g)^2}{\mathbf{l}^*\sin\psi}(\mathbf{n}_0)^2\frac{(t-\tau)^2}{2}. \tag{88}$$

Equation (74) gives us our desired result. It must be remembered that this equation is valid only in the early stages of the crystallization process, and only when diffusional effects are negligible. The term $\mathbf{a}L$ is the volume of the primary crystallite, and the second term represents the additional volume at time t due to accretion of new molecules on the lateral surfaces.

3.4. Value of n for the Overall Crystallization Process From Dilute Solution

In discussing crystallization from dilute solution we define the quantity, χ, as the mass fraction of the total amount of polymer in the solution that is

crystalline. χ will then be zero when no crystals have been formed, and will attain the value of unity if all the polymer present has entered the crystalline state. The crystalline mass is

$$\mathbf{M}_c=\boldsymbol{\rho}_c\mathbf{V}_c \tag{89}$$

where $\boldsymbol{\rho}_c$ and $\mathbf{V}_c$ are the density and volume of the crystalline phase. The total number of polymer molecules is $\mathbf{n}_0\mathbf{V}_s$, where $\mathbf{V}_s$ is the initial volume of the solution and $\mathbf{n}_0$ is the initial number density of polymer molecules. If all polymer molecules were crystallized, the crystalline volume would be approximately $\mathbf{n}_0\mathbf{V}_s\mathbf{a}L$, where L is the mean length of a polymer molecule. Hence the total mass of polymer is

$$\mathbf{M}_{\text{tot}}=\boldsymbol{\rho}_c\mathbf{n}_0\mathbf{V}_s\mathbf{a}L, \tag{90}$$

and by definition

$$\chi=\frac{\mathbf{M}_c}{\mathbf{M}_{\text{tot}}}=\frac{\mathbf{V}_c}{\mathbf{n}_0\mathbf{a}L\mathbf{V}_s}. \tag{91}$$

Since $(\mathbf{n}_0\mathbf{a}L\mathbf{V}_s)$ is independent of time, the time dependence of χ is determined by the time dependence of $\mathbf{V}_c$. The crystalline volume as a function of time is

$$\mathbf{V}_c=\mathbf{V}_s\int_0^t \boldsymbol{I}(\tau)\,\mathbf{v}_c(t,\tau)\,d\tau \tag{92}$$

where $\mathbf{V}_s\boldsymbol{I}(\tau)d\tau$ is the number of stable nuclei formed between τ and $\tau+d\tau$, and $\mathbf{v}_c(t,\tau)$ is the volume of a crystal that was nucleated at τ. From eqs (91) and (92).

$$\chi=\frac{1}{\mathbf{n}_0\mathbf{a}L}\int_0^t \boldsymbol{I}(\tau)\,\mathbf{v}_c(t,\tau)\,d\tau \tag{93}$$

Both the nucleation rate and the crystal growth rate will be reduced as crystallization proceeds due to the depletion of crystallizable material. Also $\mathbf{v}_c(t,\tau)$ will be reduced in value if long range diffusion effects are important, and at the beginning of the crystallization process the nucleation rate $\boldsymbol{I}(\tau)$ will not have attained its equilibrium value. These circumstances introduce serious difficulties into an accurate evaluation of χ from eq (93). Instead of attacking these problems, we shall limit ourselves to the presentation of an approximate expression for χ in a form that has been widely used in the interpretation of experimental data.

In order to introduce this approximate expression, we define a new quantity, χ', which is the value of χ that would result if all crystals were growing in a solution where the number density of uncrystallized polymer molecules remained at the constant value $\mathbf{n}_0$. From its definition it is clear that χ' may take on values from 0 to ∞. We shall assume that an adequate representation of the effect of the depletion of crystallizable material is given by

$$\frac{d\chi}{dt}=\frac{d\chi'}{dt}\left[1-\frac{\chi}{\mathbf{X}_w}\right]. \tag{94}$$

Here $\mathbf{X}_w$ is the limiting value of χ. In dilute solution it is expected that $\mathbf{X}_w$ is very close to unity, and it will be assumed henceforth that $\mathbf{X}_w=1$. (In the corresponding expression for bulk polymers [6], $\mathbf{X}_w$ can be considerably less than unity as a result of impingements). Equation (94) is clearly accurate at small values of t, and probably reasonably accurate up to moderate values of χ. From an integration of eq (94) it is found that

$$\chi=1-e^{-\chi'}. \tag{95}$$

We have cast our expression for χ into this form for convenience in comparing our results with experimental data. Expressions of the form of eq (95) with $\chi'=\mathbf{Z}_n t^n$ have been derived phenomenologically by Mandelkern, Quinn, and Flory [9] and others [6], and have been widely used in interpreting experimental data. These expressions are plotted for various integral values of n and comparison is made with experimental isotherms. The value of n which yields the best fit provides information concerning the geometry of the crystal growth. For example, if the crystals are nucleated sporadically in time and exhibit lineal two dimensional growth, n will be equal to three. It should also be noted that if $\chi'=\mathbf{Z}_n t^n$, the isotherms defined by eq (95) obtained at various temperatures should be superposable simply with a shift in the time scale.

The quantity χ' is defined as that value of χ which would result if all crystals were growing in a solution of constant number density $\mathbf{n}_0$ of polymer molecules. Then the equilibrium nucleation rate is given by eq (51) and $\mathbf{v}_c(t,\tau)$ by eq (88). Substituting these values in eq (93) it is found that

$$\chi'=\mathbf{Z}_1 t+\mathbf{Z}_3 t^3 \tag{96a}$$

where

$$\mathbf{Z}_1=\frac{kT}{h}\,e^{-\Delta\mathbf{F}_p^*/kT}e^{-\Delta\boldsymbol{\phi}_p^*/kT} \tag{96b}$$

$$\mathbf{Z}_3=\frac{(2\pi\boldsymbol{\lambda}^2\mathbf{n}_0)^2}{3}\,\frac{\mathbf{a}L}{\mathbf{l}^*\sin\psi}\left(\frac{kT}{h}\right)(\mathbf{p}_g)^2 e^{-\Delta\mathbf{F}_p^*/kT}e^{-\Delta\boldsymbol{\phi}_p^*/kT} \tag{96c}$$

where $\mathbf{p}_g$ is probably of the form given by eq (72).

It can be shown that the linear term $(\mathbf{Z}_1 t)$ often lies in an experimentally inaccessible region. Then

$$\chi'=(t)^3\,\frac{(2\pi\boldsymbol{\lambda}^2\mathbf{n}_0)^2}{3}\,\frac{\mathbf{a}L}{\mathbf{l}^*\sin\psi}\left(\frac{kT}{h}\right)(\mathbf{p}_g)^2 e^{-\Delta\mathbf{F}_p^*/kT}e^{-\Delta\boldsymbol{\phi}_p^*/kT}. \tag{97}$$

Substitution of eq (97) into eq (95) yields

$$\chi=1-e^{-\mathbf{Z}_3 t^3} \tag{98}$$

It is in order at this point to mention the principal approximations made in deriving eq (98) for simple loop-type crystals: (a) the depletion of crystallizable material was approximated by eq (94); (b) the growth of the crystals was assumed to be nucleation con-

trolled instead of diffusion controlled; (c) the equilibrium nucleation rate was assumed to hold at all times; and (d) nucleation on the end surface of the crystals has been neglected.

The approximation for depletion of crystallizable material should be reasonably accurate for small and moderate values of χ, although not valid for values of χ near unity. Since at sufficiently low concentrations of crystallizable material the crystal growth must become diffusion controlled, eq (98) cannot be accurate when χ is near unity. The validity of the assumption of nucleation controlled growth for low and moderate values of χ is more difficult to evaluate. It is believed reasonable by the authors that, except at very low concentrations of the crystallizable material, the effects of long range diffusion will not predominate. When these effects do predominate, the exponent of the time in eq (98) will be lowered somewhat. Finally, it is expected that the growth rate of the crystals is much more rapid than the primary nucleation rate. Under these circumstances the effects of the transient nucleation rate may be observed for low values of χ. This could cause the observed exponent of the time in eq (98) to be quite large for small values of χ, even exceeding $n=4$. (In this region, the value of n is fictitious in the sense it does not reflect the type of nucleation and growth of the crystals.) If growth through secondary nucleation on the end surfaces is important the value of the exponent will be increased over what it would have been in the absence of such growth.

Our results may be summarized as follows: If the phenomenological expression

$$\chi = 1 - e^{-\mathbf{Z}_n t^n} \tag{99}$$

is fitted to experimental data, we should expect that the best fit at moderate values of χ should be obtained for values of n near three. If long range diffusion limits crystal growth, somewhat lower values of n can be expected, whereas growth of the crystals through nucleation on the end surfaces will raise the value of n. At low degrees of crystallinity, higher values of n might be observed due to the effects of a transient nucleation rate. The value $n=3$ is, of course, that appropriate to (lineal) two-dimensional growth of objects born sporadically in time.

These results agree reasonably well with the experimental isotherms obtained dilatometrically by Mandelkern and Quinn [17, 18] on crystallization of polyethylene from a 0.25 percent solution of α-chloronaphthalene. Mandelkern has not investigated the morphology of the resulting polyethylene crystals, but he states that this concentration is comparable to that in which platelike crystals are formed. Superposable isotherms were obtained for crystallization temperatures from 97° to 104°C. The superposability of these isotherms is in marked contrast to the results he obtained with more concentrated solutions, but similar to that obtained for bulk crystallization. In addition, Mandelkern compared curves of the form of eq (99) with his isotherms and concluded that if the first 5 percent of the transformation is neglected, an almost exact fit is obtained for the major portion of the process if values of $n=3$ and $n=4$ are used. The first 5 percent of the crystallization process would require considerably higher values of n for a proper fit.

The agreement between our results and the experimental isotherms is consistent with the assumption that these isotherms result from the formation of crystals with folds. We shall proceed on this assumption and investigate the temperature dependence of the rate of overall crystallization in section 3.6. In order to perform this analysis we must estimate the equilibrium melting temperature, $\mathbf{T}_m$. In estimating $\mathbf{T}_m$, certain pitfalls can be avoided by elucidating some properties of crystals with folds that result from their metastability. This is done in the next section.

3.5. Metastability of Crystals Formed by Chain Folding

In previous sections the nucleation and growth of polymer crystals with loops has been discussed. We shall now give a brief treatment of the metastable character of these crystals. It will be demonstrated first that crystals with loops formed isothermally will have a relatively sharp melting point $\mathbf{T}'_m$, appreciably below the equilibrium melting temperature in the presence of solvent, $\mathbf{T}_m$. The possibility that crystals with loops may have a tendency to increase their step height when stored at elevated temperatures will also be discussed. Before these points can be treated, it is necessary to consider the free energy difference between the crystalline state and the solution state for a crystal with loops.

If a crystal has ν step elements of length $\mathbf{l}$, its free energy with respect to the solution state is

$$\Delta\phi_c = 2\nu\mathbf{a}\sigma_e + C\sigma_s\sqrt{\nu\mathbf{al}} - \nu\mathbf{al}\Delta\mathbf{f}. \tag{100}$$

Equation (100) is formally identical with expressions for the free energies of nuclei that have been presented in previous sections, but several important distinctions must be noted. The crystal under consideration has been formed with a length $\mathbf{l}$ in an isothermal manner. We redefine the temperature of crystallization as $\mathbf{T}_x$. Equation (100) represents the free energy of the crystal at a temperature T, which is not necessarily the same as the temperature of crystallization, $\mathbf{T}_x$. The variation of the free energy of the crystal, $\Delta\phi_c$, with temperature is primarily due to the variation of the thermodynamic driving force, $\Delta\mathbf{f}$, with temperature. The approximate variation of $\Delta\mathbf{f}$ with temperature was given in eq (28) which is rewritten here for convenience

$$\Delta\mathbf{f} = \Delta\mathbf{h}_f\left(\frac{\mathbf{T}_m - T}{\mathbf{T}_m}\right). \tag{101}$$

Finally, ν is a very large number since eq (100) applies to a crystal, not a nucleus.

The volume of the crystal is νal. Then the free energy difference per unit volume of crystal between the crystalline and solution states is

$$\left(\frac{\Delta\phi_c}{\nu al}\right)=\frac{2\sigma_e}{l}+\frac{C\sigma_s}{\sqrt{\nu a}}-\Delta h_f\left(\frac{T_m-T}{T_m}\right). \tag{102}$$

Since the crystal has a large number of step elements, $\nu^{-1/2}$ is small, and the second term on the right hand side of eq (102) will be neglected. Then

$$\left(\frac{\Delta\phi_c}{\nu al}\right)=\frac{2\sigma_e}{l}-\Delta h_f\left(\frac{T_m-T}{T_m}\right). \tag{103}$$

The most stable crystal at any temperature will be that crystal which has a minimum value of $\Delta\phi_c/\nu al$. It is clear from eq (103) that crystals with large step heights are more stable than crystals with smaller step heights. It is, of course, not surprising that a larger crystal is more stable than a smaller one. However, when a loop-type crystal of length l and of a given volume has been formed, it will probably be difficult for the step height to increase simply by having the crystal change its shape. Such an increase of step height would tend to be slow because of the complicated diffusion mechanism with lengthwise "sliding" of the polymer chains that would be involved. The ensuing discussion is carried out on the assumption that, in a melting experiment of sufficiently short duration, l will not increase appreciably.

If crystals with loops with length l^* are formed isothermally at a temperature of crystallization, T_x, they will melt at a temperature appreciably below the equilibrium melting temperature. In order to find the melting point we shall first derive an expression valid for any l. The temperature at which a crystal melts can be deduced from eq (103). A crystal with loops, which has a step height l, is stable at its temperature of formation with respect to the solution state. If, after the crystal was formed, the temperature is increased, the free energy increases. When the free energy of the crystal with respect to the solution state vanishes, the crystal will melt. Then the temperature of melting of a crystal with step height, l, is obtained by equating eq (103) to zero and solving for the temperature:

$$T'_m(l)=T_m\left[1-\frac{2\sigma_e}{\Delta h_f l}\right]. \tag{104}$$

We see that T_m is the melting temperature of a crystal with infinite step height.

The above expression, eq (104) has been derived with two tacit assumptions. It has been assumed that the rate of heating in the melting experiment is sufficiently rapid so that the step height, l, does not increase and sufficiently slow so that the actual melting temperature of the crystal will be observed to a close approximation. The recrystallization at greater step heights after melting need not be considered since the large negative temperature coefficient of the crystallization process ensures that recrystallization is very slow.

We have seen that in an isothermal crystallization the step heights of the crystals will be very close to a characteristic value, l^*. Thus all the crystals formed in an isothermal crystallization will melt at almost the same temperature. This temperature, T'_m, which is where these crystals melt, i.e., redissolve, is obtained by substituting the appropriate value of l^* into eq (104):

$$T'_m=T_m\left[1-\frac{2\sigma_e}{\Delta h_f l^*}\right] \tag{105}$$

Let us first consider the case where the edge free energy, ϵ, of nucleating a monomolecular layer is negligible. Then from eq (71) and eq (28)

$$l^*=\frac{2\sigma_e}{\Delta h_f}\cdot\frac{T_m}{T_m-T_x}+\frac{kT_x}{C\sigma_s}. \tag{106}$$

Since $kT_x/C\sigma_s$ is 20 Å or less and l^* is characteristically near 120 Å, it follows that when eq (106) is substituted into eq (105), then T'_m is only a few degrees greater than T_x. Thus, if the edge energy is negligible, the crystals formed at a temperature of crystallization, T_x, will melt only a few degrees above T_x. Hence, an investigation of the temperature at which the crystals melt in solution can determine whether ϵ is negligible or not. The combination of these results with an accurate determination of the variation of step height l^* with the temperature of crystallization, T_x, should determine the importance of ϵ and ϵ_p. If the step height of the crystal is as large as that of the critical primary nucleus with ϵ_p neglected, then

$$l^*=\frac{4\sigma_e}{\Delta h_f}\cdot\frac{T_m}{T_m-T_x}. \tag{107}$$

Substituting this value in eq (105) it is found that

$$T'_m=\frac{1}{2}(T_x+T_m). \tag{108}$$

Then even if the step height is as large as that of a primary nucleus the crystal will tend to melt at a temperature approximately midway between the equilibrium melting temperature in the presence of solvent, and the temperature of crystallization.

The presence of a substantial number of crystallites with a small number of step elements would tend to broaden the melting curve, and imperfections due to branches might have a similar effect. It is to be understood that T'_m is to be measured under conditions where the warming rate is slow enough so that thermal equilibrium is established, but not so slow that l^* has time to increase appreciably.

A direct determination of the equilibrium melting temperature in dilute solution, T_m, by slow warming may prove very difficult because of the persistence

of the step height. The "$\mathbf{T}_m$" value so obtained could easily be somewhat low.

The above results were derived for crystals in solution, but it is believed that they would be qualitatively true if the crystals were removed from the solution and the solvent eliminated from the crystals. For example, a mass of dried loop-type crystals, previously initiated and grown to large **x** and **y** dimensions in an isothermal manner from dilute solution at a temperature below $\mathbf{T}_m$, should melt fairly sharply and well below T_m, the (bulk) equilibrium melting temperature.

It is not difficult to show that *a crystal with loops is more stable than a bundlelike crystal of the same size and shape* in a sufficiently dilute solution. The free energy difference between a loop-type crystal and the solution state is given in eq (100) The free energy difference between a bundlelike crystal of the same size and shape and the solution state is obtained by replacing **a**, $\boldsymbol{\Delta f}$, $\boldsymbol{\sigma}_s$, and $\boldsymbol{\sigma}_e$ in eq (100) by a, Δf_d, σ_{sd}, and $(\sigma_{ed}-kT\log_e v_2/2a)$. The quantities a, Δf_d, and σ_{sd} are comparable to **a**, $\boldsymbol{\Delta f}$, and $\boldsymbol{\sigma}_s$. The end surface free energy for a bundlelike crystal in dilute solution was seen to be $(\sigma_{ed}-(kT\log_e v_2/2a)$ in section 3.2, and in a sufficiently dilute solution this surface energy is greater than $\boldsymbol{\sigma}_e$. Then in a sufficiently dilute solution the loop-type crystal is more stable than a bundlelike crystal of the same shape and volume, because the end surface energy contribution to the bundlelike crystal is much larger. In fact if the solution is sufficiently dilute so that loop-type nuclei are kinetically favored over bundlelike nuclei, the grown loop-type crystal are at the same time more stable than a bundlelike crystal of the same shape and volume. This result applies to crystals in solution.

If a loop-type crystal *of a given volume and cross-sectional shape* is in a dilute solution, the step height of this crystal will eventually approach an "equilibrium" value, where the total surface energy of the crystal will be minimized. The "equilibrium" value of the step height can be obtained by differentiating eq (100) with respect to **l** with the volume, $\boldsymbol{\nu}\mathbf{al}$, held constant, and then equating this result to zero. If the resulting equation is solved for **l**, it is found that the "equilibrium" value of the step height is $(4\boldsymbol{\sigma}_e/C\boldsymbol{\sigma}_s)^{2/3}V^{1/3}$, where V is the volume of the crystal. This result is based on the assumption that the polymer chains are much longer than the step heights considered. From this formula it follows that the "equilibrium" value of the step height is roughly equal to the lateral dimensions of the crystal. From this it is clear that the experimentally observed polyethylene crystals with characteristic step heights near 120 Å have not attained their "equilibrium" step height through "sliding" diffusion.

3.6. Kinetics of the Overall Crystallization Process for Dilute Solution

In this section the theoretical expressions for the rate of overall crystallization are compared with the available experimental data with particular emphasis on the temperature dependence of the rate expressions. Unfortunately there are no available rate data in those systems where crystals with loops have been identified through morphological studies. The only accurate rate data for crystallization from dilute solution are the dilatometric measurements of Mandelkern and Quinn [17, 18] on the crystallization of linear polyethylene from a 0.25 percent solution of α-chloronaphthalene. The morphology of these crystals was not investigated, but Mandelkern states that the concentration range is comparable to that in which platelike crystals are developed. This encourages the belief that crystals with folds were predominant, especially since the temperature dependence of the shape of the isotherms is in marked contrast to results obtained for crystallization from more concentrated polymer solutions. An analysis will be performed on the assumption that crystallization through chain folding was predominant.

In preparation for an analysis of the experimental data a brief discussion will be given of the temperature dependence of the overall crystallization rates. Expressions for the overall crystallization rate were presented in eq (97) and (98) and will be rewritten here for convenience:

$$\chi = 1-e^{-\mathbf{Z}_3 t^3} \tag{109}$$

where

$$\mathbf{Z}_3=\frac{(2\pi\boldsymbol{\lambda}^2\mathbf{n}_0)^2}{3}\frac{\mathbf{a}L}{\mathbf{l}^*\sin\psi}\left(\frac{kT}{h}\right)^3(\mathbf{p}_g)^2 e^{-\Delta\mathbf{F}_p^*/kT}e^{-\Delta\boldsymbol{\phi}_p^*/kT}. \tag{110}$$

When the temperature of crystallization is not too far from the melting point so that $\boldsymbol{\Delta T}$ is small, the principal variation of $\mathbf{Z}_3$ with temperature is due to the factor $\mathbf{p}_g^2\exp\{-\boldsymbol{\Delta\phi}_p^*/kT\}$. The quantity $\boldsymbol{\Delta\phi}_p^*$ has been previously obtained:

$$\boldsymbol{\Delta\phi}_p^*=\frac{2C'^2\boldsymbol{\sigma}_s^2\boldsymbol{\sigma}_e\mathbf{T}_m^2}{(\boldsymbol{\Delta h}_f)^2}\frac{1}{(\boldsymbol{\Delta T})^2}. \tag{111}$$

The temperature dependence of $\mathbf{p}_g$ is much smaller than $\exp\{-\boldsymbol{\Delta\phi}_p^*/kT\}$. In fact it seems more likely that $\log\mathbf{p}_g$ has a different temperature dependence than $\boldsymbol{\Delta\phi}_p^*$. In any case we may write

$$\mathbf{Z}_3=\mathbf{Z}_{30}e^{-\frac{\boldsymbol{\alpha}'}{T(\boldsymbol{\Delta T})^2}}, \tag{112}$$

where at low degrees of supercooling, $\mathbf{Z}_{30}$ varies slowly with temperature compared to $\exp\{-\boldsymbol{\alpha}'/T(\boldsymbol{\Delta T})^2\}$. In the case where $\mathbf{p}_g$ does not contribute appreciably to $\boldsymbol{\alpha}'$ we have

$$\boldsymbol{\alpha}'\simeq\boldsymbol{\alpha}=\frac{2C'^2\boldsymbol{\sigma}_s^2\boldsymbol{\sigma}_e\mathbf{T}_m^2}{(\boldsymbol{\Delta h}_f)^2 k}. \tag{113}$$

For the remainder of this section it will be assumed that eq (113) is valid, although this is not essential to our analysis.

It has been shown that eq (109) is an adequate description of the isotherms of crystallization at moderate values of χ for the crystallization of linear polyethylene from a dilute solution of α-chloronaphthalene. If the temperature of crystallization is changed, the value of $\mathbf{Z}_3$ is changed. The shape of the isotherm remains unchanged although the time scale is shifted. This allows us to specify the rate of the crystallization process by the time required for the value of χ to reach 0.5. Then from eq (109)

$$\mathbf{Z}_3(t_{1/2})^3=\log_e 2. \tag{114}$$

If the logarithm to the base 10 is taken of both sides, and eq (112) is substituted into the result, it is found after some manipulation that:

$$\log_{10}\left[\frac{1}{t_{1/2}}\right]=\frac{1}{3}\log_{10}\left[\frac{\mathbf{Z}_{30}}{\log_e 2}\right]-\frac{1}{3}\frac{\boldsymbol{\alpha}\log_{10} e}{T(\boldsymbol{\Delta T})^2}. \tag{115}$$

It is clear from eq (115) that if experimental values of $\log_{10}(1/t_{1/2})$ were plotted against $T^{-1}(\boldsymbol{\Delta T})^{-2}$ for various crystallization temperatures, an approximately straight line should be obtained. The value of the product $(\boldsymbol{\sigma}_s^2\boldsymbol{\sigma}_e)$ could be obtained from the slope of this straight line. Since $\boldsymbol{\Delta T}=\mathbf{T}_m-\mathrm{T}$, it is clear that the equilibrium melting temperature, $\mathbf{T}_m$, must be known before such a plot could be constructed.

Mandelkern and Quinn [17, 18] have observed the isothermal crystallization of linear polyethylene from a 0.25 percent solution of α-chloronaphthalene dilatometrically. The shapes of their isotherms agree at values of moderate χ with eq (109), so that it seems reasonable to apply eq (115) to the temperature dependence of these isotherms. Mandelkern has tabulated the values of $t_{1/2}$ for one degree intervals of the crystallization temperature between 97° C and 104° C. He also quotes the equilibrium melting temperature as being between 109° C and 110° C [18], and presents a plot of $\log(1/t_{1/2})$ versus $100/(\boldsymbol{\Delta T})^2$ which is based on this value of $\mathbf{T}_m$. In figure 9 a similar plot is presented. Figure 9 is constructed from the tabulated values of Mandelkern, plotting $\log(1/t_{1/2})$ against $10^5/T(\boldsymbol{\Delta T})^2$ with $\mathbf{T}_m=110°$ C. The curve shown in figure 9 is certainly not a straight line, but is rather concave upwards. Moreover, the slope at the lower degrees of supercooling is smaller in magnitude than the corresponding slope for bulk polyethylene which would appear to indicate that $\boldsymbol{\sigma}_s^2\boldsymbol{\sigma}_e$ is smaller than the corresponding product for the bulk polymer. These facts stand in apparent contradiction to the theory presented in this paper.

The morphology of the crystals was not investigated by Mandelkern and Quinn. It is therefore possible that the theory developed in this paper is not applicable to the data plotted in figure 9. However, it is no easier to explain the curvature in figure 9 if one assumes that *bundlelike* crystals were nucleated either homogeneously or heterogeneously. Since the deviation from a straight line of $\log(1/t_{1/2})$ plotted against $T^{-1}\boldsymbol{\Delta T}^{-2}$ or $T^{-1}\boldsymbol{\Delta T}^{-1}$ is not accounted for by the hypotheses just given, a further discussion of the data will be given. This discussion will show that the experimental data are not necessarily inconsistent with the theory presented in this paper and will serve the useful purpose of emphasizing the care required in obtaining experimental evidence that provides a critical test of this theory.

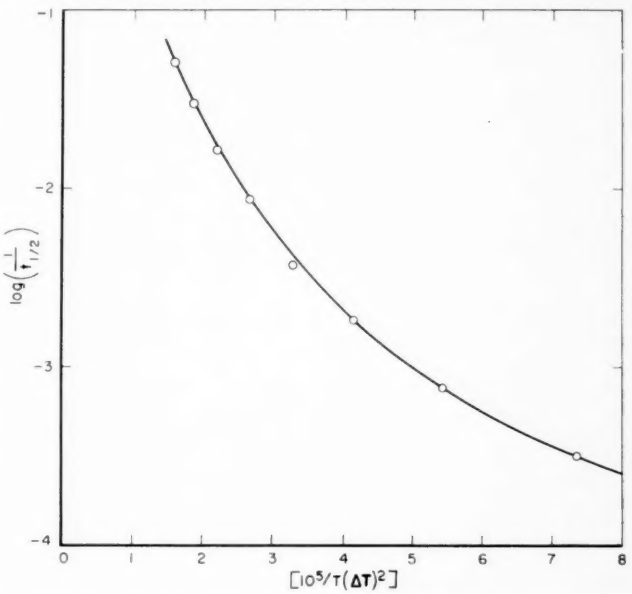

FIGURE 9. *Plot of log $(1/t_{1/2})$ against $[10^5/T(\boldsymbol{\Delta T})^2]$ for a 0.25 percent polyethylene solution in α-chloronaphthalene with $\mathbf{T}_m=110°$ C.*

(After Mandelkern, see ref. [18]).

Upon reflection, a possible resolution of the apparent discrepancy can be seen. Suppose that the value $\mathbf{T}_m=110°$ C was obtained by dilatometrically observing the melting of the crystals in the solution. In the previous section it was shown that crystals formed in dilute solution may melt sharply well below the equilibrium melting temperature for dilute solution. Then the correct value of $\mathbf{T}_m$ might be appreciably higher than 110°. Rough estimates of $\mathbf{T}_m$ can be made by two separate methods. First, if it is assumed that eq (108) is accurate, and that the observed melting temperature, $\mathbf{T}_m'$, is 110° C, the equilibrium melting temperature is obtained if the crystallization temperature is given. For example, if it is assumed that for a sample crystallized at 96° C the observed melting temperature of these crystals is 110° C, then $\mathbf{T}_m=124°$ C. If the temperatures of crystallization and observed melting were 103° and 110° C, $\mathbf{T}_m=117°$ C. This method of estimating $\mathbf{T}_m$ has two drawbacks: (a) the estimate furnishes a range of values of $\mathbf{T}_m$ instead of a single value, and, (b) eq (108) is probably not very accurate. Another method of estimating $\mathbf{T}_m$ is to plot $\log_{10}(1/t_{1/2})$ against $(10^5/T(\boldsymbol{\Delta T})^2)$ for various values of $\mathbf{T}_m$. $\mathbf{T}_m$ is taken to be that value which yields a straight line plot, if such a value exists. This method of estimating $\mathbf{T}_m$ is based on the correctness of eq (115). In figure 10 plots of $\log(1/t_{1/2})$ against $10^5/T(\boldsymbol{\Delta T})^2$ are presented for the assumed values of $\mathbf{T}_m=117°$ C

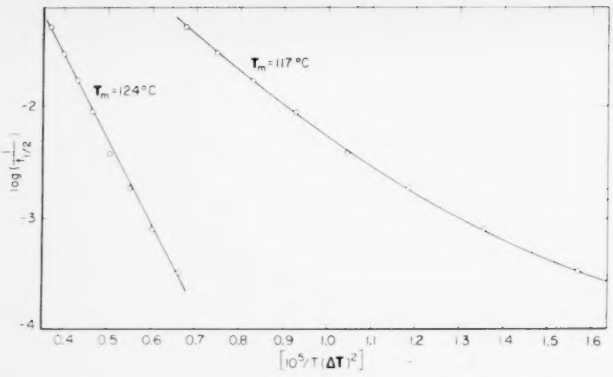

FIGURE 10. *Plot of log $(1/t_{1/2})$ against $(10^5/T(\Delta T)^2)$ for 0.25 percent polyethylene solution in α-chloronaphthalene for two assumed values of T_m showing approach to straight-line behavior.*

The slope of the line obtained with T_m=124° C implies a $\sigma_s^2\sigma_e$ value of ~1070 erg^3 cm^{-6}.

and T_m=124° C. The plot for T_m=117° C has considerable curvature, but the plot for T_m=124° C is fitted well by a straight line.

It is found from the slope of the plot in figure 10 for T_m=124° C that $(\sigma_s^2\sigma_e)$=1070. This value is much larger than the corresponding value obtained from the data on bulk polyethylene where $(\sigma_s^2\sigma_e) \sim$ 100, as calculated from the slope of the plot of (log $1/t_{1/2}$) against $100/(\Delta T)^2$ presented by Mandelkern [18]. This is consistent with the concept that $\sigma_e > \sigma_s$, eq (27). Then the supposition that T_m= 124° C resolves each of the apparent discrepancies between the theory presented in this paper and the experimental rates. It is, of course, not clear that the plot of log$(1/t_{1/2})$ should be exactly straight since Z_{30} in eq (115) is temperature dependent. However, even if T_m is as low as 117° C the plot in figure 10 corresponds to a value of $\sigma_s^2\sigma_e$ which is larger than that observed for the bulk polymer. It is clear that there is no inconsistency between this data and the theory presented in this paper if T_m is appreciably larger than 110° C.

Such high values of T_m are not inconsistent with the errors in estimating T_m. In determining the heat of fusion of polyethylene, Quinn and Mandelkern [14] measured the melting temperature of polyethylene as a function of concentration in various solvents. The heat of fusion per mole of repeat units, ΔH_u, was calculated by fitting the experimental data to the equation

$$\frac{1}{T_{m(d)}} - \frac{1}{T_m} = \frac{R}{\Delta H_u}\left[\frac{V_u}{V_1}\right]\left\{v_1 - \frac{BV_1}{RT_{m(d)}}v_1^2\right\}. \quad (116)$$

Here T_m is the equilibrium melting temperature of the bulk polymer, V_u and V_1 are the molar volumes of the repeating unit and the diluent respectively, B is the interaction energy density characteristic of the solvent solution pair, and $T_{m(d)}$ the equilibrium melting temperature in the presence of diluent. (We adhere to the assumption that a value of $T_{m(d)}$ for $v_1 \to 1$ obtained under equilibrium conditions is very close to T_m.) While ΔH_u was determined within a few percent, Quinn and Mandelkern state that B could be in error by several cal·cm^{-3}. For polyethylene in α-chloronaphthalene they obtain a value $B \cong 0$. If a value of B=2 cal·cm.$^{-3}$ were assigned and ΔH_u left unchanged $T_{m(d)} \to 124°$ C as $v_1 \to 1$. Thus $T_m(_d)$=124° C lies within the assigned experimental error. On the other hand it is somewhat difficult to reconcile the data of Quinn and Mandelkern for moderate concentrations of polyethylene in α-chloronaphthalene with a value of $T_{m(d)}$ for $v_1 \to 1$ as high as 124° C. In short, no definite conclusion can be drawn, but the authors feel that the apparent discrepancy may arise from an incorrect value of T_m.

Even if the correct value of T_m is 110° C for a dilute solution of polyethylene in α-chloronaphthalene, the data of Mandelkern and Quinn are not necessarily inconsistent with the theory presented in this paper. Equation (115) was derived on the assumption that the equilibrium nucleation rate was attained. If, however, the growth rate of the crystals is so great compared to the nucleation rate that the early nucleation transient determines the overall crystallization rate, a different type of expression may be expected. No attempt will be made to obtain an accurate expression for the transient nucleation rate, but the influence of ΔF_p^*, the free energy barrier to addition of another step element, will be very pronounced. This would lead to a plot of log $(1/t_{1/2})$ versus $T^{-1}\Delta T^{-2}$ similar to that shown in figure 9. It should be noted that the first 5 percent of the isotherms obtained by Mandelkern seemed to imply a transient nucleation rate. It should also be noted that if transient nucleation is determining the rate of crystallization of crystals with loops, a reduction in the concentration of the solution will reduce the growth rate and straighten the plot of log $(1/t_{1/2})$ versus $T^{-1}(\Delta T)^{-2}$. The curvature of the plot obtained by Mandelkern and Quinn could apparently be explained if ϵ_p were not negligible because then $\Delta\phi_p^*$ would be given by eq (78) and hence a straight line plot would not be expected. This, however, does not account for the low value of $\sigma_s^2\sigma_e$ obtained from their data when T_m is 110° C. The data of Mandelkern and Quinn may also be explained by other special assumptions, but these possibilities do not appear to be as likely as the ones cited.

It is clear that for a proper evaluation of the experimental data an accurate value of T_m must be obtained. Since it has been shown in section 3.4 that crystals with loops may melt well below equilibrium melting temperature, it is possible that this represents a serious problem for dilute solutions. One possibility is to measure the temperature of melting and the characteristic step height, l^*, as a function of crystallization temperature and attempt to extrapolate to the equilibrium melting temperature by the use of eq (105).

4. Discussion

4.1. Brief Summary of Results

The general predictions yielded by the present study can be summarized in the following manner:

When a crystallizable linear polymer is precipitated from sufficiently dilute solution by supercooling, platelike crystals with a definite step height $\mathbf{l}^*$ will form. In these crystals, the chain axes of the polymer molecules will be perpendicular to the two large flat faces of the platelike crystals. The aforementioned flat faces will contain chain folds, i.e., they will consist of loops. The step height depends on the temperature of crystallization, and on the surface free energy, $\boldsymbol{\sigma}_e$, of the interface containing the loops. The step height is larger for higher crystallization temperatures, and increases with $\boldsymbol{\sigma}_e$. The latter quantity will be fairly large, owing to the fact that the work required to form a loop is involved. (The corresponding quantity for bundlelike nuclei, σ_e, is considerably smaller since it contains no loop energy.) At the degree of supercooling commonly encountered in practice, $\boldsymbol{\Delta T}=10$ to 40° C, $\mathbf{l}^*$ may be expected to lie in the range 50 to 500A. The most perfect crystals will be formed from highly dilute solution, and with unbranched polymer. More imperfect specimens will be formed from more concentrated solution, and a threshold will be reached where very poor crystals will form. The step height will be remarkably uniform if the crystallization is carried out isothermally from a highly dilute solution. Pyramidal growth, where one crystal with fixed step height grows on the flat (loop containing) face of another, is to be expected at moderate dilution, but single crystals should be common at low concentration. In exceptional cases, crystals consisting of but one molecule may be observed. Much more common will be crystals that have grown to fairly large dimensions by successive addition of new polymer molecules through secondary nucleation on the lateral surfaces. These will have substantially the same step height as the primary crystallite. In many cases, distinct protrusions on the lateral surfaces due to secondary nucleation and growth may be seen. The more perfect crystals will often have a regular shape of simple geometric form when viewed normal to the surface containing the loops. Depending on the crystal system, the crystals could, for example, be diamond- or hexagon-shaped.

The overall rate of crystallization will probably follow a law where $n=3$ or $n=4$, most likely nearer the former, over the main part of the process, but deviations from the suggested range in the early and late stages are a distinct possibility. In the early stages a steady-state rate of nucleation may take some time to develop, and in the late stage, where the majority of the molecules have already been swept from the solvent, n may fall.

The crystals containing chain folds formed in dilute solution are metastable: Even in the case where a crystallite of step height $\mathbf{l}^*$, which is formed in solution at a crystallization temperature, $\mathbf{T}_x$, is allowed to grow to very large size in the other two dimensions, it will still melt appreciably lower than $\mathbf{T}_m$, the melting temperature in the presence of solvent of a crystallite that is large in all three dimensions. (Crystals free of solvent formed by drying crystals with loops formed in dilute solution will behave in a qualitatively similar manner, and melt well below the equilibrium bulk melting temperature, T_m.) The observed melting point, $\mathbf{T}'_m$, of a set of crystallites formed isothermally from dilute solution may be surprisingly sharp (but low) owing to the uniformity of the step height. This will be especially true for large crystals precipitated from very dilute solution. If a set of crystals with loops with characteristic step height $\mathbf{l}_1^*$, is formed at an isothermal crystallization temperature T_1, and then the temperature of the solution raised to T_2, where the characteristic step height is $\mathbf{l}_2^*$, $\mathbf{l}_1^*$ will still tend to persist for some period of time at T_2. Thus the melting point $\mathbf{T}'_m$ characteristic of ($\mathbf{l}_1^*$, T_1) will tend to persist even though the temperature of the solution is raised. The equilibrium melting temperature of crystals with loops in dilute solution may thus be very difficult to determine accurately in some cases by the conventional method of slowly raising the temperature.

An isothermal increase of $\mathbf{l}$ due to "sliding" type diffusion in the crystal may occur.

The temperature dependence of the rate of nucleation for nuclei with loops should follow a law of the general form $\ln (\boldsymbol{I}/\boldsymbol{I}_0) \propto \boldsymbol{\alpha}/T(\boldsymbol{\Delta T})^2$. The value of $\boldsymbol{\sigma}_s^2\boldsymbol{\sigma}_e$ that may be estimated from $\boldsymbol{\alpha}$ should be larger than the value of $\sigma_s^2\sigma_e$ obtained for the bundlelike nuclei characteristic of homogeneous bulk nucleation in the same polymer. In order to test the temperature dependence of $\boldsymbol{I}/\boldsymbol{I}_0$, it is necessary to have a reliable value of $\mathbf{T}_m$, so that $\boldsymbol{\Delta T}$ is known accurately.

4.2. Crystals With Loops in Bulk Polymers, and Heterogeneities

The theory given in the foregoing sections deals with *homogeneous* initiation of loop-type crystals in dilute solution. The theory renders it clear that near and below some threshold value of the concentration, that loop-type nuclei will begin to predominate, provided that loop formation is sterically feasible. The theory does not attempt to predict what type of crystal might tend to form in an intermediate concentration range where bundlelike and loop-type nuclei compete. We have indicated that in crystallizable linear polymers in bulk that the conventional bundlelike nucleus seems highly probable. It should be clearly understood that what is meant here is that bundlelike nuclei of *homogeneous* origin seem probable in such bulk polymers; this is not necessarily related to what type of nucleus might form by *heterogeneous* nucleation on the surface of a wettable foreign particle. Moreover, we do not incline to the view that crystals with loops are impossible to form by a homogeneous process in a bulk polymer, and this subject, though obviously speculative, deserves brief discussion.

In a bulk polymer, where $v_2=1$, bundlelike homogeneous *nuclei* should certainly predominate if $\boldsymbol{\sigma}_e > \sigma_e$. (There is little reason to expect that the free energies of activation controlling the jump-rate at the super-

cooled-liquid—crystal interface would be such as to cause a preponderance of loop-type nuclei in bulk.) Then if bundlelike nuclei can grow, the polymer will crystallize without loop formation. However, if the radial growth of the bundlelike nucleus is severely impeded by the strain effect mentioned in section 2.2, which results from the increasing difference in the lattice spacing of the crystal and "liquid" just outside the ends of the bundlelike nucleus as it grows radially, actual crystallization resulting from such nuclei may be greatly subdued. Then another crystallization process may enter. Since according to our formulation, the formation of a few loop-type nuclei is possible at $r_2=1$, and in view of the fact that these would grow if crystallizable material were present, the majority of crystallites actually observed in the bulk phase in such a case would be of the loop-containing variety. The hypothesis that bundlelike nuclei may be prevented from growing to large size by strain, coupled with the reasonable belief that loop-type nuclei, once formed, might not be subject to such a strain effect on growth, thus leads to the possibility that loop-type crystals could make up the main part of the crystallization in the bulk phase. Even then, numerous bundlelike nuclei would be present. The main point of the present theory, however, is that loop-type nuclei (and subsequently crystals derived from them) are quite certain to appear at sufficiently great dilution, provided that loop formation consistent with crystal structure is sterically possible. The theoretical prediction of homogeneously induced loop-type crystals in bulk depends on additional factors, and is altogether more of an open question.

At various places in the literature, evidence has been given suggesting that crystals with folds may arise in bulk polymers (see ref. [1]). The presently available evidence that such "structures" as are seen in bulk polymers may be associated with a step height resulting from nuclei with chain folds that are of *homogeneous* origin is incomplete. If it is in fact true that step structures associated with folds actually exist in the bulk phase, we believe full consideration must be given to the possibility that heterogeneities or surfaces may be involved. We consider it possible that nuclei with folds may form at the surface of a heterogeneity in a bulk phase, some or nearly all of the energy deficit arising from the bending energy $\mathbf{q}$ being made up by the interaction energy of the polymer molecule with the heterogeneity. Also, special structures may tend to develop at the surface of a bulk polymer specimen.

From a theoretical point of view, very considerable confusion can be caused by assuming that any structure seen in a bulk polymer, or on its surface, is a result of homogeneous initiation. It is now known that quite stringent measures are frequently required to develop the intrinsic nucleation mechanism in a bulk polymer. For example, careful filtration and selection of samples coupled with strong superheating prior to crystallization is evidently advisable in some instances. Precautions of the type just mentioned, which are designed to enhance the homogeneous nucleation mechanism, do not seem to be commonly employed in morphological studies on bulk polymers.

Our views concerning the existence of loop-type crystals in bulk polymers may be summarized as follows: (a) While the evidence that loop-type crystals exist in bulk polymers is mounting, proof that such crystals are of homogeneous origin is lacking; (b) if such loop-type crystals are in some polymer proved to be of homogeneous origin, consideration should be given to the possibility that strain subdues or prevents the growth of bundlelike nuclei and, since a few loop-type nuclei will be present, thus allow the predominant crystalline form to possess loops; (c) a likely source of loop-type nuclei is a heterogeneity, and full consideration must be given to this fact in interpreting data on bulk polymers that have not been subjected to special treatment; (d) a proof that crystals with chain folds occurred in a bulk polymer by either homogeneous or heterogeneous initiation would not invalidate the general approach here for the formation of loop-type nuclei and crystals from dilute solution.

With regard to the effect of heterogeneities in dilute solution, it is clear that they will accelerate the crystallization process. However, by careful filtration, centrifugation, or previous precipitation, it should be possible to eliminate the effect of foreign bodies to a degree sufficient to permit the intrinsic mechanism to manifest itself. Judging from the remarks of Keller and O'Connor [1] concerning their technique and results, it would appear that many of the crystals that they discussed were formed in the body of the solution, and not on motes in the solution, or on the container walls. There is also reason to believe that some of the other work cited, notably the rate studies of Mandelkern [17, 18], may refer to homogeneous initiation. Nevertheless, it is mandatory to exercise considerable care in carrying out rate experiments in dilute solution in such a way as to subdue the effect of foreign bodies.

4.3. Concluding Remarks

In this paper, a point of view is expressed that leads to a number of definite predictions concerning the formation of polymer crystals with loops from dilute solution. Perhaps the most important and compelling prediction is that crystals of this type will be deposited from sufficiently dilute solution if it is physically possible to form a fold that is consistent with lattice structure and steric considerations. Definite predictions are also given, under certain assumptions, concerning the variation of step height with crystallization temperature, metastability and melting point, the n law connected with the appearance of loop-type crystals from dilute solution, the temperature dependence of the kinetics of crystallization, and the constancy of step height in a crystal grown in an isothermal manner. In addition, rough numerical estimates of important fundamental quantities, such as σ_e, are given.

Insofar as it can be tested, the theory seems to be in at least approximate accord with the facts presently known. It is believed that the theory is sufficiently to the point as to provide a reasonable framework for future experimental studies even if it proves not to be quantitatively correct. Moreover, specific experimental approaches, together with their attendant (and sometimes formidable) difficulties are mentioned. No claim is made that the theory is complete. For example, it is obvious that the interesting details of the structure of the fold itself have been largely passed over, and some of the possibilities concerning the growth mechanism which could, for instance, lead to a ramp-type of growth due to spiral dislocations have not been mentioned.

5. Appendix

5.1. Equilibrium Nucleation Rates of Crystals With Chain Folds

We wish to calculate the equilibrium nucleation rate per unit volume of crystals formed by chain folding. The method of derivation, which is merely outlined below, is that used by Turnbull and Fisher [8]. The reader is referred to that paper for details.

A nucleus of ν step elements of length, $\mathbf{l}$, can gain or lose a step element by an elementary process. This nucleus may be specified by $\mathbf{l}$ and ν where ν may possess the values

$$\nu_m, \nu_m+1, \nu_m+2, \ldots .$$

ν_m is the minimum number of step elements in a nucleus. The number of nuclei per unit volume with ν segments and a length between $\mathbf{l}$ and $\mathbf{l}+\mathbf{dl}$ is $\eta(\nu,\mathbf{l})d\mathbf{l}$. The free energy of a primary embryo or nucleus is

$$\Delta\phi_p(\nu) = (\mathcal{O}\sigma_s\mathbf{l}\sqrt{\mathbf{a}})\sqrt{\nu} - [\mathbf{l}\Delta\mathbf{f} - 2\sigma_e]\mathbf{a}\nu. \qquad \text{(A-1)}$$

This function has a maximum value at

$$\nu^* = \frac{(\mathcal{O}\sigma_s\mathbf{l})^2}{4\mathbf{a}(\mathbf{l}\Delta\mathbf{f}-2\sigma_e)^2}. \qquad \text{(A-2)}$$

The value of $\Delta\phi_p$ when expanded about ν^* is

$$\Delta\phi_p = \Delta\phi_p^* - \frac{\mathbf{a}^2(\mathbf{l}\Delta\mathbf{f}-2\sigma_e)^3(\nu-\nu^*)^2}{(\mathcal{O}\sigma_s\mathbf{l})^2} + \ldots \qquad \text{(A-3)}$$

where

$$\Delta\phi_p^* = \frac{(\mathcal{O}\sigma_s\mathbf{l})^2}{4(\mathbf{l}\Delta\mathbf{f}-2\sigma_e)}. \qquad \text{(A-4)}$$

A nucleus of length $\mathbf{l}$ can only become stable by addition of step elements. $\mathbf{l}$ cannot vary without dissolution of the minimum size nucleus. The free energy diagram for nuclei of ν and $\nu+1$ step elements with some fixed length $\mathbf{l}$ is shown in figure 11. The rate that nuclei with ν step elements become nuclei with $\nu+1$ step elements is

$$\eta(\nu,\mathbf{l})d\mathbf{l}\left(\frac{kT}{h}\right)\exp\left\{-\frac{W_1}{kT}\right\},$$

whereas the rate of the backward reaction is

$$\eta(\nu+1,\mathbf{l})d\mathbf{l}\left(\frac{kT}{h}\right)\exp\left\{-\frac{W_2}{kT}\right\}.$$

Then the net rate of nucleation $i(\mathbf{l})d\mathbf{l}$ is

$$i(\mathbf{l})d\mathbf{l} = \left(\frac{kT}{h}\right)\left[\eta(\nu,\mathbf{l})d\mathbf{l}\exp\left\{-\frac{W_1}{kT}\right\} - \eta(\nu+1,\mathbf{l})d\mathbf{l}\exp\left\{-\frac{W_2}{kT}\right\}\right]. \qquad \text{(A-5)}$$

Now

$$W_1 = \Delta\mathbf{F}_p^* + \tfrac{1}{2}[\Delta\phi_p(\nu+1,\mathbf{l}) - \Delta\phi_p(\nu,\mathbf{l})]$$
$$W_2 = \Delta\mathbf{F}_p^* - \tfrac{1}{2}[\Delta\phi_p(\nu+1,\mathbf{l}) - \Delta\phi_p(\nu,\mathbf{l})], \qquad \text{(A-6)}$$

where $\Delta\mathbf{F}_p^*$ is the free energy barrier associated with addition or subtraction of a segment from the nuclei. The value of $\Delta\mathbf{F}_p^*$ will be independent of ν and probably independent of $\mathbf{l}$.

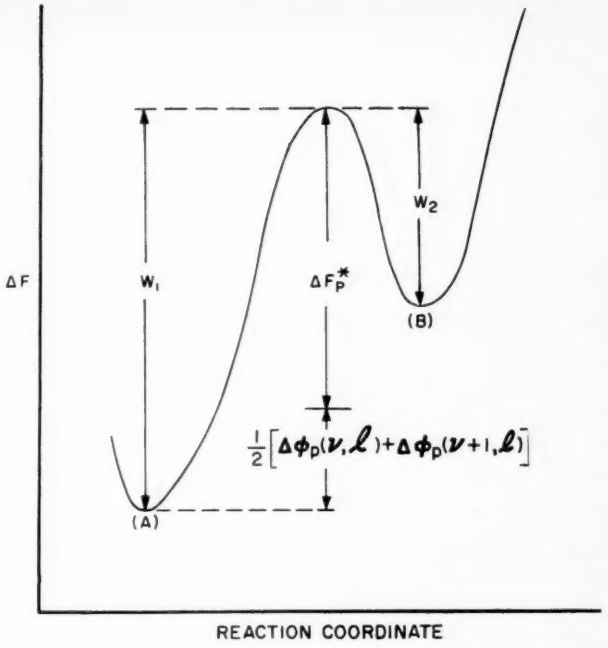

FIGURE 11. *Cross section of free energy surface for the most probable reaction path between embryos of ν step elements o length $\mathbf{l}$ and embryos of $(\nu+1)$ step elements of length $\mathbf{l}$.*

The energy minima at (*A*) and (*B*) represent the free energy difference from the liquid state of the two different embryos, respectively.

Now if ν is a large number we are justified in treating ν as a continuous variable. With this approximation eqs (A–5) and (A–6) become

$$i(\mathbf{l})d\mathbf{l}=-\frac{kTd\mathbf{l}}{h}\left\{\frac{\partial\eta}{\partial\nu}+\frac{\eta}{kT}\frac{\partial(\Delta\phi_p)}{\partial\nu}\right\}e^{-\Delta\mathbf{F}_p^*/kT} \tag{A–7}$$

where higher derivatives with respect to ν have been neglected. This equation is easily integrated from $\nu=s$ to $\nu=\infty$. Using the boundary condition $\eta(\infty,\mathbf{l})=0$ for the equilibrium case we have

$$i(\mathbf{l})=\frac{kT}{h}\frac{[\eta_s e^{\Delta\phi_p(s)/kT}]}{\int_s^\infty d\nu e^{\Delta\phi_p(\nu)/kT}}e^{-\Delta\mathbf{F}_p/kT}. \tag{A–8}$$

The right hand side of eq (A–8) may be evaluated if s is chosen so $\nu_{\nu_0}<<s<<\nu^*$. We find then by use of eq (A–3) that

$$\int_s^\infty d\nu\, e^{\Delta\phi_p(\nu)/kT}\cong\left[\frac{\mathbf{a}^2(\mathbf{l}\Delta\mathbf{f}-2\sigma_e)^3}{\pi(C\sigma_s\mathbf{l})^2kT}\right]^{-1/2}e^{\Delta\phi_p^\ddagger/kT} \tag{A–9}$$

which is a good approximation when $\Delta\phi_p^\ddagger/kT>>1$.

We may evaluate $\eta(s,\mathbf{l})$ if s is sufficiently small that a Maxwellian distribution holds. Then

$$\eta(s,\mathbf{l})d\mathbf{l}=A d\mathbf{l}\, e^{-\Delta\phi_p(s)/kT}. \tag{A–10}$$

If s is sufficiently small we may assume that only the surface energy terms are important. Then

$$\Delta\phi_p\cong\Delta\phi_p'=(C\sigma_s\mathbf{l}\sqrt{\mathbf{a}})\sqrt{\nu}+2\sigma_e\mathbf{a}\nu. \tag{A–11}$$

Since the sum over all states $s,\mathbf{l}$ must equal the number of polymer molecules per unit volume we may evaluate A. Treating s and $\mathbf{l}$ as continuous variables running from zero to infinity

$$A=\mathbf{n}_0\left\{\int_0^\infty d\nu\int_0^\infty d\mathbf{l}\, e^{-\Delta\phi_p'/kT}\right\}^{-1}. \tag{A–12}$$

Substitution of eq (A–11) into (A–12) gives us

$$\eta(s,\mathbf{l})\, e^{\Delta\phi_p(s)/kT}=\left[\frac{C\sigma_s\mathbf{a}\sqrt{2\sigma_e}}{\sqrt{\pi}(kT)^{3/2}}\right]\mathbf{n}_0. \tag{A–13}$$

Then substituting (A–13) and (A–9) into (A–8) we have the desired expression

$$i(\mathbf{l})=\left[\frac{\mathbf{a}^2\sqrt{2\sigma_e}(\mathbf{l}\Delta\mathbf{f}-2\sigma_e)^{3/2}}{\pi(kT)^2\mathbf{l}}\right]\frac{\mathbf{n}_0kT}{h}e^{-\Delta\mathbf{F}_p^*/kT}e^{-\Delta\phi_p^\ddagger/kT}. \tag{A–14}$$

We may calculate the total nucleation rate by integrating eq (A–14) over all $\mathbf{l}$. The number of stable nuclei formed per unit volume of solution per unit time is

$$I=K\frac{\mathbf{n}_0kT}{h}e^{-\Delta\mathbf{F}_p^*/kT}e^{-\Delta\phi_p^*/kT} \tag{A–15}$$

where

$$\Delta\phi_p^*=\frac{2\sigma^2\sigma_s^2\sigma_e}{(\Delta\mathbf{f})^2} \tag{A–16}$$

$$K=\frac{(2\sigma_e)^{3/2}(\Delta\mathbf{f})\mathbf{a}^2}{\sqrt{\pi}C\sigma_s(kT)^{3/2}}. \tag{A–17}$$

Throughout this appendix it has been assumed that each nucleus is composed of step elements of uniform length. This assumption has simplified the derivation of eq (A–15) and has led to an explicit expression for the distribution of the lengths of the step elements in stable nuclei in eq (A–14). It is, of course, possible that an embryo or nucleus could be composed of step elements of different lengths. The remainder of this appendix is devoted to discussing this more general case. This discussion will support the validity of the above results.

In the general case an embryo or nucleus will have ν step elements which have lengths: $\mathbf{l}_1$, $\mathbf{l}_2$, . . . $\mathbf{l}_\nu$. The principal difficulty in treating this case is in obtaining and handling appropriate expressions for the free energy of such nuclei. Fortunately for the purposes of this paper the problem is considerably simplified. When the edge energy, ϵ, needed to form a monomolecular layer is large, the free energy gained by packing the loops in a flat surface is appreciable. Hence embryos or nuclei with different step heights $\mathbf{l}_1$, $\mathbf{l}_2$, . . . $\mathbf{l}_\nu$, are energetically improbable compared to nuclei whose step elements have the same step height. Then in this case it is clearly justified to treat nuclei which may be characterized by a single step height. But it is only when ϵ is a large quantity that the distribution of step heights in primary critical nuclei need to be considered, for it is only then that the step height of the crystal will be determined by the step height of the critical primary nucleus, so that the distribution in step heights of the primary nuclei control the distribution in step heights of the crystals. If ϵ is a smaller quantity the distribution of the step heights of the crystals will be independent of that of the primary nuclei, and only the total nucleation rate is of interest. The total nucleation rate is given by eq (A–15) in any case.

5.2. Equilibrium Rate of Formation of Monomolecular Nuclei on a Crystal Face

We wish to calculate the equilibrium nucleation rate of monomolecular nuclei on a crystal face. This problem is similar to the one treated in the previous appendix, except that the free energy surface is different. In particular, the activated nucleus is reached in a single elementary process from the supercooled liquid. It will be assumed that the

nucleus can contain ν step elements where ν can possess the values

$$0, 1, 2, \ldots \tag{B-1}$$

The free energy required to form a nucleus of ν step elements is

$$\begin{aligned} \Delta\phi'_0 &= 0, & \nu &= 0 \\ \Delta\phi'_\nu &= \Delta\phi'^{\ddagger} - (\nu-1)E, & \nu &= 1, 2, \ldots \end{aligned} \tag{B-2}$$

Then the activated state is at $\nu=1$, where $\Delta\phi'_1=\Delta\phi'^{\ddagger}$. The same method of derivation will be used as in appendix 5.1. Then the rate at which nuclei with ν step elements become nuclei with $(\nu+1)$ step elements is

$$\eta_\nu\left(\frac{kT}{h}\right)e^{-\Delta F^*/kT}\exp\left[-\frac{(\Delta\phi'_{\nu+1}-\Delta\phi'_\nu)}{2kT}\right], \tag{B-3}$$

whereas the rate of the backward reaction is

$$\eta_{\nu+1}\left(\frac{kT}{h}\right)e^{-\Delta F^*/kT}\exp\left[+\frac{(\Delta\phi'_{\nu+1}-\Delta\phi'_\nu)}{2kT}\right]. \tag{B-4}$$

Here η_ν is the number of nuclei per unit volume with ν step elements. The net rate of nucleation per unit volume, $\mathbf{r}$, is

$$\mathbf{r}=\left(\frac{kT}{h}\right)e^{-\Delta F^*/kT}\left\{\eta_\nu\exp\left[\frac{-(\Delta\phi'_{\nu+1}-\Delta\phi'_\nu)}{2kT}\right] - \eta_{\nu+1}\exp\left[\frac{(\Delta\phi'_{\nu+1}-\Delta\phi'_\nu)}{2kT}\right]\right\}. \tag{B-5}$$

If the rate is an equilibrium rate, $\mathbf{r}$ does not depend on ν. Combining (B–2) with (B–5)

$$\mathbf{r}=\frac{kT}{h}e^{-\Delta F^*/kT}\{\eta_\nu e^{E/2kT}-\eta_{\nu+1}e^{-E/2kT}\} \qquad \nu=1, 2, \ldots \tag{B-6}$$

and

$$\mathbf{r}=\left(\frac{kT}{h}\right)e^{-\Delta F^*/kT}\{\eta_0 e^{-\Delta\phi'^{\ddagger}/2kT}-\eta_1 e^{\Delta\phi'^{\ddagger}/2kT}\}. \tag{B-7}$$

From eq (B–6)

$$\eta_\nu=\eta_1 e^{+\nu E/kT}-\mathbf{r}\left(\frac{h}{kT}\right)e^{\Delta F^*/kT}\left\{\frac{[e^{\nu E/kT}-1]}{2\sinh E/2kT}\right\}. \tag{B-8}$$

Since we are concerned with the equilibrium rate, η_ν must be bounded as $\nu\to\infty$. In order that this is satisfied

$$\mathbf{r}=2\eta_1\left(\frac{kT}{h}\right)e^{-\Delta F^*/kT}\sinh\left(\frac{E}{2kT}\right). \tag{B-9}$$

Combining eq (B–7) and (B–9) we may solve for $\mathbf{r}$:

$$\mathbf{r}=\eta_0\left(\frac{kT}{h}\right)e^{-\Delta F^*/kT}\,e^{-\Delta\phi'^{\ddagger}/kT}\left\{\frac{2\sinh(E/2kT)}{1+2e^{-\Delta\phi'^{\ddagger}/2kT}\sinh(E/2kT)}\right\} \tag{B-10}$$

This then is the desired equilibrium rate of formation of these nuclei.

Three points in this derivation are worthy of comment. First the derivation in this appendix differs from that in appendix 5.1 in that the activated state is attained by a single elementary process. Then the expression obtained in eq (B–10) must be applied with due caution since more detailed knowledge of the nucleation process is assumed than in the previous appendix. The second point is that by solving for η_ν from eqs (B–8), (B–9), and (B–10) it is found that

$$\eta_\nu=\frac{\eta_0 e^{-\Delta\phi'^{\ddagger}/kT}}{1+2\exp\{-\Delta\phi'^{\ddagger}/2kT\}\sinh(E/2kT)}. \tag{B-11}$$

Thus η_ν is independent of ν, and does not vanish as ν becomes infinitely large. This raises the question of whether a very large time is required before the equilibrium rate is achieved so that the transient rate cannot be neglected. This question can be answered by a solution of the time dependent problem. It can be shown for the case treated here that the equilibrium rate is closely approached after the number of nuclei with a few step elements have nearly reached the value found in eq (B–11). Thus the equilibrium rate derived in eq (B–10) is applicable to the case at hand. Thirdly in both appendixes 5.1. and 5.2. it has been assumed tacitly that nuclei can be initiated at only one point in the polymer chain. If this assumption is taken into account in an appropriate manner, a numerical factor will be introduced into the nucleation rates obtained. This factor will almost certainly be less than 10^4.

Equation (B–10) is first used in section 3.2. to describe the formation of a primary crystallite through monomolecular accretion from a critical-sized loop-type nucleus. It is later used to describe the growth of a crystallite in section 3.3., i.e., $\Delta\phi'^{\ddagger}\to\Delta\phi^{\ddagger}_v$. Since in sections 3.2. and 3.3. the quantity $\mathbf{r}d\mathbf{l}$ is taken as the rate of formation of nuclei with step heights between $\mathbf{l}$ and $\mathbf{l}+d\mathbf{l}$, the quantity η_0 will contain a normalization constant C, which arises because the rates of more than one competing process are considered.

The authors are deeply indebted to Dr. C. H. Klute of the Diamond Ordnance Fuze Laboratories and Drs. F. P. Price and D. Turnbull of the General Electric Research Laboratory for their careful and penetrating review of the manuscript. Thanks are also due Dr. A. M. Bueche of the General Electric Research Laboratory for originally stimulating our interest in this problem, as well as for his criticism of the manuscript. Also, the authors wish to especially

express their gratitude for the receipt of extremely helpful criticism and comment from Prof. F. C. Frank of the University of Bristol, England, and Drs. E. Passaglia and D. Keith of the American Viscose Co. Finally, we wish to thank Dr. A. Keller of the University of Bristol for information he kindly passed on to us prior to publication, and for his most helpful comments on the original manuscript.

6. References

[1] A. Keller and A. O'Connor, Discussions, Faraday Soc. **25,** 114 (1958).
[2] A. Keller, Phil. Mag. **2,** 1171 (1957).
[3] P. H. Till, Jr., J. Polymer Sci. **24,** 301 (1957).
[4] E. W. Fischer Z. Naturforsch., **12a,** 753 (1957).
[5] K. H. Storks, J. Am. Chem. Soc. **60,** 1753 (1938).
[6] J. D. Hoffman, J. J. Weeks, and W. M. Murphey, J. Research NBS **63A,** 67 (1959).
[7] L. Mandelkern, Chem. Rev. **56,** 903 (1956).
[8] D. Turnbull and J. C. Fisher, J. Chem. Phys. **17,** 71 (1949).
[9] L. Mandelkern, F. A. Quinn, Jr., and P. J. Flory, J. Appl. Phys. **25,** 830 (1954).
[10] J. D. Hoffman, J. Chem. Phys. **29,** 1192 (1958).
[11] J. I. Lauritzen, Jr. (to be published).
[12] C. W. Bunn, Trans. Faraday Soc. **35,** 482 (1939).
[13] L. Mandelkern, J. Appl. Phys. **26,** 443 (1955).
[14] F. A. Quinn, Jr., and L. Mandelkern, J. Am. Chem. Soc. **80,** 3178 (1958).
[15] P. J. Flory, Principles of polymer chemistry, p. 569 (Cornell Univ. Press, Ithaca, N.Y., 1958).
[16] D. G. Thomas and L. A. K. Staveley, J. Chem. Soc. 4569 (1952).
[17] L. Mandelkern and F. A. Quinn, Jr. (paper presented before 134th meeting of the Am. Chem. Soc., Chicago, Ill., Sept. 7–12, 1958).
[18] L. Mandelkern, SPE Journal **15** (1959).
[19] F. P. Price, J. Polymer, Sci. (to be published).

Washington, D.C. (Paper 64A1–30)

JOURNAL OF RESEARCH of the National Bureau of Standards—A. Physics and Chemistry
Vol. 64A, No. 1, January–February 1960

Studies of Beryllium Chromite and Other Beryllia Compounds With R_2O_3 Oxides

C. E. Weir and A. Van Valkenburg

(August 10, 1959)

Reactions between BeO and R_2O_3 oxides at high temperatures were studied. Compound formation was observed between BeO and the following oxides: B_2O_3, Al_2O_3, Ga_2O_3, Y_2O_3, La_2O_3, and Cr_2O_3. No reaction was observed with Sc_2O_3, In_2O_3, and Fe_2O_3. Detailed studies were made of $BeO{\cdot}Cr_2O_3$ which is isostructural with $BeO{\cdot}Al_2O_3$. $BeO{\cdot}Cr_2O_3$ is a semiconductor. Optical and X-ray data are given for all reaction products.

1. Introduction

In hydrothermal experiments involving the system $BeO+Al_2O_3+SiO_2$ with small amounts of added Cr_2O_3 at 850° C, it was found that X-ray patterns of reaction products persistently showed evidence for an unidentified material. It was found that this material was a compound between BeO and Cr_2O_3. The compound has been reported earlier to be $BeO{\cdot}Cr_2O_3$ by Lang, Roth, and Fillmore [1][1] who studied the system $BeO\text{-}Cr_2O_3\text{-}ZrO_2$. They found that it was orthorhombic, isostructural with $BeO{\cdot}Al_2O_3$, with unit call parameters a=10.0 A, b=5.8 A, and c=4.5 A. The present report describes the preparation and some of the properties of $BeO{\cdot}Cr_2O_3$ as well as preliminary studies on the reactions between BeO and the R_2O_3 oxides in group III of the periodic system.

2. Experimental Materials and Methods

All reagents used were oxides of reagent grade except Ga_2O_3, In_2O_3, and Y_2O_3. The former two were made by solution of chemically pure metal in nitric acid followed by thermal decomposition of the nitrate. The available specimen of Y_2O_3 was of commercial origin with a purity of 99.7 percent.

Hydrothermal reactions were carried out in the well-known cold-seal apparatus [2], using platinum containers. Solid state reactions were made through repeated heating and grinding of oxides. Materials were heated to temperatures as high as 1,550° C in platinum, while BeO containers were used between 1,550° C and 2,100° C. Temperatures to 1,550° C were obtained with platinum wire furnaces and higher temperatures with a carbon resistance furnace using a He atmosphere. Early results indicated the desirability of a rapid screening process. This was accomplished by using a small d-c carbon arc as a furnace. Component oxides were mixed and treated with a sufficient quantity of 10 percent aqueous starch solution to form a paste. The paste was extruded from glass tubing to form small rods ⅛ in. in diameter, which were dried and melted in the arc using the tubing as a handle. All oxides studied were melted rapidly in the arc and a single small fused bead was sufficient to permit X-ray and microscopic analysis. The possible reduction and volatilization of the oxides precludes knowledge of the purity or composition of the arc-fused product, but rapid search for reactions is quite simple with this method.

[1] Figures in brackets indicate the literature references at the end of this paper.

3. Results

3.1. $BeO{\cdot}Cr_2O_3$

This material formed hydrothermally at temperatures as low as 800° C in the presence of water. In this temperature range, however, the reaction rate is very low and crystals are very small.

In the solid state, slow reaction was observed at temperatures as low as 1,400° C. Microscopic comparisons of the surface with the body of specimens showed that prolonged heating of oxide mixtures at 1,450° C produces some surface loss of Cr_2O_3. The loss accelerates as the temperature is raised so that only BeO crystals remain on the surface after 4 hr at 1,750° C. Below about 1,600° C the rate of loss is believed to be sufficiently low that the bulk composition is essentially unaffected in normal heating periods. That the Cr_2O_3 vapor was at least partially due to vapor pressure of the compound was shown by the fact that $BeO{\cdot}Cr_2O_3$ sintered in BeO at 1,750° C also showed much surface loss of Cr_2O_3. The competitive processes of reaction of the oxides and vaporization of Cr_2O_3 from the oxide mixture and the compound indicate that there is an optimum temperature for formation of $BeO{\cdot}Cr_2O_3$. These experiments indicate that this temperature is probably between 1,300° C and 1,600° C. As a result of vaporization of Cr_2O_3 large single crystals would not be expected in open systems; however, crystals as large as 0.05 mm are readily formed under these conditions. The compound forms readily in the arc crystallizing from the liquid phase. Experiments in the arc also showed that the compound $BeO{\cdot}Cr_2O_3$ was a semiconductor as conductivity of specimens became so high at elevated temperatures that resistance heating could be effected.

Microscopic examination showed that $BeO{\cdot}Cr_2O_3$ forms well-terminated, transparent, deep green crystals having a reddish pleochroism. The crystals are biaxial negative with $2V\approx45°$ and indices, α=2.143, β not measured, γ=2.230. Pseudohexagonal, highly

TABLE 1. *X-ray powder pattern for* $BeO \cdot Cr_2O_3$

Cu K_α, $\lambda = 1.5405$

$BeO \cdot Cr_2O_3$[1]		
$d_{obs.}$	hkl	$d_{calc.}$
A		A
4.135	101	4.131
3.337	111	3.337
2.653	301	2.654
2.452	220	2.451
2.402	311	2.403
2.335	121	2.335
2.157	401	2.157
1.936	321	1.936
1.715	{421	1.715
	{511	1.716
1.668	222	1.669
1.539	331	1.538
1.519	003	1.519
1.4159	040	1.4155
1.4140	620	1.4141
1.3765	303	1.3771

[1] Unit cell parameters $a = 9.792$ A, $b = 5.663$ A, $c = 4.555$ A; calculated density 4.654 g/cm³ at 25° C.

twinned crystals similar to those of $BeO \cdot Al_2O_3$ are obtained on reaction via the liquid phase.

Polycrystalline material appears black and opaque. It has a hardness on the Moh's scale of about 9 by the scratch test. The melting point was not measured but it was found that a eutectic between BeO and $BeO \cdot Cr_2O_3$ melts below approximately 2,050° C. The measured specific gravity is 4.42 and the principal X-ray powder lines are given in table 1 with the indices and unit cell parameters. X-ray studies conducted on mixtures rich in BeO or Cr_2O_3 showed no appreciable solid solution of the parent oxides in $BeO \cdot Cr_2O_3$.

X-ray powder patterns show $BeO \cdot Al_2O_3$ and $BeO \cdot Cr_2O_3$ are isostructural. Several solid solutions were prepared from the component oxides and the variation of the unit cell parameters with composition is shown in figure 1. Although some curvature is possible in the variation of "a" with composition, the deviations from linearity are probably within the experimental error of determining the cell parameters. In addition the compositions denoted by the points are determined from the known quantities of oxides added and may be subject to some error arising from loss of Cr_2O_3 on firing. This error is believed to be small. From these data it appears that a complete series of solid solutions exists between $BeO \cdot Al_2O_3$ and $BeO \cdot Cr_2O_3$. This conclusion differs from that of Gjessing, Larrson, and Major [3] who found only partial substitution of Cr_2O_3 for Al_2O_3 in the $BeO \cdot Al_2O_3$ structure.

In view of the electrical conductivity of $BeO \cdot Cr_2O_3$ at elevated temperatures, it was of interest to determine the temperature-resistance characteristics. These measurements were made on polycrystalline sintered bars using platinum electrodes. Specimens were measure in a temperature-controlled furnace using a commercial megohm bridge which applied 500 v across the specimen. Since single crystals were not used, and the bars possessed pores, the resistivities could not be determined, the resulting data

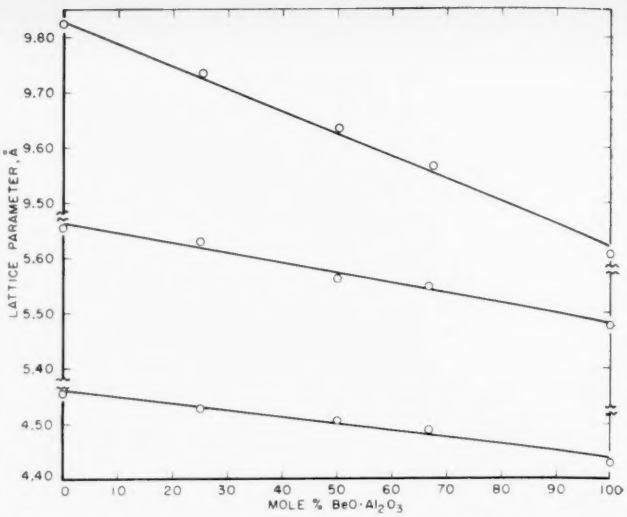

FIGURE 1. *Variation of unit cell parameters in the solid solution series* $BeO \cdot Al_2O_3$-$BeO \cdot Cr_2O_3$.

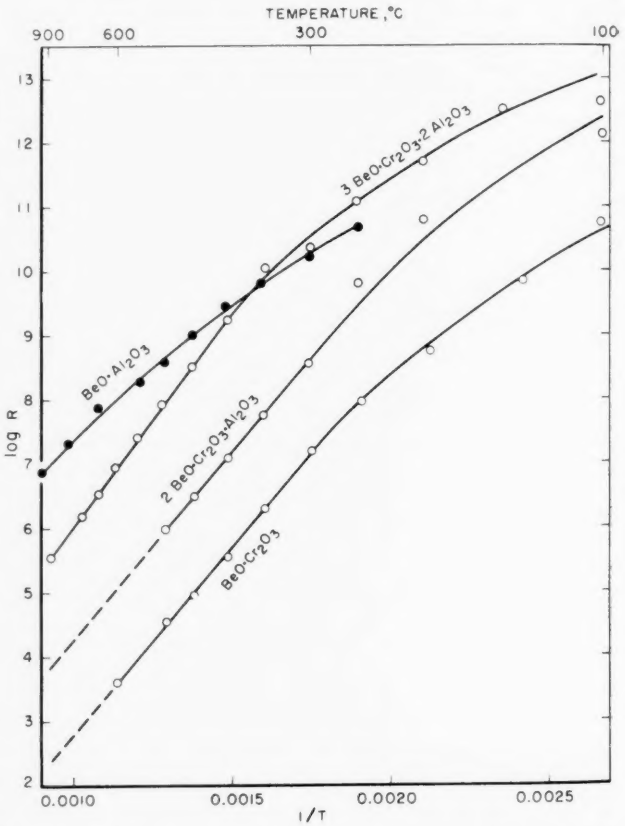

FIGURE 2. *Temperature variation of resistance of* $BeO \cdot Al_2O_3$, $BeO \cdot Cr_2O_3$ *and solid solutions.*

being valid only for showing the temperature dependence of resistance. The resistance was measured at temperature intervals of approximately 100° C and the data are shown for $BeO \cdot Cr_2O_3$ as well as $BeO \cdot Al_2O_3$ and two solid solutions in figure 2. The data are plotted in the usual manner using $1/T$ and log R. From the figure it will be observed that data for

specimens containing Cr_2O_3 are not inconsistent with the interpretation that they are intrinsic semiconductors, above about 300° C. If this interpretation is correct the average energy gap is calculated to be 2.4 ev and appears to be independent of the Al_2O_3/Cr_2O_3 ratio.

The magnetic characteristics of $BeO \cdot Cr_2O_3$ are being studied by W. E. Henry of the Naval Research Laboratory. Preliminary results show the material to be antiferromagnetic.

3.2. $BeO \cdot R_2O_3$ Reactions

a. $BeO \cdot B_2O_3$

A crystalline product is formed by heating BeO and crystalline B_2O_3 at 800° C. The principal X-ray lines for the material are given in table 2. Crystals are biaxial with $2V \approx 90°$ and indices $\alpha = 1.62$, β not measured, $\gamma = 1.574$. The material is not isostructural with $BeO \cdot Al_2O_3$. From the X-ray pattern the product can be identified with the compound $3BeO \cdot B_2O_3$ reported by Menzel and Sliwinski [4] and by Mazelev [5].

TABLE 2. *X-ray powder patterns for* $BeO \cdot R_2O_3$ *compounds*

Cu Kα, $\lambda = 1.5405$

$3BeO \cdot B_2O_3$		$BeO \cdot 2Ga_2O_3$				$nBeO \cdot Y_2O_3$		$nBeO \cdot La_2O_3$	
d, A	*I*	*d*, A	*hkl*[1]	*I*	$d_{calc.}$	*d*, A	*I*	*d*, A	*I*
7.302	vw	6.717	100	m	6.716	7.190	w	3.768	vs
6.067	w	3.875	110	m	3.877	5.196	w	3.718	m
5.921	w	3.379	200	s	3.358	4.607	vw	3.673	m
3.967	m	2.728	101	s	2.723	4.469	s	3.296	m
3.872	vs	2.539	210	vs	2.538	3.146	m	3.063	m
3.826	m	2.230	202	s	2.228	2.922	vs	3.008	s
3.635	m	1.938	220	w	1.939	2.838	m	2.681	m
3.188	s	1.934	211	w	1.932	2.786	m	2.628	m
2.901	s	1.863	310	w	1.863	2.765	w	2.620	m
2.863	w	1.791	301	m	1.790	2.600	w	2.612	s
2.718	w	1.636	221	w	1.625	2.479	w	2.494	m
2.480	m	1.579	311	w	1.579	2.412	w	2.465	w
2.446	w	1.541	320	w	1.541	2.213	w	2.224	w
2.365	w	1.489	002	w	1.495	2.193	w	2.167	m
2.204	w	1.465	410	w	1.466	2.060	w	2.127	m
2.168	w	1.369	321	m	1.369	1.979	m	2.055	w
2.061	w	1.316	411	w	1.316	1.975	w	2.030	w
1.932	w	1.286	212	w	1.286	1.945	w	1.980	m
1.901	w	1.269	420	vw	1.269	1.888	w	1.965	w
1.751	w	1.207	510	vw	1.206	1.767	m	1.883	m
1.737	w	1.183	222	vw	1.182	1.705	w	1.838	w
1.656	w	1.169	421	vw	1.168	1.682	w	1.820	w
1.430	w					1.631	w	1.785	m
1.275	w					1.460	w	1.763	m
						1.455	w	1.740	w
						1.289	w	1.700	w
								1.698	w
								1.678	w
								1.652	w
								1.647	w
								1.638	w
								1.627	w
								1.610	w
								1.608	w
								1.542	w
								1.515	w
								1.483	w
								1.446	m
								1.209	w
								1.201	m

[1] Indexed on the basis of a hexagonal unit cell with parameters $a = 7.78$ A and $c = 2.98$ A.

b. $BeO \cdot Al_2O_3$

In addition to $BeO \cdot Al_2O_3$, the product $BeO \cdot 3Al_2O_3$ is readily formed by arc fusion of the 1:3 oxide mixture. This material is identified with the X-ray powder pattern given originally by Foster and Royal [6] and extended by Budnikov et al. [7].

c. $BeO \cdot Sc_2O_3$

Mixtures of BeO and Sc_2O_3 can be fused with difficulty in the arc. However, despite numerous attempts no evidence for reaction was observed. X-ray powder patterns of fused beads showed only BeO and Sc_2O_3 lines.

d. $BeO \cdot Ga_2O_3$

Arc fusion studies showed reaction between BeO and Ga_2O_3, but X-ray patterns showed the product was not isostructural with $BeO \cdot Al_2O_3$. Gjessing, Larrson, and Major [3] have previously reported a compound, $BeO \cdot 2Ga_2O_3$, which is not isostructural with $BeO \cdot Al_2O_3$. Solid state reactions indicated that the material was readily formed at 1,350° from a mixture of oxides. Although complete reaction was not obtained in short periods at this temperature as shown by X-ray lines of unreacted BeO or Ga_2O_3 the product is believed to be identical with the $BeO \cdot 2Ga_2O_3$ reported earlier [3]. Microscopic examination showed the material to be uniaxial positive with indices 1.747 and 1.774. The X-ray powder pattern lines given in table 2 were obtained by deleting the known lines of BeO from the pattern. This pattern has been indexed in the hexagonal system with $a = 7.78$ A and $c = 2.98$ A, with the indices given in table 2.

e. $BeO \cdot Y_2O_3$

Arc fusion studies showed reaction between BeO and Y_2O_3. All attempts to produce a similar material by solid state reactions at temperatures as high as 1,600° C were unsuccessful. Therefore the composition as well as the purity of the material are not known. Microscopic examination showed biaxial crystals with $2V \approx 90°$ and indices, $\alpha = 1.84$, β not measured, $\gamma = 1.85$. The X-ray powder pattern lines are listed in table 2 but it should be noted that extraneous lines from impurities introduced by the arc may be present. This material is obviously not isostructural with $BeO \cdot Al_2O_3$ and does not appear to have been reported previously.

f. $BeO \cdot In_2O_3$

Repeated efforts at high and low temperatures, in open and closed systems, both with and without water present failed to give any evidence for reaction. Ensslin and Valentiner [8] reported $BeO \cdot In_2O_3$ as having the same lattice constant as In_2O_3. Gjessing, Larrson, and Major [3] found no reaction. On the basis of the present work it is concluded that reaction between the oxides does not occur to 1,600° C.

g. $BeO \cdot La_2O_3$

These oxides react readily in the arc. Solid state reactions may be carried out at 1,300° C and indicate that the product is probably $2BeO \cdot La_2O_3$. Microscopic examination shows biaxial crystals with $2V \approx 90°$ having indices, $\alpha = 1.995$, β not measured, $\gamma = 2.047$. X-ray powder pattern lines are given in table 2.

h. $BeO\cdot Cr_2O_3$

In addition to the compound $BeO\cdot Cr_2O_3$ the question of a 1:3 compound analogous to $BeO\cdot 3Al_2O_3$ was investigated. Evidence was found that only the 1:1 compound was formed, X-ray patterns showing lines for $BeO\cdot Cr_2O_3$ and Cr_2O_3 only.

i. $BeO\cdot Fe_2O_3$

Several experiments were performed to prepare the $Beo\cdot Fe_2O_3$ analog of $BeO\cdot Al_2O_3$ starting from the oxides. None were successful. In most instances Fe_3O_4 was formed. The question of the existence of $BeO\cdot Fe_2O_3$ from previous work is not clear [9, 3]. However, from the present experiments it appears that such a compound does not form from the oxides at temperatures up to the liquidus.

4. Summary

High temperature reactions of BeO with the R_2O_3 oxides have been studied.The compound $BeO\cdot Cr_2O_3$ has been studied in some detail. It is isostructural with $BeO\cdot Al_2O_3$ and a continuous series of solid solutions forms between these compounds. The unit cell parameters in the solid solutions show nearly ideal behavior. $BeO\cdot Cr_2O_3$ is a semiconductor.

Compound formation was verified between BeO and the following oxides: B_2O_3, Ga_2O_3, Y_2O_3, and La_2O_3. Powder X-ray diffraction patterns are given for all compounds and that for $BeO\cdot 2Ga_2O_3$ is indexed in the hexagonal system. No reaction was observed between BeO and Sc_2O_3, In_2O_3, and Fe_2O_3.

The authors thank Mrs. Eloise Evans for indexing the $BeO\cdot Cr_2O_3$ X-ray pattern.

5. References

[1] S. M. Lang, R. S. Roth, and C. L. Fillmore, J. Research NBS **53,** 201 (1954) RP2534.
[2] J. Van den Huerk, Bull. Geol. Soc. Am. **54,** 993 (1953).
[3] L. Gjessing, T. Larrson, and H. Major, Norsk Geol. Tidsskr. **22,** 92 (1942).
[4] H. Menzel and S. Sliwinski, Z. anorg. u. allgem. Chem. **249,** 357 (1942).
[5] L. Y. Mazelev, Izvest. Akad. Nauk Belorus S.S.R. **4,** 105 (1953).
[6] W. R. Foster and H. F. Royal, J. Am. Ceram. Soc. **32,** 26 (1949).
[7] P. P. Budnikov, V. G. Avetikov, E. I. Dudavskii, and A. A. Zvyagilskii, Doklady Akad. Nauk S.S.S.R. **68,** 313 (1949).
[8] F. Ensslin and S. Valentiner, Z. Naturforsch. **2B**, 5 (1947).
[9] A. Michel, Ann. chim. **8,** 352 (1937).

WASHINGTON, D.C. (Paper 64A1–31).

JOURNAL OF RESEARCH of the National Bureau of Standards—A. Physics and Chemistry
Vol. 64A, No. 1, January-February 1960

Uranium-Platinum System

J. J. Park and D. P. Fickle

(August 31, 1959)

The phase diagram of the uranium-platinum system was constructed from data obtained by thermal analysis, metallographic examination, and X-ray diffraction. The system is characterized by four intermetallic compounds: UPt, formed peritectoidally at 961° C; UPt_2, formed peritectically at 1,370° C; UPt_3, melting congruently at 1,700° C; and UPt_5, formed peritectically at 1,460° C. One eutectic occurs at 1,005° C and 12 a/o platinum, and a second at 1,345° C and 87.5 a/o platinum. The maximum solubilities are 4.5 a/o uranium in platinum and 5 a/o platinum in gamma-uranium. Platinum lowers the gamma-beta uranium transformation to 705° C and the beta-alpha transformation to 589° C.

1. Introduction

The study of the uranium-platinum system, reported herein, represents the completion of the initial phase of a program designed to establish the binary phase relationships between uranium and the platinide metals; the data from these studies will be correlated in the light of modern alloy theory, as an extension of earlier efforts in this field [1].[1] The data upon which this proposed uranium-platinum diagram was constructed were obtained primarily from thermal analysis, X-ray diffraction, and metallographic studies.

2. Previous Work

A survey of the literature up to 1948 revealed that information on the constitution of the uranium-platinum system was meager [2]. A more recent compilation of the literature by Saller and Rough [3] in 1955 reported the unpublished information that the UPt_2 compound had the hexagonal C–36 type $MgNi_2$ structure. It was also claimed that the beta uranium phase had been retained at room temperature by quenching alloys of low platinum content. Heal and Williams [4] later reported the compound UPt_3; however, their investigation was limited to preparing this particular compound.

3. Preparation and Analysis of Alloys

The component metals consisted of uranium of about 99.9 percent purity (Mallinckrodt biscuit) and 99.5 percent pure platinum sponge.[2] The platinum sponge was compressed into small pellets with a hydraulic press prior to preparing the charge.

Alloys in the range 0 to 45 a/o platinum were induction melted under vacuum using beryllia crucibles. Because an alloy of 54.8 a/o platinum showed evidence of reaction with the refractory, alloys in the composition range of 45 to 99.5 a/o platinum were prepared by arc melting under an atmosphere of helium. However, additional melts showed that alloys of greater than 75 a/o platinum did not react with beryllia crucibles.

Chemical analyses were made for one constituent on the as melted alloys. When determining the platinum content, alloys containing less than 6 a/o platinum were assayed spectrophotometrically, and alloys containing more than 6 a/o platinum were assayed gravimetrically. The uranium determinations were made spectrophotometrically for alloys with less than 12 a/o uranium and volumetrically for alloys containing more than 12 a/o uranium. The difference between the nominal and analyzed compositions was small, being less than 0.5 w/o when the alloys were prepared by arc melting and less than this when induction melted. The compositions of the alloys used in this investigation are given in table 1.

4. Procedures

4.1. Thermal Analysis

Thermal arrests were determined from time-temperature curves, the samples being heated in a molybdenum-wound resistance furnace. The accessory apparatus included an electronic controller to maintain uniform heating and cooling rates and an electronic recorder to plot automatically the heating and cooling curves. The thermal curves were obtained from specimens weighing approximately 100 g, heated and cooled under vacuum (about 10μ) at a rate of approximately 3° C/min. A nickel cylinder, which was originally used as a thermal reservoir, limited the maximum temperature to about 1,400° C; a molybdenum cylinder was later used as a thermal reservoir. The maximum temperature of the furnace was about 1,550° C. Temperature determinations were made with an annealed Pt versus Pt–10 percent Rh thermocouple, compared prior to use against a reference thermocouple calibrated at NBS. Under experimental conditions, temperature measurements are estimated to be accurate to ± 2° C.

[1] Figures in brackets indicate the literature references at the end of this paper.
[2] Spectrochemical analysis of platinum: 0.01 to 0.1 percent of Pd and Be; 0.001 to 0.01 percent of Au; 0.0001 to 0.001 percent of Ca, Mg, and Si; and <0.0001 percent of Cu (all percentages by weight).

TABLE 1. *Chemical composition of the uranium-platinum alloys*

Alloy No.	Uranium	Platinum	
	Wt %	Wt %	Atomic %
P-1	99.8	0.2	0.25
P-2	99.6	.4	.5
P-25	99.3	.7	.9
P-16	99.0	1.0	1.2
P-17	98.1	1.9	2.35
P-26	95.9	4.1	5.0
P-15	94.2	5.8	7.0
P-40	91.7	8.3	10.0
P-39	89.8	10.2	12.1
P-13	89.0	11.0	13.1
P-18	85.0	15.0	17.7
P-4	83.7	16.3	19.2
P-20	71.9	28.1	32.3
P-19	69.7	29.3	33.6
P-37	65.8	34.2	39.0
P-29	60.1	39.9	44.7
P-27	55.1	44.9	49.8
P-12	50.1	49.9	54.8
P-3	46.4	53.6	58.8
P-30	44.8	55.2	60.4
P-11	41.0	59.0	63.7
P-38	38.0	62.0	66.7
P-28	36.2	63.8	68.2
P-10	29.4	70.6	74.6
P-31	28.4	71.6	76.0
P-32	23.6	76.4	80.0
P-21	23.1	76.9	80.3
P-9	21.2	78.8	82.0
P-33	20.3	79.7	82.8
P-22	20.2	79.8	83.0
P-34	18.5	81.5	84.5
P-23	16.2	83.8	86.3
P-14	13.6	86.4	88.6
P-8	9.1	90.9	92.4
P-24	6.5	93.5	94.6
P-7	4.4	95.6	96.4

The thermal arrests of all alloys were derived from the cooling curves. When determining liquidus temperatures in alloys of greater than 74.6 a/o platinum above 1,500° C, thermal analyses were made in an induction furnace under vacuum, and temperature measurements were made with an annealed molybdenum-tungsten thermocouple contained in a beryllia protection tube. This thermocouple was calibrated against the melting point of the platinum sponge; it is believed to be accurate to within ±10° C under the experimental conditions. For these determinations, a premelted alloy was remelted by induction so that the thermocouple and its protection tube could be inserted from above. A cooling curve was obtained on an electronic recorder while the decrease in temperature was achieved by reducing the input to the converter gradually and uniformly by means of a motor-driven gear and chain drive.

Thermal analyses of alloys in the range 0 to 45 and 75 to 100 a/o platinum were made with the alloys contained in beryllia crucibles. Since alloys in the range 45 to 75 a/o platinum sometimes showed a reaction with the beryllia crucibles, thermal analyses on these alloys were made with the samples resting on either thoria or beryllia plates and heated by induction. Whenever metallographic observation indicated that contamination was excessive, the results were discarded. For some of the high temperature determinations, a filament furnace in which the specimen was heated by its electrical resistance was employed, with temperatures being determined with an optical pyrometer to an accuracy of ±10° C. Values thus obtained with no possibility of contamination by a crucible were considered to be reliable data. Only one temperature determination, either the melting point or the decomposition temperature, could be made with the optical pyrometer. The observed temperatures were used, no correction being made for the emissivity of the specimens.

4.2. Metallographic Analysis

The specimens for metallographic analysis were mounted in Bakelite and then rough ground on a series of silicon carbide papers, the final paper being 000 grit. The specimens were then finished on a wet broadcloth lap with either levigated alumina or with 1-μ diam diamond powder as the abrasive. In many instances, the uranium-rich alloys required a final electrolytic polish; the electrolytic solution consisted of 5 parts orthophosphoric acid, 8 parts ethylene glycol, and 8 parts ethyl alcohol. This final polish required 3 to 6 immersions of 15 sec each at 30 v and 10 amp/cm^2.

The structures of the uranium-rich alloys were developed by electrolytic etching consisting of 2 to 4 immersions of 10 sec each at 5 v and 1 amp/cm^2 in a 10 percent chromic acid solution. Alloys in the range 50 to 75 a/o platinum exhibited a high degree of resistance to chemical attack. Immersion periods as long as 5 min in an aqueous solution of 60 percent nitric acid were often required to obtain a satisfactory etch. Some platinum-rich alloys were etched by immersion in aqua regia, but, as this reaction was not easily controlled, an electrolytic etching method was developed using alternating current and a solution of 5 percent sodium cyanide and employing 2 to 4 immersions of 20 sec each at 10 v and 10 amp/cm^2.

All of the alloys were homogenized prior to quenching from various temperatures for subsequent metallographic examination. The samples were sealed, under helium atmosphere, in high-silica glass tubes, homogenized for 8 days at temperature, and furnace cooled. Alloys in the composition range 0 to 55 a/o platinum were homogenized at 800° C, those in the range 55 to 75 a/o at 950° C, and those in the range 75 to 99.5 a/o at 1,000° C. The examination of samples from the initial heat treatments revealed that, in the composition range of 55 to 65 a/o platinum, a large amount of contamination from the silica tubing had occurred. To avoid this, alloys for subsequent heat treatment were wrapped in molybdenum sheet prior to sealing in the silica tubing; no molybdenum contamination was detected by chemical tests. The homogenized specimens were subsequently sealed individually in silica tubing, reheated to selected temperatures, and quenched in ice water, using the nickel-block technique [5]. Quenching temperatures were measured with a Pt versus Pt–10 percent Rh thermocouple, previously calibrated against a standard thermocouple, which under the experimental conditions was accurate to

$\pm 2°$ C. In determining the solubility of platinum in uranium, the specimens were heated into the gamma range, then cooled to the desired temperature, and quenched. When quenching to determine the solidus line, the samples were quenched from the highest temperature attained. To determine the uranium solubility in platinum, homogenized specimens were heated to above 1,250° C before cooling to the quenching temperature. For temperatures above 1,250° C, the specimens were quenched when the desired temperature was attained on heating.

Because several of the phases were observed to be optically active, the phase boundaries were located by using polarized light. The alloys were examined under crossed Nicols and the characteristic extinctions of each of the various phases observed. In some cases, no extinctions were observed when the stage of the microscope was rotated through 360°. In others, when the stage was rotated through 360°, two extinctions were observed and the phase was designated as two-fold active. In still other instances four extinctions were apparent as the specimen was rotated through 360°, and this phase was designated as four-fold active.

4.3. X-Ray Analysis

The specimens which were used for the metallographic studies were subsequently placed in an X-ray diffractometer, and their room temperature diffraction patterns obtained by the use of either Cu-Kα or Co-Kα radiation. Powder patterns and film techniques were subsequently employed to supplement the diffractometer data. By the application of these techniques, and the utilization of the disappearing-phase method of analysis, it was possible to approximate the composition at which phase boundaries occurred. These results were then correlated with the thermal and metallographic data.

4.4. Hardness Determinations

The hardnesses of the various microconstituents were determined by the static indentation method, using a Bergsman hardness tester. The applied load ranged from 1 to 10 g, with an indentation time of 10 sec, and measurements were made at $\times$ 750. The results were then converted to diamond pyramid hardness (DPH), kg/mm^2.

5. Results

5.1. Thermal Analysis Data

The results of the thermal analyses are given in table 2, with the "arrest points," as determined from cooling curves, listed. These data indicate that additions of platinum to uranium lower the melting points of uranium alloys to a projected minimum of 1,005° C at about 12 a/o platinum. From this point, the melting points of the uranium-platinum alloys rise to a maximum of 1,700° C at 75 a/o platinum. From this maximum the liquidus temperatures drop rapidly to an indicated low of 1,345° C at about 87.5 a/o platinum and then rise rapidly to the melting point of the platinum sponge at 1,760° C.

TABLE 2.—*Summary of thermal data*

Composition, *a/o Pt*	Thermal arrests					
	a. Pt versus Pt—10% Rh thermocouple					
	Liquidus	U Pt$_3$	Eutectic	U Pt	$\gamma \rightarrow \beta$	$\beta \rightarrow \alpha$
	°C	°C	°C	°C	°C	°C
0.0	1131				767	657
.25	1131				759	599
.5	1120				759	589
1.2	1110				741	588
2.35	1102				715	589
5.0	1098				703	597
7.0	1072				705	596
10.0	1043		996		697	579
12.1	1005		1005	961	702	563
13.1	1020		999		706	590
17.7	1051		1009		705	583
19.2	1066		1005	967	704	567
32.3	1222		1002	959	708	576
33.6	1239		1009	963	709	571
39.0			993	953	689	591
44.7	1385		1030	963	734	
84.5	1481	1460	1340			
86.3			1336			
	b. Optical pyrometer					
39.0	[a] 1310					
49.8	1415					
54.8	1515					
60.4	1385					
68.2	1360					
74.6	1700					
	c. W–Mo thermocouple					
80.3	1655					
82.0	1548	1455				
82.8	1525	1458				
88.6	1545		1360			
94.6	1550		1363			
96.4	1660					
99.5	1760					

[a] Liquidus or reaction temperature.

The transformation temperatures of the allotropic forms of uranium were affected by the addition of platinum. The gamma-beta transformation temperature of uranium was lowered from 762° C to 705° C by the addition of platinum. This arrest temperature was fairly constant for alloys containing from 5 to 33 a/o platinum. The beta-alpha transformation temperature was similarly lowered from 657° C to 589° C in the composition range of 0.5 to 13 a/o platinum. A suppressing effect was noted in alloys containing from 13 to 33 a/o platinum, resulting in the beta-alpha transformation sometimes occurring as low as 567° C. Greater variation in the beta-alpha uranium transformation temperature than in the gamma-beta uranium transformation temperature is evident from the thermal analysis data. These data may indicate the greater likelihood of retaining the beta- rather than the gamma-uranium phase on quenching.

In the composition range of 0 to 75 a/o platinum, liquidus determinations show that the melting points of the alloys decrease from 1,131° C to about 1,005° C over a composition range of 0 to 12 a/o platinum.

The arrest at about 1,005° C occurred in alloys containing up to 33.6 a/o platinum, thus being indicative of a eutectic reaction. A second reaction horizontal was similarly observed to occur near 961° C in alloys containing up to 44.7 a/o platinum, thus indicating the solid state decomposition of an intermetallic compound. A third horizontal was observed at about 1,370° C in alloys of 60.4 and 68.2 a/o platinum, and this was considered to be indicative of the formation of a second intermetallic compound.

The melting point of the 75 a/o platinum phase was estimated to be 1,700° C, which was the approximate melting point of a 74.6 a/o platinum alloy as determined from optical pyrometer measurements.

In the composition range of 75 to 84 a/o platinum, the eutectic horizontal at 1,345° C was not observed, although a peritectic reaction was detected near 1,460° C. An alloy of 84.5 a/o platinum developed thermal arrests at 1,340°, at 1,460°, and at its melting temperature of 1,481° C, thus indicating that the alloy must lie in the eutectic field adjoining the terminal solid solution field but still be below the peritectic horizontal. An alloy of 82.8 a/o platinum did not develop the eutectic arrest, but it did show a definite arrest at 1,458° C, thus indicating that a phase boundary must lie between the 82.8 and 84.5 a/o platinum compositions.

In the composition range of 75 to 100 a/o platinum, the minimum located near 1,345° C was determined to be due to a eutectic reaction, inasmuch as a thermal arrest was observed in alloys having nominal compositions in the range 84.5 to 94.6 a/o platinum. No other arrests were observed below this temperature in this composition range.

The eutectic horizontal at the platinum-rich end was located by quenching techniques, using an alloy of 88.6 a/o platinum—the approximate eutectic composition. While this alloy showed no fusion at 1,340° C, it both fused and shattered on quenching from 1,350° C. This behavior established the fusion temperature within the range observable in this procedure, and thereby confirmed the results of thermal analysis of alloys of 84 to 95 percent.

5.2. Microstructures of the Alloys

The microstructures of alloys containing less than 5 a/o platinum varied appreciably depending on quenching temperature, and thus served to indicate the solubility variations in the several allotropic phases of uranium. The microstructure of the 5.0 a/o platinum alloy aided in determining the approximate maximum solid solubility of platinum in gamma-uranium, for when quenched from 720° C, the structure of this 5.0 a/o platinum alloy was two phase (fig. 1a). The second phase was observed to be spherodized at 990° C and had almost entirely disappeared, thereby indicating that this composition closely approximated the limit of solid-solubility of platinum in gamma-uranium. Thus it was concluded that the limit of solubility at the eutectic temperature was approximately 5 a/o platinum. The alloy of 2.35 a/o platinum varied in appearance according to the quenching temperature. For example, the structure of a slowly-cooled sample (3° C/min) was two-phase (fig. 1b); whereas quenching from 590° C produced what appeared to be a transition structure, and quenching from 700° C produced a structure which appeared to be almost entirely of the eutectoid type (fig. 1c). Furthermore, the structures of samples of this alloy quenched from temperatures of 720° C and above were of the solid solution type. It therefore appears that this composition (2.35 a/o platinum) closely approaches the eutectoid of the gamma decomposition.

The beta-uranium solvus was located approximately by quenching experiments. A 1.2 a/o platinum alloy, when quenched from 590° C, revealed what appeared to be a eutectoid decomposition (fig. 1d) but became a single phase structure when quenched from 600° C (fig. 1e). On the other hand, the 2.35 a/o platinum alloy was two-phase both at 590° C and at 700° C, thus locating the beta solvus between these two compositions. The room temperature solubility of platinum in uranium was shown to lie between 0.9 and 1.2 a/o platinum (figs. 1f, g). Even though thermal analysis indicates that the platinum solubility in alpha-uranium may be below 0.5 a/o, consideration of homogenized and alpha-quenched specimens indicates the higher solubility of between 0.9 and 1.2 a/o platinum.

The solidus line in the uranium-rich field was located by quenching techniques. An alloy of 1.2 a/o platinum showed evidence of melting in the temperature range between 1,060° C and 1,090° C. For an alloy of 2.35 a/o platinum the solvus lies between 1,050° C where solid solution was evident and 1,075° C, where fusion occurred.

Metallographic evidence for the eutectic temperature was sought by using a 13.1 a/o platinum alloy which was estimated to be near the eutectic composition. A sample of this composition, on being quenched from 1,000° C, showed a eutectic structure while another such sample, quenched from 1,010 °C, showed partial fusion, thus bracketing the eutectic horizontal within ± 5° C at 1,005° C.

The homogenized specimens in the composition range of 0 to 50 a/o platinum showed an increasing amount of second phase with increasing platinum content. The two phases present in the homogenized 33.6 a/o platinum alloy and their relative amounts indicated that no compound of 33.3 a/o platinum exists. Both of the phases were optically active with the terminal solid solution showing fourfold activity and the second phase showing twofold activity under polarized light. The microstructure of the 49.8 a/o platinum specimen was practically single phase (fig. 1h). In view of the structures observed in the two ranges of 0 to 49.8 a/o platinum and of 49.8 to 60.4 a/o platinum, it was concluded that a phase existed at the apparent composition of UPt.

The metallographic and thermal data for the uranium-rich alloys have been summarized in figure 2.

Instead of the expected two-phase structure, alloys in the range of 55 to 64 a/o platinum showed

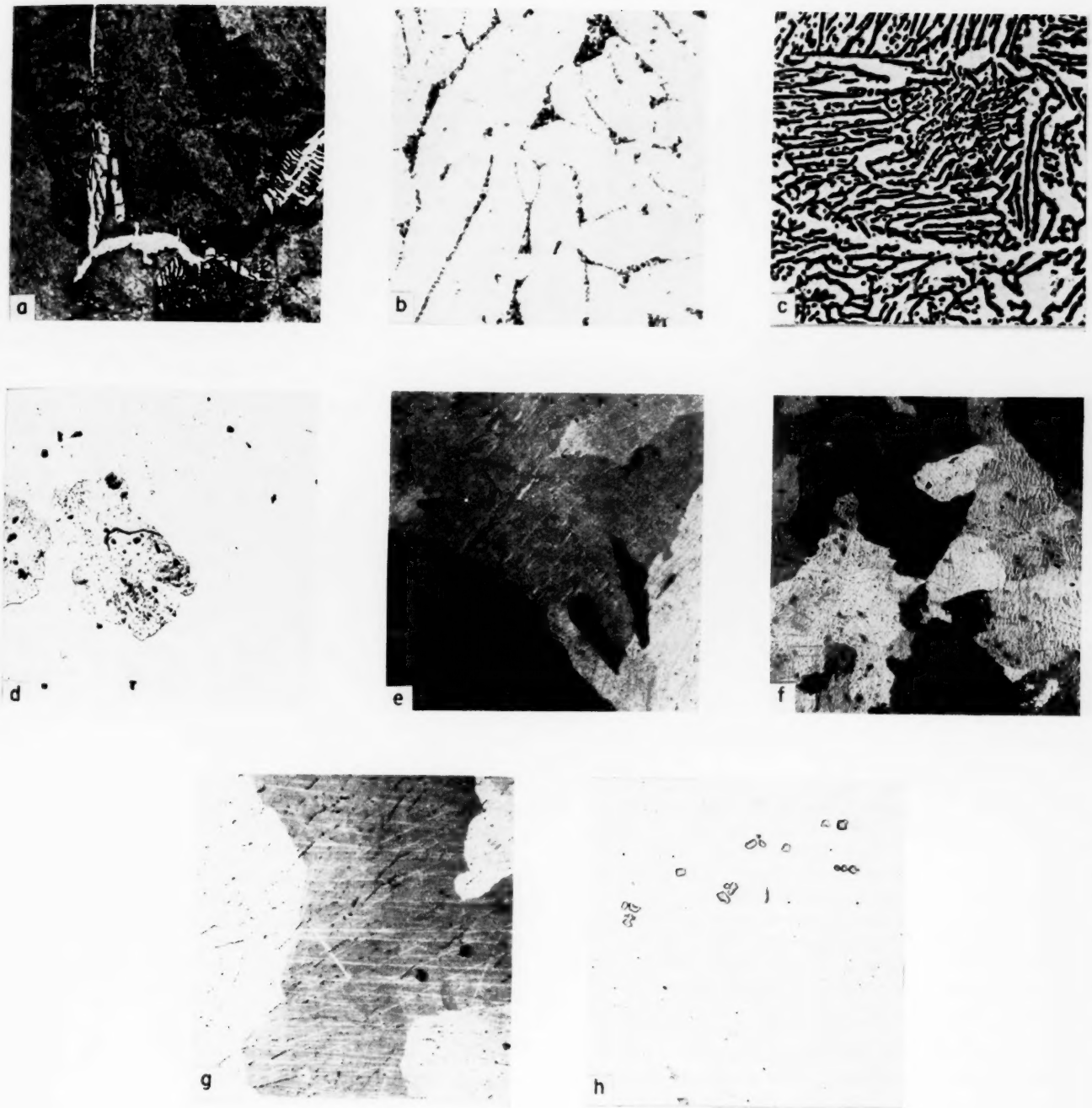

FIGURE 1. *Microstructures of uranium-platinum alloys.*

Samples a, b were etched in chromic acid; c, d, e, f, g were electropolished in solution of orthophosphoric acid, ethylene glycol, and ethyl alcohol; h was not etched.

a. Alloy of 5.0 a/o platinum, quenched from 720° C, UPt in uranium matrix. × 500.
b. Alloy of 2.35 a/o platinum, after thermal analysis, UPt in uranium matrix. × 1000.
c. Alloy of 2.35 a/o platinum, quenched from 700° C, UPt in uranium matrix. × 200.
d. Alloy of 1.2 a/o platinum, quenched from 590° C, UPt in uranium matrix. × 100.
e. Alloy of 1.2 a/o platinum, quenched from 600° C, uranium solid solution. × 500.
f. Alloy of 0.9 a/o platinum, homogenized, uranium solid solution. × 100.
g. Alloy of 1.2 a/o platinum, after thermal analysis, UPt in uranium matrix. Polarized light. × 100.
h. Alloy of 49.8 a/o platinum, uranium in UPt matrix. × 200.

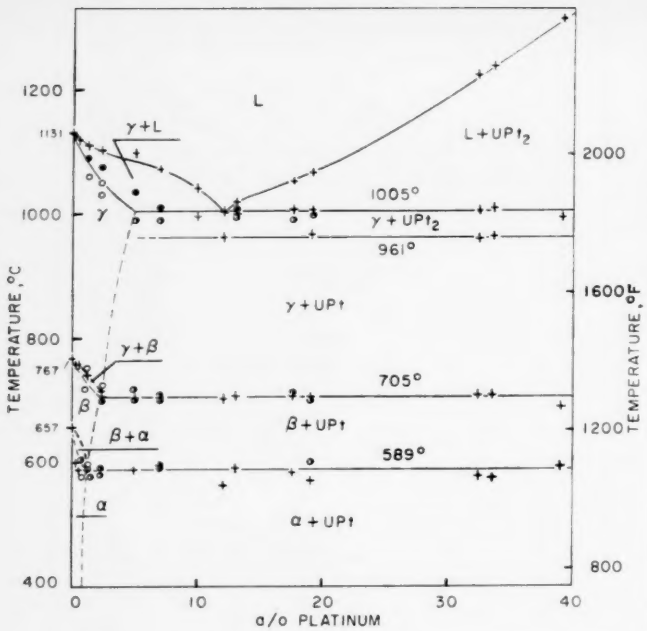

FIGURE 2. *Uranium-rich section of uranium-platinum phase diagram.*

○ indicates single phase alloy, ◑ indicates two phase alloy, ● indicates fusion; + indicates thermal arrest.

a single phase structure after homogenization. However, quenched specimens in this range showed increasing amounts of silica contamination upon quenching from higher temperatures. Since alloys in this range had also showed a reaction with beryllia when induction melted, these alloys were protected from contact with silica by molybdenum sheet. After homogenization these alloys then showed two phases, consistent with their "as cast" structure. In addition, the X-ray patterns were also consistent with the observed microstructures and indicated no apparent molybdenum contamination.

The two phase structures occurring in the alloys between 50 and 75 a/o platinum showed one optically inactive phase, one that revealed twofold optical activity, and one that revealed fourfold optical activity under polarized light. In the alloys between 50 and 64 a/o platinum the phase of twofold activity (UPt) and an optically inactive phase were present, and the alloys in the range of 68.2 to 74.6 a/o platinum contained an optically inactive phase and one of fourfold activity. The presence of the phase having no optical activity was interpreted to signify that a new homogeneous "field" was to be encountered between 63.7 and 68.2 a/o platinum. The distribution of the constituents of the microstructures indicated the phase boundary to have the apparent composition of UPt_2. In confirmation of this, a single phase structure was developed in an alloy of 66.7 a/o platinum (fig. 3a) when heated by its own electrical resistance to about 1,350° C, thus serving to substantiate the existence of the UPt_2 compound.

In the composition range of 75 to 96 a/o platinum three phases were identified. However, alloys in this range reacted readily with silica tubing and consequently had to be protected with beryllia during quenching studies. Alloys in this range also exhibited varying degrees of optical activity under polarized light. The structure of the alloy at 74.6 a/o platinum consisted almost entirely of a single phase having fourfold optical activity (fig. 3b), thus apparently indicating the existence of the UPt_3 phase. Alloys in the composition range 84 to 95 a/o platinum were two phase, consisting of the terminal solid solution which was not active under polarized light and a second phase which displayed twofold activity under polarized light. The 84.5 a/o platinum alloy showed an active and an inactive phase under polarized light, and it consisted predominantly of the active phase. The 80.0 a/o platinum alloy consisted of two phases both of which were active under polarized light, one being twofold and the other fourfold active. In view of this, it was concluded that an intermetallic compound must be located between 80.0 and 84.5 a/o platinum; of the two possible compound compositions in this range, UPt_4 and UPt_5, that of UPt_4 must be eliminated since the 80.0 a/o platinum alloy definitely consisted of two phases. Also, since an alloy of 82.8 a/o platinum was predominantly single phase (fig. 3c) and showed twofold activity under polarized light, it would seem to indicate proximity to the nominal phase composition. Thus the existence of the UPt_5 (83.3 a/o Pt) phase was postulated, and its existence persisted to at least 1,340° C, as indicated from observation of quenched specimens. In the range of 75 to 83.3 a/o platinum (UPt_3 to UPt_5) only two phases were observed, both being optically active.

The solid solubility of uranium in platinum was determined by metallographic observation of alloys containing more than 94 a/o platinum. An alloy of 96.4 a/o platinum was entirely single phase (fig. 3d) whereas a 94.6 a/o platinum alloy showed a small amount of second phase, from which it may be concluded that the room temperature solubility of uranium in platinum is approximately 4 a/o. At elevated temperatures the 96.4 a/o platinum alloy was single phase up to the maximum quenching temperature of 1,340° C, and the 94.6 a/o platinum alloy contained two phases to the same temperature. Thus, these quenching experiments indicate that the solvus lies between 94.6 and 96.4 a/o platinum up to 1,340° C.

5.3. Microhardness Results

Microhardness tests were made to assist in the differentiation between the various constituents in the several fields occurring in the uranium-platinum system (table 3).

Hardness data provided additional evidence which helped to clarify the peculiarities noted in an alloy of 54.8 a/o platinum. After homogenization in silica tubing, samples of this alloy showed a single phase

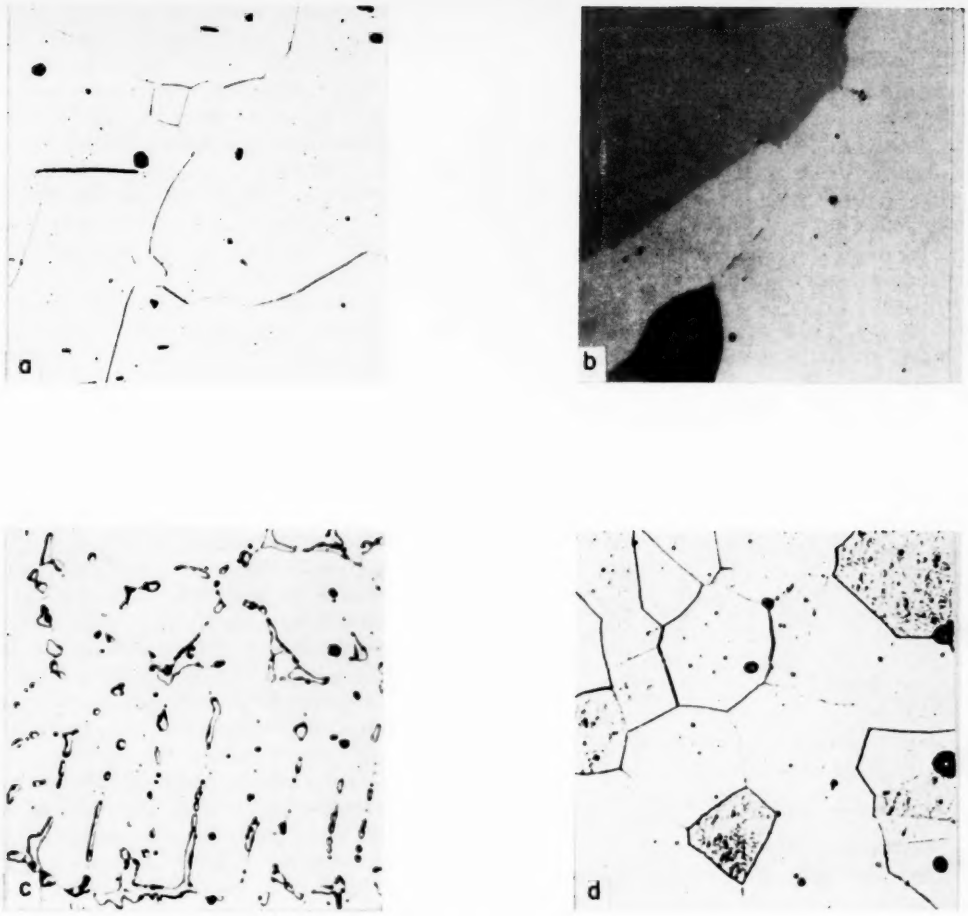

FIGURE 3. *Microstructures of uranium-platinum alloys.*

Specimens a, d were etched in sodium cyanide; b, c were not etched.
a. Alloy of 66.7 a/o platinum, UPt_2 phase. × 100.
b. Alloy of 74.6 a/o platinum, UPt_3 phase. Polarized light, × 500.
c. Alloy of 82.8 a/o platinum, UPt_3 in a matrix of UPt_5. × 500.
d. Alloy of 96.4 a/o platinum, platinum terminal solid solution. × 250.

TABLE 3. *Hardness of phases in uranium-platinum alloys*

	Diamond pyramid hardness [a]
Uranium solid solution	425
UPt	385
UPt_2	905
UPt_5	405
UPt_3	610
Platinum solid solution	250

[a] Average of 5 or more determinations.

having a diamond pyramid number of 565. However, after homogenization using a protective molybdenum sheet, the samples exhibited two phases having hardnesses of DPH 419 and 822 which were comparable to the hardnesses of the two phases present in this alloy after a thermal analysis run. The hardnesses of phases in alloys containing from 33.6 to 74.6 a/o platinum served to substantiate the conclusion that the alloy-refractory reaction resulted in the peculiarities noted in the 54.8 a/o platinum alloy.

5.4. X-Ray Data

X-ray diffraction patterns were obtained from the same specimen surfaces that were used for the metallographic examinations, and the data obtained were correlated with the microstructures. The characteristic *d*-values of the intermetallic phases are listed in table 4. The alloys in the composition range 75 to 85 a/o platinum were very brittle and could be readily crushed to powder; hence, camera techniques were employed to supplement the diffractometer data.

X-ray patterns were analyzed and compared with the known diffraction patterns for uranium [6, 7, 8], with the pattern for platinum [9], and with the reported UPt_3 pattern [3].

The diffraction patterns for the homogenized specimens in the range of 0 to 49.8 a/o platinum showed, with increasing platinum content, decreasing relative intensity of lines and in the number of lines attributable to the terminal uranium phase, as well as in the appearance of additional lines which could

TABLE 4. *X-ray diffraction data of uranium-platinum intermetallic compounds*

UPt		UPt_2		UPt_3		UPt_5	
d	*I* [a]	*d*	*I*	*d*	*I*	*d*	*I*
Å		Å		Å		Å	
2.80	*w*	2.93	*w*	3.14	*w*	2.60	*m*
2.76	*m*	2.33	*w*	2.72	*vw*	2.23	*s*
2.65	*w*	2.31	*w*	2.48	*m*	2.13	*m*
2.56	*vw*	2.26	*s*	2.44	*s*	2.06	*vw*
2.36	*s*	2.09	*m*	2.21	*s*	1.85	*w*
2.28	*w*	2.03	*w*	1.98	*vw*	1.70	*vw*
2.18	*w*	1.95	*w*	1.93	*w*	1.58	*vw*
2.11	*m*	1.84	*m*	1.74	*m*	1.513	*m*
2.00	*w*	1.77	*w*	1.69	*w*	1.426	*m*
1.92	*m*	1.65	*s*	1.435	*m*	1.173	*m*
1.85	*vw*	1.62	*vw*	1.364	*s*	1.131	*w*
1.78	*w*	1.49	*w*	1.308	*vw*	1.070	*vw*
1.72	*m*	1.44	*w*	1.253	*vw*	1.039	*vw*
1.66	*m*	1.280	*m*	1.230	*m*	1.005	*w*
1.64	*m*	1.247	*w*	1.223	*w*		
1.56	*w*	1.032	*w*	1.206	*w*		
1.52	*vw*	1.013	*w*	1.115	*vw*		
1.471	*w*	0.985	*vw*	1.110	*m*		
1.415	*s*	.970	*vw*	1.052	*w*		
1.385	*m*	.906	*w*	0.990	*w*		
1.347	*w*			.942	*w*		
1.314	*w*			.933	*w*		
1.277	*vw*			.925	*w*		
1.270	*vw*			.912	*w*		
1.192	*w*						
1.181	*m*						
1.166	*w*						
1.147	*w*						
1.103	*vw*						
1.093	*w*						
1.083	*vw*						
1.070	*vw*						
1.043	*vw*						
1.006	*vw*						
0.998	*w*						
.978	*w*						
.965	*w*						
.954	*w*						
.918	*w*						

[a] *I* is intensity; *s*—strong; *m*—medium; *w*—weak; *vw*—very weak.

not be ascribed to any previously reported compound. Alloys containing more than 49.8 a/o platinum had no lines corresponding to the uranium phase but did have lines believed to be caused by presence of the compound UPt which existed at 50 a/o platinum. The lines obtained from the UPt phase had almost disappeared in an alloy containing 63.7 a/o platinum, and a still different pattern attributable to another phase had become apparent. In an alloy of 68.2 a/o platinum the UPt lines had disappeared, being replaced by the lines of a new phase. These results indicated the existence of a phase containing 66.7 a/o platinum, UPt_2. An alloy of 74.6 a/o platinum had lines believed to be obtained from UPt_3 and none that could be assigned to either the UPt_2 or the platinum-rich terminal solid solution. As the amount of platinum increased beyond 75 a/o platinum, the UPt_3 pattern became weaker, and a new pattern, that attributed to the UPt_5 phase, appeared. The presence of the UPt_5 phase was indicated in the patterns from alloys of up to 82.0 a/o platinum. Progressive changes in the powder patterns of alloys having 76.0, 83.0, and 84.5 a/o platinum clearly indicated the presence of a compound having the apparent UPt_5 composition. In the range between 84.5 and 96.4 a/o platinum the characteristic *d*-values of the terminal solid solution were observed in conjunction with a set of *d*-values which had also been associated with the UPt_5 values determined by camera techniques.

Diffraction patterns were also obtained from alloys having essentially a single phase. In most cases the patterns exhibited strong, sharp diffraction lines, although the pattern from the 49.8 a/o platinum alloy (UPt phase) was very weak and poorly defined. No special effort was made to determine crystal structures. However, it was apparent that the characteristic *d*-values of the UPt_3 phase obtained from these experiments did not coincide with the calculated values for the proposed UPt_3 compound [3]. The discrepancies may be attributed to the different methods of preparing the samples.

The solid solubility of uranium in platinum was determined from quenched specimens by means of back-reflection X-ray methods. The film-to-specimen distance was calibrated by using the known "reflections" from the 420 plane of silver in the powder form. The change of lattice parameter with the increase of uranium solubility is positive (table 5). From these data, the solubility of uranium in platinum increases from a value of 4.0 a/o at room temperature to a maximum of 4.5 a/o at the eutectic temperature. The calculated increase in volume of the platinum lattice at the eutectic temperature is a maximum of 3 percent.

The X-ray data obtained from quenched specimens containing low platinum percentages, 0.25 to 5.0 a/o platinum, were compared with the data for the uranium phases. There was no evidence of retention of the beta-uranium or gamma-uranium phases in the diffractometer patterns.

TABLE 5. *Solubility determination of uranium in platinum*

Quenching temperature	Lattice parameters, Å				Resultant uranium solubility
	99.5 a/o Pt	96.4 a/o Pt	94.6 a/o Pt	92.4 a/o Pt	
°C					a/o
Room	3.925	3.953	3.956	3.956	4.0
1200	3.927	3.958	3.964	3.965	4.3
1340	3.927	3.958	3.966	3.967	4.5

6. Discussion

6.1. Uranium Terminal Solid Solution

The degree of solubility of platinum in uranium was determined primarily by metallographic data. The microstructures of alloys containing greater than 5 a/o platinum consisted of two phases when quenched from near the eutectic temperature. The 5.0 a/o platinum alloy quenched from 990° C contained only a trace of a second phase. Hence, it was concluded that the maximum solubility of platinum in uranium at the eutectic temperature was approximately 5 a/o. The structure of a quenched beta alloy having 2.35 a/o platinum was typically eutectoid and thus located the gamma-uranium decomposition, and the structure of this alloy quenched from the gamma field was typically solid solution. The

0.5 a/o platinum alloy was solid solution throughout the beta field. However, a 1.2 a/o platinum alloy was two phase at 590° C and solid solution at 600° C. The 2.35 a/o platinum alloy was two phase both at 590° C and at 700° C. Hence, the maximum solubility of platinum in beta-uranium lies between 1.2 a/o and 2.35 a/o. The room temperature solubility of platinum in uranium was shown to lie between 0.9 and 1.2 a/o platinum.

X-ray data of alloys containing up to 5 a/o platinum, obtained from quenched specimens, gave no conclusive evidence of the retention of beta- or gamma-uranium, as previously reported for this system [3].

6.2. Uranium-UPt_2 Eutectic

Thermal analysis data indicated a decrease in the melting point of uranium alloys to a minimum at approximately 1,005° C at about 12 a/o platinum. The existence of a reaction horizontal was noted by thermal analysis of alloys in the composition range of 10 to 39 a/o platinum. A metallographic survey of quenched alloys in the composition range of 5 to 50 a/o platinum indicated the existence of a eutectic horizontal at approximately 1,005° C. The application of lever analysis to the distribution of the microconstituents indicated the placement of the eutectic point at about 12 a/o platinum. Based on these data, it was concluded that a eutectic between the terminal solid solution and UPt_2 exists at an apparent composition of 12 a/o platinum at a temperature of 1,005° C.

6.3. UPt Phase

Thermal analysis data show the presence of the arrests characteristic of the allotropic transformations of uranium in the composition range of 0 to 45 a/o platinum, and the data fail to show the presence of these arrests in alloys in excess of 50 a/o platinum. Also, when this information is coupled with the presence of an arrest at 961° C, it must be considered indicative of a compound formed by a peritectoid reaction at 961° C and 50 a/o platinum. Since the 49.8 a/o platinum alloy was essentially single phase after homogenization while the 33.6 a/o and 39.0 a/o platinum alloys were definitely two phase, the most likely composition for a compound was in the 1 to 1 atomic ratio. X-ray techniques utilizing the disappearing phase method also indicate the presence of a phase boundary at 50 a/o platinum. Observations of the specimens under polarized light indicated two active phases in the 0 to 50 a/o platinum range and only one active phase in the field between 50 and 66 a/o platinum. Based on all these data, it was concluded that the compound formed peritectoidally at 961° C has the apparent composition of UPt.

6.4. UPt_2 Phase

X-ray data for alloys in the range 55 to 75 a/o platinum indicated the presence of a phase in the vicinity of 67 a/o platinum. The increasing strengths of certain diffraction lines and the comparison of the *d*-values for the UPt and UPt_3 phases permitted the separation of the pattern for the UPt_2 phase.

The microstructures of the alloys in the composition range 66 to 75 a/o platinum contained two phases, one of which showed fourfold activity under polarized light and a second which was not active. This differed from two phase alloys in the 50 to 66 a/o platinum composition range, for these showed one constituent very strongly twofold active and a second constituent not optically active. Thus the metallographic data indicated a change of the phases being located near 67 a/o platinum. The single phase microstructure developed in a 66.7 a/o platinum alloy heated by its own electrical resistance completely substantiated the conclusion that the UPt_2 phase was present.

In view of these data, it was concluded than an intermetallic compound UPt_2 exists and thermal analysis data indicate that it is formed peritectically at 1,370° C.

6.5. UPt_3 Phase

The alloy having 74.6 a/o platinum had a melting point of 1,700° C, the highest observed in the melting point determinations. This was indicative of a congruently melting compound situated near the 75 a/o platinum composition. The X-ray data revealed that a phase boundary should exist at 75 a/o platinum, for the data showed that one specific pattern became easily identifiable as the 75 a/o platinum content was approached. The essentially single phase microstructure of a homogenized 74.6 a/o platinum alloy indicated a possible phase boundary. In addition, a change of optical activity under polarized light was apparent near the 75 a/o platinum composition. In view of these data, it was concluded that UPt_3, a congruently melting compound, exists in this system.

6.6. UPt_5 Phase

Alloys in the neighborhood of the stoichiometric UPt_5 composition were extremely reactive, being contaminated by either silica or molybdenum. These reactions completely masked UPt_5 on the preliminary survey though certain inconsistent data were noted. Protection of the alloys with beryllia permitted heat treatment without contamination. The compound was eventually located by thermal analysis data in that the 82.8 a/o platinum alloy did not develop a thermal arrest at 1,340° C while the 84.5 a/o platinum alloy did show such an arrest. However, both of these alloys did develop an arrest near 1,460° C. Metallographic data in the UPt_5-terminal solid solution field showed that the UPt_5 had twofold activity under polarized light while the terminal solid solution revealed no activity. In the two phase field of alloys of 75 to 83 a/o platinum one of these phases showed twofold activity, whereas the other displayed fourfold activity under polarized light. The microstructure of the alloy at 82.8 a/o platinum was predominantly single phase and showed twofold activity under polarized light. Thus the

metallographic data indicated the existence of a compound at approximately 83 a/o platinum. Both X-ray diffractometer data obtained from the metallographic specimens and the diffraction data obtained from unsieved powder specimens indicated, by the disappearing phase method, the existence of a compound at UPt_5. This, coupled with the existence of a reaction horizontal at 1,460° C, indicated the existence of UPt_5 which forms peritectically at 1,460° C.

6.7. Platinum Terminal Solid Solution

Results of both the X-ray and metallographic examinations show that the solvus of the platinum terminal solid solution rises very steeply from room temperature to the eutectic temperature. The high temperatures involved and the economics of platinum alloy studies did not permit more extensive alloy preparation with the resultant more precise location of the solvus. However, the X-ray and metallographic data, coupled with the thermal analysis data, locate the solvus within the composition range of 94.6 to 96.4 a/o platinum for the temperature range from room temperature to 1,340° C. In view of this, the solubility of uranium in platinum is considered to be 4.0 a/o at room temperature, increasing to 4.5 a/o at 1340° C.

A combination of thermal and metallographic data fixed the eutectic composition near 87.5 a/o platinum and at 1,345° C.

7. Summary

The platinum-uranium system (fig. 4) was constructed from data obtained by thermal, metallographic, and X-ray analysis.

This system is characterized by two eutectics, one occurring at 1,005° C and a composition of 12 a/o platinum and the second at 1,345° C and 87.5 a/o platinum; and four intermetallic compounds, one formed peritectoidally at 961° C with an apparent composition of 50 a/o platinum (UPt), the second formed peritectically at 1,370° C with an apparent composition of 66.7 a/o platinum (UPt_2), the third melting congruently at about 1,700° C with an apparent composition of 75 a/o platinum (UPt_3), and the fourth formed peritectically at 1,460° C with an apparent composition of 83.3 a/o platinum (UPt_5).

The solubility of uranium in platinum is approximately 4.5 a/o at the eutectic temperature of 1,345° C, decreasing with temperature to about 4.0 a/o at room temperature. The solubility of platinum in uranium is approximately 5 a/o at the eutectic

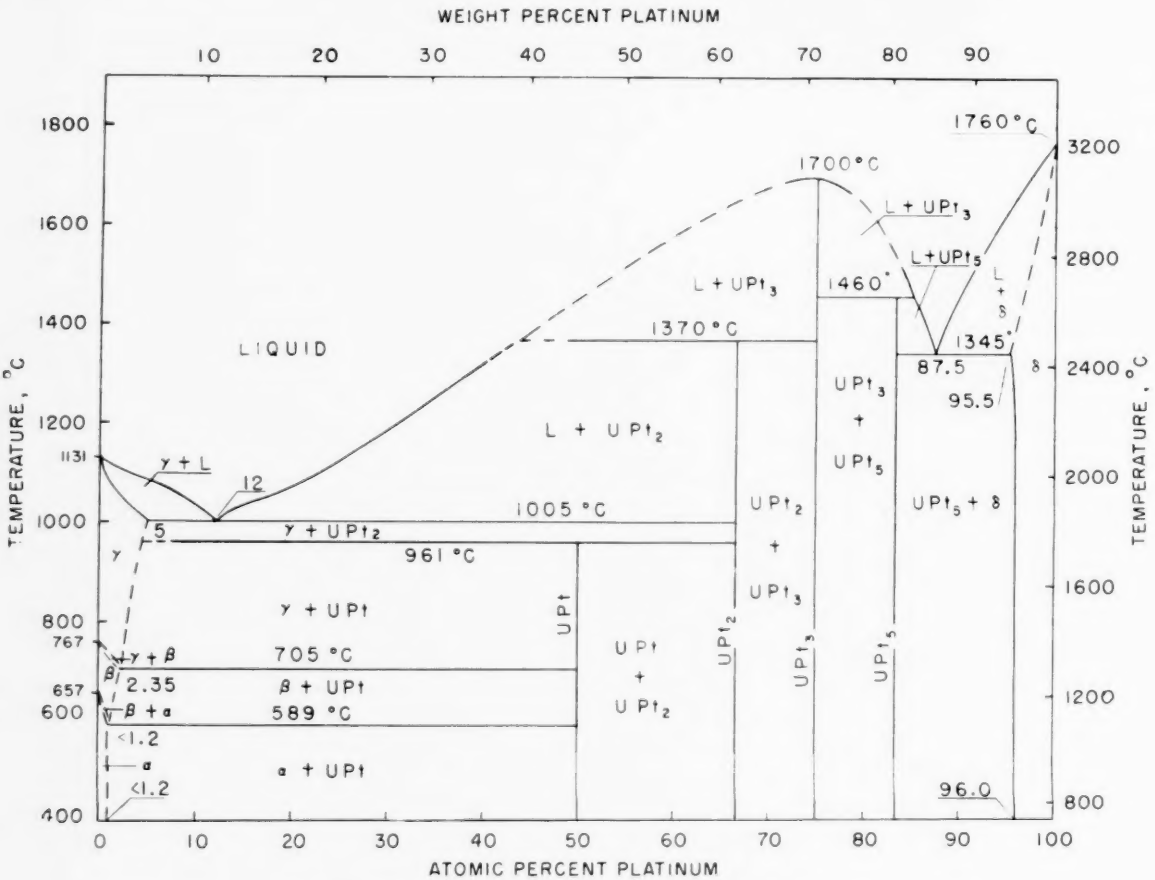

FIGURE 4. *Uranium-platinum phase diagram.*

temperature of 1,005° C, decreasing to near 2.35 a/o at the gamma-beta transformation; it is less than 1.2 a/o at the beta-alpha transformation, and is greater than 0.9 a/o at room temperature.

The gamma-beta transformation temperature of uranium was lowered from 767° to 705° C, and the beta-alpha transformation temperature was lowered from 657° to 589° C by the addition of platinum.

The authors express their appreciation of the sponsorship of this investigation by the Atomic Energy Commission, Division of Research, and for its permission to publish this paper.

The authors also express their appreciation to L. L. Wyman for his advice, assistance, and for many fruitful discussions; to J. T. Sterling for preparing certain of the alloys; to M. I. Cohen for assistance in the accumulation of the data; and to Martha Richmond and J. R. Baldwin for the chemical analyses.

8. References and Notes

[1] R. W. Buzzard (informal communication).
[2] R. W. Buzzard and H. E. Cleaves, J. Met. and Ceram. (TID65) **1,** 43 (1948).
[3] H. A. Saller and F. A. Rough, Battelle Memorial Inst., BMI–1000 (1955).
[4] T. J. Heal and G. I. Williams, Acta Cryst. **8,** 494 (1955).
[5] R. W. Buzzard, R. B. Liss, and D. P. Fickle, J. Research NBS, **50,** 209 (1953), RP2412.
[6] C. W. Jacob and B. E. Warren, J. Am. Chem. Soc. **59,** 2588 (1937).
[7] J. Thewlis, Acta Cryst. **5,** 790 (1952).
[8] The Reactor Handbook, p. 391, AECD–3647.
[9] H. E. Swanson and E. Tatge, NBS Circ. 539 (1953).

Washington, D.C. (Paper 64A1–32)

JOURNAL OF RESEARCH of the National Bureau of Standards—A. Physics and Chemistry
Vol. 64A, No. 1, January-February 1960

Nitriding Phenomena in Titanium and the 6Al-4V Titanium Alloy

J. R. Cuthill, W. D. Hayes, and R. E. Seebold [1]

(September 21, 1959)

Nitriding unalloyed titanium in purified nitrogen at 1,800° F produced a uniformly thick case that consisted of five distinct zones. The same treatment applied to a 6Al-4V titanium alloy resulted in a thinner nitride case that consisted of three zones and elongated nitride grains that penetrated into the core at approximately 45 degrees to the specimen surface. The aluminum appears to be responsible for the formation of the elongated grains. These grains, in turn, appear to be responsible for the nitriding having a more adverse effect on the toughness of the alloy than of the unalloyed titanium, as indicated by preliminary impact test results. The nitride case on the titanium appears to increase in thickness with increase in nitriding time without limit. The nitride case exhibits a hardness equivalent to about 77 Rockwell C at the surface down to almost 50 Rockwell C at the interface.

1. Introduction

Titanium is known to have a strong affinity for nitrogen and to form a nitride case of high hardness when heated in the presence of nitrogen or ammonia. However, there has been little previous investigation of the effect of metallic alloying elements on the morphology of the nitride phase or phases generated in the course of the nitriding treatment. This paper is concerned primarily with the effect of aluminum and vanadium. The morphology of the nitride case produced in commercially pure titanium is compared with the nitride formations produced in a titanium 6Al-4V alloy. The work was carried out in the course of a broader program of materials investigation for the Navy Bureau of Aeronautics regarding an application where good resistance to galling and wear between surfaces in sliding contact is required, as well as high surface hardness, light weight, good salt water corrosion resistance, and good machinability. Wyatt and Grant's [1][2] experiments indicated that the nitriding of titanium did produce a surface with satisfactory properties required for the maintenance of surfaces in sliding contact.

Many procedures for surface hardening titanium have been tried by previous investigators, including carburizing, nitriding, and anodizing [2, 3, 4, 5]. It has been generally concluded that nitriding is the most promising method for producing a hard, wear-resistant surface [6]. There has been somewhat less agreement as to the best type of nitriding procedure to use. Wyatt and Grant report a preference for nitriding in ammonia because they found the nitriding time-and-temperature to be lower than that required when using purified nitrogen to produce the same case thickness [4]. On the other hand, some investigators are of the opinion that hydrogen embrittlement of the titanium may be induced during nitriding in ammonia [6]. Therefore, in the initial phase of this current program, it was decided to nitride in purified nitrogen in order to avoid any potential complications involving hydrogen embrittlement.

2. Materials

The Armour Research Foundation [5] investigated the effect of various alloy additions on the nitriding characteristics of titanium, and reported that vanadium and boron were the only elements found to result in an increased nitriding rate and increased ultimate hardness. The 6Al-4V alloy, which recently has come into widespread use, therefore, appeared to be of sufficient theoretical as well as practical interest to warrant inclusion in the program along with commercially pure titanium.

The chemical compositions and tensile properties of both materials, as furnished by the supplier, are given in table 1. The material was specified as double arc melted "aircraft quality" 0.050-in. thick sheet, No. 2 finish.

TABLE 1. *Composition and properties of titanium and 6Al-4V alloy* [a]

	Titanium	6Al-4V alloy
Yield strength:		
Longitudinal, psi	54,400	128,000
Transverse, psi	53,500	128,300
Tensile strength:		
Longitudinal, psi	68,200	131,600
Transverse, psi	67,500	132,900
Elongation:		
Longitudinal, %	27.0	19.0
Transverse, %	27.0	13.0
Composition:		
C, wt %	0.027	0.01
Fe, wt %	.046	.14
Al, wt %	----	6.0
V, wt %	----	4.1
N_2, wt %	0.020	0.012
H_2, wt %	.005	.010
Ti, wt %	99.6	89.5

[a] Data furnished by manufacturer.

[1] Physical chemist at the Naval Research Laboratory, Washington, D.C.
[2] Figures in brackets indicate the literature references at the end of this paper.

3. Experimental Procedures

Specimens, approximately 5/16 in. by 2½ in., were cut from the 0.050-in. thick sheet; all of the specimens of each material were cut from the same sheet. The edges were milled so as to permit the accurate determination of the cross section of specimens used for unnotched Charpy-type impact tests. Preparatory to nitriding, the specimens were pickled for 15 min in the following standard pickling solution [7] at 80° F:

HNO_3	47 parts by volume
HF	2 parts by volume
H_2O	51 parts by volume

Upon removal from the pickling solution the specimens were thoroughly washed in tap water and air dried.

Specimens were nitrided at 1,800° F for 4, 16, 24, 48, 96, or 168 hr, to obtain data on case thickness versus time. Figure 1 is a drawing of the nitriding furnace. The nitriding chamber was an Inconel tube with water-cooled ends. The specimens were held in the cool zone at the rear of the nitriding chamber until the chamber with its purified nitrogen atmosphere was brought up to temperature. Each specimen was then individually drawn into the hot zone by magnetic attraction acting on the iron bob attached to the specimen by means of a fine wire. Each specimen, at the end of its prescribed time, was drawn into the cool zone at the front of the chamber by the same mechanism.

"Water-pumped" grade nitrogen was passed through a liquid oxygen cold trap to remove water and then over titanium turnings at 1,800° F to remove oxygen before entering the nitriding chamber. In spite of its strong affinity for nitrogen, titanium was used in the getter furnace because of its superiority in removing oxygen. Fortunately, the oxide reaction is more rapid than the nitride reaction, but, more important, the titanium nitride that is formed eventually reverts to the oxide. However, to insure high efficiency in oxygen removal, the charge of titanium turnings was replaced before every run.

Gas leaving the nitriding chamber was passed through a mercury bubble trap and then exhausted through a wet-test gas meter, which permitted the absolute pressure in the nitriding chamber to be maintained anywhere between 1 and 2 atm. However, tests early in the program revealed no significant difference in nitriding characteristics resulting from varying the pressure over this entire range. Therefore, the bulk of the specimens were nitrided with a pressure of 2 in. of mercury above atmospheric in the nitriding chamber.

More than 300 specimens were nitrided for 48 hr in the course of this program. To facilitate nitriding of this many specimens a much larger chamber was also used. This larger chamber was also of Inconel and the same type of gas purifying system was used, but of correspondingly larger capacity. The specimens were sealed in the chamber, and, with the purified nitrogen flowing through the system, the chamber

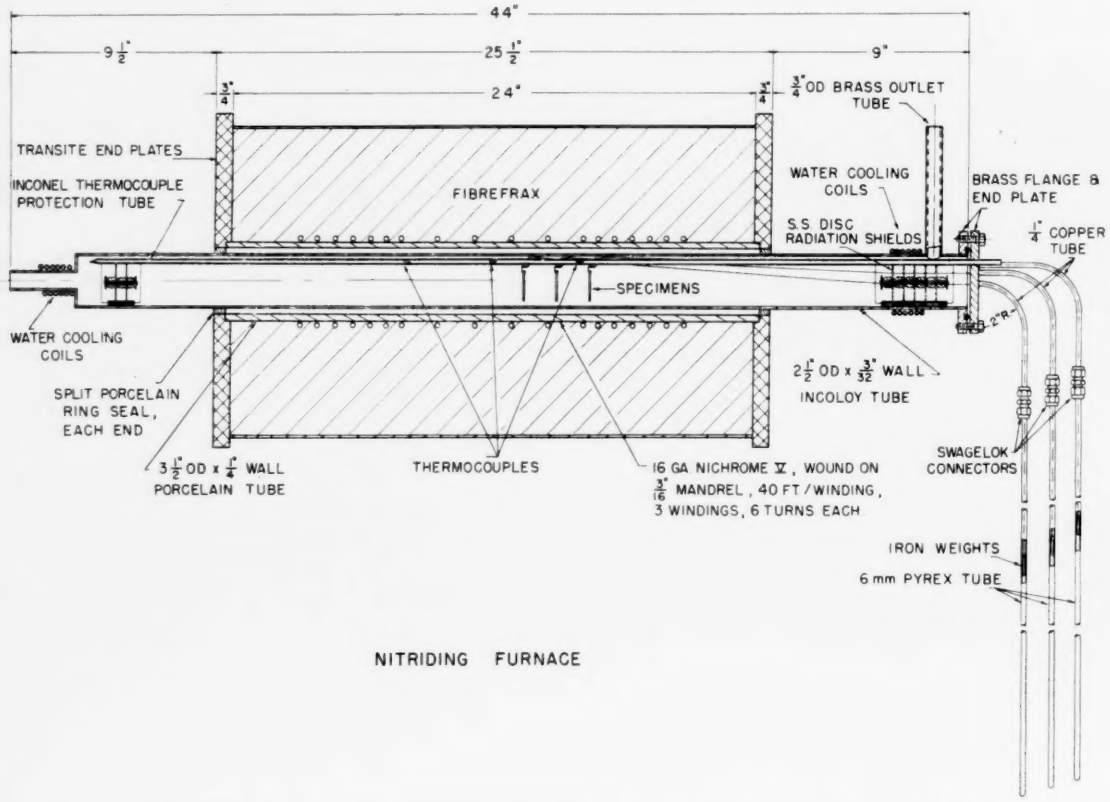

FIGURE 1. *Schematic diagram of apparatus for nitriding specimens for different lengths of time without opening chamber.*

was then rolled into the furnace after the latter was up to temperature. At the end of the prescribed time, the chamber was rolled out of the furnace and allowed to cool to room temperature before the atmosphere was turned off and the chamber opened.

4. Results and Discussion

4.1. Microstructure

The typical structures obtained in titanium and in 6Al-4V titanium alloy by nitriding in purified nitrogen are shown in figures 2 and 3, respectively. The immediately evident difference between the metal and the alloy, considering only the gross characteristics, is that the metal forms a uniformly thick case with a sharp line of demarcation between the case and the core, whereas the alloy exhibits elongated nitride grains penetrating as far as the center of the core, given sufficient time, and with the long axes at approximately 45 deg to the surface. These elongated grains are below the uniformly thick case but frequently exhibit apparently common grain boundaries with nitride grains of the surface layer. Also, many of these grains show evidence of having boundaries coherent with the cube planes of the

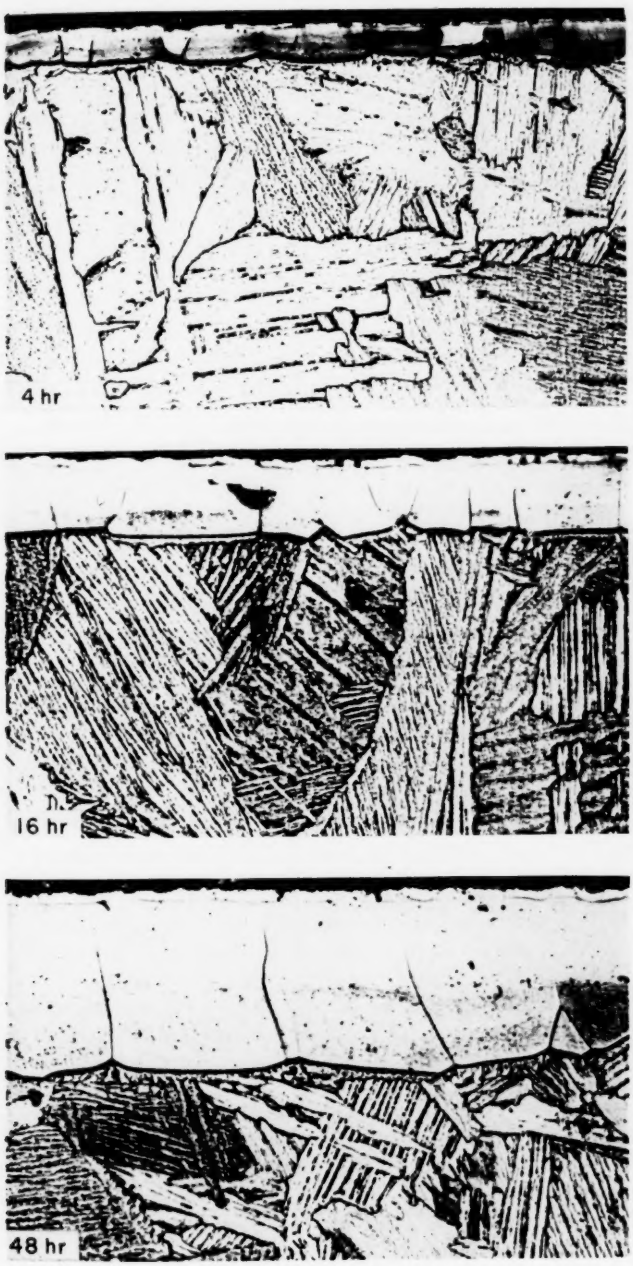

FIGURE 2. *Titanium nitrided in purified nitrogen at 1,800° F for the lengths of time indicated.*
Etched in 1 part HF (48%), 12 parts HNO_3 (conc), and 87 parts H_2O. × 200

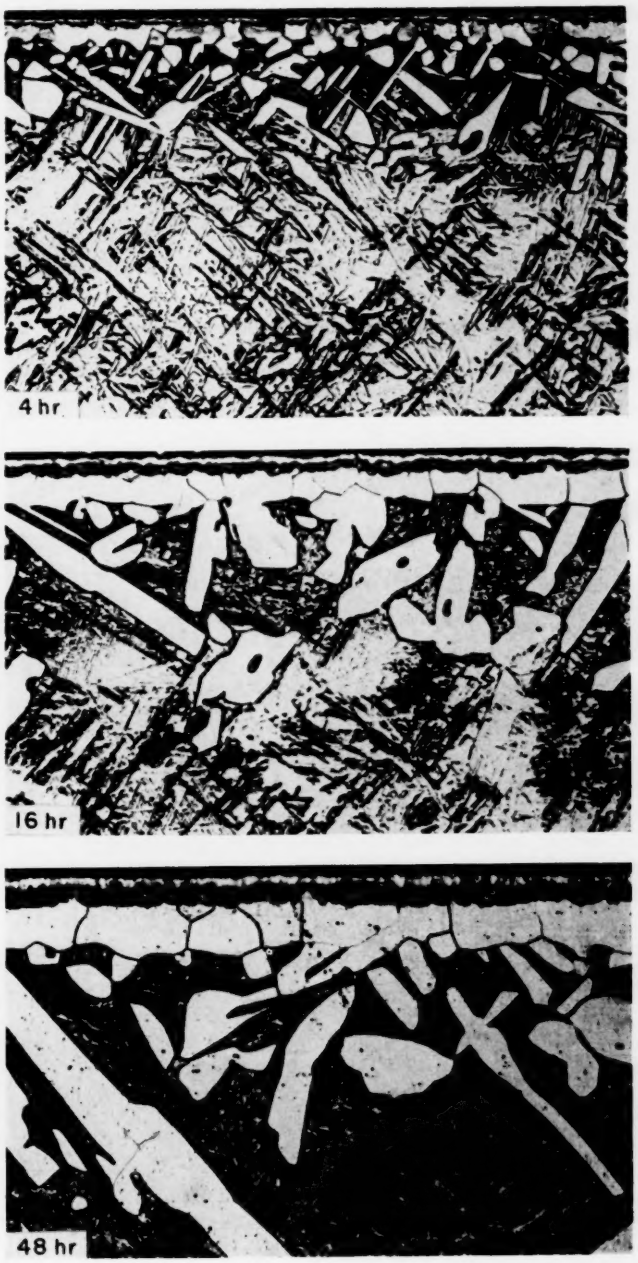

FIGURE 3. *6Al-4V titanium alloy nitrided in purified nitrogen at 1,800° F for the lengths of time indicated.*
Same etchant as for figure 2. × 200.

matrix. These elongated grains penetrating into the core might be expected to act as stress raisers and result in lower impact values. Preliminary results do indicate that nitriding has a more adverse effect on the impact properties of the alloy than of the unalloyed titanium.

The hardness of the surface film on both materials was equivalent to about Rockwell C 77, and decreased to approximately C 50 at the interface between the case and the core. The elongated grains in the alloy also exhibited hardnesses equivalent to about Rockwell C 50, in contrast to only about C 35 in the adjacent matrix.

Upon closer examination the "uniform case" on the unalloyed titanium (fig. 2) is seen to consist of a surface film covering a thicker or principal layer. This principal layer is approximately 0.004-in. thick and the surface film is about 0.0005-in. thick on specimens that have been nitrided for 48 hr. There is an abrupt change in etching characteristics at the middle of the layer. Nitriding for a longer time brings out a sharply defined transition band between the upper and lower halves of the layer, as may be seen in figure 4 which also shows a microhardness

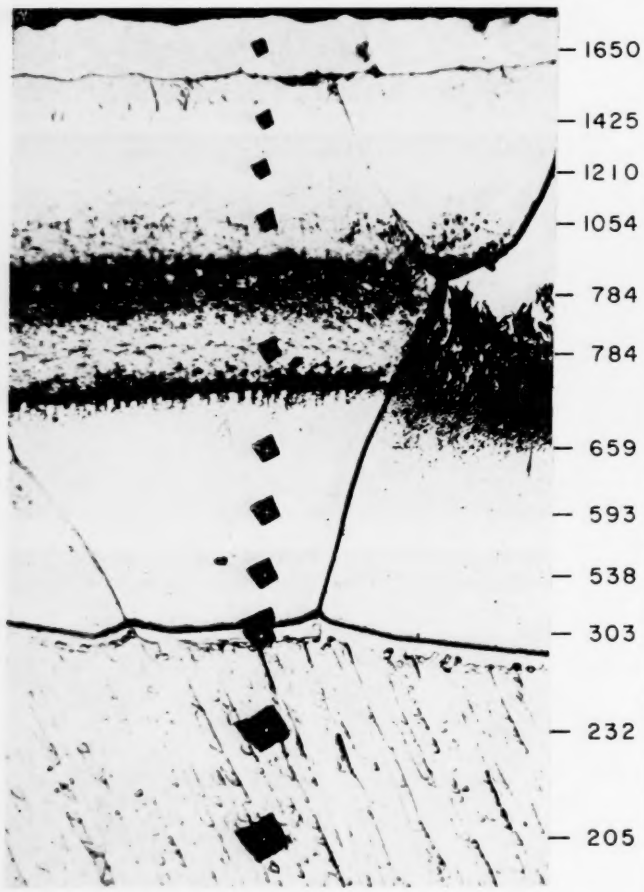

FIGURE 4. *Microstructure and Vickers microhardness indentation (50-g load), and corresponding Vickers hardness numbers, across the case on a titanium specimen nitrided 168 hr at 1,800° F in purified nitrogen.*

Hardness range corresponds to Rockwell C 77 to Rockwell C 12. Same etchant as for figure 2. × 350.

traverse across the case. The change in etching characteristics is not unexpected because the TiN structure is retained from the stoichiometric composition down to a deficiency in nitrogen corresponding to the composition, $TiN_{0.42}$[8]. It might be mentioned here that to retain the surface film on specimens prepared for metallographic examination, it was necessary to insert sheet plastic between the specimens before placing the pack of specimens in the mounting press for moulding in plastic in the conventional manner. Also, it was preferable that the polishing be done on a wax lap.

At the interface between the case and the core of the unalloyed titanium there is a "fringe" of each of the nitride grains of the case protruding over the prominent boundary of the case into the region of the core. That this fringe is actually an integral part of the respective grains of the case is revealed by polarized light, as will be seen by comparing the upper and lower photographs in figure 5. Polarized light (lower photograph) also reveals that the case is composed of grains of different orientations but generally with each grain extending completely through the principal layer of the case and including the "fringe" at the interface with the core. However, the thin surface film is seen to be composed of grains separate from those of the principal layer. Figure 6 is an interference pattern of the same region shown in figure 5, obtained with a Zeiss vertical interferometer microscope. The "fringe" of the "hour glass" shaped grain is revealed to be below the portion of the grain making up the principal layer. Note that the scratches, which are valleys in the specimen surface, provide a means of identifying which are high and which are low areas in the interferometer patterns.

Wyatt and Grant [3] concluded that a maximum case of approximately 0.004 in. was attained when unalloyed titanium was nitrided in ammonia. The time to produce this maximum was a function of the nitriding temperature. If nitriding were continued beyond the time required to produce the maximum thickness, the case was reported to actually decrease in thickness. They concluded that the mechanism responsible for the decrease in case thickness was the decomposition of the TiN structure at the interface between the case and the core and the nitrogen diffusing into the core at a faster rate than nitrogen diffused through the TiN case to form new case. However, in the present investigation, no evidence for a maximum was found. As shown in figure 7, the thickness of the nitrided case on titanium increased with an increase in time at 1,800° F; a thickness in excess of 0.008 in. was obtained by nitriding 168 hr. Also it is seen that the plotted points fall reasonably well on a straight line, which indicates that the increase in total case thickness with time is a parabolic relationship.

The growth of the elongated nitride grains into the matrix of the 6Al–4V titanium alloy at 45° with the surface in both directions (fig. 3), appears to be associated with the cube planes of a beta phase matrix at 1,800° F. With an electron-probe micro-

analyzer, vanadium content in these elongated nitride grains was found to be only one-half of that in the matrix. Furthermore, there was no observable vanadium composition gradient in the matrix in the immediate vicinity of the nitride grains. Determinations were made on 18 of the elongated nitride grains in a specimen which had been nitrided for 48 hr. On a sample of pure vanadium, 480 counts per second were recorded, and on a sample of pure titanium 66 cps were recorded when the Geiger counter was set on the $V_{K\alpha}$ wavelength. Correcting for this background, 22 to 24 cps were

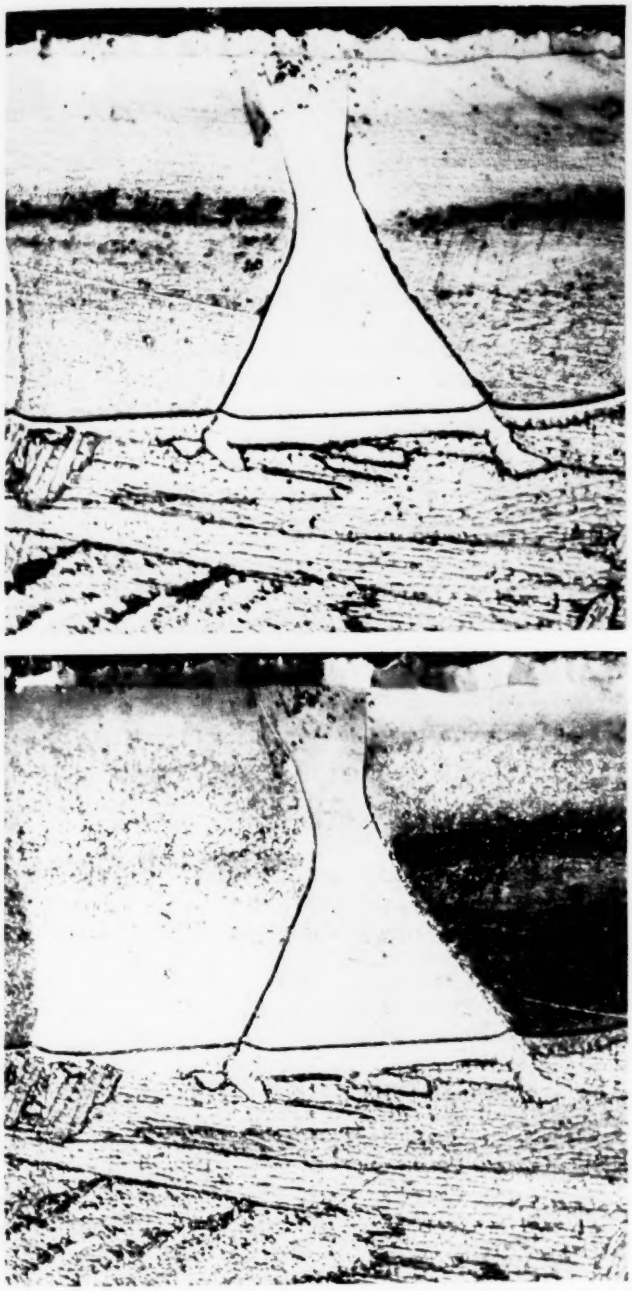

FIGURE 5. *Case and interface between case and core in titanium nitrided 48 hr at 1,800° F in purified nitrogen.*

Same etchant as for figure 2. × 500. Upper: white light. Lower: polarized light.

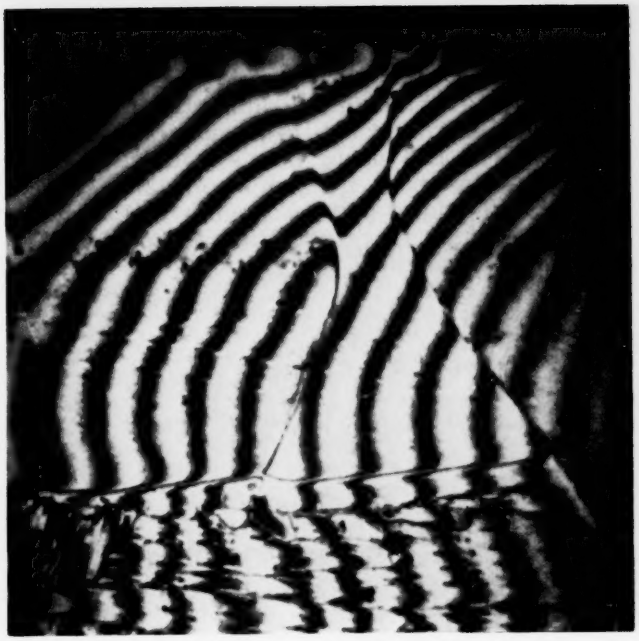

FIGURE 6. *Interference microscope pattern of same specimen as shown in figure 5.*

One fringe = 11.8×10^{-6} inch difference in elevation.

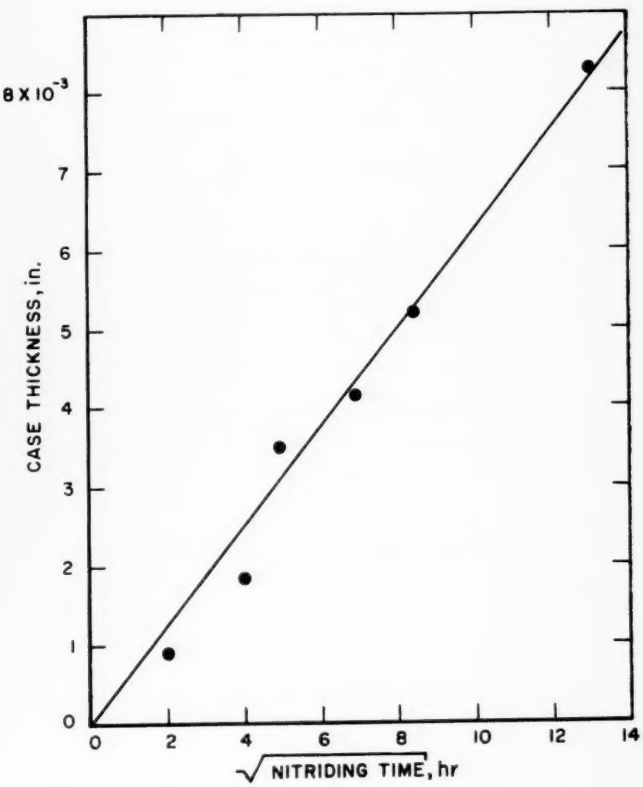

FIGURE 7. *Case thickness in titanium versus square root of nitriding time at 1,800° F.*

obtained recording the $V_{K\alpha}$ wavelength on the nitride grains and 44 to 48 cps on the matrix.

The growth of these elongated nitride grains is obviously a function of nitriding time. Nitrogen and aluminum are strong alpha stabilizers in titanium but vanadium is a strong beta stabilizer. The following calculation of equilibrium constants suggests that the aluminum plays a prominent role in the formation of the elongated nitride grains.

From Kubaschewski and Evans [9], the heats of formation, ΔF, are:

$$2V+N_2 \rightarrow 2(VN) \qquad \Delta F$$
$$= -83{,}300+39.7\ T \text{ cal/mole} \qquad \text{(a)}$$
$$= -33{,}500 \text{ cal/mole at } 982^\circ \text{ C } (1{,}800^\circ \text{ F}).$$

$$2Al+N_2 \rightarrow 2(AlN) \qquad \Delta F$$
$$= -121{,}000+44.5\ T \qquad \text{(b)}$$
$$= -65{,}200 \text{ cal/mole at } 982^\circ \text{ C } (1{,}800^\circ \text{ F}).$$

$$2Ti+N_2 \rightarrow 2(TiN) \qquad \Delta F$$
$$= -160{,}500+44.4\ T \qquad \text{(c)}$$
$$= -104{,}750 \text{ cal/mole at } 982^\circ \text{ C } (1{,}800^\circ \text{ F}).$$

However, to give a more realistic comparison, the data for aluminum and vanadium should be corrected for a 4 and a 6 percent solution, respectively, of aluminum and vanadium in titanium. As a "best approximation," in lieu of the necessary experimental data on these systems, an ideal solution is assumed and the free energy of dissolution for the corresponding atomic percent concentrations, i.e., 10.2 atomic percent aluminum in titanium, and 3.8 atomic percent vanadium in titanium, is computed from the relationship

$$\Delta F^M = RT \ln N$$

where,

ΔF^M = the free energy of mixing cal/mole of solute. The expression on the right is really the entropy of mixing but because the heat of solution is zero for an ideal solution, the entropy term constitutes the entire free energy.
R = the gas constant, 1.987 cal/mole/deg
T = the absolute temperature, ° K
N = mole fraction of solute

At 1,800° F, one obtains for,

$$Al \rightarrow [10.2 \text{ a/o Al}]_{Ti}, \quad \Delta F = -5{,}700 \text{ cal/mole}$$

and for,

$$V \rightarrow [3.8 \text{ a/o V}]_{Ti}, \quad \Delta F = -8{,}200 \text{ cal/mole.}$$

Combining these results with the values given for the original reactions, (a) and (b), gives

$$2[V]_{Ti}+N_2 \rightarrow 2(VN), \quad \Delta F = -17{,}100 \qquad \text{(a')}$$

$$2[Al]_{Ti}+N_2 \rightarrow 2(Al), \quad \Delta F = -53{,}800. \qquad \text{(b')}$$

Using the relationship between the free energy, ΔF, and the equilibrium constant, K,

$$\log K = -\frac{\Delta F}{2.30\ RT}.$$

The equilibrium constants for the formation of VN, AlN, and TiN, at 1,800° F, are,

$$\log K_{VN} = +\frac{17{,}100}{2.30\ RT} = 3.05$$

$$K_{VN} = 1 \times 10^3$$

$$\log K_{AlN} = +\frac{53{,}800}{2.303\ RT} = 9.37$$

$$K_{AlN} = 2.4 \times 10^9$$

$$\log K_{TiN} = +\frac{104{,}750}{2.303\ RT} = 18.22$$

$$K_{TiN} = 1.7 \times 10^{18}$$

These results imply that the nitrogen would combine preferentially with the aluminum in respect to vanadium, and support the experimental result that the aluminum must be largely responsible for the development of the elongated nitride grains which do not occur in the absence of both the aluminum and the vanadium. Furthermore, both the thermodynamic calculations and the electron probe results indicate that the vanadium is not responsible for the formation of these nitride grains. Obviously, a determination of the aluminum content of the elongated grains is needed to confirm or refute this conclusion. Such a determination will be made when a vacuum spectrometer-equipped electron probe, now under construction, becomes available.

4.2. X-Ray Diffraction Results

X-ray diffraction patterns were obtained of the surface of the titanium and 6Al-4V alloy before and after nitriding, and again after the nitride surface layer had been polished off.

Un-nitrided titanium exhibited the expected alpha titanium pattern except that the (002) reflection was equally as intense as the (011), the most intense line as reported in the ASTM Index. This is probably due to preferred orientation as a result of rolling. The pattern from the nitrided surface revealed the expected TiN pattern, except that the most intense line was also the (002) reflection instead of the (220) reflection as given in the ASTM Index, and also an extra line corresponding to a "d" spacing of 1.52 A. This was the most intense line in the diagram. After polishing off most of the nitride layer, this extra line had not diminished in intensity although the TiN had been reduced drastically and the alpha titanium pattern was beginning to appear.

The alloy, before nitriding, exhibited the expected titanium "d" spacings, but the relative intensities

differ appreciably from those normally expected from the pure alpha titanium pattern. There was no indication of beta phase. The extra line corresponding to a "d" spacing of 1.52 A occurred also in the pattern of the nitrided alloy surface and in the pattern of the alloy after the nitrided surface had been polished off.

5. Summary and Conclusions

Nitriding of unalloyed titanium in purified nitrogen produced a sharply defined and uniformly thick case which increased in thickness with increase in nitriding time and apparently would continue to increase without limit. Five distinct zones could be identified. There is no evidence of a maximum case thickness being reached followed by a decrease in case thickness with continued nitriding, as reported by other investigators who nitrided titanium in ammonia.

The same treatment applied to a 6Al-4V alloy of titanium resulted in a thinner nitride case that consisted of three zones and in elongated nitride grains that penetrated into the core at approximately 45° with the surface of the specimen in both directions. The aluminum is indicated to be primarily responsible for the formation of the elongated nitride grains.

The elongated nitride grains, penetrating into the core of the alloy at 45 deg to the surface, apparently act as stress raisers causing a significant reduction in the impact strength of the 6Al-4V alloy.

6. References

1] J. L. Wyatt and N. J. Grant, Nitriding improves titanium properties, Iron Age, pp. 124 to 127 (Jan. 28, 1954).

[2] A. J. Griest, P. E. Moorehead, P. D. Frost, and J. H. Jackson, Surface hardening of titanium by carburizing and induction heat treatment, ASM Trans. **46,** 257 (1954).

[3] J. L. Wyatt and N. J. Grant, Nitriding of titanium with ammonia, ASM Trans. **46,** 540 (1954).

[4] J. L. Wyatt and N. J. Grant, Nitriding produces better hard case on titanium, Iron Age, p. 112 (Jan. 14, 1954).

[5] R. W. Hanzel and V. Pulsifer, Surface hardening of titanium with metalloid elements, June 1, 1952, to May 31, 1953 Rept. (Armour Research Foundation to Watertown Arsenal on Contract No. DA–11–022–ORD–289).

[6] E. L. White, P. D. Miller, and R. S. Peoples, Antigalling coatings and fabricants for titanium, Battelle TML Rept. No. 34, p. 10 (Feb. 24, 1956).

[7] Metals Handbook, 1954 Suppl., Am. Soc. Metals, p. 83 (1954).

[8] P. Ehrlich, Z. Anorg. Chem. **259,** 1 (1949).

[9] O. Kubaschewski and E. LL. Evans, Metallurgical Thermochemistry (John Wiley & Sons, New York, N.Y., 1956).

WASHINGTON, D.C. (PAPER 64A1–33)

JOURNAL OF RESEARCH of the National Bureau of Standards—A. Physics and Chemistry
Vol. 64A, No. 1, January–February 1960

Stability of Silver and Pyrex in Perchloric Acid–Silver Perchlorate Solutions and in Conductivity Water

D. Norman Craig, Catherine A. Law, and Walter J. Hamer

(September 28, 1959)

The stability of mint silver, purified mint silver, and Pyrex fritted crucibles in aqueous solutions of perchloric acid, in aqueous solutions of perchloric acid containing silver perchlorate, and in conductivity water at room temperature was determined. The stability of the silver in various states of subdivision was studied. The corrosion current-density for mint silver in sheet form is 1.1×10^{-8} amp cm^{-2} for 20 percent aqueous solutions of perchloric acid, 1.3×10^{-9} amp cm^{-2} for 20 percent aqueous solutions of perchloric acid containing 0.5 percent silver perchlorate, and within the limits of detection is zero for conductivity water. Pyrex has high stability at 25° C in 20 percent aqueous solutions of perchloric acid and in 20 percent aqueous solutions of perchloric acid containing 0.5 percent silver perchlorate. Finely-divided silver contained in Pyrex crucibles was found to be highly stable when the crucibles were filled repeatedly with aqueous solutions of perchloric acid containing silver perchlorate, rinsed with conductivity water, and dried at 105° C. These observations are important in the determination of the faraday by the anodic dissolution of silver in aqueous solutions of perchloric acid which is now underway at the National Bureau of Standards.

1. Introduction

As part of a program for the determination of the faraday at the National Bureau of Standards by anodic dissolution of metallic silver in aqueous solutions of perchloric acid it is essential to know the extent and rate of solution or the stability of silver at room temperature in: (1) Aqueous solutions of perchloric acid, (2) aqueous solutions of perchloric acid containing silver perchlorate, and (3) conductivity water. Obviously metallic silver should not dissolve or otherwise react with perchloric acid solutions at a significant rate if the anodic dissolution of silver in aqueous solutions of perchloric acid or of perchloric acid-silver perchlorate is to be used in accurate determinations of the faraday; otherwise the loss in weight of the silver cannot be correlated accurately with the quantity of electricity passed through the coulometer. Thermodynamic data [1, 2][1] show that silver does not undergo chemical reaction with perchloric acid; the free energy change for the postulated reaction is positive and, therefore not a spontaneous one. However, thermodynamically, silver may dissolve in perchloric acid solutions containing oxygen or go into solution as a result of galvanic corrosion arising from local anodic and cathodic areas on the silver surface or by "air-line" corrosion in such solutions. Therefore it is important to study the rates of these reactions in order to establish their effect on the accuracy of the faraday determinations by the proposed method.

During a coulometric run silver is anodically dissolved and silver perchlorate is formed. Therefore, the stability of silver in solutions of perchloric acid containing silver perchlorate must be determined. Furthermore, at the end of a coulometric run the silver anode which remains undissolved must be washed free of coulometric solution with conductivity water, dried, and weighed. Accordingly, the solubility or stability of silver in conductivity water must also be determined.

During the anodic dissolution of silver in perchloric acid it has been observed that a small amount of silver invariably falls from the anode to the bottom of the coulometer vessel (Pyrex beaker). This dislodged silver (or sediment), identified as silver by spectroscopic analysis, must be collected, washed free of coulometric solution with conductivity water, dried, and weighed in suitable crucibles. Pyrex fritted-crucibles are used for this purpose. Obviously, then, it is also necessary to determine the effect of perchloric acid, perchloric acid-silver perchlorate solutions, and conductivity water on the stability of the crucibles.

It is the purpose of this paper to present data on the stability of silver in various states of subdivision and of Pyrex in aqueous solutions of perchloric acid (20 wt %), in aqueous solutions of perchloric acid (20 wt %) containing silver perchlorate (0.5 wt %), and in conductivity water at room temperature. Changes in the combined mass of a Pyrex crucible and finely-divided silver during reheating at 105° C and during rewashing and redrying at 105° C are also presented.

2. Materials

Mint silver in rolled sheet form obtained from the United States Mint in Philadelphia, Pa., and purified mint silver in rod form were used in these experiments. The purified silver was prepared from mint silver by electrolytic transport in acidified silver-nitrate solution; the purified silver collected at the cathode was leached first in hydrofluoric acid, then

[1] Figures in brackets indicate the literature references at the end of this paper.

in conductivity water. It was dried in a silver dish and fused in quartz tubes. The resulting silver rods were soaked in hydrofluoric acid to remove any surface layer of silica. Spectroscopic analysis showed the mint silver contained less than 10-ppm total metallic impurities and similar analysis showed the purified rods contained less than 1-ppm total metallic impurity.

The perchloric acid was reagent grade. Solutions of the desired concentration were made by dilution with conductivity water having a conductivity of 0.6 to 1.0×10^{-6} (ohm cm)$^{-1}$ at room temperature. The conductivity water was produced in a conductivity still wherein one third of the condensate is collected; the feed was distilled water treated with alkaline permanganate. The silver perchlorate used in some of the solutions was prepared from reagent grade silver oxide and perchloric acid solution. The perchloric acid-silver perchlorate solutions were always filtered before using them.

The Pyrex crucibles used to collect the finely-divided silver as well as the Pyrex breakers used in the experiments were soaked in nitric acid solutions and thoroughly rinsed with conductivity water before using them. Both the inside and the outside of the glassware were cleaned. The crucibles had a capacity of 17 ml and an inner surface area of 28 cm^2, exclusive of the glass frit the diameter of which was 1.8 cm.

3. Procedure

Unless otherwise noted the silver was weighed, immersed in the respective solutions for specified time intervals, removed, washed with conductivity water, dried at 105° C, and reweighed. Heating at 105° C was at times repeated. A plastic-paneled cabinet in a room free of fumes was used to protect the silver and the solutions from dust.

A semi-microbalance was used in the weighings involving unpurified mint silver. A microbalance was used in the weighings involving purified mint silver. The weighings were made by double transposition, with sensitivity measurements interspersed, in a temperature-controlled room maintained at 25±1° C and with a relative humidity of always less than 50 percent. The balances were supported on an Alberene slab anchored to a wall of the laboratory. All weighings were corrected for buoyancy using the density of the weights, the prevailing density of air, 10.50 as the density of silver, and 2.245 as the density of Pyrex. The weights were calibrated by the Mass and Scale Section of the National Bureau of Standards and were used periodically to check the performance of the balances.

4. Results

4.1. Stability of Silver in Aqueous Solutions of 20 Percent Perchloric Acid

Sheets of mint silver, about 0.03 cm in thickness and 100 cm^2 in surface area were used in these studies. The sheets were only 60 percent immersed in the solution with 40 percent above the solution in order to include air-line corrosion if it occurred (the silver is used in this fashion in the coulometer, i.e., part of the silver protrudes into the coulometer solution). Each time the silver was reimmersed in the solution that part previously exposed to air was immersed. Results of these studies are given in table 1.

TABLE 1. *Stability of mint silver at 25° C in 20 percent aqueous solutions of perchloric acid*

Time [a]	True mass in a vacuum	Total change in mass	Rate of change in mass	
Hours	*Grams*	*μg*	*μg/hour*	*(μg/hr)/cm²*
0	14.139731			
25.5	14.139662	−69	2.7	0.045
72.0	14.139531	−200	2.8	.047
125.5	14.139444	−287	2.3	.038
241.5	14.139363	−368	1.5	.025
387.0	14.139278	−463	1.2	.020
504.0	14.139248	−483	0.96	.016
895.0	14.139151	−580	.65	.011
898.0	14.139172	−559	.62	.010

[a] Time of immersion of silver in the solution.

These data show that mint silver is quite stable in 20 percent aqueous solutions of perchloric acid and that the rate of corrosion does not proceed at a constant rate but decreases with time as the Ag^+ content of the solution increases (see curve A of fig. 1). The initial corrosion current per cm^2 of surface

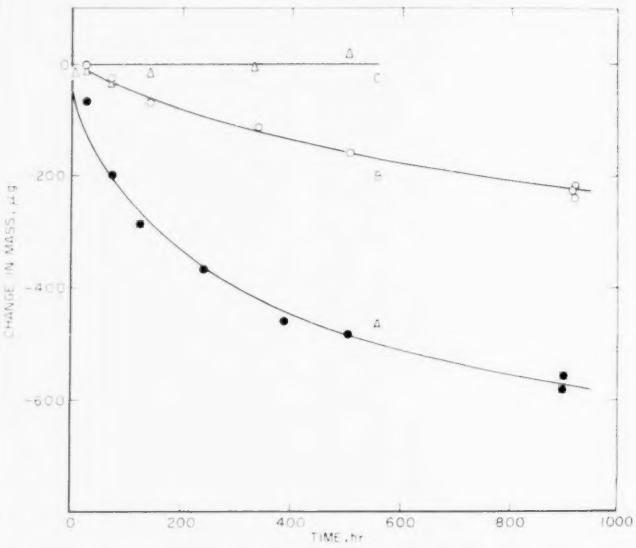

FIGURE 1. *Stability of mint silver in sheet form at room temperature: in 20 wt percent of* $HClO_4$ (A), *in 20 wt percent* $HClO_4$ *containing 0.5 wt percent of* $AgClO_4$ (B), *and in conductivity water* (C).

area for mint silver in 20 percent perchloric acid at 25° C is 1.1×10^{-8} amp and decreases with time to 2.5×10^{-9} amp, or lower (see later), as the Ag^+ content of the solution increases. Thus, for 1 cm^2 of surface area only 40 microcoulombs of electricity would be dissipated per hour for mint silver in 20 percent perchloric acid and only 9 microcoulombs or less per hour (see later) for 20 percent perchloric acid containing minute quantities of Ag^+ ion (see curve

A of fig. 2). Since faraday determinations have shown that silver is readily dissolved anodically at rates higher than 360 coulombs per cm^2 of silver surface per hour, even the higher corrosion current viz. 40 microcoulombs per hour for a solution containing minute quantities of Ag^+ introduces an uncertainty of about 1 part in 10^7, or 0.1 ppm.

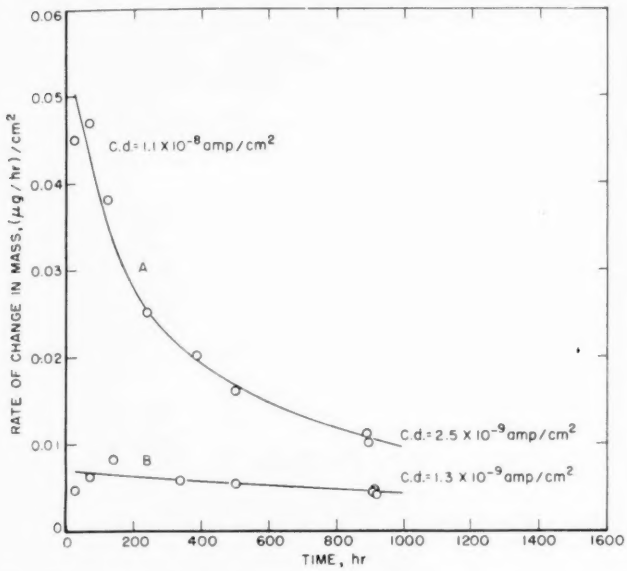

FIGURE 2. *Rate of change in mass of mint silver in sheet form at room temperature: in 20 wt percent of* $HClO_4$ (A) *and in 20 wt percent of* $HClO_4$ *containing 0.5 wt percent of* $AgClO_4$ (B).

4.2. Stability of Silver in Aqueous Solutions of 20 Percent Perchloric Acid Containing 0.5 Percent Silver Perchlorate

Sheets of mint silver, 0.03 cm in thickness and 100 cm^2 in surface area and rods (or anodes) of purified mint silver (estimated dimensional surface area ranged from 5 to 11.4 cm^2) were used in these experiments. The sheets of mint silver were 60 percent immersed in the solutions, as above, whereas in most cases the rods were completely immersed. Results for mint silver are given in table 2. These data again show that the presence of silver ions in small amount curtails the rate of corrosion of silver in aqueous solutions of $HClO_4$ (see curve B of fig. 1). The apparent increase in weight during the first 3½ hr, shown in table 2, is inconsistent with other observations. Neglecting this value and starting with the second it may be seen that the loss in weight per hour is nearly constant, although a slight decrease in rate is still evident. The average rate is 0.33 μg/hr or (0.0054 μg/hr)/cm^2 of surface area (see curve B of fig. 2).

Results for purified mint silver in the form of rods are given in table 3. The average loss in (mass/hour)/cm^2 for these samples, excluding the first value which is abnormally high, is 1.7 times that for the average of the values given in table 2 for mint silver in the form of sheets. It can be seen in table 3 that the changes in mass of the silver rods or anodes are nevertheless extremely small and that for the experiments involving long immersion of the samples the changes in (mass/hour)/cm^2 is nearly the same as that for the sheet silver. The values of change, (mass/hour)/cm^2, in table 3 calculated for short periods of immersion magnify any small uncertainty in the determination of the mass of the silver. Even the first and abnor-

TABLE 2. *Stability of mint silver at 25° C in aqueous solutions containing 20 percent perchloric acid and 0.5 percent silver perchlorate*

Time[a]	True mass in a vacuum	Total change in mass	Rate of change in mass	
Hours	*Grams*	*μg*	*μg/hour*	*(μg/hr)/cm²*
0	13.848807			
3.5	13.848845	+38[b]	[b]	[b]
24.5	13.848838	−7	0.33	0.0055
71.0	13.848819	−26	.38	.0063
141.5	13.848776	−69	.50	.0083
339.0	13.848731	−114	.34	.0057
504.5	13.848685	−160	.32	.0053
912.5	13.848617	−228	.25	.0042
915.0	13.848611	−234	.26	.0043
917.0	13.848625	−220	.24	.0040
Average			0.33	0.0054

[a] Time of immersion of silver in the solution.
[b] See context.

TABLE 3. *Stability of purified mint silver at 25° C in aqueous solutions containing 20 percent perchloric acid and 0.5 percent silver perchlorate*

Time[a]	Initial mass in a vacuum	Final mass in a vacuum	Estimated surface area	Change in mass	Rate of change in mass	
Anode No. 1						
Hours	*Grams*	*Grams*	*cm²*	*μg*	*μg/hr*	*(μg/hr)/cm²*
3	13.657300	13.657289	8.6	−11	−3.70	−0.43
46	9.542583	9.542576	6.3	−7	−0.15	−.024
49	5.833381	5.833374	5.0	−7	−.14	−.028
65	5.833374	5.833363	5.0	−11	−.17	−.034
17	5.833373	5.833368	5.0	−5	−.29	−.058
Average					−0.19	−0.036[b]
Anode No. 2						
65	20.483577	20.483569	11.4	−8	−0.12	−0.010
94	16.377775	16.377773	9.3	−2	−.02	−.002
94	12.274162	12.274163	7.3	+1	+.01	+.001
330	8.174357	8.174357	6.6	0	.000	.000
787	8.174074	8.174044	6.6	−30	−.04	−.006
Average					−0.04	−0.004
Anode No. 4						
259	7.487765	7.487762	6.0	−3	−0.01	−0.005
907	7.487762	7.487685	6.0	−77	−.08	−.013
Average					−0.04	−0.009
Anode No. 5						
13	20.069326	20.069335	11.2	+9	+0.69	+0.062
3,550	11.256877	11.256821	6.8	−56	−0.016	−0.002
Average					+0.33	
Average of all						−0.039
Average omitting the first						−0.009
Average of those above 200 hr						−0.0052

[a] Time of immersion of silver in the solution.
[b] Omit first value.

mally high value of (0.43 μg/hour)/cm² given in this table would cause an error of only 1 in 10^6 for a faraday determination if a current density as low as 0.1 amp/cm² were used, neglecting the fact that in a determination the Ag^+ ion concentration would increase rapidly after electrolysis was started.

4.3. Stability of Silver in Conductivity Water

Sheets of mint silver about 0.03-cm thick and 100-cm² in surface area and rods of purified mint silver (anodes no. 1 and no. 2) were used in these experiments. Again the sheets were 60 percent immersed in the water whereas the rods were completely immersed. The data of table 4 show that the mint

TABLE 4. *Stability of mint silver in conductivity water at room temperature (immersed area 60 cm²)*

Time [a]	True mass in a vacuum	Deviations from average mass	Rate of change in mass	
Hours	*Grams*	*μg*	*μg/hour*	*(μg/hr)/cm²*
0	14.139733	+9		
4.0	14.139718	−6	−3.75	−0.062
24.0	14.139723	−1	−0.04	<−.001
73.0	14.139700	−24	−.45	−.008
141.5	14.139718	−6	−.11	−.002
332.0	14.139728	+4	−.02	<−.001
502.5	14.139749	+25	+.03	<+.001

Average ±10
Average mass = 14.139724 g
Standard deviation of mean = 5.7 μg

[a] Time of immersion of silver in water.

silver in sheet form is practically inert in conductivity water at 25° C. The changes in weight are random; the average spread in values is only 10 μg in 14 g, or less than 1 ppm. The standard deviation of the individual observations is 15.1 μg; the standard deviation of the mean is 5.7 μg. The data in table 5 for several samples of purified mint silver likewise show that silver is inert in conductivity water, and therefore the washing of the silver in conductivity water should cause no significant error in the determination of the faraday by the proposed method.

Figure 1 shows the stability of mint silver in sheet form, in perchloric acid (curve A), in perchloric acid-silver perchlorate (curve B), and in conductivity water (curve C). It is evident that mint silver exhibits high stability in conductivity water and in perchloric acid solutions, especially those containing silver perchlorate.

TABLE 5. *Stability of purified mint silver in conductivity water at room temperature*

Time [a]	Initial mass in a vacuum	Final mass in a vacuum	Estimated surface area	Rate of change in mass	
Anode No. 1					
Hours	*Grams*	*Grams*	*cm²*	*μg/hr*	*(μg/hr)/cm²*
18	9.542576	9.542565	6.3	−0.61	−0.097
22	5.833363	5.833374	5.0	+.50	+.100
75	5.833374	5.833373	5.0	−.01	−.002
Anode No. 2					
236	8.174357	8.174354	6.6	−0.01	−0.002
21	8.174343	8.174342	6.6	−.05	−.007
16	8.174342	8.174348	6.6	+.37	+.057
16	8.174077	8.174061	6.6	−1.00	−.151

[a] Time of immersion of silver in water.

4.4. Stability of Finely-Divided Silver in Aqueous Solutions Containing 20 Percent Perchloric Acid and 0.5 Percent Silver Perchlorate

In section 4.2 it was shown that silver in sheet or rod form is highly stable in aqueous solutions containing 20 percent perchloric acid and 0.5 percent silver perchlorate. In this section data are given on the stability of finely-divided silver in a similar solution. The finely-divided silver used was that which is produced in a coulometer during a coulometric run, i.e., the sediment that falls from the anode during anodic dissolution; no attempt was made to measure the state of subdivision of the silver (see later). The finely-divided silver was collected in Pyrex fritted-crucibles of 17-ml capacity. The crucibles were then filled with 12 to 14 ml of solution, placed in the cabinet, and allowed to stand at room temperature for specified times. The solution was then drawn from the crucibles by suction and the crucibles dried at 105° C to constant weight. Since the changes in weight may have arisen not only from the solubility of the silver but also from the solubility of the crucible in the perchloric acid-silver perchlorate solutions the latter was also determined. As noted in the next section the crucibles lose weight at the rate of 0.5 μg per hour in the perchloric acid-silver perchlorate solutions. Using this rate the results given in table 6 were obtained.

The data of table 6 show that, on a weight basis, finely divided silver is considerably more soluble or less stable than the bulk silver in sheet or rod form. This fact is to be expected since finely-divided silver, on a weight basis, has a much greater surface area than the bulk silver. Using the data obtained for the rate of solution of sheet silver, micrograms per hour (table 2) as a basis, the surface area of the sediment or finely-divided silver formed from sheet silver was calculated to be about twice that of the sheet silver and the sediment formed from purified silver rods from 100 to 900 times that of the sheet silver. Visual inspection also showed that sediment from sheet silver was much less finely-divided than sediment from the purified rods. However, in the faraday determinations that have been made it has been found that the weight of the sediment from the corrosion of a given weight of the purified rods or anodes is about 1/20 that of the sediment from sheet silver.

In the faraday determinations filtering of the sediment is finished within 2 hours after the end of electrolysis. The data in table 6 show that the maximum loss in weight of the sediment from purified anodes is 1.38 ug/hr. This would cause an error no greater than 2.5 ppm for a 5-hr run at 0.2 amp. The data presented thus far for finely-divided silver relates to its solubility or stability after is has been collected

TABLE 6. *Stability of finely-divided silver at 25° C in aqueous solutions containing 20 percent perchloric acid and 0.5 percent silver perchlorate*

Time [a]	Initial mass of silver, in a vacuum	Final mass of silver, in a vacuum	Change in mass (assumed to be silver)	Change in mass (corrected for solubility of crucible)	Rate of change in mass of silver	
Mint Silver						
Hours	*Grams*	*Grams*	*μg*	*μg*	*μg/hour*	*(μg/hr)/cm² [b]*
285	2.384495	2.384309	−186	−43	0.15	0.0087
325	2.165701	2.165476	−225	−62	.19	.012
Purified Mint Silver Sample No. 1						
19	0.038370	0.038335	−35	−25	1.32	4.77
40	.038335	.038301	−34	−14	0.45	1.62
Sample No. 2						
146	0.064493	0.064218	−275	−202	1.38	2.96
71	.064201	.064144	−57	−21	0.29	0.62
Sample No. 3						
60	0.068271	0.068200	−71	−41	0.68	1.38
Sample No. 4						
309	0.069862	0.069524	−338	−183	0.59	1.17
Sample No. 5						
13	0.070480	0.070456	−24	−17	1.31	2.57
16	.071283	.071260	−23	−15	0.94	1.82
Sample No. 6						
20	0.071937	0.071912	−25	−15	0.75	1.44

[a] Time solution was in crucible.
[b] Calculated by assuming area was a weight percent of area of sheet silver per gram (7.22 cm² per gram).

in a Pyrex crucible at the end of a number of faraday determinations. However, the question arises whether some of the sediment as it is formed at the anode during a faraday determination exists in an even finer state of subdivision than the sediment collected in the crucible and accordingly may have not only a greater rate of solubility than that collected in the crucible but may be also collodial and some of it transported from the anode chamber by electrophoresis. The latter question was investigated after a number of faraday determinations by filtering the solution in the beaker adjacent to and connected with the anode compartment by a syphon. In no case was a significant change in weight of the crucible found showing that migration of silver particles from the anode compartment does not occur, even though the rate of filtering was slower for successive runs owing to the closing of the pores of the frit by the accumulation of finely-divided silver.

In the process of corroding silver anodically for a faraday determination there is the possibility that some silver is formed in an extremely finely-divided and very reactive state which, because of its increased solubility, may not be collected in the crucible at the end of the run. Evidence that this does not occur and therefore does not introduce a significant error consists in the agreement between the values of the faraday obtained for runs in which the amount of the finely-divided silver collected varied widely and for runs in which the current density was also varied widely. Examination of the results obtained in the runs made, shows no evidence that this is a source of significant error in the experimental procedure.

4.5. Stability of a Pyrex Crucible Containing Finely-Divided Purified Mint Silver and Conductivity Water

After filtering the sediment at the end of faraday determinations it is of course necessary to wash the crucible containing the collected silver. Although this requires only a relatively short time, nevertheless tests were made to determine the effect of conductivity water on the mass of the crucible containing finely-divided silver that fell from purified anodes during several faraday determinations. In these tests the crucible containing the finely-divided silver was about two-thirds filled with conductivity water and allowed to stand for varying periods. The water was then withdrawn by suction and the crucible and silver washed with an additional 100 ml of conductivity water, dried at 105° C and weighed. The results of these tests are given in table 7. Since the weight of the crucible was very nearly that of the tare the weights in columns 2 and 3 are very nearly those of the finely-divided silver. These results show that the mass of the crucible and the contained silver is not changed by conductivity water even over prolonged periods of time.

TABLE 7. *Stability of a Pyrex crucible containing finely-divided purified mint silver in conductivity water*

Time [a]	Initial mass of crucible and silver in a vacuum	Final mass of crucible and silver in a vacuum	Change in mass (assumed to be silver)
Sample No. 1			
Hours	*Tare plus grams*	*Tare plus grams*	Micrograms
16	0.038301	0.038307	+6
16	.038307	.038329	+22
Sample No. 2			
45	0.064218	0.064201	−17
Sample No. 3			
60	0.068265	0.068271	+6

[a] Time water was in crucible.

4.6. Stability of a Pyrex Crucible in Aqueous Solutions of Perchloric Acid

A Pyrex crucible of known weight was two-thirds filled with a 20 percent perchloric acid solution or a 20 percent perchloric acid solution containing 0.5

percent silver perchlorate, allowed to stand at room temperature for a week or more in the cabinet, the solution was then withdrawn by suction and the crucible washed with 100 to 150 ml of conductivity water, and dried at 105° C, and reweighed. The pertinent data are given in table 8, and show that Pyrex crucibles are quite stable in perchloric acid and perchloric acid-silver perchlorate solutions at room temperature. For perchloric acid solutions the average loss in weight is 0.07 μg/hr while for perchloric acid-silver perchlorate solutions the loss for a single observation is somewhat higher but probably not significantly so. The latter value, however, was used for the corrections made in table 6, mentioned above.

Since the filtering process at the end of a faraday determination does not require 2 hr even the largest value in table 8 for the loss in weight per hour, viz, 0.54 μg, would not introduce an error for a 4-g run greater than 0.25 ppm in the value of the faraday. Wichers, Finn, and Clabaugh [3] have made comparative tests of the effects of various reagents on chemical glassware. In those tests they found that Pyrex is extremely resistant to attack by 60 percent perchloric acid solutions at the boiling point and somewhat less resistant to attack by distilled water at 100° C. Even if the surface area of the frit in the crucible were known, other differences in the experimental conditions employed by the above authors from those employed in the present work preclude the possibility of making strict comparisons of their results with those given in table 8. Although we are primarily concerned with the stability of the fritted crucible under the conditions prevailing in the faraday determinations it is, nevertheless, significant that the above authors found Pyrex to be highly resistant to 60 percent perchloric acid solutions and also to distilled water.

TABLE 8. *Stability of a Pyrex crucible in aqueous solutions of perchloric acid (20%) with or without silver perchlorate (0.5%)*

Time[a]	Initial mass of crucible in a vacuum	Final mass of crucible in a vacuum	Change in mass per day	Change in mass per hour
		Perchloric Acid-Silver Perchlorate		
Days	*Grams*	*Grams*	*μg/day*	*μg/hour*
7	11.329483	11.329393	−12.9	−0.54
		Perchloric Acid		
15	11.329393	11.329438	+3.0	+0.13
25	11.329438	11.329344	−3.8	−.16
15	11.329344	11.329280	−4.3	−.18

[a] Time solution was in crucible.

4.7. Changes in Mass of a Pyrex Crucible Containing Finely-Divided Silver During Reheating at 105° C and During Rewashing and Redrying at 105° C

In the foregoing sections the stability of a Pyrex crucible and the stability of bulk and finely-divided silver in perchloric acid and perchloric acid-silver perchlorate solutions and in conductivity water was considered. In the experiments with finely-divided silver the silver was collected in Pyrex crucibles, washed free of perchloric acid or perchloric acid-silver perchlorate solutions with conductivity water and dried at 105° C. The question arises whether reheating or rewashing and redrying at 105° C cause any significant change in the combined mass of the crucible and the finely-divided silver. Therefore, in a series of faraday determinations the finely-divided silver that fell from the corroding anodes was transferred from the anode vessel and collected by filtration in a Pyrex crucible of known weight. The silver anode was then suspended in the anode beaker and rinsed repeatedly with separate portions of conductivity water. Each portion of water and any silver that fell from the anode during this washing procedure were transferred to the crucible. The anode was then suspended in an oven and dried at 105° C for 1 hr. The crucible was finally washed with an additional portion of water and dried for 2 hr at 105° C. The silver anode and the crucible were then reweighed separately and the above washing procedure was repeated using 100 ml of conductivity water after which the silver anode and the crucible were again dried and weighed.

The data for the crucible and the finely-divided silver obtained in these operations are given in table 9. The changes in mass are shown in the bottom portion of the table. The maximum change in mass is −15 μg for reheating and +43 μg for rewashing and redrying. For a faraday determination in which 4 g of silver are corroded these changes are 4 and 11

TABLE 9. *Stability of a Pyrex crucible containing finely-divided silver during reheating at 105° C and during rewashing and redrying at 105° C*

Time [a]	Mass of crucible and silver in a vacuum (before run)	Mass of crucible and silver in a vacuum (after run and one heating)	Mass of crucible and silver in a vacuum (after reheat)	Mass of crucible and silver in a vacuum (after rewashing and redrying)
		Masses		
Hours	*Grams*	*Grams*	*Grams*	*Grams*
0	13.314242	13.380023	13.380010	13.380029
48	13.380053	13.494553	13.494556	13.494542
432	13.494369	13.572640	13.572634	13.572619
48	13.572619	13.607940	13.607931	13.607932
120	13.608002	13.644927	13.644926	13.644925
72	13.644966	13.713368	13.713353	13.713379
456	13.713243	13.765658	13.765661	13.765704
		Changes in Mass		
Hours		*Grams*	*Micrograms*	*Micrograms*
0		0.065781	−13	+19
48		.114500	+3	−14
432		.078271	−6	−15
48		.035321	−9	+1
120		.036925	−1	−1
72		.068402	−15	+26
456		.052415	+3	+43
Average			−5	+8

[a] Time between coulometric runs.

ppm, respectively. The average change is -5 μg for reheating and $+8$ μg for rewashing and reheating. These changes for a 4-g run are 1 and 2 ppm, respectively.

The data for the silver anodes used in the above operations are given in table 10. The maximum

TABLE 10. *Stability of sheet silver anodes during reheating at 105° C and during rewashing and redrying at 105° C*

Time [a]	Mass of silver in a vacuum (before run)	Mass of silver in a vacuum (after run and one heating)	Mass of silver in a vacuum (after reheat)	Mass of silver in a vacuum (after rewashing and redrying)
	Masses			
Hours	*Grams*	*Grams*	*Grams*	*Grams*
0	13.848625	8.321713	8.321709	8.321711
48	8.321700	2.062902	2.062902	2.062899
432	14.139172	9.282122	9.282125	9.282119
48	9.282119	5.150961	5.150955	5.150948
120	5.096498	2.498740	2.498738	2.498736
72	3.866473	1.237163	1.237162	1.237159
456	14.468994	10.318351	10.318337	10.318351

	Changes in mass		
Hours	*Grams*	*Micrograms*	*Micrograms*
0	5.526912	−4	+2
48	6.258798	0	−3
432	4.857050	+3	−6
48	4.131158	−6	−7
120	2.597758	−2	−2
72	2.629310	−1	−3
456	4.150643	−14	+14
Average		−3	−1

[a] Time between coulometric runs.

change in mass of an anode is -14 μg for reheating and $+14$ μg for rewashing and reweighing. For a faraday determination in which 4 g of silver are corroded these changes are 3 ppm. The average change is -3 μg for reheating and -1 μg for rewashing and reheating. These changes for a 4-g run are less than 1 ppm.

Finally, if the average change, -5 μg, shown in table 9 for reheating the crucible is combined with the average change, -3 μg, shown in table 10 for reheating the sheet-silver anodes the average change in the calculated value of the faraday for a 4-g run would be -2 ppm. The average change, $+8$ μg, shown in table 9 for rewashing and redrying the crucible if combined with the average, -1 μg, shown in table 10 for rewashing and redrying the anodes would cause a change of $+2$ ppm in the calculated value of the faraday.

5. Conclusions

The above results show that the analytical operations required for the determination of the faraday by the anodic dissolution of silver in perchloric acid can be performed accurately. In the absence of an electric current, silver in various states of subdivision is highly stable in aqueous solutions of 20 percent perchloric acid, especially in aqueous solutions of 20 percent perchloric acid containing 0.5 percent or more of silver perchlorate, and in conductivity water at 25° C. The Pyrex apparatus and particularly fritted Pyrex crucibles needed in the analytical procedures are likewise highly stable in the above solutions.

6. References

[1] F. D. Rossini, D. D. Wagman, W. H. Evans, S. Levine, and I. Jaffe, Selected values of chemical thermodynamic properties, NBS Circ. 500 (1952).

[2] K. K. Kelley, Contributions to the data on theoretical metallurgy. IX. The entropies of inorganic substances, Revision (1940) of Data and Methods of Calculation, Bulletin 434, Bureau of Mines, U.S. Dept. Interior (1948).

[3] E. Wichers, A. N. Finn, and W. S. Clabaugh, J. Research NBS 26, 537 (1941) RP1394.

WASHINGTON, D.C.

(Paper 64A1–34)

JOURNAL OF RESEARCH of the National Bureau of Standards—A. Physics and Chemistry
Vol. 64A, No. 1, January–February 1960

Note on the Preparation of Sodium Amalgam in the Form of Pellets

H. S. Isbell, H. L. Frush, and N. B. Holt

(August 26, 1959)

A procedure is described for the preparation of sodium amalgam in the form of pellets.

In connection with the development of methods for the synthesis of radioactive carbohydrates,[1] a procedure and apparatus were previously described [1, 2, 3][2] for the reduction of semimicro quantities of aldonic lactones to sugars. The method employs sodium amalgam together with a slightly soluble, acid salt (sodium binoxalate) as buffer.[3] The amalgam is used in the form of pellets made by dropping the molten amalgam into a "shot tower" of oil. Because other workers have had difficulty in making these pellets, the procedure is now given in detail.

The amalgam is prepared in a 500-ml, round-bottomed, stainless-steel flask having a single neck, with a 24/40 standard-taper joint (outer),[4] and a thermometer inlet. The joint is fitted with a stainless-steel stopper, which has an inlet tube bent at right angles to the stopper and covered with asbestos for convenience in handling. The flask is held in a sturdy, asbestos-covered clamp, which serves as a handle for the vessel during the heating step. An alundum (Soxhlet extraction) thimble 45 mm in diam, in the bottom of which six 1.5-mm holes have been drilled, is held in a second asbestos-covered clamp. The oil bath is a thick-walled heat-resistant glass jar, 6 in. in diam and 18 in. high, containing paraffin oil to within 3 in. of the top (see fig. 1).

To prepare the amalgam, a weighed amount of mercury is placed in the flask, into which a continuous stream of dry nitrogen is passed by means of the inlet tube of the stopper. The required amount of sodium [5] is weighed under paraffin oil, and then cut into pieces just small enough to be readily slipped through the neck of the flask. Each piece is rinsed in a hydrocarbon solvent, such as heptane or toluene, quickly blotted dry, and dropped through the neck of the flask into the mercury; the stopper is immediately replaced. The sodium reacts quickly with the mercury and may be added fairly rapidly because of the atomosphere of nitrogen. After the addition of the sodium is completed, the flask is heated with a

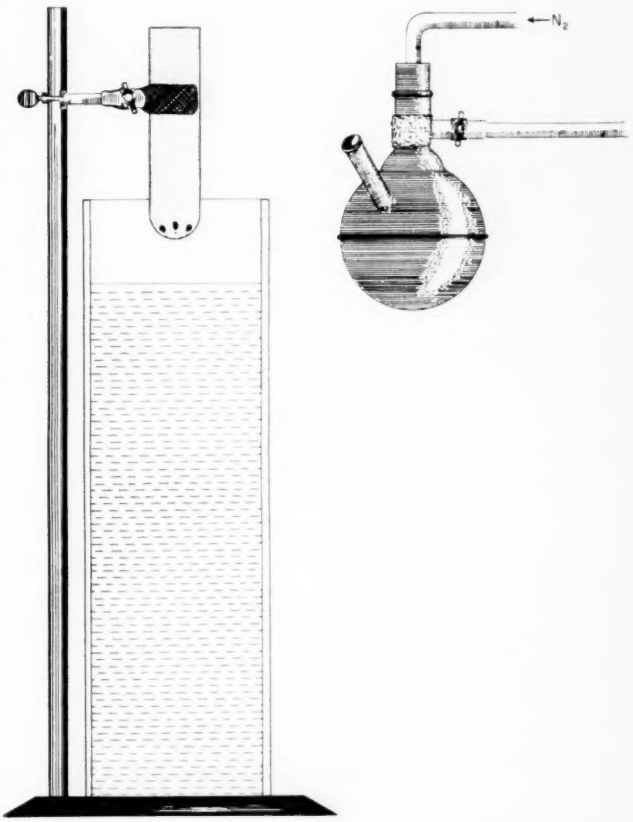

FIGURE 1. *Apparatus used in the preparation of sodium amalgam pellets.*

[1] A project sponsored by the Division of Research of the Atomic Energy Commission.
[2] Figures in brackets indicate the literature references at the end of this paper.
[3] The reduction procedure has also been modified for use with macro quantities of lactones [4].
[4] Scientific Glass Company, Bloomfield, N.J.
[5] For the reduction of aldonic lactones under the conditions employed in this laboratory a 5-percent amalgam has been found to be satisfactory.

Meeker burner until the amalgam is entirely molten. (The presence of remaining solid particles in the amalgam may be detected by the sound of their impact on the walls of the flask when it is given a gentle, swirling motion.) While the amalgam is being prepared, the alundum thimble is heated over another Meeker burner by a second operator. The hot thimble is then so clamped that its bottom is 1 to 2 in. above the surface of the oil, and the molten amalgam is poured into the thimble from the thermometer inlet of the flask. The amalgam flows through the holes in the bottom of the thimble, drops through the oil, and collects at the bottom of the oil bath as small, rather flat pellets.

Optimal conditions for the production of smooth pellets must be determined by trial. If the flask and thimble have not been sufficiently heated, the amalgam may solidify in the thimble. If the holes in the thimble are too large, the product may be somewhat "thready." However, once the optimal conditions have been established, the procedure may be repeated without difficulty.

The entire operation must be performed in an efficient hood. The amalgam is stored under paraffin oil in a wide-mouthed, screw-capped bottle (see fig. 2). Pellets are removed as needed, weighed under oil, and rinsed with an inert, volatile solvent immediately before use.

References

[1] H. S. Isbell, J. V. Karabinos, H. L. Frush, N. B. Holt, A. Schwebel, and T. T. Galkowski, J. Research NBS **48,** 163 (1952) RP2301.

[2] H. S. Isbell, U.S. Patent No. 2,632,005, Mar. 17, 1953.

[3] H. L. Frush and H. S. Isbell, J. Research NBS **50,** 133 (1953) RP2400.

[4] H. L. Frush and H. S. Isbell, J. Research NBS **54,** 267 (1955) RP2588.

FIGURE 2. *Sodium amalgam pellets.*

WASHINGTON, D.C.

(Paper 64A1–35)

Publications of the National Bureau of Standards*

Selected Abstracts

Surface-wave resonance effect in a reactive cylindrical structure excited by an azial line source, A. L. Cullen, *J. Research NBS* **64D,** *No. 1, 13 (1960).*

It is shown that a purely reactive cylinder excited by a neighboring line source can, under suitable conditions, give rise to a radiation pattern closely approximating the function $\cos n\theta$.

In a numerical example, a cylinder of three T.E.M. wavelengths circumference has a surface reactance chosen to emphasize the term $\cos 6\theta$ in the Fourier series of the resultant radiation pattern. It is shown that only 1.1 percent of the total power delivered to the line source is radiated in unwanted modes.

It is also shown that the position of the line source does not affect this result to first order provided that $k(b-a)<<1$, where $b-a$ is the distance of the line source from the cylindrical surface.

Basic experimental studies of the magnetic field from electromagnetic sources immersed in a semi-infinite conducting medium, M. B. Kraichman, *J. Research NBS* **64D,** *No. 1, 21 (1960).*

Using electromagnetic sources, consisting of various dipoles and loops immersed in a concentrated sodium chloride solution, measurements were made verifying the magnetic field propagation equations in air, derived previously by several authors. The receiver was farther away from the source than a wavelength in the conducting medium, but much closer than a wavelength in air.

An expression is derived giving the value of the magnetic field in air due to a rectangular loop with a horizontal axis by assuming the loop to consist of two electric dipoles corresponding to the horizontal members. Experimental data verifying this expression are presented.

Also, using submerged electric dipoles, measurements were made of the magnetic field in air which show that the field is determined solely by the current in the horizontal radiating wires of the dipoles.

Determination of the amplitude-probability distribution of atmospheric radio noise from statistical moments, W. G. Crichlow, C. J. Roubique, A. D. Spaulding, and W. M. Beery, *J. Research NBS* **64D,** *No. 1, 49 (1960).*

During the International Geophysical Year, the National Bureau of Standards established a network of atmospheric noise recording stations throughout the world. The ARN–2 noise recorder at these stations measures three statistical moments of the noise: average power, average voltage, and average logarithm of the voltage. An empirically derived graphical method of obtaining an amplitude-probability distribution from these three moments, and its development, is presented. Possible errors and their magnitudes are discussed.

Recorder survey: Recording surfaces and marking methods, G. Keinath, *NBS Circ. 601, 41 (1959) 30 cents.*

This Circular surveys the characteristics and comparative advantages of continuous traces, dotted traces, and printed characters, as produced by inking, incision, impression, indentation, deposition, heat, light, electric discharge, electron beam, magnetism, chemical action, or fluid streamlines. Descriptive and reference material is included on three physical components of the recording system—the reservoir of material or energy, the marking point or matrix positioned by the measuring element, and the chart surface which preserves the record.

Energy dissipation by fast electrons, L. V. Spencer, *NBS Monograph 1, 70 (1959) 45 cents.*

Tabulations are given of the energy dissipated by fast electrons at different distances from nomoenergetic electron sources, for plane perpendicular and point isotropic sources. A summary of the theoretical methods and data utilized, and a table of spatial moments are also included.

Calculated behavior of a fast neutron spectrometer based on the total absorption principle, J. E. Leiss, *Tech. Note 10 (PB151369) $1.00.*

Performance calculations for a total absorption fast neutron spectrometer are presented. The spectrometer detecting element is a boron-10-loaded liquid scintillator. By making the scintillator a thin disk, only those neutrons whose first collision is a large-energy-loss hydrogen collision have appreciable chance of remaining in the spectrometer long enough to be captured. The expected energy resolution and efficiency of this type of spectrometer are determined, and are comparable to other types of fast neutron spectrometers.

Penetration of gamma rays from isotropic sources through aluminum and concrete, M. J. Berger and L. V. Spencer, *Tech. Note 11 (PB151370) 50 cents.*

Semianalytical expressions, with numerically specified parameters, are given which represent the gamma ray dose distribution in infinite aluminum or concrete media for sources that are monoenergetic (with energies between 10.22 Mev and 0.0341 Mev), isotropic, and have the form of an infinite plane, point, disk, or spherical surface.

Precise time synchronization of widely separated clocks, A. H. Morgan, *Tech. Note 22 (PB151381) $1.50.*

This paper describes known prescise methods of setting a group of widely separated clocks to precisely the same time and keeping them in close agreement indefinitely; most of the proposed methods are now available. An estimate of the accuracies of each method are given. Some discussion of high frequency radio propagation theory pertinent to two of the methods and a few sets of measurements of the propagation delay time of high frequency signals from WWV to WWVH are given. Several graphs and tables are included to simplify some of the calculations.

Design of single frequency filters, F. F. Fulton, Jr., *Tech. Note 23 (PB151382) 50 cents.*

Efficient procedures are shown for designing filters formed by a number of identical resonant circuits loosely coupled together, and which are required to accept one narrow band of frequencies and reject another narrow band somewhat removed in frequency without any special requirements on the shape of the attenuation curve in between these regions. The design is based on using a large number of sections.

Note on bivariate linear interpolation for analytic functions, W. Gautschi, *Math. Tables and Other Aids to Computation* **13,** *No. 66, 91 (1959).*

A detailed study of the accuracy of bivariate linear interpolation is applied on real and imaginary parts of an analytic function with some suggestions for improving the accuracy.

Absorption of radiation by a cylindrical sample of a strong absorber, P. H. Fang and I. A. Stegun, *Letter to Editor, J. Chem. Phys.* **31,** *267 (1959).*

The connection between the Bessel function and an integral which occurs in an absorption of radiation by a strong absorber is discussed. The effect of using this exact evaluation in the analysis of experimental data is indicated.

PILOT—A new multiple computer system, A. L. Leiner, W. A. Notz, J. L. Smith, and A. Weinberger, *J. Assoc. Computing Mach.* **6,** *No. 3, 313 (1959).*

The PILOT data processor is a high-speed multiple computer system, more than 100 times faster than SEAC. It contains three interconnected computers for rapid processing of data, and also contains multiple input-output channels for rapid transfer of data into and out of the system. All of these units operate concurrently in a coordinated fashion. A summary description is given of the overall logical plan of the system including the principal characteristics of the first computer, the second computer, the third computer, the internal controls, and the external controls.
The system combines internal processing capabilities that are fast and versatile with external communication capabilities that are exceptionally flexible. This combination permits the internal power of the machine to be exploited readily by the outside world, either by other automatic devices or by human operators.

Analysis of vibrational relaxation data in shock wave experiments, K. E. Shuler, *J. Chem. Phys.* **30,** *No. 6, 1631 (1959).*

In the analysis of the data on vibrational relaxation behind shock waves it is necessary to take account of the fact that more than the two lowest vibrational states may be appreciably populated. An analysis for systems with many quantum states is carried out for an ensemble of harmonic oscillators.

Branched-chain higher sugars. I. A 9-aldo-4-C-formyl-nonose derivative, R. Schaffer and H. S. Isbell, *J. Am. Chem. Soc.* **81,** *2178 (1959).*

Two molecules of 5-aldo-1,2-*O*-isopropylidene-D-*xylo*-pentofuranose in alkaline solution combine to form a branched-chain decose derivative (I) by an aldol condensation. An explanation is offered for the occurrence of this condensation, which is not a typical carbohydrate reaction. A proof of the complete structure and configuration of I is presented and the compound is named 9-aldo-4-*C*-formyl-1,2:8,9-di-*O*-isopropylidine-L-*xylo*-L-*ido*-nono-1,4:9,6-difurano-4(1),7-α-pyranose.

The use of a vacuum microbalance in studies of electron tube materials, G. F. Rouse, *Proc. 4th Natl. Conf. on Tube Technigues, Sept. 10 to 12, 1958, Sponsored by the Advisory Group on Electron Tubes, p. 262 (New York University Press, New York, N.Y., 1959).*

Several of the physical and chemical processes which occur in an electron tube involve changes of mass. For instance, sublimation from the cathode or breakdown of the coating decrease the cathode mass. Absorption or adsorption of gas by a tube part increases its mass. If change of mass can be measured with sufficient accuracy and the measured change can be correlated with controlled experimental conditions, a better understanding of the factors governing particular processes may be possible. This greater understanding may make it possible to control the processes so as to minimize any harmful effects which might arise from them.
A study based on this idea of measuring change of mass was initiated some time ago, a vacuum microbalance being the test device.

Effects of gamma radiation on collagen, J. Cassel, *J. Am. Leather Chemists' Assoc.* **LIV,** *No. 8, 432 (1959).*

The effect of gamma radiation was determined on collagen exposed as a purified steerhide powder and as kangaroo tail tendon. Absorbed radiation ranged from 5 to 220 megarads. Apparent even at low radiation levels were the decrease in shrinkage temperature and increased water-solubility. The same decrease in shrinkage temperature was observed for tendons irradiated in the presence or absence (vacuum) of air. The shrinkage temperature was not influenced by the moisture content of the tendon during irradiation. Relatively little damage to amino acid structure was observed at absorption doses less than 20 megarads. The amino acid components most susceptible to alteration by radiation are methionine, phenylalanine, and threonine, while those least damaged were alanine, glycine, hydroxyproline, proline, and arginine. Radiation causes a nonhydrolytic type of peptide chain scission. High ultraviolet absorbance by the water-soluble fractions is due to formation of specific complex ultraviolet-absorbing groups rather than to light scattering.

Standards for neutron flux measurement and neutron dosimetry, R. S. Caswell, E. R. Mosburg, Jr., and J. Chin, *2d United Nations Intern. Conf. on the Peaceful Uses of Atomic Energy* **21,** *Health and Safety: Dosimetry and Standards, P 752 USA, p. 92 (1959).*

Known neutron fluxes for laboratory use may be obtained from sources in which neutrons are produced by a natural radioactivity. An absolutely calibrated radium-beryllium photoneutron source is used as a primary standard of source strength. Methods for intercomparisons and calibrations of neutron sources are given, together with the results of international source intercomparisons. A standard thermal neutron flux geometry, absolutely calibrated by $B^{10}(n, \alpha)$ reaction rate is described. Methods for separating neutron and gamma ray dose in mixed radiation fields by use of proportional counters with pulse-height discrimination are discussed.

A study of limb flares and associated events, C. Warwick and M. Wood, *Astrophys. J.* **129,** *No. 3, 801 (1959).*

Measured heights of limb flares were used to derive a frequency distribution of flare height and to assess the importance of height in the production of flare associated events. The observed height distributions can be explained by a real distribution with maximum at zero, decreasing toward greater heights. The occurrence of SWF (shortwave fadeout) depends strongly on flare height. This dependence could be explained as an effect either of absorption of the ionizing radition in the sun's atmosphere or of a mechanism of production of ionizing radiation that depends critically on the height of the flare. Center-to-limb variation of SWF occurrence, while not conclusive, favors the former interpretation. The relation between optical flare characteristics and occurrence of associated bursts of radionoise is strongest for decimeter bursts and weaker for bursts at meter wavelengths.

Low even configurations in the first spectrum of ruthenium (Ru I), R. E. Trees, *J. Opt. Soc. Am.* **49,** *838 (1959).*

The theory of intermediate coupling with configuration interaction is used to calculate energy levels and g-values in the $4d^6\ 5s^2$, $4d^7\ 5s$, and $4d^8$ configurations of Ru I. By using 15 parameters, the positions of 57 observed levels are calculated with a mean deviation of ± 54 cm^{-1} between theory and experiment. There are unexplained differences greater than 500 cm^{-1} for two other levels, one of which is well-confirmed by experiment. Overall agreement between observed and calculated g-values is within ± 0.006. Linear relations are obtained between similarly defined electrostatic parameters in the three configurations.

Magnetic study of the frozen products from the nitrogen microwave discharge, B. J. Fontana, *J. Chem. Phys.* **31,** *No. 1, 148 (1959).*

Magnetic susceptibility measurements have been made during the deposition in a solid N_2 matrix of nitrogen atoms produced in a microwave discharge. From the nitrogen atom concentration in the gas reaching the condensing surface and the magnetic measurements on the deposited solid, it is concluded that a concentration of about 0.2 to 0.5 mole percent N cannot be exceeded in the solid phase. Such concentrations are observed only for relatively brief intervals after which catastrophic recombination occurs. Stable, long-lived concentrations which account for the previously reported thermal and light emission effects which accompany warmup of such deposits are estimated to be less than 0.01 to 0.04 mole percent N. Susceptibility measurements are based on comparison with solid molecular oxygen and the calculation of N atom concentrations assumes that the susceptibility of dilute N atoms in an N_2 matrix approximates that of the free gas.

The thermal E.M.F. of several thermometric alloys, R. L. Powell and M. D. Bunch, *Suppl. au Bull. inst. intern. froid (Delft, Holland), Comm.* **1,** *129 (1958).*

Measurements of the thermal emf of Au-2.1 at. percent Co, Constantan and "normal" silver versus copper have been made from 4° K to 300° K, with reference termperatures at the boiling points of liquid helium, liquid hydrogen, and liquid nitrogen. The uniformity of each type of thermo element was tested by simultaneous cablibration of several samples from the same melt.

Geometrical anistropy of magnetic materials in waveguides and cavities, L. A. Steinert, *J. Appl. Phys.* **30,** *1109 (1959).*

The perturbations caused by magnetized ferrite materials placed inside waveguides or resonant cavities depend upon the geometrical shape of the material as well as its intrinsic properties.
In the case of isotropic ferrite ellipsoids, a general formulation is given for the ratio of the radiofrequency magnetization $4\pi\vec{m}$ of the material to the uniform radiofrequency field $\vec{h}_0$ external to the material. A few special examples are included.

Radioactivity standardization in the United States, W. B. Mann and H. H. Seliger, *2d United Nations Intern. Conf. on the Peaceful Uses of Atomic Energy* **21,** *Health and Safety: Dosimetry and Standards, P/750 USA, p. 90 (1959).*

Recent developments are described in radioactivity standardization by compensated gas counting and liquid scintillation counting.

Magnetic interaction of H_3, V. Griffing, J. L. Jackson, and B. J. Ransil, *J. Chem. Phys.* **30,** *No. 4, 1066 (1959).*

The results of an LCAO–MO–SCF–CI calculation of the $^2\Sigma_u$ ground state of linear H_3 are presented and the wave functions obtained from this calculation are used to calculate the general features of the electron spin resonance spectrum. The calculation is carried through for the Fermi contact interaction, which is the principal interaction between the proton and electron spins. It is found that the off-diagonal elements of the hyperfine interaction matrix may not be neglected in that they split degenerate levels. The predicted spectrum, however, does not agree with the observed electron spin resonance spectrum of discharged hydrogen deposited at liquid helium temperatures. In addition the expected electron spin resonance spectrum of H_2^+ has been calculated from the exact wave function.

The nature, cause and effect of the porosity in electrodeposits. IV. Influence of gas bubbles on the formation of pores, F. Ogburn and D. W. Ernst, *Plating* **46,** *957 (1959).*

One mechanism for the formation of a pore in electrodeposits involves the inclusion of a surface gas bubble. Whether the pore becomes continuous or bridged-over depends upon the relative rates of hydrogen discharge and nickel deposition. A cell is described which permits the observation of a simulated "cross section" of a nickel deposit while it is being formed. A series of photomicrographs obtained with this cell shows the enclosing of a gas bubble.

The nature, cause and effect of the porosity in electrodeposits. V. An evaluation of the sensitivity of the ferroxyl test, F. Ogburn, D. W. Ernst, and W. H. Roberts, *Plating* **46,** *1052 (1959).*

The importance of a good porosity test prompted the determination of the sensitivity of the ferroxyl test. Strausser's modification of the test was used to determine the porosity of the gold coatings on steel. A photographic process determined the porosity of goldfoil obtained by stripping the steel away with acid. A filar micrometer was used to measure the size of the pores present in the goldfoil. A comparison of the porosities of the goldfoil as determined by both methods gave the following results for pores between 0.05 and 0.5 mil in diameter: (1) less than 50 percent of all pores present are detected by the ferroxyl test; and (2) of this number, the larger the pore the more likely it will be detected.

Electrical discharge induced luminescence of solids at low temperatures, L. J. Schoen and R. E. Rebbert, *J. Mol. Spect.* **3,** *No. 4, 417 (1959).*

Luminescence of condensed nitrogen-oxygen-argon systems at low temperatures has been excited by a-c and d-c discharge techniques. Typical atomic and molecular spectra obtained by these methods are described. The structure and wavelengths of the β line group attributed to trapped oxygen atoms ($^1S \rightarrow {}^1D$) and the wavelengths of the A and Vegard-Kaplan band systems are compared in nitrogen and argon matrices. In argon a line group interpreted as the $^1S \rightarrow {}^3P$ atomic oxygen transition has been observed. The principal mechanism of excitation under the conditions employed appears to be ion-electron bombardment of the deposited solid.

Program of the International Commission on radiological units and measurements, L. S. Taylor, L. H. Gray, and H. O. Wyckoff, *2d United Nations Intern. Conf. on the Peaceful Uses of Atomic Energy* **21,** *Health and Safety: Dosimetry and Standards, P/2243 WHO, p. 81 (1959).*

A short review is given of the history of the ICRU, the program which resulted in its 1956 report, and the current program under way which will result in a new report next year. Special emphasis is placed upon the international character of the organization and its efforts to achieve international agreement on the measurement of radiation sources.

Spectrum of thin target bremsstrahlung bounded by a forward circular cone, J. H. Hubbell, *J. Appl. Phys.* **30,** *No. 7, 981 (1959).*

The Schiff expression for the cross section per nucleus, for thin-target bremsstrahlung into the angular and energy ranges $d\theta_0$ and dk, is integrated analytically over angle from zero to $\bar{\theta}_0$. Results are shown for the case $Z=78$, $E_0-mc^2=40$ Mev and $\bar{\chi}=0.5$, 1, 2, 4, and 8, where E_0-mc^2 is the kinetic energy of the incoming electron and $\bar{\chi}$ is the reduced angle $\bar{\theta}_0 E_0/mc^2$. The fraction of the total cross section included in

a cone of angle $\bar{\theta}_0$ can be approximated to within 20 percent by $\bar{\chi}^2/(1+\bar{\chi}^2)$. At $\bar{\chi}=1$, or $\bar{\theta}_0=0.723°$, the ratio of energy delivered by photons above $(E_0-mc^2)/2$ to that below is 9 percent greater than for the limiting spectral shape at $\bar{\theta}_0=0$, or that given by the Schiff expression at $\theta_0=0$, and 13 percent greater than for the spectrum integrated over all angles. For a target of finite thickness, multiple electron scattering should partially suppress the spectral dependence on $\bar{\ }$.

Negative atomic ions, H. R. Johnson and F. Rohrlich, *J. Chem. Phys.* **30,** *1068 (1959).*

A semiempirical method is proposed for the computation of the electron affinities of negative atomic ions by extrapolation from the ionization potentials of the corresponding isoelectronic sequences. The method is based on a formula which can be justified on physical grounds and of which at least two parameters have direct physical interpretation. The results for the two short periods agree with experiments, with the important exception of S^-. The method predicts a stable N^- ion of small binding energy. The excited states and the fine-structure splitting can also be obtained by extrapolation based on theoretical formulas. The use of these formulas seems preferable to the method by Bates and Moiseiwitsch, but the results on excited states are the same.

The very low-frequency emissions generated in the earth's exosphere, R. M. Gallet, *Proc. IRE,* **47,** *No. 2, 211 (1959).*

Naturally occurring, very low-frequency signals not associated with lightning discharges, and strongly correlated with solar activity, have been recognized nearly as long as the atmospheric whistlers which have their genesis in lightning discharges. Whereas whistlers have been satisfactorily explained, until recently these other phenomena have not.
From the examination of a large quantity of high resolution spectograms, it has been deduced that a major fraction, if not all, of these other "noises" are excited in the exosphere by streams and bunches of high-speed ionized particles precipitating into the ionized atmosphere in the presence of the earth's magnetic field. The electromagnetic waves excited are then propagated in the manner of whistlers.
The excitation mechanism is similar to the operation of a traveling-wave tube. Two frequencies are simultaneously generated, and their values depend only on the three parameters: local electronic density in the exosphere, local magnetic field intensity, and particle velocity V.

Reaction of hydrogen atoms with solid oxygen at 20° K, R. Klein and M. D. Scheer, *J. Chem. Phys.* **31,** *No. 1, 278 (1959).*

Hydrogen atoms, produced in the gas phase by thermal decomposition on a hot tungsten ribbon, react with solid oxygen at 20° K. The primary reaction is most probably $H+O_2 \rightarrow HO_2$.

Application of the Williams-Landel-Ferry equation to silicate glasses, A. B. Bestul, *Glastech. Ber. (Frankfurt, Germany)* **32 K,** *No. VI, 59 (1959).*

Viscosity data for silicate glasses in the glass transformation region have been fitted to the Williams-Landel-Ferry equation. The values resulting for one of the two constants are about the same as those obtained for organic glasses. The values for the second constant are much different from those for organic glasses. This second constant has been shown by Bueche to contain the volume coefficient of thermal expansion, α_2, about the transformation temperature. If the applicable values of α_2 are extracted from the second constant, the residues are about the same for silicate glasses and organic glasses. These findings confirm for silicate glasses the conclusion of Williams, Landel, and Ferry and of Bueche concerning the insensitivity to details of molecular structure of the properties of glass-forming substances which control their temperature dependence of molecular relaxation times.

Glow discharge spectra of copper and indium above aqueous solutions, D. E. Couch and A. Brenner, *Tech. Notes, J. Electrochem. Soc.* **106,** *628 (1959).*

An unusual glow discharge was produced between a tungsten electrode and an aqueous solution of cupric or indium salts. This glow was not produced by other salts or by a discharge to a fused salt bath containing copper.

Gaseous heat conduction at low pressures and temperatures, R. J. Corruccini, *Vacuum* **7–8,** *19 (Pergamon Press Ltd., London, England, 1959).*

Over the large temperature differences that can exist in vacuum insulation of cryogenic devices some of the assumptions on which the formulas for free molecule heat conduction are based are not strictly valid. The consequences of this are discussed, and some incorrect usages are pointed out. Working formulas and auxiliary data on mean free paths and accommodation coefficients at cryogenic temperatures are presented.

Multiple ionization of sodium vapor by electron impact, V. H. Dibeler and R. M. Reese, *J. Chem. Phys.* **31,** *No. 1, 282 (1959).*

Mass spectrometric studies are made of multiply-charged ions in sodium vapor. The results indicate that within a few volts of threshold, the probability of ionization increases as the nth power of the energy in excess of threshold, where n is the number of charges on the ion. This is in agreement with Geltman's theoretical treatment of the threshold law for ionization by electrons.

Vibrational intensity distributions in the nitrogen afterglow, U. H. Kurzweg and H. P. Broida, *J. Mol. Spect.* **3,** *No. 4, 388 (1959).*

Nitrogen afterglows produced in a fast-flow system by an electrodeless discharge have been studied as a function of pressure, flow, diluent, and temperature. Intensity measurements of the N_2 1st positive bands ($B^3\Pi - A^3\Sigma$) responsible for the visible afterglow were obtained by means of a photoelectric recording monochromator. It is shown that the vibrational intensity distributions are not explainable by the generally accepted, preassociation model of the afterglow phenomena. High resolution scans depicting the relative intensity behavior of the $B^3\Pi - A^3\Sigma$ system under a variety of conditions are presented.

Influence of crystallographic orientation on the pitting of iron in distilled water, J. Kruger, *J. Electrochem. Soc.* **106,** *No. 8, 736 (1959).*

The frequency of pitting on iron exposed to distilled water was found to depend on crystallographic orientation. The number of pits per unit area was highest for {110}.

A direct-reading viscometer, M. R. Shafer, *Instruments and Control Systems* **32,** *No. 7, 1044 (1959).*

Prototype instruments for determining directly the kinematic viscosity of liquids have been developed using the restrictions-in-series principle. Although not an absolute method, a simple calibration with liquids of known viscosities permits the subsequent measurement of the viscosities of other liquids by reading a single manometric column; no corrections or other calculations are required. Theory, construction, and operation of instruments having the range 0.5 to 5.0 centistokes are discussed.

Journal of Research, Section 64D, No. 1, January–February 1960. 70 cents.

Effect of antenna size on gain, bandwidth, and efficiency, R. G. Harrington.

Surface-wave resonance effect in a reactive cylindrical structure excited by an azial line source, A. L. Cullen. (See above abstract.)

Basic experimental studies of the magnetic field from electromagnetic sources immersed in a semi-infinite conducting medium, M. B. Kraichman. (See above abstract.)

A very-low-frequency antenna for investigating the ionosphere with horizontally polarized radio waves, R. S. Macmillan, W. V. T. Rusch, and R. M. Golden.

Effects of high-altitude nuclear explosions on radio noise, C. A. Samson.

Measured frequency spectra of vlf atmospheries. T. Obayashi.

Determination of the amplitude-probability distribution of atmospheric radio noise from statistical moments, W. G. Crichlow, C. J. Roubique, A. D. Spaulding, and W. M. Beery. (See above abstract.)

Measurements of coastal deviation of high-frequency radio waves, C. W. McLeish.

An exact earth-flattening procedure in propagation around a sphere. B. Y.-C. Koo and M. Katzin.

Limit of spatial resolution of refractometer cavities, W. J. Hartman. Conference on arctic communication.

Tropospheric scatter propagation and atmospheric circulations, W. F. Moler and D. B. Holden.

Layered earth propagation in the vicinity of Point Barrow, Alaska, G. M. Stanley.

Announcement of systematic ionospheric electron density data.

Tables of the bivariate normal distribution function and related functions. NBS AMS50, $3.25.

Prediction of the cumulative distribution with time of ground wave and tropospheric wave transmission loss. Part 1. The prediction formula, P. L. Rice, A. G. Longley, and K. A. Norton, Tech. Note 15 (PB151374), $1.50.

Analysis of ionospheric vertical soundings for electron density profile data. 1. Facilities for convenient manual reduction of ionograms, J. W. Wright and R. B. Norton, Tech. Note 14 (PB-151373), 50 cents.

Analysis of ionospheric vertical soundings for electron density profile data. II. Extrapolation of observed electron density profiles above h_{max} F2, J. W. Wright, Tech. Note 19 (PB151378), 50 cents.

New approach in the theory of satellite orbits, J. P. Vinti, Phys. Rev. Letters **3,** No. 1, 8 (1959).

Production of embossing plates from texture patterns by electroforming methods, J. P. Young and V. A. Lamb, Plating **46,** 1033 (1959).

Method of evaluating the clinical effect of warping a denture: Report of a case, J. B. Woelfel and G. C. Paffenbarger, J. Am. Dental Assoc. **59,** 250 (1959).

The sound transmission loss of some building construction, R. V. Waterhouse, R. D. Berendt, and R. K. Cook, Noise Control **5,** No. 4, 40 (1959).

Cryogenic insulation, R. H. Kropschot, Am. Soc. Heating, Refrig. and Air-Conditioning Engrs. **1,** No. 9, 48 (1959).

End plate modification of X-band TE011 cavity resonators, M. S. Thompson, F. E. Freethey, and D. M. Waters, IRE Trans. on Microwave Theory Tech. **MTT–7,** 388 (1959).

Evolution of amplified waves leading to transition in a boundary layer with zero pressure gradient, P. S. Klebanoff and K. D. Tidstrom, NASA Tech. Note D–195, 1 (1959).

Microwave reflectometer, G. F. Engen and R. W. Beatty, IRE Trans. on Microwave Theory Tech. **MTT–7,** 351 (1959).

Penetration and diffusion of X-rays, U. Fano, L. V. Spencer, and M. J. Berger, Encyclopedia of Phys. **38,** No. 2, 660 (1959).

Problems of the experimeter, W. J. Youden, Natl. Conv. Trans. Am. Soc. Quality Control, p. 41 (1959).

Some characteristics of VLF propagation using atmospheric waveforms, W. L. Taylor and L. J. Lange, Recent Advances in Atmospheric Electricity (Proc. 2d Conf. on Atmospheric Elec.), Portsmouth, New Hampshire, May 20 to 23, 1958, p. 609 (Pergamon Press, Inc., New York, N.Y., 1958).

The changing character of chemical research in government, E. Wichers, The Chemist **XXXVI,** No. 7, 260 (1959).

Study of the setting of plaster, K. D. Jorgensen and A. S. Posner, J. Dental Research, **38,** No. 3, 491 (1959).

Optimum antenna height for ionospheric scatter propagation, R. G. Merrill, IRE Conv. Record **7,** Pt. 1, 10 (1959).

Corrosion of type 310 stainless steel by synthetic fuel oil ash, H. L. Logan, Corrosion **15,** 443t (1959).

Physical research, Pt. 2, G. C. Paffenbarger and W. Souder, J. Am. Dental Assoc. **58,** 98 (1959).

The structure of electrolytic solutions, W. J. Hamer (John Wiley and Sons, Inc., New York, N.Y., 1959).

Width of cracks in concrete at the surface of reinforcing steel evaluated by means of tensile bond specimens, D. Watstein and R. G. Mathey, J. Am. Concrete Inst. **31,** No. 1, 47 (1959).

Recent advances in cryogenic engineering, R. B. Jacobs, Am. Rocket Soc. ARS J. **29,** 245 (1959).

Transistorized velocimeter for measuring speed in the sea, C. E. Tschiegg, J. Acoust. Soc. Am. **31,** No. 7, 1038 (1959).

Inclusion theorems for congruence subgroups, M. Newman and I. Reiner, Trans. Am. Math. Soc. **91,** No. 3, 369 (1959).

Factors affecting modulation techniques for VHF scatter systems, J. W. Koch, IRE Trans. Commun. Systems **CS–7,** No. 2, 77 (1959).

Calculated patterns of slotted elliptic-cylinder antennae, J. R. Wait and W. E. Mientka, Appl. Sci. Research **B 7,** 449 (1959).

Free radical chemistry, J. W. Moyer and A. M. Bass, Chem. and Eng. News p. 51 (Aug. 24, 1959).

Discussion of the papers of Messrs. Satterthwaite and Budne, W. J. Youden, Technometrics **1,** No. 2, 157 (1959).

A new aid for the rapid determination of absorption corrections by Albrecht's method, D. K. Smith, Acta Cryst. (Copenhagen, Denmark) **12,** Pt. 6, 479 (1959).

Radiation attenuation data, H. O. Wyckoff, Radiation Hygiene Handbook, edited by H. Blatz, sec. 8, p. 1 (McGraw-Hill Book Co., New York, N.Y.) (1959).

Exposure standards and radiation protection regulations, L. S. Taylor, Radiation Hygiene Handbook, edited by H. Blatz, sec. 3, p. 2 (McGraw-Hill Book Co., New York, N.Y., 1959).

Properties of rutile (titanium dioxide), F. A. Grant, Rev. Modern Phys. **31,** 646 (1959).

The interlaboratory evaluation of testing methods, J. Mandel and T. W. Lashof, ASTM Bull. No. 239, 53 (1959).

Measurements made by matching with known standards, W. J. Youden, W. S. Connor, and N. C. Severo, Technometrics **1,** No. 3, 101 (1959).

Evacuated powder insulation for low temperatures, M. M. Fulk, Progress in Cryogenics—1, 65 (Heywood and Co., Ltd., London, England, 1959).

The following papers were published in the Proc. 5th Tech. Session on Bone Char, 1957 (Bone Char Research Project, Inc., Charlestown, Mass., 1959):

Introductory remarks, A. V. Astin, p. 1.
Analysis of liquid sugars, E. J. McDonald, p. 77.
Development of a new test for the abrasion hardness of bone char, F. G. Carpenter, p. 99.
Effects of controlled decarbonization on the performance of service synthad, F. W. Schwer, W. V. Loebenstein, and E. P. Barrett, p. 145.
Some mechanisms of color and ash removal by bone char, A. Gee, p. 163.
Survey of variations in use for conducting laboratory-scale column filteration tests, V. R. Deitz, p. 237.
Comparison of column decolorization experiments with theory, W. V. Loebenstein, p. 253.
Sugar retention by char, F. G. Carpenter, p. 279.
Removal or organic anions by bone char, V. R. Deitz and H. M. Rootare, p. 297.

**Publications for which a price is indicated (except for Technical Notes) are available only from the Superintendent of Documents, U.S. Government Printing Office, Washington 25, D.C. (foreign postage, one-fourth additional). Technical Notes are available only from the Office of Technical Services, U.S. Department of Commerce, Washington 25, D.C. (order by PB number). Reprints from outside journals and the NBS Journal of Research may often be obtained directly from the author.*

UNITED STATES
GOVERNMENT PRINTING OFFICE
DIVISION OF PUBLIC DOCUMENTS
WASHINGTON 25, D.C.

OFFICIAL BUSINESS

PENALTY FOR PRIVATE USE TO AVOID PAYMENT OF POSTAGE, $300 (GPO)

National Bureau of Standards Journal of Research
A. Physics and Chemistry

Vol. 64A, No. 1

January–February 1960

Contents

	Page
The "1958 He^4 scale of temperatures." F. G. Brickwedde, H. van Dijk, M. Durieux, J. R. Clement, and J. K. Logan.	1
Energy levels and spectrum of neutral helium (^{4}He I). William C. Martin.	19
Vibration-rotation structure in absorption bands for the calibration of spectrometers from 2 to 16 microns. Earle K. Plyler, Alfred Danti, L. R. Blaine, and E. D. Tidwell.	29
Combustion calorimetry with fluorine: constant pressure flame calorimetry. G. T. Armstrong and R. S. Jessup.	49
Pits in metals caused by collision with liquid drops and rigid steel spheres. Olive G. Engel.	61
Theory of formation of polymer crystals with folded chains in dilute solution. John I. Lauritzen, Jr., and John D. Hoffman.	73
Studies of beryllium chromite and other beryllia compounds with R_2O_3 oxides. C. E. Weir and A. Van Valkenburg.	103
Uranium-platinum system. J. J. Park and D. P. Fickle.	107
Nitriding phenomena in titanium and the 6Al-4V titanium alloy. J. R. Cuthill, W. D. Hayes, and R. E. Seebold.	119
Stability of silver and Pyrex in perchloric acid-silver perchlorate solutions and in conductivity water. D. Norman Craig, Catherine A. Law, and Walter J. Hamer.	127
Note on the preparation of sodium amalgam in the form of pellets. H. S. Isbell, H. L. Frush, and N. B. Holt.	135
Publications of the National Bureau of Standards.	137

For sale by the Superintendent of Documents, U.S. Government Printing Office, Washington 25, D.C. Price 70 cents (single copy). Subscription price: $4.00 a year; $0.75 additional for foreign mailing.

UNITED STATES GOVERNMENT PRINTING OFFICE, WASHINGTON : 1960